

Opportunities in electrically tunable 2D materials beyond graphene: Recent progress and future outlook

Cite as: Appl. Phys. Rev. **8**, 041320 (2021); <https://doi.org/10.1063/5.0051394>

Submitted: 25 March 2021 • Accepted: 07 September 2021 • Published Online: 30 November 2021

 Tom Vincent,  Jiayun Liang,  Simrjit Singh, et al.



View Online



Export Citation



CrossMark

ARTICLES YOU MAY BE INTERESTED IN

[Recent progress on 2D magnets: Fundamental mechanism, structural design and modification](#)
Applied Physics Reviews **8**, 031305 (2021); <https://doi.org/10.1063/5.0039979>

[Domain wall dynamics in two-dimensional van der Waals ferromagnets](#)
Applied Physics Reviews **8**, 041411 (2021); <https://doi.org/10.1063/5.0062541>

[Neuromorphic computing: Devices, hardware, and system application facilitated by two-dimensional materials](#)
Applied Physics Reviews **8**, 041313 (2021); <https://doi.org/10.1063/5.0067352>



Applied Physics
Reviews

Read. Cite. Publish. Repeat.

19.162
2020 IMPACT FACTOR*

Opportunities in electrically tunable 2D materials beyond graphene: Recent progress and future outlook

Cite as: Appl. Phys. Rev. **8**, 041320 (2021); doi: [10.1063/5.0051394](https://doi.org/10.1063/5.0051394)

Submitted: 25 March 2021 · Accepted: 7 September 2021 ·

Published Online: 30 November 2021



View Online



Export Citation



CrossMark

Tom Vincent,¹  Jiayun Liang,²  Simrjit Singh,³  Eli G. Castanon,¹  Xiaotian Zhang,²  Amber McCreary,⁴ 
 Deep Jariwala,^{3,a)}  Olga Kazakova,^{1,b)}  and Zakaria Y. Al Balushi^{2,c)} 

AFFILIATIONS

¹Department of Quantum Technology, National Physical Laboratory, Hampton Road, Teddington TW11 0LW, United Kingdom

²Department of Materials Science and Engineering, University of California, Berkeley, California 94720, USA

³Department of Electrical and Systems Engineering, University of Pennsylvania, Philadelphia, Pennsylvania 19104, USA

⁴Nanoscale Device Characterization Division, Physical Measurement Laboratory, National Institute of Standards and Technology, Gaithersburg, Maryland 20899, USA

^{a)}dmj@seas.upenn.edu

^{b)}olga.kazakova@npl.co.uk

^{c)}Author to whom correspondence should be addressed: albalushi@berkeley.edu

ABSTRACT

The interest in two-dimensional and layered materials continues to expand, driven by the compelling properties of individual atomic layers that can be stacked and/or twisted into synthetic heterostructures. The plethora of electronic properties as well as the emergence of many different quasiparticles, including plasmons, polaritons, trions, and excitons with large, tunable binding energies that all can be controlled and modulated through electrical means, has given rise to many device applications. In addition, these materials exhibit both room-temperature spin and valley polarization, magnetism, superconductivity, piezoelectricity that are intricately dependent on the composition, crystal structure, stacking, twist angle, layer number, and phases of these materials. Initial results on graphene exfoliated from single bulk crystals motivated the development of wide-area, high purity synthesis and heterojunctions with atomically clean interfaces. Now by opening this design space to new synthetic two-dimensional materials “beyond graphene,” it is possible to explore uncharted opportunities in designing novel heterostructures for electrically tunable devices. To fully reveal the emerging functionalities and opportunities of these atomically thin materials in practical applications, this review highlights several representative and noteworthy research directions in the use of electrical means to tune these aforementioned physical and structural properties, with an emphasis on discussing major applications of beyond graphene 2D materials in tunable devices in recent years and an outlook of what is to come in the next decade.

Published under an exclusive license by AIP Publishing. <https://doi.org/10.1063/5.0051394>

TABLE OF CONTENTS

I. INTRODUCTION	2	B. Ferroelectric memristors.	7
II. MATERIALS BEYOND GRAPHENE	3	C. Photonics and electro-optic devices.	8
III. CURRENT STATUS IN ELECTRICAL TUNABILITY OF 2D MATERIALS BEYOND GRAPHENE.	3	1. Light harvester	8
A. Logic and memory devices	3	2. Vertical heterostructures	8
1. Gate tunable transport in diodes and switching devices	3	3. Light emitting devices	9
2. Gate-tunable memristive phenomena in atomically thin materials.	6	4. Optical modulators, mirrors, etc.	12
		D. Sensors	14
		1. Gas sensors	14
		2. Biosensors	18
		3. Strain sensors	21

IV. OUTLOOK ON EMERGING AREAS AND APPLICATION OPPORTUNITIES	23
A. Tunable quasiparticle dynamics in 2D vdW materials	23
1. Interlayer excitons	23
2. Exciton-polaritons	23
B. Electrically controlled magnetism in 2D vdW materials	24
1. Magnetism in 2D van der Waals materials and opportunities	24
2. Gate controlled magnetism in 2D vdW materials	25
3. Gate control of critical spin fluctuations	28
4. Emerging device applications	28
C. Piezo- and ferro-electricity in 2D vdW materials	31
1. Piezoelectricity in 2D vdW materials	31
2. Ferroelectricity in 2D vdW materials	33
3. 2D multiferroic materials	35
D. Phase modulation in 2D materials	36
1. Charge induced phase transformations through chemical means	36
2. Charge induced phase transformations through non-chemical means	39
3. Field induced phase transformations	39
E. Controlling correlated states with electric fields in twisted heterostructures	39
1. Twisted TMD homobilayers	40
2. TMD heterobilayers	41
3. Future directions in moiré magnets and magnon bands	43
V. CONCLUSIONS AND FUTURE OUTLOOK	44
AUTHOR DECLARATIONS	45
Author Contributions	45

I. INTRODUCTION

Ever since the successful isolation of a single sheet of graphene (GR) from bulk graphite in 2004,¹ research into two-dimensional (2D) materials, where the interlayer interactions are governed by van der Waals (vdW) forces, has surged. Graphene, with its linear electronic dispersion, has been the most well-studied thus far, with significant progress toward commercialization.^{2,3} Graphene, however, is just the tip of the iceberg in terms of vdW materials, where a plethora of materials have vdW bonding between the layers and thus can be isolated down to the atomically thin limit.⁴ Depending on the composing elements, the crystal structure, and even relative angles between two layers, these materials can display a wide variety of electrical properties, including semi-metallic, metallic, semiconducting, and insulating behavior. They even support exotic phenomena such as charge density waves and superconductivity.^{5–10} Furthermore, magnetism at the monolayer limit has now been discovered,^{11,12} opening applications in nm-scale magneto-optoelectronic and spintronic devices.^{13,14} The transition metal dichalcogenide family (TMD) (MoS₂, WS₂, WSe₂, etc.) has been the most well studied after graphene, but large strides are being made regarding other 2D materials as well.

2D vdW materials display some truly fascinating properties that are inherently not possible with their thicker, three-dimensional (3D)

counterparts. For one, it has been well-documented that the electrical, optical, and magnetic properties can dramatically change at the few-layer thickness regime, or even between even vs odd number of layers.^{11,15–17} Additionally, 2D materials display extremely large mechanical flexibility, where large amounts of strain can be applied to tune their properties before rupture.^{18,19} The vdW bonding between the layers allows for these materials to be grown or transferred onto a wide variety of substrates without the difficulty of epitaxial requirements, enabling easy integration with silicon technology that is technologically mature. Multi-layer heterostructures can be created with a variety of 2D materials, even with sub-degree control of the rotational alignment between the layers.^{9,20}

Another immense benefit for using 2D materials in next-generation electronics and opto-electronics, and the focus of this review, is that they are able to be strongly tuned using electric fields in ways that are not possible for 3D materials due to their reduced dielectric screening.²¹ Furthermore, the existence of 2D insulating materials such as few-layer h-BN allows researchers to bring materials within atomic-scale proximity to the backgate, allowing for extremely efficient tuning via electric fields. To fully reveal the emerging functionalities and opportunities of these atomically thin materials in practical applications, this review thoroughly details several representative and noteworthy research directions regarding the use of electrical means to tune both the physical and structural properties of layered vdW materials, with an emphasis on discussing the major advancements in 2D materials beyond graphene in the past 5 years and an outlook of what is to come in the next decade. A schematic overview of current and perspective applications of 2D materials beyond graphene is presented in Fig. 1.

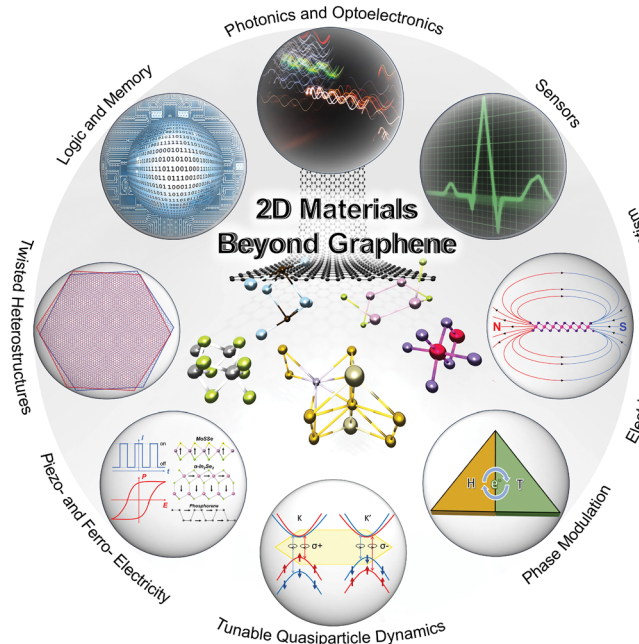


FIG. 1. Current and prospective applications of 2D materials beyond graphene in logic and memory devices, photonics and optoelectronic devices, sensors, electrically controlled magnetism, phase modulation, tunable quasiparticle dynamics, piezo- and ferro-electricity, and electrically tunable twisted heterostructures.

First, a broad overview of the materials beyond graphene is presented, detailing crystal structure, optical and electrical properties, and other relevant features that are important for the review. Next, we outline the current status of electrical tunability in materials beyond graphene, including in applications for logic and memory devices, photonics and optoelectronic devices, and sensors (gas, bio, and strain sensors). We then turn our attention to more emerging areas and application opportunities that are showing exciting potential. These novel research areas include tunable quasiparticle dynamics, electrically controlled magnetism, piezo- and ferro-electricity, phase modulation, and electrically tunable twisted heterostructures.

II. MATERIALS BEYOND GRAPHENE

Since the first discovery of graphene, 2D vdW materials have attracted immense research interest, thanks to their unique layered structures. As shown in Fig. 2,^{22–58} common vdW materials can be divided into groups based on their crystal systems, structure, and tunable properties. Atoms are bonded with each other in each layer, but the interactions between neighboring layers are mostly dominated by vdW forces. Thanks to the weak vdW interactions, pristine surfaces of atomic, ultrathin layers can be easily preserved through mechanical exfoliation and other synthesis methods. Weak vdW interactions also allow the stacking of different 2D vdW materials without the limitation of lattice matching, which provides researchers more degrees of freedom in the design of complex vdW heterostructures with desired functionalities. In addition, the surface properties become extremely significant due to the ultrathin geometry of vdW materials and can be tuned with surface modification.

Transition metal dichalcogenides (TMDs) and Janus structures are of the type MX_2 ($M = \text{Mo, W, etc.},$ and $X = \text{S, Se, or Te}$) where a layer of M-atoms is sandwiched between two layers of X atoms for each monolayer. While conventional TMDs possess the same chalcogen layer on both sides of the transition metal layer, Janus structures have a different chalcogen layer on either side. Based on the varied stacking orders of M- and X-atom layers, TMDs can be categorized into 2H (ABA) and 1T (ABC) phase. The 1T phase can be further divided into the 1T' and the T_d phase as a result of structural distortion.

Hexagonal boron nitride (h-BN) is an insulator isostructural to graphene, where lattice points of the honeycomb structure are alternatively occupied by B and N atoms.

MXenes are layered structures resulting from selectively etching the A atom layer of the parent MAX phase, where M is an early transition metal, A is a group 13 or 14 element, and X is C or N.

Fe_3GeTe_2 consists of a Fe_3Ge layer sandwiched between two Te layers. The Fe_3Ge layer is composed of a hexagonal network formed by Fe atoms, which is covalently bonded to the remaining Fe and Ge atoms.

III–VI compounds are of the type A_2X_3 or AX, where A and X are group 13 and 16 elements, respectively. Among them, In_2Se_3 is one of the most well-studied materials. It consists of a Se–In–Se–In–Se quintuple layer, with distinct 2H- and 3R-phases differentiated by the stacking of the quintuple layers. Similarly, $InSe$ consists of Se–In–In–Se quadruple layers. For its β -phase, the second quintuple layer is rotated by 60° around the [001] direction.³¹

Elemental 2D materials include silicene, germanene, and black phosphorus (BP). Silicene and germanene are analogous to graphene.

The major difference is that they are buckled structures, while graphene is flat. Black phosphorus has a pleated honeycomb-like structure.

$Cr_2Ge_2Te_6$ consists of $CrTe_6$ octahedra arranged in a honeycomb-like structure, where the center of each cell in the network is occupied by a Ge–Ge dimer.

Graphitic carbon nitride has a monolayer form which consists of an energetically preferred tri-s-triazine structure.

Group-IV monochalcogenides are of the type AX, where A and X are group 14 and 16 elements, respectively. They have a highly distorted rock salt structure, where each A atom is placed in the distorted octahedron and bonded with six X atoms.

Chromium trihalides are of the type CrX_3 ($X = \text{Cl/Br/I}$). For each monolayer, CrX_6 octahedra pairs with a shared edge are arranged in a honeycomb-like structure.

Transition metal thiophosphates are denoted by the chemical formula $A^{II}B^{II}P_2X_6$ or $A^{III}B^{III(I)}P_2X_6$, where both A and B are transition metals, and X refers to group 16 elements. Among them, $CuInP_2S_6$ is one of the most important compounds. Its monolayer consists of a sulfur framework where the octahedral voids are filled by the Cu, In, and P–P triangular patterns.

III. CURRENT STATUS IN ELECTRICAL TUNABILITY OF 2D MATERIALS BEYOND GRAPHENE

Strong electrostatic tunability is the highlight feature of all 2D semiconductor-based field-effect devices. This is also the principle reason for their suitability as a channel material in extremely scaled transistors.^{59,60} The suitability of vdW 2D channels for post-Si electronics or “more than Moore” electronics is well known and extensively discussed in reviews exclusively focused on transistor devices.^{59–61} Here, we will focus on the following question: What does this electrostatic or gate tunability enable in 2D semiconductor devices that is unattainable or not demonstrated yet in other known semiconductors?

A. Logic and memory devices

1. Gate tunable transport in diodes and switching devices

In the context of electronic devices, the impact of the electrostatic tunability of 2D materials can be looked at by first examining the simplest semiconductor device, which is the p–n junction. When a p–n junction is comprised of atomically thin semiconductors, it can be electrostatically tuned across both p and n layers that are vertically stacked resulting in unusual electrical characteristics. This was first reported on n-type 2D MoS_2 and p-type 1D carbon nanotube (CNT) junctions.⁶² Both a tunable rectification ratio of the diode and the first evidence of anti-ambipolar (Λ -shaped) transfer characteristics were demonstrated, with two OFF states at either extremes of gate bias and one ON state in the center [Fig. 3(a)].⁶² This observation of tunable rectification and anti-ambipolar transfer characteristics has since been generalized to several other 2D–2D,⁶³ 2D–organic,⁶⁴ all-organic⁶⁵ and other unconventional, mixed-dimensional^{66,67} heterojunction systems, emanating from strong electrostatic modulation in 2D material-based device examples.

Numerous reports on various applications of such anti-ambipolar and tunable diode characteristics in 2D heterojunction devices have now been published, as summarized in other reviews.⁶⁸

Crystal System	Material	Structure		Space group	Tunable Electronic Property	Crystal System	Material	Structure		Space group	Tunable Electronic Property
		Side view	Top view					Side view	Top view		
Hexagonal	2H-TMDC (2H-MoTe ₂ , 2H-MoSe ₂ , 2H-MoS ₂ , 2H-WTe ₂ , etc.) + Janus Structure (MoSSe, etc.)			P6 ₃ /mmc (#194)	Charge density ^{40,46} Exciton binding energy ⁴⁷ Correlated states ^{48,49}	Trigonal	1T-TMDC (1T-MoS ₂ , etc.)			P $\bar{3}$ m1 (#164)	Charge density ³⁵
	h-boron nitride (h-BN)			P6 ₃ /mmc (#194)	Charge density ⁴¹ Correlated states ⁴²		Cr₂Ge₂Te₆			R $\bar{3}$ (#148)	Magnetization ^{36,52}
	MXenes (Ti ₃ C ₂ , etc.)			P6 ₃ /mmc (#194)	Polarization ⁴³	Orthorhombic	g-C₃N₄			Cmcm (#63)	Charge density ⁵³
	Fe₃GeTe₂			P6 ₃ /mmc (#194)	Magnetization ⁴⁴		Black Phosphorus			Cmca (#64)	Charge density ³⁷
	III-VI compound family (α -2H-In ₂ Se ₃ , etc.)			P6 ₃ mc (#186)	Polarization ⁵⁰		Group-IV monochalcogenides (SnS, GeS, SnSe, GeSe, etc.)			Pnma (#62)	Polarization ⁵⁴
	β-InSe			P6 ₃ /mmc (#194)	Charge density ⁴⁵		T_d-WTe₂			Pmn2 ₁ (#31)	Charge density Polarization ⁵⁵
	Silicene/ Germanene			P6/mmm (#191)	Charge density ³⁴		Monoclinic	1T'-TMDC (1T'-MoTe ₂ , etc.)			P2 ₁ /m (#11)
Trigonal	III-VI compound family (α -3R-In ₂ Se ₃ , etc.)			R3m (#160)	Polarization ⁵¹	CrI₃, CrBr₃				C2/m (#12)	Magnetization ⁵⁶ Curie Temperature ⁵⁷
						CuInP₂S₆				Cc (#9)	Polarization ^{39,58}

FIG. 2. Summary of crystal system, crystal structure, space group, and corresponding tunable electronic properties for 2D vdW materials mentioned in this work.²²⁻⁵⁸

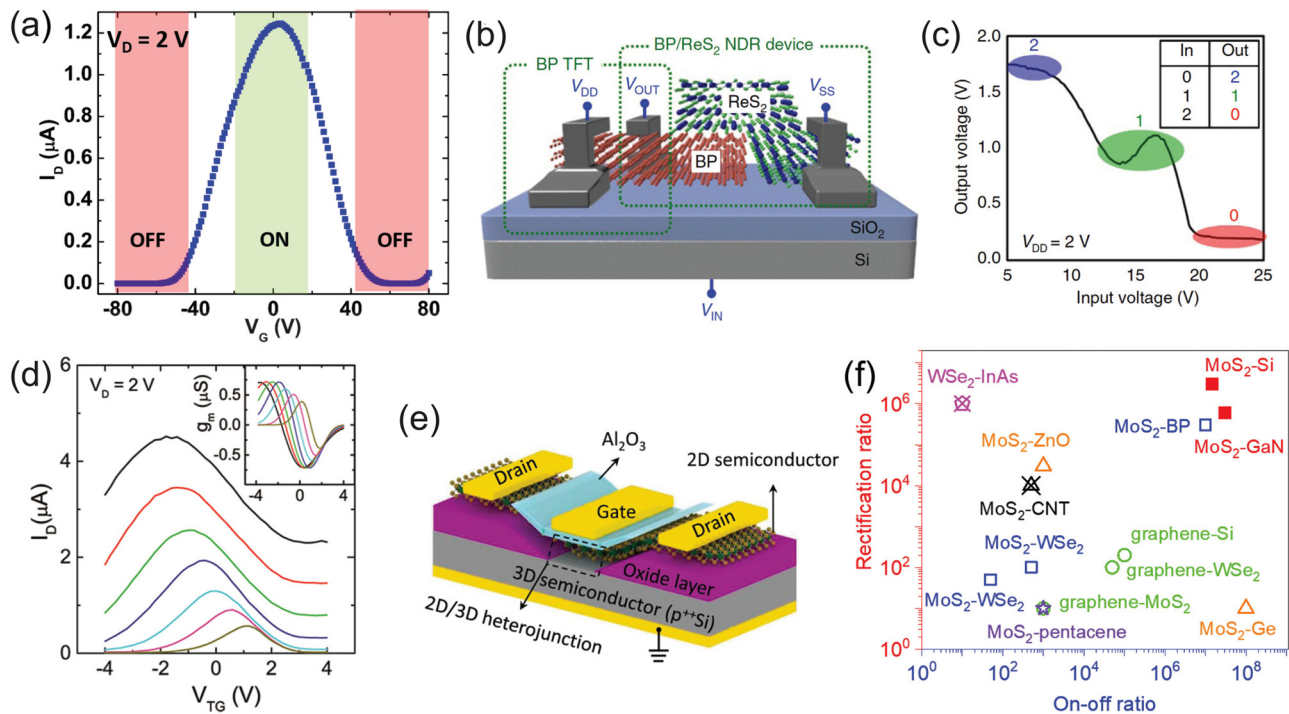


FIG. 3. Gate tunable transport properties in 2D materials. (a) Anti-ambipolar transfer characteristic of a carbon nanotube-MoS₂ p-n heterojunction diode, showing a characteristic Λ -shaped curve.⁵² Adapted with permission from Jariwala *et al.*, Proc. Natl. Acad. Sci. U. S. A. **110**, 18076 (2013). Copyright 2013 National Academy of Sciences. (b) Schematic of a ReS₂-BP gated heterojunction diode in series with a p-type BP FET that forms a tri-state inverter. (c) Inverter voltage transfer characteristic showing three distinct logic states.⁶⁹ Adapted with permission from Shim *et al.*, Nat. Commun. **7**, 13413 (2016). Copyright 2016 Nature Publishing Group. (d) Tunable anti-ambipolar transfer characteristics and transconductance (inset) of a dual gated MoS₂-BP heterojunction.⁷³ Adapted with permission from Sangwan *et al.*, Nano Lett. **18**, 1421 (2018). Copyright 2018 American Chemical Society. (e) Schematic of a gated 2D(MoS₂)/3D(Si) semiconductor heterojunction. (f) Comparison of various gate-tunable p-n heterojunction diodes comprising at least one 2D semiconductor on the metrics of ON-OFF ratio and rectification ratio, both of which signify the degree of tunability.⁷⁸ Adapted with permission from Miao *et al.*, Nano Lett. **20**, 2907 (2020). Copyright 2020 American Chemical Society.

One of the most prominent applications is in tunable, multivalued logic. A ternary inverter with three logic states has been demonstrated using an anti-ambipolar heterojunction between small-gap black phosphorus (BP) and larger gap ReS₂, which form a type III junction, connected in series with a p-type BP FET device⁶⁹ [Figs. 3(b) and 3(c)]. Similar results have also been obtained in gated type II p-n heterostructures of BP/MoS₂,⁷⁰ MoS₂/WSe₂,⁷¹ and SnS₂/WSe₂.⁷² Anti-ambipolarity provides both positive and negative transconductance with a steep transition between them that can be tuned either actively with dual gates⁷³ [Fig. 3(d)], as seen in MoS₂/BP self-aligned dual gated junctions, or passively with device geometry.⁶⁴ This allows frequency modulation and⁶⁶ multiplication applications, and opens room for constructing spiking neurons.^{73,74}

The above listed semiconductor combinations and device applications are promising for enhanced complementary metal-oxide-semiconductor (CMOS) or even neuromorphic and analog computing. However, all of them are comprised of materials that are still far from the maturity level of Si or III-V s. Among 2D materials beyond graphene, only MoS₂, WS₂, MoSe₂, WSe₂, and h-BN have been synthesized at wafer-scale uniformity on CMOS-compatible substrates.⁷⁵ Therefore, a more practical way to take advantage of 2D materials in heterojunctions is to combine them with commercial-scale 3D

materials such as Si and III-V s. Along this direction, several recent breakthroughs have been made.^{67,76} The earliest reports of gate-tunable 2D/3D heterojunctions include integration of graphene on Si to make gate-tunable Schottky diodes or barristors.⁷⁷ A key disadvantage of 2D/3D semiconductor junctions is that the 3D material does not allow significant electric field tunability or even a dual-gated structure. On the other hand, complementary doping type and density in 3D semiconductors are already well established and controlled, leading to high tunability of rectification and ON/OFF current ratios. Recent reports on junctions of MoS₂ with Si and GaN have established superior performance, as seen in Figs. 3(e) and 3(f).⁷⁸ The large rectification ($>10^6$ times) and resistance ($>10^7$ times) tunability suggest that these tunable heterojunctions can be dynamically configured to operate as both diodes and transistors, renewing the opportunity to explore the long-abandoned concept of diode-transistor logic in a new way.

Finally, 2D/3D junctions are also an important research avenue for tunneling field effect transistors (T-FETs). The controlled degenerate doping in the 3D case combined with strong gate-tunability in the 2D layer makes a compelling case for T-FETs. However, all T-FET demonstrations in this regard have thus far been limited by low ON/OFF ratios for sub-thresholds <60 mV/dec or low ON currents. To overcome this, several attributes are desired from the 2D/3D

combination: (1) Near-intrinsic doping and clean semiconductors with large density of states at band edges, (2) clean and defect-free interfaces, and (3) superior coupling to the gate with a gate dielectric that is both thin and has high breakdown strength. Meeting all these criteria is challenging and therefore presents plenty of space for exploration of material combinations and interface design/engineering. Likewise, there is also opportunity for more complex designs, such as p-n-p or n-p-n bipolar junction transistors. While some attempts have been made in this regard, the performance and properties remain far from optimal.^{79,80} Controlled interfaces and controlled doping will once again hold the key to higher performance and more mature devices.

2. Gate-tunable memristive phenomena in atomically thin materials

As silicon-based, nonvolatile memory (NVM) devices are anticipated to approach their fundamental scaling limits, new technologies and devices are continuously being investigated to meet ever-increasing demands of high-density data storage. Resistive random-access memory (RRAM) devices have emerged as potential candidates in the pursuit of cheaper and smaller NVM devices with high write/erase speed and greater endurance and retention.^{81–83} RRAM technology is foreseen to play a leading role in the future of memory industry, owing to its superiority over flash memory devices in terms of

scalability without compromising on data storage, lower power consumption, and CMOS compatibility. So far, the most widely used functional materials for RRAM are based on insulating transition metal oxides; however, these materials are facing the bottleneck of scalability.^{84–86} Therefore, extensive research efforts have been devoted to explore new functional materials for RRAM devices. Two-dimensional vdW material-based RRAMs have received tremendous research attention over the past few years,^{87–89} with the advantage of highly scalable memory cells with low power consumption and fast switching speed. Several reports have explored the use of graphene as either a highly conductive electrode material or as an active layer in RRAM based NVM devices.^{90–92} Likewise, other 2D materials such as TMDs have also been used in order to improve the performance of NVMs. Here, we provide a comprehensive overview of the most recent advancements in NVM devices based on 2D materials beyond graphene with a focus on electrical tunability of memory device properties.

Among 2D TMDs, MoS₂ is the most widely explored semiconductor as the channel material in NVM devices due to the combined effect of excellent mechanical flexibility and high charge-carrier mobility ($>20 \text{ cm}^2 \text{ V}^{-1} \text{ s}^{-1}$ for $N \approx 10^{11} \text{ cm}^{-2}$).⁹³ Memristive phenomena in monolayer MoS₂-based lateral devices through the inclusion of grain boundaries (GBs) have been investigated.⁹⁴ Resistance switching ratios of $\sim 10^3$ at small bias and small set fields ($\sim 10^4 \text{ V cm}^{-1}$) [Fig. 4(a)] were observed in devices with GBs connected to just one electrode.

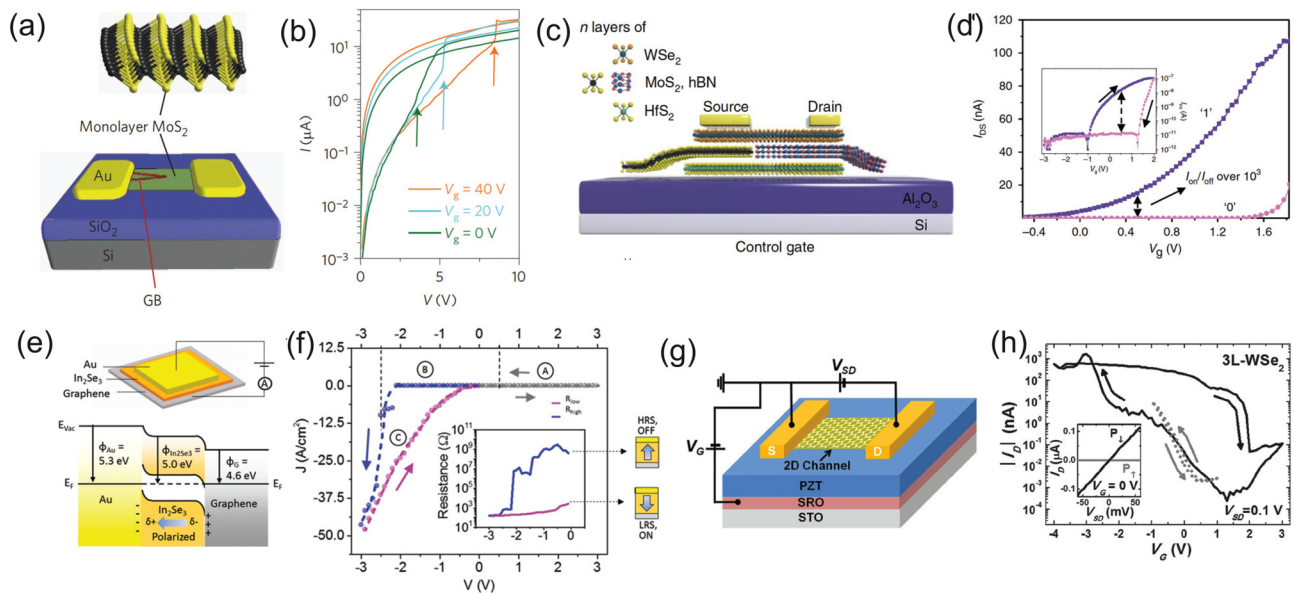


FIG. 4. 2D materials-based memory devices. (a) Schematic of an intersecting-GB MoS₂ memristor with two GBs connected to one of the electrodes. (b) Log-linear plot of the I - V characteristics of an intersecting-GB memristor at different gate voltages (V_g) which shows a shift in the set voltage with V_g .⁹⁴ Adapted with permission from Sangwan *et al.*, *Nat. Nanotechnol.* **10**, 403 (2015). Copyright 2015 Nature Publishing Group. (c) Schematic structure of the 2D semi-floating gate memory. The WSe₂, h-BN, and HfS₂ serve as the channel, blocking layer, and floating gate, respectively. In addition, the inserted MoS₂ layer and the WSe₂ channel form the p-n junction switch. (d) Transfer characteristics showing a shift in threshold voltage resulting in a large I_{on}/I_{off} ratio exceeding 10^3 .⁹⁶ Adapted with permission from Liu *et al.*, *Nat. Nanotechnol.* **13**, 404 (2018). Copyright 2018 Nature Publishing Group. (e) Schematic of the ferroelectric memory junction fabricated on the as-grown 6 nm α -In₂Se₃ and its corresponding band alignments at equilibrium. (f) J - V characteristics measured from the ferroelectric memory device, showing the modulation of resistance state with ferroelectric polarization direction.¹⁰⁶ Adapted with permission from Poh *et al.*, *Nano Lett.* **18**, 6340 (2018). Copyright 2018 American Chemical Society. (g) Schematic of the 2D TMD/PZT heterostructure device with a circuit diagram for the back-gating. (h) Hysteresis loop of I/I_0 - V_g , measured from a representative p-type 3L-WSe₂ channel based FeFET.¹⁰⁹ Adapted with permission from Ko *et al.*, *Adv. Mater.* **28**, 2923 (2016). Copyright 2016 John Wiley and Sons.

Owing to their atomically thin nature, these MoS₂ GB memristors exhibit gate-tunability of the set voltage from 3.5 to 8.0 V [Fig. 4(b)]. The same authors have shown multi-terminal memtransistors using polycrystalline (PC) monolayer MoS₂ for complex neuromorphic computing operations.⁹⁵ These memtransistors also exhibit high cycling endurance (≈ 475 cycles) and long retention times (24 h). However, these devices rely on GBs with site-specific orientation, which is difficult to control. Recently, a focused helium ion beam was used for precisely introducing sulfur vacancy-related, site-specific defects into TMDs (MoS₂). The device exhibited high endurance (>1180 cycles) and retention ($>10^3$ s), as well as gate-tunable smaller set voltages.⁹⁶ Another recent study has shown a high gate tunability of the switching ratio from $\approx 10^0$ to 10^5 using a few-layer MoS₂-based transistor.⁹⁷

A quasi-nonvolatile memory utilizing a semi-floating gate architecture was also used, achieving ultrahigh writing speeds of ≈ 15 ns and refresh times of ≈ 10 s, which is comparable to or higher than commercial dynamic random access memory [Fig. 4(c)].⁹⁸ The high writing performance was obtained due to the presence of two different charge transport mechanisms, e.g., switch path and flash memory path, in the device. Furthermore, the gate tunability of the device resulted in a high resistive switching ratio exceeding 10^3 [Fig. 4(d)]. In another report, a vertically stacked MoS₂/h-BN/graphene heterostructure exhibited a significantly low off-state current $\approx 10^{-14}$ A, resulting in a ultrahigh switching ratio of over 10^9 .⁹⁹

Another prototype approach for obtaining tunable memory operation has been demonstrated by adding redox-active molecules on a 2D MoS₂ channel material (≈ 7 layers). By controlling molecular configurations through the gate voltage, carrier concentration in the 2D MoS₂ could be modulated, resulting in the multistate memory operation.¹⁰⁰ The device exhibited a reasonable switching ratio of $\approx 10^3$ but showed relatively poor endurance (≈ 50 cycles). Thus, further efforts to improve the retention and endurance of such kind of devices are required to be useful for memory applications.

B. Ferroelectric memristors

Recently, research in the area of NVM devices has focused on designing 2D ferroelectric field effect transistors (FeFETs), where a ferroelectric layer with high polarization field and dielectric constant is used as the gate dielectric material for producing efficient gating effect in the semiconductor channel layer.^{101,102} Due to switchable electric dipoles and large retention properties, FeFETs are considered as potential candidates for building NVM with low-power consumption and ultrafast logic operation. Earlier studies on 2D FeFETs were focused on using graphene as the conducting channel with bulk ferroelectric materials such as lead zirconate titanate (PZT) or organic poly(vinylidene fluoride-trifluoroethylene) (PVDF-TrFE) thin films. In these, the resistance of the conducting channel was effectively tuned by the reversible electrical polarization of the ferroelectric thin film.^{92,103,104} In line with the conventional approach, integration of a graphene channel with an atomically thin 2D ferroelectric as the gate dielectric has also been demonstrated. The use of ultrathin ferroelectric materials increases the effective gate field, which reduces the writing or erasing voltage needed to flip the electric polarization and leads to a low-power consumption memory device.^{105,106}

The fabrication of a 2D FeFET with graphene as the conducting channel and ferroelectric 2D α -In₂Se₃ as the top gate dielectric has been recently demonstrated, where the resistance states of the graphene channel were efficiently modulated by sweeping the ferroelectric gate voltage, leading to switching of the polarization direction in the α -In₂Se₃ layer. The device exhibited excellent endurance for $\approx 10^5$ switching cycles and retention performance for ≈ 1000 s.¹⁰⁵ Another recent study achieved a giant electroresistance switching ratio $\approx 10^6$ through the modulation of Schottky barrier height and width via ferroelectric switching in large area α -In₂Se₃ grown on graphene using molecular beam epitaxy [Figs. 4(e) and 4(f)].¹⁰⁶ Devices with semiconducting 2D materials have also been investigated. Ferroelectric memory transistors using monolayer to few-layer MoS₂ as a channel and P(VDF-TrFE) as the ferroelectric top gate insulator exhibited an ON/OFF ratio of $\approx 10^3$, concurrently with retention properties for more than 1000 s.¹⁰⁷ A similar approach has been adopted for BP¹⁰¹ and MoSe₂¹⁰⁸ FE-FETs, which showed similar or higher ON/OFF ratios, retention, and endurance. However, slow dipole dynamics of ferroelectric polymers and low thermal durability compared to its inorganic counterparts can hamper the practical applicability of organic ferroelectric-based FETs. Thus, FeFETs integrating 2D materials with inorganic ferroelectric materials were also investigated. Nonvolatile memory devices using mono- to few-layer TMDs (WSe₂ for p-type and MoS₂ for n-type) as the channels and epitaxial PZT thin films as the FE layer have been fabricated [Fig. 4(g)].¹⁰⁹ The ferroelectric gate tunability of the device (3L-WSe₂) was demonstrated, and an ON/OFF ratio was tuned from $\approx 10^4$ to $\approx 10^5$ with positive gate bias [Fig. 4(h)]. Furthermore, the device exhibited endurance over 400 switching cycles and retention for up to 10^4 s. Another recent work reported high-performance FE-FET using MoS₂ channel on top of AlScN dielectric and achieved a high ON/OFF ratio of $\approx 10^6$ and retention up to 10^4 s.¹¹⁰ A 2D/2D vdW heterostructure FeFET for nonvolatile ReRAM applications has also been designed, wherein 2D CuInP₂S₆ was integrated on top of the MoS₂ channel as a ferroelectric insulator.¹¹¹ The MoS₂/CuInP₂S₆ FeFET showed an ON/OFF ratio of $>10^4$ via ferroelectric polarization switching-induced changes in the band alignment between the metal and CuInP₂S₆.

So far, the most intensively explored device concept for FeFETs consists of a ferroelectric gate dielectric integrated with a semiconductor channel layer. However, this conventional approach suffers from charge trapping and gate leakage issues, resulting in short retention times. Recently, a few 2D vdW materials have been shown to exhibit ferroelectricity as well as semiconducting properties, e.g., α -In₂Se₃¹¹² and CuInP₂S₆.⁵⁸ A few reports have realized FeFETs using ferroelectric 2D materials as the channel layer, where the resistance states of the devices were controlled by ferroelectric polarization switching.^{113,114} In a recent study, both planar and vertical memristors using α -In₂Se₃ were investigated, demonstrating memristive phenomena based on both in-plane and out-of-plane polarization.¹¹⁵ Both the devices exhibited a resistive switching ratio $>10^3$ due to modulation of the Schottky barrier height with ferroelectric gate bias and showed excellent endurance and retention properties for over 100 cycles and up to 1000 s, respectively. Another recent study has also observed similar performance (ON/OFF ratio $>10^3$) using an α -In₂Se₃ FeFET.¹¹⁶ To provide an overview of the performance of different 2D material-based NVM devices, a comparison between the ON/OFF ratio and the retention time is plotted in Fig. 5.^{94–96,99–102,105,107–109,115,117,118}

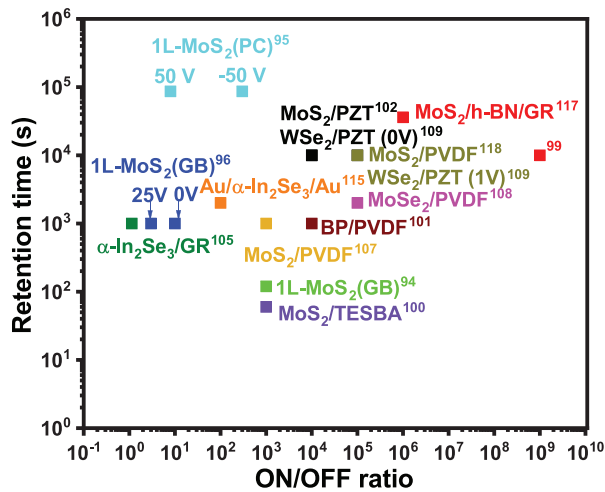


FIG. 5. A comparative analysis of experimentally observed ON/OFF ratios vs retention time for different 2D materials-based memory devices reported in literature precedent. ON/OFF is a measure of distinction between two memory states, while retention time is a measure of temporal robustness of storing information in the memory device. The square symbols of varying colors correspond to the experimental data points adopted from Refs. 94–96, 99–102, 105, 107–109, 115, 117, and 118. Abbreviations: GB (Grain boundary), PC (Polycrystalline), GR (Graphene), PZT (Pb[Zr_{0.2}Ti_{0.8}]O₃), BP (Black phosphorus), TESBA [4-(Triethoxysilyl)butanal], and PVDF (Polyvinylidene fluoride).

C. Photonics and electro-optic devices

1. Light harvester

Harnessing solar energy using photovoltaic (PV) cells is by far the most promising strategy to fulfill the ever-increasing demand of renewable energy. PV cells using Si, III–V compounds, and, very recently, organic/inorganic hybrid perovskites have been investigated, and significant conversion efficiency has also been achieved.^{119–121} However, the fabrication of these devices is associated with certain complexities, such as the requirement of epitaxial growth techniques, limited abundance of some elements, and chemical stabilities, which raise concerns about their long-term economic viability. Recently, 2D TMDs, which have bandgaps with energies ranging from the ultraviolet to the near infrared (NIR) regions, have been considered as a new class of functional materials to potentially serve as thin absorbers for high performance PV cells. This is due to their high absorption coefficient and appropriate bandgaps in the bulk (1.3–1.4 eV) for attaining maximum power conversion efficiency (PCE) per Shockley–Quiesser (SQ) limit.¹²² Two-dimensional TMDs are inherently flexible, and the lack of dangling bonds at the surface encourages the creation of high-quality heterointerfaces, resulting in low-cost, flexible, and lightweight PV devices operating in a large region of the solar spectrum. PV cells based on 2D TMD heterostructures are also expected to exhibit high power conversion efficiency (PCE) as the maximum photovoltage is not limited by the built-in electrical potential energy, as is the case for conventional p–n junctions. The charge generation process in 2D TMDs is associated with strongly bound excitons instead of weakly bound electron–hole pairs. The exciton generation and dissociation occur simultaneously in a narrow region near the heterojunction, resulting in a large carrier concentration gradient that acts as a

powerful PV driving force. Their atomically thin nature offers a unique platform for achieving electrically tunable PV properties for high efficiency. The tuning of carrier density in active layers of a p–n junction also has strong implications for photodetectors. For instance, increasing carrier density in a p–n junction results in a greater built-in potential; this leads to a smaller reverse saturation current, directly impacting the sensitivity and responsivity of the photodiode detectors. Conversely, decreasing the carrier density results in a lower depletion width and an increased reverse saturation current. In this section, we highlight p–n junctions based on 2D semiconductors where electric-field-induced tuning of the semiconductor induces modulation of the electrical response to light absorption.

a. Homojunctions. PV energy conversion was first reported in lateral p–n homojunctions using several electrostatically doped monolayer 2D materials such as WSe₂, MoS₂, and BP.^{123–126} Biasing a pair of gate electrodes with opposite polarities, the carrier type and density were controlled in the channel, resulting in the formation of a p–n junction. The maximum PCE achieved using such junctions is ≈0.5%. However, it can be further enhanced to ≈14% under a standard air mass (AM)-1.5 solar spectrum using multilayer (≈10 atomic layers) MoSe₂ crystals stacked onto dielectric h-BN.¹²⁷ Recently, using high-resolution angle-resolved photoemission spectroscopy, the surface PV effect has been observed in a β-InSe semiconductor that allows for further tuning by *in situ* surface potassium doping. This study can be further extended to engineer the photovoltaic effect in InSe-based p–n devices.⁴⁵ Furthermore, vertical p–n homojunctions have also been designed. A vertical homojunction using thin and thick flakes of MoSe₂ has been fabricated, and a gate tunable PV effect was obtained due to different gate modulation levels of the carrier densities in these flakes. The PV effect as a function of gate voltage (V_g) showed a maximum open-circuit voltage (V_{oc}) ≈ −0.24 V and PCE ≈ 1.9% [Figs. 6(a) and 6(b)].⁴⁶ Similarly, a gate-tunable PV effect has also been demonstrated in a vertical homojunction of n-type MoS₂:Fe and p-type MoS₂:Nb few-layer flakes by changing the charge carrier density through the Si-gate electrode.¹²⁸

2. Vertical heterostructures

In contrast to homojunctions, the vdW heterojunctions, made by stacking 2D materials of different bandgaps, are expected to exhibit enhanced PV effect. A type-II vdW heterojunction composed of MoS₂ and WSe₂ monolayers has been fabricated, with gate tunability of the short-circuit current (J_{sc}) and V_{oc} resulted in a PCE of ≈0.2%.¹²⁹ In another work, external quantum efficiency (EQE) ≈ 2.4% has been achieved using a monolayer MoS₂/WSe₂ heterojunction sandwiched in between graphene electrodes, which can be further improved by increasing the number of atomic layers in the MoS₂/WSe₂ heterojunction.⁶³ A polymeric gate was also used on top of MoS₂/InP to obtain an electrically tunable PV effect, leading to maximum PCE of ≈7.1%.¹³⁰ Recently, a vertical vdW heterostructure consisting of multilayer InSe and Te has been fabricated, exhibiting a PV effect as well as a broadband photoresponse with an ultrahigh photo/dark current ratio exceeding 10⁴ and a high detectivity of ≈10¹² Jones under visible light illumination [Fig. 6(c)].¹³¹ In a vertical vdW p–n junction between few-layer p-BP and n-InSe, the band alignment and intrinsically high carrier mobilities in BP and InSe resulted in an EQE as high

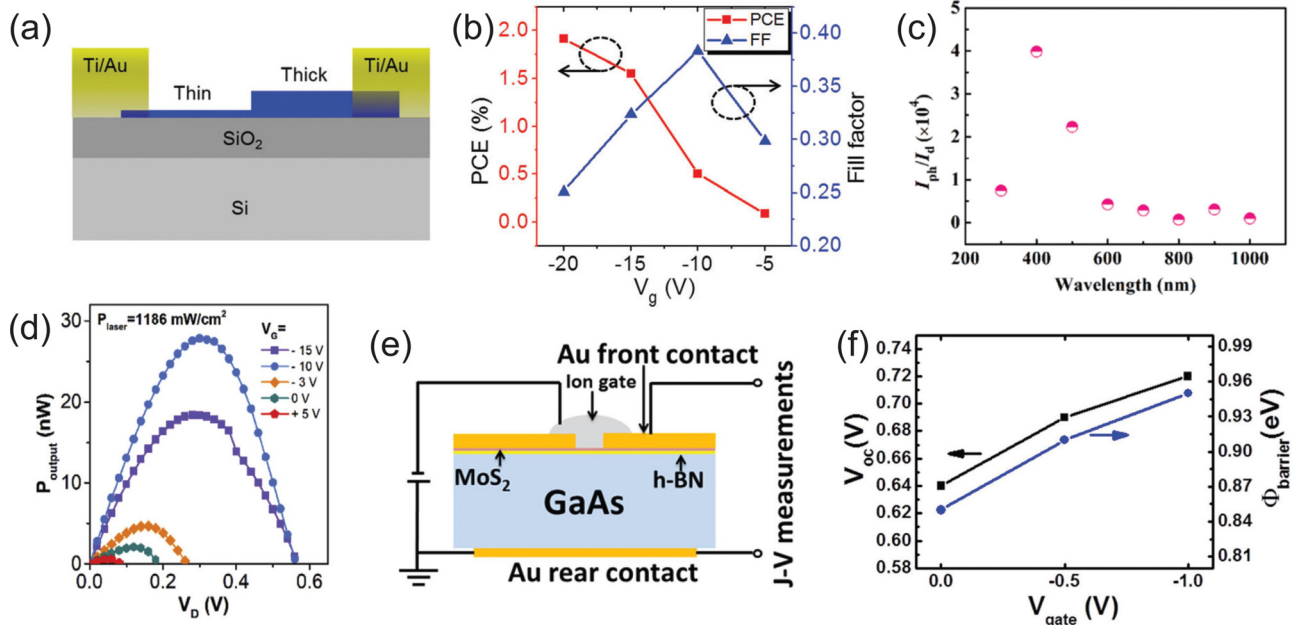


FIG. 6. Photovoltaic devices based on 2D materials. (a) Schematic side view of the MoSe₂ homojunction device. (b) The back gate-dependent fill factor (FF) and power conversion efficiency (PCE). The PCE increases up to 1.9% with the increasing negative gate.⁴⁶ Reprinted with permission from Yang *et al.*, *J. Mater. Chem. C* **5**, 7051 (2017). Copyright 2017 Royal Society of Chemistry. (c) Photo/dark current ratio under various wavelength light at $V = -2$ V in an InSe-Te vdW heterostructure.¹³¹ Adapted with permission from Qin *et al.*, *ACS Appl. Mater. Interfaces* **12**, 37313 (2020). Copyright 2020 American Chemical Society. (d) The output electrical power $P_{\text{output}}-V_D$ characteristics of the WSe₂/WS₂ heterojunction at different gate voltages.¹³⁴ Reprinted with permission from Lin *et al.*, *J. Alloys Compd.* **842**, 155890 (2020). Copyright 2020 Elsevier B.V. (e) Schematic structure of the field effect MoS₂/h-BN/GaAs solar cell. (f) Variation of ϕ_{barrier} and V_{oc} at the heterojunction at different gate voltages.¹³⁶ Reproduced with permission from Wang *et al.*, *Appl. Phys. Lett.* **109**, 023502 (2016). Copyright 2016 AIP Publishing LLC.

as 3%, indicating an efficient separation of the photogenerated charge carriers. The polarization-dependent photoresponse of the device was also investigated through scanning photocurrent microscopy which showed a substantially higher polarization sensitivity (photocurrent anisotropy ratio ≈ 0.83) than those of traditional BP photodetectors.¹³²

To scale up the process, CVD-grown large area vertical heterostructures have also been employed. A gate-tunable PV effect has been obtained in CVD-grown WS₂/MoS₂ and MoS₂/WS₂ vertical heterostructures sandwiched between graphene electrodes.¹³³ The I_{sc} and V_{oc} increased monotonically from 30 nA and 0.7 mV to 120 nA and 2.4 mV, respectively, by varying the gate voltage. However, this enhancement is smaller than what has been reported for mechanically exfoliated samples.

In another recent report, high performance PV effect was demonstrated in WSe₂/WS₂ heterostructures due to effective modulation of the junction transport properties as a function of gate voltage due to the ambipolar nature of WSe₂,¹³⁴ where a significant modulation of the output electrical power P_{output} of the device with gate voltage was achieved [Fig. 6(d)]. The heterostructure exhibited a maximum V_{oc} of ≈ 0.58 V and PCE of $\approx 2.4\%$. The modulation of the PV properties was correlated with the combined effect of channel conductivity and quasi-Fermi level tuning at the interface. Theoretically, it has been further proposed that a high PCE $\approx 30.7\%$ can be obtained using a dual-gated semiconducting 2H-phase WTe₂/MoSe₂ vdW heterostructure.¹³⁵ By adjusting the dual-gate voltages, the photocurrents in the two subcells can be matched, leading to tandem-cell operation of the device.

Another research area is the study of the PV effect in 2D/3D heterostructures, which can theoretically absorb more of the incident light. By varying the gate voltage through an ionic polymer top gate in a MoS₂/GaAs heterostructure, the PCE was improved from 6.87% to 9.03%,¹³⁶ caused by the improved barrier height (ϕ_{barrier}) induced by the shift in the MoS₂ Fermi level [Figs. 6(e) and 6(f)]. Similarly, MoS₂/Si and MoS₂/GaN 2D/3D semiconductor heterojunctions have been fabricated for switching and rectification applications. By tuning the Fermi levels of MoS₂ via electrical gating, the devices exhibited over seven orders of magnitude modulation in the rectification ratio and an ON/OFF ratio exceeding 10^7 .⁷⁸ In another recent study, a large lateral photovoltaic effect (LPVE) with ultrafast relaxation time (≈ 2 μs) in a SnSe/*p*-Si junction has been reported. The diffusion of electrons laterally in the inversion layer formed at the SnSe/*p*-Si interface resulted in the large LPVE with ultrafast relaxation time.¹³⁷

3. Light emitting devices

In general, 2D vdW materials exhibit layer dependent optical bandgaps, large exciton binding energies, and high carrier mobilities, making them exciting candidates for designing novel optoelectronic devices such as phototransistors and LEDs.^{122,138–140} Electrical tuning is the most preferred approach to control optical excitations in 2D materials due to its fast action and easy on-chip integration in nano/micrometer scale. This has been implemented to control excitonic emission in 2D TMD-based LED devices.¹⁴¹ Electroluminescence (EL)

emerging from desired exciton species with unique emission characteristics is of fundamental importance for the practical implementation of LEDs. In view of this, 2D TMDs represent a new class of functional materials for realizing electrically tunable, exciton-mediated LEDs. In this section, we summarize the progress in realizing electrically controlled electroluminescence in 2D TMDs and their heterostructures using different device configurations.

a. Lateral p–n junctions. Gate-tunable EL has been reported in numerous TMD-based lateral p–n junctions, formed by either electrostatic gating or ionic liquid gating, where EL originating from different excitonic complexes is tuned by changing the carrier density.^{123,124,141–144} The recent research efforts in this direction have focused on using CVD-grown TMDs for fabricating large area LED devices. Lateral p–n junctions using CVD-grown, polycrystalline WSe₂ and MoS₂ monolayers have been realized by placing an electrolyte on top of the TMDs, where the electronic charges are induced by the formation of electric double layers.¹⁴⁵ The tunability of the EL intensity with the applied bias was demonstrated. However, the EQE obtained in such devices was significantly low ($\approx 10^{-3}\%$ for WSe₂ and $\approx 10^{-5}\%$ for MoS₂), likely due to the poor quality of the CVD-grown samples.¹⁴⁵ Apart from the inorganic 2D-material LEDs, LEDs using 2D molecular semiconductors have also been fabricated, which hold great promise for ultrafast on-chip optical communication applications.¹⁴⁶ The lack of suitable bipolar Ohmic contacts for achieving high injection levels of electrons and holes in the 2D material is a bottle neck for obtaining enhanced performance from the lateral p–n junction devices. In a recent study, EL from a dopant-free two-terminal device was observed by applying an AC voltage between the gate and the semiconductor [Fig. 7(a)].¹⁴⁷ An excess of electron and hole populations simultaneously present in the monolayer TMD (MoS₂, WS₂, MoSe₂, and WSe₂) during the AC transient resulted in pulsed light emission at each V_g transition [Fig. 7(b)].

b. Vertical heterojunctions. In lateral p–n junctions, emission is spatially localized only near the contact regions due to difficulty in achieving uniform carrier injection throughout the monolayer, leading to low quantum efficiency. An improved LED performance can be realized using vertical vdW heterostructures due to the reduced contact resistance, large luminescence area, and wider choice of TMDs, which can result in significantly improved EL efficiency. Light emission from p–n junctions composed of 2D/3D heterostructures such as n-type MoS₂/p-type silicon and¹⁴⁸ MoS₂/GaN¹⁴⁹ has been demonstrated, in which an electric field/current-driven tuning of the band alignment at the heterostructure interface or carrier redistribution was proposed as the origin of the EL tuning.

Recent research work has focused on investigating light-emitting properties of interlayer excitons (X_i) in 2D/2D type-II heterostructures, which show great promise for novel excitonic device applications. Interlayer exciton emission in electrostatically gated MoSe₂/WSe₂ heterobilayers has been investigated.¹⁵⁰ By biasing gate electrodes with opposite polarities ($V_{BG1} = -1$ V and $V_{BG2} = 5$ V), a p–n junction was realized and EL was obtained, which was dominated by interlayer exciton emission under forward bias condition. The EL peak was found to shift from 1.35 to 1.38 eV with a vertical electric field via the Stark effect. In another recent report, electrically tunable interlayer exciton emission was demonstrated, along with upconverted EL via

Auger scattering of interlayer excitons by injecting high carrier density into a WSe₂/MoS₂ type-II heterostructure [Figs. 7(c) and 7(d)].¹⁵¹

c. Quantum well (QW) structures. An extremely high EQE has been achieved in quantum well (QW) structures comprising vertically stacked metallic graphene, insulating h-BN, and semiconducting TMDs. An EQE as high as $\approx 8.4\%$ in a MoS₂-based, multiple QW structure has been obtained at low temperatures,¹⁵² and a high EQE ($\approx 5\%$) at room temperature has been obtained using a WSe₂-based QW, in which a monotonic increase in the EQE as a function of bias voltage and injection current density was observed [Fig. 7(e)].¹⁵³ In a recent study, high-speed electrical modulation of light emission by integrating a photonic nanocavity (GaP) with a WSe₂ QW structure was reported.¹⁵⁴ The light emission intensity of the cavity-coupled EL peak enhanced ≈ 4 times compared to the cavity-decoupled peak as the bias voltage was increased. Furthermore, electrical modulation of the EL revealed fast rise and decay times of ≈ 320 and ≈ 509 ns, respectively, by turning the voltage on and off, resulting in fast-operational speed (≈ 1 MHz) of the device [Fig. 7(f)].

An ultralow turn-on current density of $4 \text{ pA} \cdot \mu\text{m}^{-2}$, which is ≈ 5 orders of magnitude lower than that of the best single QW device, has been obtained in a metal-insulator-semiconductor (MIS) vdW heterostack comprising few-layer graphene (FLG), few-layer h-BN, and monolayer WS₂.¹⁵⁵ EL from the positively charged (X^+) or negatively charged (X^-) trions was reversibly controlled by electrostatic tuning of the TMD (WSe₂) into n- and p-type doping regimes under forward bias.¹⁵⁶ The EL intensity increased almost linearly with the tunneling current, and the lower-bound EQE was estimated to be $\approx 0.1\%$ for X^+ and 0.05% for X^- . Furthermore, electrically driven light emission from multi-particle exciton complexes in TMDs (WSe₂ and WS₂) has been demonstrated using a MIS-type structure [Fig. 7(g)].¹⁵⁷ By tailoring the parameters of the pulsed gate voltage, an electron-rich or a hole-rich environment can be created in the 2D semiconductors, where the emission intensity from different exciton species is tunable [Fig. 7(h)].

d. Valley polarized EL. Owing to inherent broken inversion symmetry, monolayer 2D TMDs have been exploited to obtain valley-polarized EL. Electrically controlling circularly polarized EL was first demonstrated in monolayer and multilayer WSe₂ using ionic liquid gating.¹⁵⁸ Due to large carrier injection capability with ionic gating, inversion symmetry breaking and band structure modulation can be obtained in multilayer 2D TMDs. Consequently, circularly polarized EL from monolayer and multilayer samples has been observed under forward bias. The EL intensity linearly increased with increasing bias voltage. Electrically tunable, chiral EL from large area CVD-grown monolayer WS₂ in a p⁺-Si/i-WS₂/n-ITO heterojunction was found to be dominated by negatively charged excitons, with an increase in the injection current from 2.5–4.0 μA due to imbalanced carrier injection under forward bias, resulting in an enhanced n-type doping. EL with a high degree of circular polarization $\approx 81\%$ at 0.5 μA was reported in the same device [Fig. 7(i)].¹⁵⁹ Similarly, EL from MoSe₂ with circular polarization $\approx 66\%$ has also been obtained.¹⁶⁰

Another popular approach for obtaining electrically controlled, valley-polarized EL is via spin-polarized charge carrier injection through a ferromagnetic semiconductor or electrode (Ni/Fe Permalloy) into the TMD monolayers due to the spin-valley locking

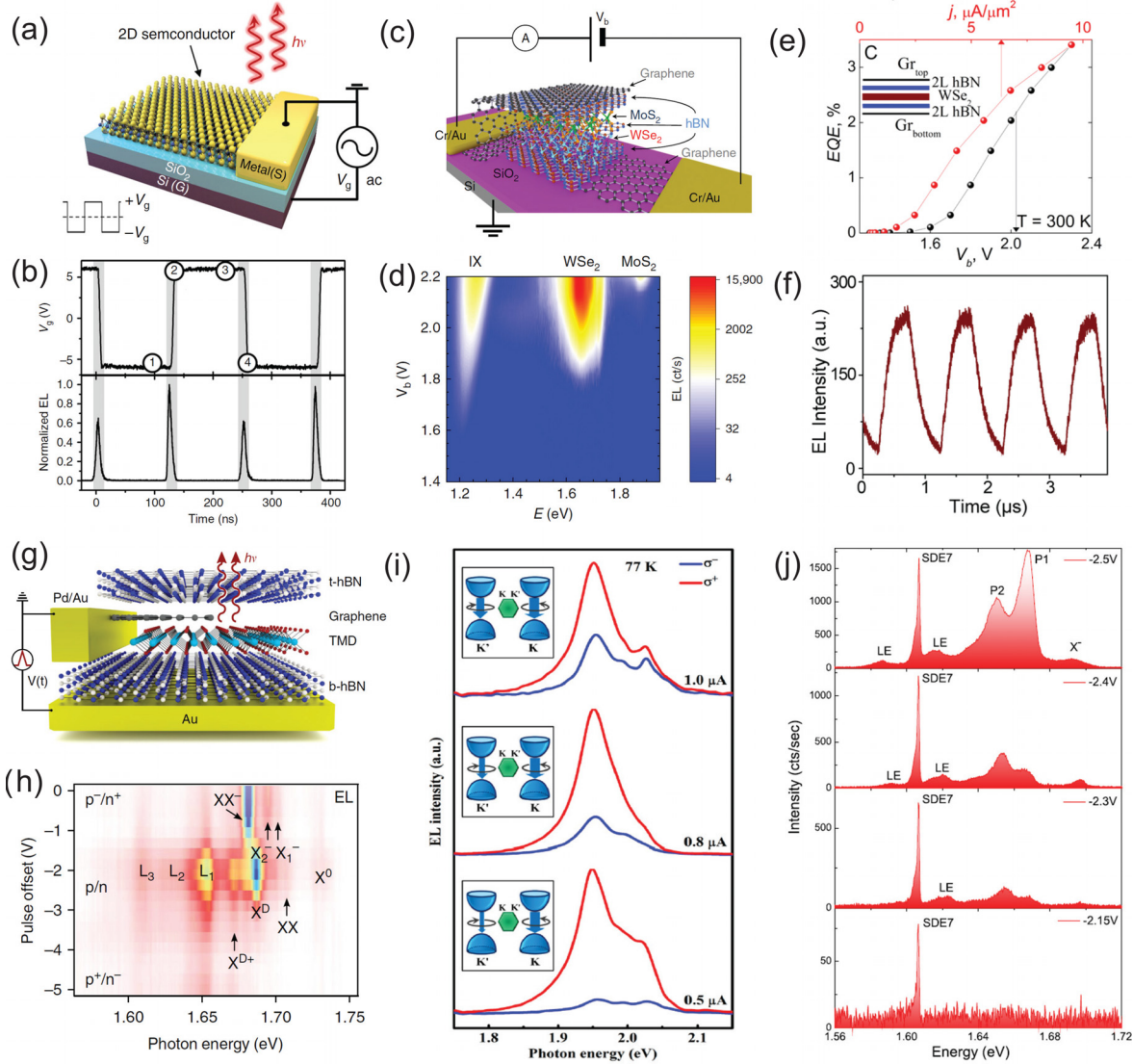


FIG. 7. Light emitting devices based on 2D materials. (a) Schematic of the t-EL device. An AC voltage is applied between the gate and source electrodes and emission occurs near the source contact edge. (b) Time-resolved EL and the corresponding V_g , showing that EL occurs at the V_g transients.¹⁴⁷ Reproduced with permission from Sundaram *et al.*, *Nano Lett.* **13**, 1416 (2013). Copyright 2013 American Chemical Society. (c) Schematic drawing of the MoS₂/WSe₂ heterostructures with a middle monolayer h-BN spacer. (d) False-color heatmap of the EL spectra as a function of bias voltage for samples without a monolayer h-BN spacer.¹⁵¹ Reproduced with permission from Binder *et al.*, *Nat. Commun.* **10**, 2335 (2019). Copyright 2019 Springer Nature. (e) The external quantum efficiency for a WSe₂ quantum well plotted against bias voltage and injection current density at T = 300 K. The EQE monotonically increases even up to current densities of 1000 A/cm².¹⁵³ Adapted with permission from Withers *et al.*, *Nano Lett.* **15**, 8223 (2015). Copyright 2015 American Chemical Society. (f) Electrical modulation of EL demonstrating 1 MHz electrical switch of the light emitter.¹⁵⁴ Adapted with permission from Liu *et al.*, *Nano Lett.* **17**, 200 (2017). Copyright 2017 American Chemical Society. (g) Schematic of the vdW heterostructure. The monolayer TMD and graphene are sandwiched between two multilayer h-BN flakes. (h) Color map of EL spectra at 5K plotted as a function of pulse offset V_0 in WSe₂.¹⁵⁷ Reproduced with permission from Paur *et al.*, *Nat. Commun.* **10**, 1709 (2019). Copyright 2019 Springer Nature. (i) Circularly polarized EL of the p+-Si/i-WSe₂/n-ITO heterojunction LED device at 77 K. The current-dependent circularly polarized EL spectra are normalized to the right-handed circular (σ^+) component at each injection current.¹⁵⁹ Adapted with permission from Yang *et al.*, *Nano Lett.* **16**, 1560 (2016). Copyright 2016, American Chemical Society. (j) Evolution of EL spectra as a function of bias. SDE7 and LE correspond to the EL peaks of the single-defect emitters and other localized states, respectively.¹⁶³ Reproduced with permission from Schwarz *et al.*, *2D Mater.* **3**, 025038 (2016). Copyright 2016 IOP Science.

effect. Circularly polarized EL at a (Ga,Mn)As/WS₂ p-n heterojunction and a WSe₂/MoS₂ heterojunction under forward bias has been obtained due to the imbalance of spin-injected carrier population at K and K' valleys.^{161,162}

e. Electrically controlled single quantum emitters. In addition to the direct-gap excitons, luminescence from localized defect states in 2D TMDs can be used to obtain single-photon quantum emitters, which are the fundamental building blocks for quantum photonics

and quantum information technologies. The emission from such localized defect states can be controlled electrically, resulting in the realization of electrically controlled quantum emitters. Electrically controlled EL from the localized states has been demonstrated in graphene/h-BN/WSe₂/h-BN/graphene vertical heterostructures, where¹⁶³ a spectrally sharp emission (at ≈ 1.607 eV, $V_b \approx -2.15$ V) corresponding to a single defect state (SDE7) was obtained. As the electrical bias was increased, additional broad features corresponding to emission from other localized states also emerged [Fig. 7(j)]. The full-width-at-half-maximum (FWHM) of the localized EL peak increased from 0.6 to 1.4 meV as the bias was increased above -2.3 V. In another report, electrically driven light emission from defects in WSe₂ using both vertical and lateral vdW heterostructure devices was obtained.¹⁶⁴ The vertical structure exhibited a broad peak due to defect-bound exciton states, including a narrow emission peak (≈ 1.705 eV) that was referred to as emission from a single defect. Electrical tuning of the emission from a single defect was demonstrated, where the emission was repeatedly switched on and off by sweeping external bias V_b from 1.9 to 2.1 V. In contrast, the lateral heterojunction device exhibited EL originating from several single defects having line widths < 300 μeV and a doublet structure with ≈ 0.7 meV energy splitting. Similarly, electrically driven single-photon emission from localized states in mono- and bilayers of WSe₂ and WS₂ has also been reported.¹⁶⁵ The electric current dependence of the EL from the quantum emitter showed clear saturation, whereas the emission from the unbound monolayer WSe₂ excitons exhibited a linear relation between emission intensity and injected current.

4. Optical modulators, mirrors, etc.

Extensive research efforts have been focused on designing ultrafast, low power, and compact optical modulators for a variety of applications, such as optical interconnects, environmental monitoring, security, and biosensing.^{166–168} For designing high-performance optical modulators, materials with low optical-loss, large non-linear optical constants, broad wavelength operation, large tunability of optical constants, and ease of integration with various optical components are desired. In this category, 2D materials have attracted significant attention, owing to their atomic thickness, strong light-matter interaction, broadband optical response, and tunable opto-electronic properties.¹⁶⁸ 2D materials also offer advantages for low-cost and large-scale integration to the well-developed silica fiber and silicon-based technology. Thus far, graphene has been the leading candidate for obtaining high speed optical modulation in an extremely broad spectral range, extending from the ultraviolet to microwave regions, primarily due to its unique linear energy-momentum dispersion relation and high mobility.^{169,170} However, other 2D materials such as monolayer TMDs and black phosphorus, which offer properties complementary to graphene, also exhibit similar potential and have been explored recently. The presence of a bandgap and parabolic band structure in 2D semiconductors can allow much higher tunability of the optical dielectric functions. Different tuning methods have been demonstrated to modulate the optical response of the 2D materials that can be characterized by the change in the dielectric constants or the complex refractive index of the materials.¹⁷¹ The electrical control of optical response is particularly desired for data communication link

applications. Herein, we present state-of-the-art progress in electro-optic modulators based on 2D semiconductors beyond graphene.

For the electro-optic modulators, the application of an external electric field is desired to tune both the real and imaginary components of the refractive index such that both the amplitude and phase of the optical field can be modulated. In a recent report, a modulation of the refractive index of monolayer TMDs, such as WS₂, WSe₂, and MoS₂, by more than 60% in the imaginary part and 20% in the real part, around their excitonic resonance was demonstrated using electrical gating.¹⁷² The giant tuning in refractive index was attained by changing the carrier density, which broadened the spectral width of excitonic transitions and facilitated the interconversion of neutral and charged excitons. The gate dependence of optical absorption and optical constants of TMDs was also investigated by several other groups [Figs. 8(a) and 8(b)].^{173,174} A modulation depth as high as ~ 6 dB for visible light (red light ~ 630 nm) has been reported.

The other popular approach that can be used for the manipulation of dielectric properties of TMDs is by the interaction of excitons with metallic plasmons. In one work, narrow MoS₂ excitons coupled with broad Au plasmons led to an asymmetric Fano resonance that was effectively tuned by the applied gate voltage to the MoS₂ monolayers.¹⁷⁵ The gate-dependency of the Fano resonance is strongly sensitive to the modulation of the exciton–plasmon coupling strength and can be controlled by the MoS₂ exciton absorption at different external gate voltages. Active control of light-matter interactions is also critical for realizing plasmonic nanostructure-based electro-optic modulators. An electrical control of exciton–plasmon coupling strengths between strong and weak coupling limits in a 2D semiconductor has also been demonstrated with electrostatic doping [Figs. 8(c) and 8(d)].¹⁷⁶ In addition to the coupling of the plasmonic modes to the neutral excitons, a strong coupling with negatively charged excitons was also obtained that can be switched back and forth with the gate voltage. In another recent study, electrical modulation of plasmon-induced exciton flux was demonstrated using Ag-nanowire waveguides overlapping with TMD transistors.¹⁷⁷ The laser-coupled-plasmon propagated through the Ag nanowire in the axial direction, which sequentially excited excitons of the TMD, and the exciton flux was modulated by the gate voltage. In most of the reports, electrical tuning of the optical properties of TMDs was achieved near their excitonic resonances only, where the refractive index and absorption can be modulated simultaneously at a maximum magnitude. In a recent report, electro-optic response of monolayer TMD (WS₂) at NIR wavelength regions was probed for integrated photonics applications.¹⁷⁸ Using an ionic liquid gate, high electron doping densities ($7.2 \pm 0.8 \times 10^{13}$ cm⁻² at 2 V) were induced in the monolayer WS₂ and a large change in the real part of the refractive index ($\approx 53\%$), and a minimal change in the imaginary part ($\approx 0.4\%$) was demonstrated [Figs. 8(e) and 8(f)]. Also, a doping-induced efficient phase modulator with high $|\Delta n/\Delta k| \approx 125$ and low propagation losses was achieved.

Apart from TMDs, black phosphorus (BP) is also an emerging candidate for designing electro-optic modulators in the mid-infrared frequencies owing to its smaller bandgap. Several theoretical and experimental investigations have shown that an external electric field can result in a shift in BP's absorption edge due to the interplay between different electro-absorption mechanisms, mainly the field-induced, quantum-confined Franz-Keldysh effect, and the Pauli-blocked Burstein–Moss shift.^{179–181} These different mechanisms lead

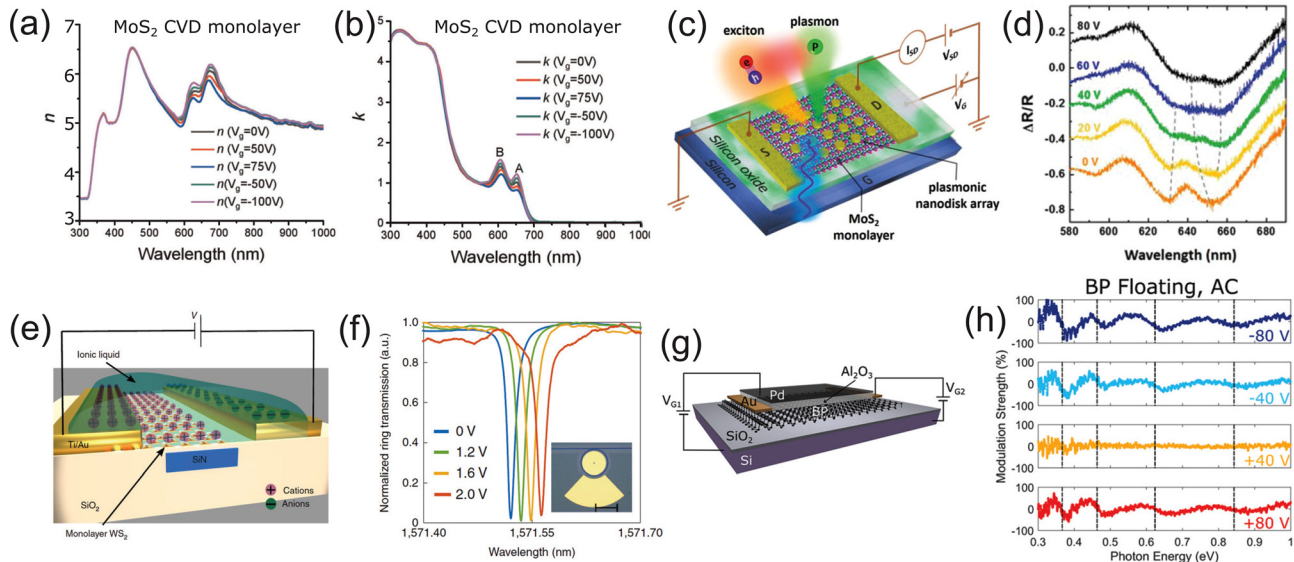


FIG. 8. 2D materials for electro-optic modulators. Gate induced changes in the complex refractive index of MoS₂ monolayer: (a) the real part and (b) the imaginary part.¹⁷³ Reproduced with permission from Kravets *et al.*, *npj 2D Mater. Appl.* **3**, 36 (2019). Copyright 2019 Springer Nature. (c) Schematic diagram of the MoS₂ monolayer-plasmonic lattice system integrated with an FET device. (d) Line cuts from the angle-resolved spectra at different gate voltage.¹⁷⁶ Adapted with permission from Lee *et al.*, *Nano Lett.* **17**, 4541 (2017). Copyright 2017 American Chemical Society. (e) Schematic of the composite SiN-WS₂ waveguide with ionic liquid cladding. By applying a bias voltage across the two electrodes through the ionic liquid, charge carriers were induced in the monolayer. (f) Normalized transmission response of the microring resonator at different voltages applied across the two electrodes.¹⁷⁶ Adapted with permission from Datta *et al.*, *Nat. Photonics* **14**, 256 (2020). Copyright 2020 Springer Nature. (g) Schematic diagram of the device to obtain anisotropic electro-optical effect in few-layer black phosphorous (BP). (h) Tuning of BP oscillator strength with a field applied to the floating device for light polarized along the AC axis.¹⁸² Adapted with permission from Sherrott *et al.*, *Nano Lett.* **19**, 269 (2019). Copyright 2017 American Chemical Society.

to distinct optical responses that are strongly dependent on the flake thickness, doping concentration, and operating wavelength. To isolate and define the working mechanism of different electro-absorption effects, a recent report used two different field-effect device configurations with different gating schemes, wherein the BP either floats electrically in an applied field or is in direct contact [Figs. 8(g) and 8(h)].¹⁸² In the electrically floating case, the dominant tuning mechanism is the quantum-confined Stark effect, while in the other case tunability is dominated by carrier concentrations effects, e.g., by the Burstein–Moss shift. Near-unity tuning of the BP oscillator strength and electro-optic tuning of linear dichroism over a broad range of wavelengths, from the mid-infrared to the visible, by controlling the thickness of the BP was reported.

While significant progress has been achieved with optical modulation using 2D materials, it is safe to say that, with the exception of graphene, the field is in its infancy. This is evident from Fig. 9, where we have compared the depth of modulation with the wavelength of modulation. Graphene-based modulators not only show exceptional modulation depth, but, due to its zero-gap nature, they can also operate well at telecom wavelengths, with performance comparable to Si, LiNbO₃ and III–V modulators. In contrast, TMDs are barely able to operate in the NIR range. The key issue at play for materials beyond graphene to serve in high-performance optical modulators is the lack of quality large-area material. Furthermore, most 2D semiconductors are in the 1.1–3 or <0.5 eV range of bandgap values. This makes it

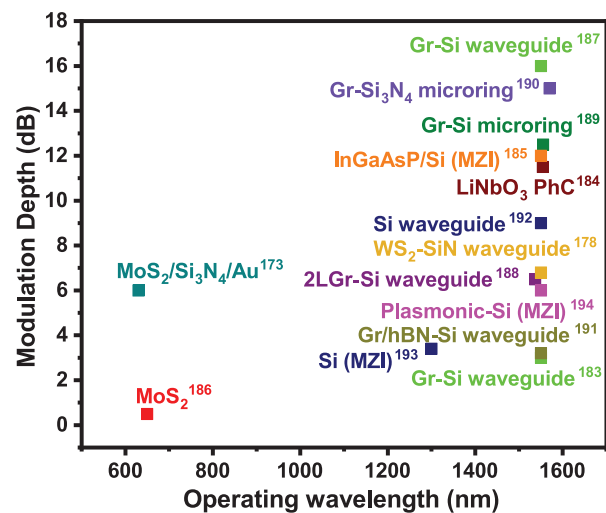


FIG. 9. A comparison plot of modulation depth vs operating wavelength for optical modulators comprising 2D materials, namely, graphene (Gr) and molybdenum disulfide (MoS₂) as the active modulation medium with state-of-the-art bulk materials [Si, LiNbO₃ and III–V (InGaAsP) on Si] based optical modulators reported in the literature. The square symbols of varying colors correspond to the experimental data points adopted from Refs. 173, 178, and 183–194. The type of modulator is also mentioned next to active medium. Abbreviation: MZI (Mach–Zehnder interferometer) and PhC (photonic crystal).

difficult to achieve modulation by means of a dominant photorefractive effect at a band or exciton edge in a 2D semiconductor in the telecom range (≈ 0.8 eV). Finally, it is equally important to attain good metal contacts to inject and extract carriers at high speed with minimal resistance or other parasitic circuit elements, particularly at high operation speeds.

D. Sensors

Due to their unique physical properties, tunability, and versatility, 2D materials are particularly attractive for multiple sensing applications. Here, we consider their use for gas (primarily environmental), humidity, and biosensing as well as in strain and pressure sensing. The fact that their electronic structure is highly susceptible to and tunable by hybridization, chemical modification, or doping makes them an ideal platform for regulation of catalytic properties. This is particularly important for their applications as chemical and biosensors, often allowing fine control of sensing by electrical means. We specifically focus our attention on the electrical means of readout and control of such sensors. For another very powerful way to control such sensors, namely, optical or optoelectronic detection, we address the readers to the other reviews in the area.^{195–197}

Based on the tremendous success of graphene-based sensors, as seen both in the published research (at the moment of the review submission (June 2021): Google search gave $\approx 36\,500\,000$ results; Web of Science search – $\approx 27\,600$ publications) and first successful commercialization,¹⁹⁸ efforts in constructing novel sensing platforms led to exploitation of other, more versatile and tunable 2D materials, e.g., TMDs, carbon nitride, boron nitride, phosphorene, and MXenes, which will be discussed in this section of the review.

1. Gas sensors

In this review, we consider the recent developments in non-graphitic 2D material sensors that have followed in the wake of graphene. We discuss the different classes of 2D materials in application to sensing as well as their figures of merits, such as Level of Detection (LoD), selectivity, response/recovery time, and detection range, and compare them with the performance of graphene sensors.

When discussing the physical mechanisms of sensor operation, we only consider non-covalent (and thus reversible) interactions between the target analyte and 2D material, which include vdW forces, hydrogen bonding, coordination, and π - π interactions. The type of interaction for each 2D material will depend on its chemical and electronic structure, distinct structural features, and surface chemistry. To be electrically detectable, any of these interactions should induce changes in physical parameters such as conductivity, work function, or permittivity. This is typically realized through fundamental mechanisms such as modulation of doping level and/or Schottky barrier, as well as the formation of dipoles and interfacial layers. For more details, see Meng *et al.*¹⁹⁵ and the references within.

In the majority of cases, the numerical output of a whole FET device is read out in the response to global gas exposure. Recently, Noyce *et al.*¹⁹⁹ provided an important insight into sensing mechanisms by realizing precise nanoscale control over the position and charge of an analyte using a charged scanning atomic force microscopy (AFM) tip acting as an effective analyte. The non-uniform sensitivity of an MoS₂ FET channel was demonstrated, showing time-

stable, sensitive hotspots, where the signal-to-noise ratio was maximized at the center of the channel, and the response of the device is highly asymmetric with respect to the polarity of the analyte charge. The work reveals the important role of analyte position and coverage in determining the optimal operating bias conditions for maximal sensitivity in 2D FET-based sensors, which provides key insights for future sensor design and control.

Sensors serve an important role in the detection of common environmental gas pollutants including nitrogen dioxide (NO₂ at 21 ppb), sulfur dioxide (SO₂ at 7.5 ppb), hydrogen sulfide (H₂S at 5 ppm), ammonia (NH₃ at 20 ppm), and carbon monoxide (CO at 4 ppm). Each of these gases is considered to be toxic for human health although the specific exposure limits vary significantly. The recommended exposure limits (as set by the Gothenburg Protocol²⁰⁰ or the Paris Climate Agreement²⁰¹) for each of these pollutants are shown in parentheses above. See Buckley *et al.*¹⁹⁶ for more details. Additionally, carbon dioxide (CO₂) and methane (CH₄) are not toxic gases but are responsible for the greenhouse effect, leading to climate change. The exposure limits indicated in the parentheses above should be taken into account when performance of individual sensors is evaluated, as in a number of cases the demonstrated LoD and detection range are far outside of specific environmental requirements.

a. TMDs. Among all 2D materials, TMDs and specifically MoS₂ have been the most intensely explored for gas sensing, where earlier works focused largely on mechanically exfoliated TMD materials of variable thickness.^{202,203} MoS₂ FETs fabricated with 2–4 layers of MoS₂ exhibited better performance compared with monolayer MoS₂, which showed unstable response. For similar MoS₂ FETs, detection of both electron acceptors (NO₂) and electron donors (NH₃) under different conditions such as gate bias and light irradiation has been explored²⁰⁴ [Fig. 10(a)]. MoS₂ FET exhibited better sensitivity, recovery, and ability to be manipulated by gate bias, e.g., sensitivity to 200 ppm NO₂ exposure increased from $\approx 50\%$ to $\approx 400\%$ for bilayer and 5-layer MoS₂, respectively, under $V_g = 15$ V. Additionally, for 5-layer MoS₂, resistance goes down when the sample is irradiated by green light, and the magnitude depends on the illuminated power density.²⁰⁴ It is noteworthy that the measurements were conducted in the high concentration range of NO₂, 10–1000 ppm. There have also been reports studying gas sensing of MoS₂ using more scalable material techniques, such as vapor phase growth of thin films²⁰⁵ and flexible transistor arrays using all solution-processable materials.²⁰⁶

Typically, the time-response of solid-state sensors is a challenging parameter, often showing unsatisfactory performance in ambient conditions. Poor response time and incomplete recovery at room temperature have often restricted the application of many 2D materials in high-performance practical gas sensors. Fast detection of NO₂ and reversibility have been demonstrated for MoS₂ gas sensors at room temperature.²⁰⁷ While incomplete recovery and a high response time of ≈ 249 s of the sensor were observed in ambient, MoS₂ exhibited an enhancement in sensitivity with a fast response time of ≈ 29 s and excellent recovery to NO₂ (100 ppm) under photoexcitation at room temperature. The effect was attributed to charge perturbation on the surface of the sensing layer under optical illumination. Driven by the same goal and using hybrid MoS₂ materials, Long *et al.*²⁰⁸ presented fast detection and complete recovery (both at <1 min) to NO₂ at 200 °C using MoS₂/graphene/hybrid aerogels. Similarly, using an

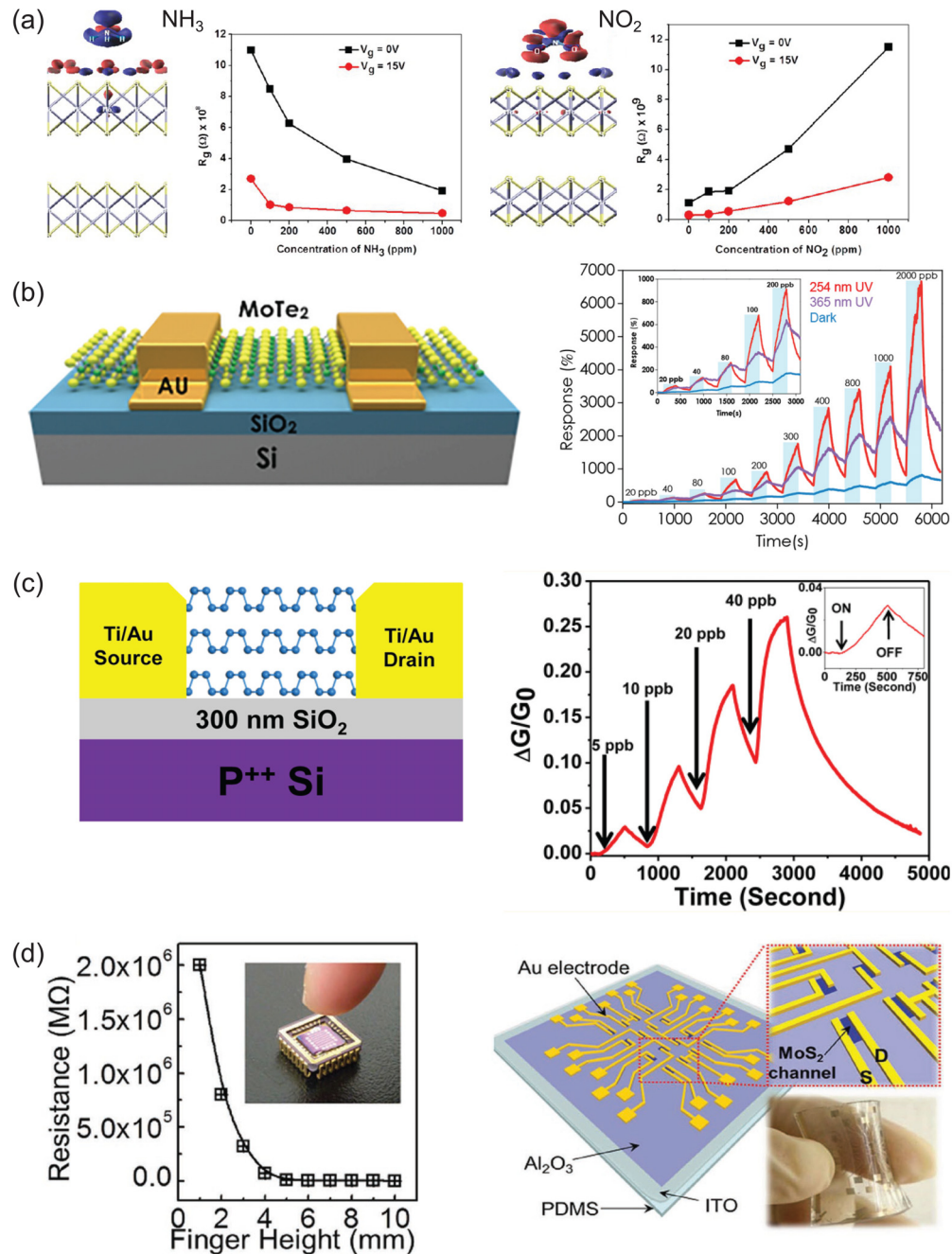


FIG. 10. 2D materials for gas sensing. (a) Left: Charge transfer for NH_3 (top) and NO_2 (bottom) molecules on bilayer MoS_2 with $V_g = 0 \text{ V}$. The red/blue isosurface indicates negative/positive charge. Right: Variation of resistance for NH_3 (top) and NO_2 (bottom) on bilayer MoS_2 at $V_g = 0$ and 15 V .²⁰⁴ Adapted with permission from Late *et al.*, ACS Nano 7, 4879 (2013). Copyright 2013 American Chemical Society; (b) Top: schematic diagram of MoTe_2 transistor. Bottom: dynamic sensing performance toward NO_2 in N_2 environment at concentration from 20 to 2 ppm under different light illuminations. Inset: dynamic sensing behaviors to NO_2 at concentration from 20 to 200 ppb. The light blue bars denote the gas concentration of each exposure.²¹⁴ Adapted with permission from Wu *et al.*, ACS Sens. 3, 1719 (2018). Copyright 2018 American Chemical Society; (c) Left: schematics of a multilayer black phosphorus (BP) FET. Right: sensing performance of BP FET to NO_2 gas exposure (0.6–10 ppm).²¹⁷ Adapted with permission from Abbas *et al.*, ACS Nano 9, 5618 (2015). Copyright 2015 American Chemical Society; (d) Left: Humidity sensor: the exponential increase in the resistance with the finger moving closer to the MoS_2 device. Right: Schematic illustration of MoS_2 FETs array on soft poly(dimethylsiloxane) (PDMS) substrate. Insets show the magnified MoS_2 channels and optical image of the sensor array, respectively.²¹⁶ Adapted with permission from Zhao *et al.*, Adv. Mater. 29, 1702076 (2017). Copyright 2017 Advanced Materials.

MoS₂ nanosheet–Pd nanoparticle composite, Kuru *et al.*²⁰⁹ showed a room-temperature H₂ response/recovery time of 40/83 s, respectively. In a work by Park *et al.*,²¹⁰ a highly porous h-MoS₂/Pt nanoparticle (NP) hybrid, synthesized by pyrolysis, was used for H₂ detection, demonstrating 8/16 s for response/recovery time, respectively, for 1% of H₂. This response is among the fastest for 2D material-based H₂ sensors in a standard ambient environment.

While experimental detection of non-polar gases (e.g., CO₂, CH₄) with 2D material-based sensors is generally problematic due to the lack of strongly pronounced adsorption mechanisms, a modeling study using first-principles and Monte Carlo simulations revealed that single and double sulfur vacancies exhibit an excellent adsorption ability for both polar and non-polar gases.²¹¹ The simulation results showed that MoS₂ with a single S vacancy could absorb 42.1 wt. % of CO₂ and 37.6 wt.% of CH₄ under a pressure of 80 bar at room temperature.

As mentioned above, heterostructures combining a 2D material and some other active component(s) often demonstrate an enhanced performance for gas sensing compared to their individual counterparts. For example, MoS₂/Co₃O₄ thin film sensors were implemented for ultra-low-concentration detection of ammonia at room temperature,²¹² revealing high sensitivity, good repeatability, stability, selectivity, and fast response/recovery characteristics. Zhang *et al.*²¹³ demonstrated a hydrogen gas sensor based on a complex Pd-SnO₂/MoS₂ ternary hybrid. The experimental results showed a response within 1%–18% resistance change, swift response-recovery time (10–20 s), good repeatability, and high selectivity toward hydrogen gas in the range of 30–5000 ppm at room temperature.

In comparison to MoS₂, WS₂ has been significantly less explored for gas sensing applications, with the most notable works including complex 3D geometries assembled of 2D nanostructures. For example, a WS₂ nanoflake-based sensor showed a good sensitivity to ammonia (1–10 ppm) at room temperature with the response/recovery time of 120/150 s, respectively. Interestingly, the sensor also demonstrated excellent selectivity to formaldehyde, ethanol, benzene, and acetone.²¹⁷ A sensor made of WS₂ nanosheets with size of 10 nm exhibited selectivity toward NO₂ and H₂S,²¹⁸ where the presence of oxygen and elevated temperatures (160 °C) were necessary for H₂S sensing. An interesting approach to increase the surface area (and thus number of active sites for molecular adsorption) of atomically thin TMDs was demonstrated by synthesizing 3D WS₂ nanowalls combined with CdSe–ZnS quantum dots (QDs), with a demonstrated detection limit of 50 ppb for NO₂ and a fast response time of ≈26 s.²¹⁹

In general, many 2D disulfides have proven selectivity toward NO₂. A sensor based on SnS₂ platelets demonstrated high sensitivity (600 ppb measured) and superior selectivity to NO₂²²⁰ due to the unique physical affinity and favorable electronic band positions of SnS₂ and NO₂. Density functional theory (DFT) studies of NbS₂ also suggest its high selectivity toward NO₂²²¹ depending on its edge configuration. In a recent work, a monolayer Re_{0.5}Nb_{0.5}S₂ sensor demonstrated high sensitivity, selectivity, and stability toward NO₂ detection, accompanied by only minimal response to other gases, such as NH₃, CH₂O, and CO₂.²²² In the presence of humidity, the monolayer sensor showed complete reversibility with fast recovery at room temperature. Including other TMDs, the fast response/recovery rate accompanied by enhanced sensitivity under UV illumination was achieved in a p-type MoTe₂ gas sensor for NO₂ detection, demonstrating full

recovery within 160 s after each sensing cycle at room temperature [Fig. 10(b)].²¹⁴ The sensitivity of the sensor to NO₂ was significantly enhanced by an order of magnitude under 254 nm UV illumination as compared to that in the dark, leading to a remarkably low detection limit of 252 ppb (as derived from noise measurements).

b. Other 2D materials. Phosphorene and blue phosphorus: Following the initial prediction of superior gas sensing applications using first-principles calculations,²²³ semiconducting phosphorene (or 2D black phosphorus) has been proven to have great potential for gas sensing of CO, CO₂, NH₃, and NO (see, e.g., Liu *et al.*²²⁴). Abbas *et al.*²¹⁵ experimentally demonstrated phosphorene-based FETs for NO₂ detection, achieving a lowest detectable concentration of 5 ppb [Fig. 10(c)]. Phosphorene functionalized with gold has been shown to display selectivity to NO₂ (compared with H₂, acetone, acetaldehyde, ethanol, hexane, and toluene).³⁷ Although pristine phosphorene is typically insensitive to H₂, functionalization with Pt NPs led to improved H₂ sensing efficiency, as seen in the decreasing of the drain–source current and increase in the ON/OFF ratio at low concentrations of H₂.^{37,225} An impedance-based phosphorene-based sensor has demonstrated a strong response to a low concentration of methanol vapor (28 ppm) at ≈1 kHz in impedance phase spectra, showing a high selectivity to methanol and absence of cross-selectivity from toluene, acetone, chloroform, dichloromethane, ethanol, isopropyl alcohol, and water, due to the different dielectric constants of these molecules.²²⁶

Sensing properties of another 2D allotrope of phosphorus—blue phosphorus—were studied by first-principles calculations with respect to the adsorption behaviors of environmental gas molecules, including O₂, NO, SO₂, NH₃, H₂O, NO₂, CO₂, H₂S, CO, and N₂.²²⁷ The calculations showed that O₂ tended to chemisorb, whereas the other gases were physisorbed on monolayer blue phosphorus, showing different interaction strengths and distinct modifications to the bandgap, carrier effective mass, and work function.

h-BN: Applications of h-BN in gas sensing have remained challenging due to its inherently low chemical reactivity. Recently, a chemiresistor-type NO₂ gas sensor based on sulfate-modified h-BN has been investigated, demonstrating a linear response over a wide NO₂ concentration range and low LoD of 20 ppb.⁴¹ Theoretical calculations predicted that the sulfate groups spontaneously grafted to the h-BN, effectively altering its electronic structure and enhancing the surface adsorption capability toward NO₂, in addition to a strong charge transfer between NO₂ and h-BN. Thus, applications of sulfate-modified h-BN in capturing environmentally hazardous exhaust from motor vehicles as well as combustion emissions monitoring have been proposed.

In a recent theoretical study, graphene/h-BN heterostructures were studied for detection of NO, NO₂, NH₃, and CO₂ gas molecules.²²⁸ The strongest interaction was observed for the case of NO_x, where NO and NO₂ molecules are more reactive at the interface regions of the heterostructure compared to the pristine ones, where large changes in the conductance with adsorption were seen. In addition, recent experimental work has successfully demonstrated NH₃ detection with graphene/h-BN devices.²²⁹ The charge transfer from NH₃ to graphene strongly depends on the average distance between the graphene sheet and the substrate. Since the average distance between graphene and h-BN crystals is one of the smallest, the graphene/h-BN heterostructure exhibited the fastest recovery times for

NH₃ exposure and revealed importance of substrate engineering for development of 2D gas sensors.

MXene: Recently a new class of 2D materials—transition-metal carbides (Ti₃C₂T_x MXene)—have received a great deal of attention for potential use in gas sensing, showing both high sensitivity and good gas selectivity. Integration of an effective superhydrophobic protection fluoroalkylsilane (FOTS) layer with MXenes has helped overcome one of the major problems typical for this class of material, which is environmental instability.²³⁰ FOTS-functionalized Ti₃C₂T_x displayed very good hydration stability in a humid environment and showed good tolerance to strong acidic and basic solutions. The experiments also demonstrated very good sensing performance (e.g., sensitivity, repeatability, stability, selectivity, and faster response/recovery time) to oxygen-containing volatile organic compounds (ethanol, acetone), as achieved in a broad relative humidity range of 5%–80%.

This review represents only a relatively small fraction of the research on the use of 2D materials sensors for gas detection. In a chart shown in Fig. 11, we summarize the recent figures of merits: LoD (a), detection range (b), and response/recovery time (c) for graphene (as well as GO and rGO) and other layered 2D materials based on the results presented here as well as recent, more specialized reviews by Buckley *et al.*¹⁹⁶ and Meng *et al.*¹⁹⁵ We limit this summary to NO₂ gas only as being generally one of the easiest substances for detection and thus the most intensely studied in literature. It is important to emphasize that in many cases, the measurements were performed in very specific physical conditions (such as temperature, illumination, etc.), which are not reflected in the chart. The red dashed/dotted lines on the chart [Figs. 11(a) and 11(b)] represent recommended annual mean limits of exposure as specified by the European Union (EU) and National Ambient Air Quality Standards (NAAQS), i.e., 21 and 58 ppb, respectively.^{231,232} The area above the EU annual mean level (as highlighted by gray) demonstrates a potentially unsafe level of exposure for humans (note the exponential scale both for LoD and range). In terms of the response and recovery time, the results also vary significantly, with the recovery time being generally (in many cases, significantly) larger than the response one [Fig. 11(c)]. Thus, the conclusions driven from these graphs are unfortunately not very positive. While each individual study often shows an interesting research breakthrough and outlines favorable detection conditions, the overall picture shows that, in the majority of cases, detection is achieved in conditions which are not suitable for environmental monitoring (e.g., falls significantly above red lines), yet may still be relevant for sensors employed in the chemical or defense industries. Graphene is generally more suitable for environmental diagnostics compared to other 2D materials, both in terms of higher sensitivity to NO₂ and generally a more favorable detection range, although this might be due to the larger number of studies conducted on graphene. Focusing on non-carbon-based 2D materials, some of the results obtained on BP and MoS₂ appear to be the most promising in terms of the LoD and detection range. The comparison between non-carbon 2D materials and graphene seems to be more encouraging in terms of the response and recovery times, where semiconducting 2D materials with a bandgap (BP, MoS₂, SnS₂) are characterized by generally faster times and would be more suitable for the immediate response to changing environmental conditions. This analysis demonstrates a crucial need not only to improve performance of the sensor but also to align it with the relevant targets dictated by the environmental detection needs, which have been unfortunately disregarded in many studies.

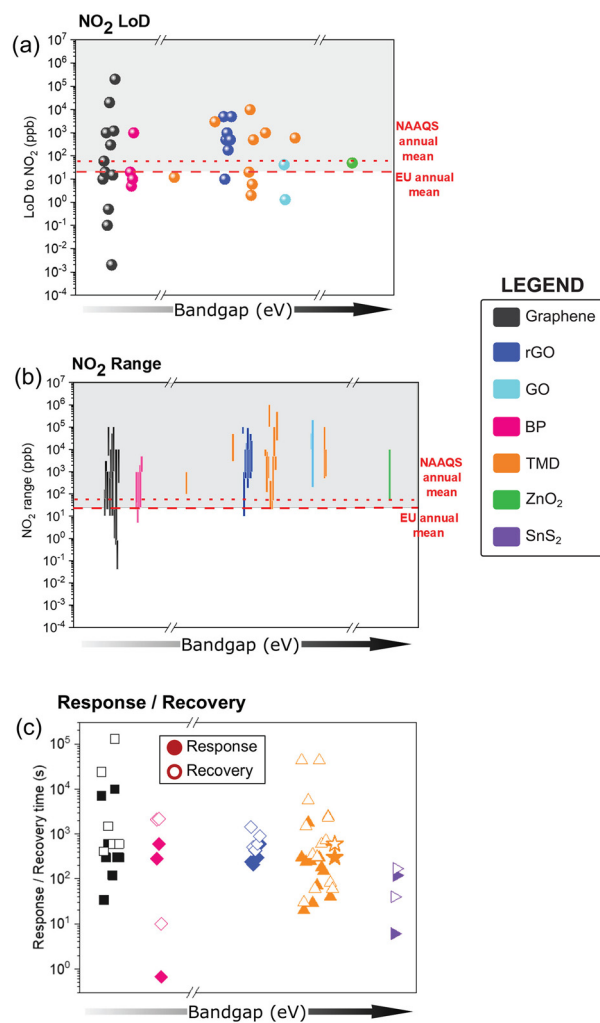


FIG. 11. Comparative analysis of gas sensors based on graphene and 2D materials toward NO₂: (a) level of detection; (b) detection range; and (c) response and recovery time. The red dashed/dotted lines in (a) and (b) represent recommended annual mean limits of NO₂ exposure as specified by EU and NAAQS, respectively. The gray panels in (a) and (b) show NO₂ concentrations above environmentally safe levels as specified in the text. The solid/open symbols in (c) represent the response/recovery time for each material. The offsets in the horizontal direction are introduced for clarity. The data are adapted from the recent reviews^{195,196} (see tables within).

c. Humidity sensors. In addition to their wide-spread application in gas sensing, 2D materials, especially TMDs, have exhibited great potential for humidity sensing. For example, monolayer MoS₂ devices on a flexible PDMS substrate have demonstrated a high humidity sensitivity >10⁴, with their mobilities and ON/OFF ratios decreasing linearly at RH = 0%–35%.²¹⁶ The authors showed an exponential increase in the resistance with a human finger moving closer to the MoS₂ device [Fig. 10(d)], with short response and decay times. In a similar approach, a hybrid ultrasensitive humidity sensor based on a MoS₂-SnO₂ nanocomposite revealed very good sensing parameters (e.g., response, fast response/recovery time and repeatability)²³³ compared

to the pure MoS₂ and SnO₂ counterparts, and graphene. In another work, a complex device, which incorporated large-area WS₂ as a sensing element, graphene as an electrode and thin flexible and stretchable PDMS as a substrate was utilized for humidity sensing (up to 90%) with fast response/recovery times (in a few seconds).²³⁴ The sensor was then laminated onto human skin and showed stable water moisture sensing behaviors, enabling real-time monitoring of human breath. Another flexible humidity sensor based on VS₂ has represented a new concept of a touchless positioning interface, based on the spatial mapping of moisture.²³⁵ In general, these flexible skin-attached chemical sensors (electronic skin or e-tattoo) are of great interest for many applications. Several interesting works have also emerged exploring applications of phosphorene in humidity sensing.²²⁴ Yasaei *et al.*²³⁶ realized a humidity sensor made of phosphorene nanoflakes. When the sensor was exposed to flows of H₂, O₂, CO₂, benzene, toluene, and ethanol, it resulted in enhancement of the electrical response only in the presence of a water atmosphere.

The several 2D sensors summarized here have proved to be strong candidates for ultrahigh-performance humidity sensors for various applications and have demonstrated a clear path toward developing low-power-consumption, wearable chemical sensors based on 2D semiconductors.

d. Summary. We have shown that, similar to graphene, 2D material FET sensors bear the advantage of miniature size and good compatibility with CMOS technology. Moreover, the existence of the bandgap allows for an additional degree of electrical control of adsorption/desorption of targeted molecules. The bandgap becomes particularly useful for manipulation of the sensor's response/recovery time. It is important to note that, while individual comparison studies may confidently prove advantages of a certain 2D material to graphene for the main figures of merit, the cumulative comparison performed in this review for the case of NO₂ demonstrated an extremely broad spread of such parameters as LoD, detection range, and response/recovery time, which overall is not dissimilar for graphene and non-carbon 2D materials. Thus, an overwhelming advantage of 2D materials over graphene has not been statistically demonstrated at the current technological level.

2. Biosensors

The success of graphene-based biosensors has stimulated a large research interest in the implementation of other 2D materials in biosensing platforms. Here, we present a short overview of the current state of the art and outline the most promising directions in the area of biosensors, focusing our attention on the electrical schemes of a sensor's control and optimization. For more detailed and insightful reviews in this area, we refer to the recent works by Bollella *et al.*,²³⁷ Zhu *et al.*,²³⁸ Hu *et al.*,²³⁹ Meng *et al.*,¹⁹⁵ and Kou *et al.*²⁴⁰

a. TMDs. Similar to gas sensing, among atomically thin 2D materials, TMDs have been the most intensely studied for electrochemical biosensing purposes.²⁴¹ Their high surface-to-volume ratio offers potential for the detection of large amounts of target analytes and low power consumption. The current state of growth is such that 2D TMDs can be readily synthesized on a large scale and can be directly dispersed in aqueous solution without the aid of surfactants, providing

environmentally friendly and even biocompatible and biodegradable solutions.^{195,242–244} Figure 12 schematically summarizes the broad range of applications of 2D TMD biosensors for the detection of various molecules. Specifically owing to its high conductivity and a large number of active defects that provide sites for adsorption of biomolecules, MoS₂ is one of the most commonly used TMD materials for biosensing.¹⁹⁵ Either in its pristine form or as a part of hybrid structures/nanocomposites, MoS₂ has been used both as a platform for non-enzymatic sensing and as a biocompatible matrix for enzyme immobilization and development of both electrochemical sensors and biosensors [Figs. 12 and 13(a)].^{237,245,246}

MoS₂-based FETs have been successfully employed as a 2D platform for detection of various biomolecules, including streptavidin and biotin,²⁴⁸ ochratoxin,^{249–251} dopamine,²⁵² anti-PSA,^{253,254} TNF- α ,^{255,256} and bisphenol A.²⁴² We will further discuss these applications in order of increasing weight and complexity of biomolecules (Fig. 12). Specifically, for streptavidin and biotin detection (one of the strongest known binding reactions in biology), it has been demonstrated that MoS₂-based sensors provide specific protein sensing at concentrations as low as 100 fM. Superior performance of a MoS₂-based FET sensor to graphene counterparts has been proven, e.g., \approx 70-fold better sensitivity of the MoS₂ biosensor was demonstrated^{245,248} [Fig. 13(a)]. The detection of glucose, one of the most important human biomarkers, using atomically thin 2D materials has been widely explored in recent years.^{257–259} In general, two common routes have been developed, implementing both enzymatic^{258,260} and non-enzymatic^{259,261} sensors. MoS₂ has also often been used as a platform for the development of hydrogen peroxide, H₂O₂, an essential

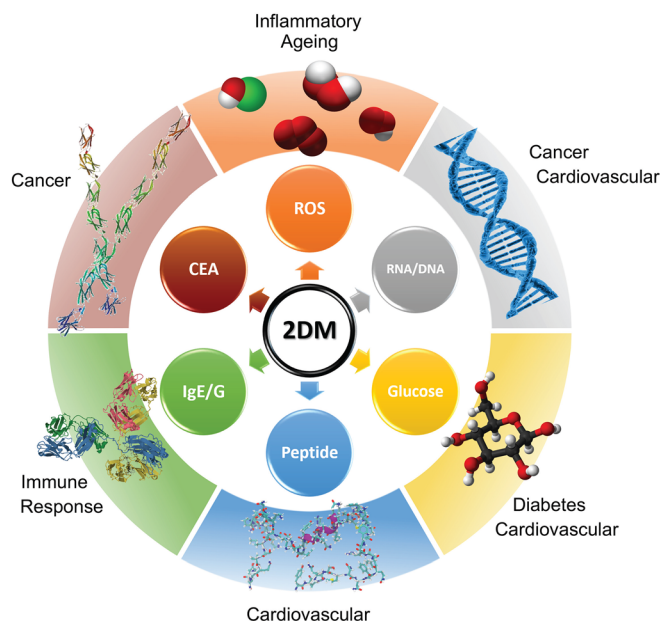


FIG. 12. Schematic diagram showing application of various 2D TMD materials in biosensing. Clockwise: in order of increasing complexity of analytes: reactive oxygen species (ROS) used in inflammatory diagnostics and aging reactions; RNA/DNA for cancer and cardiovascular diagnostics; glucose for diabetes and cardiovascular diagnostics; peptides for cardiovascular diagnostics; immunoglobulin E and G (IgE/G) for immune response; and carcinoembryonic antigen (CEA) for cancer diagnostics.

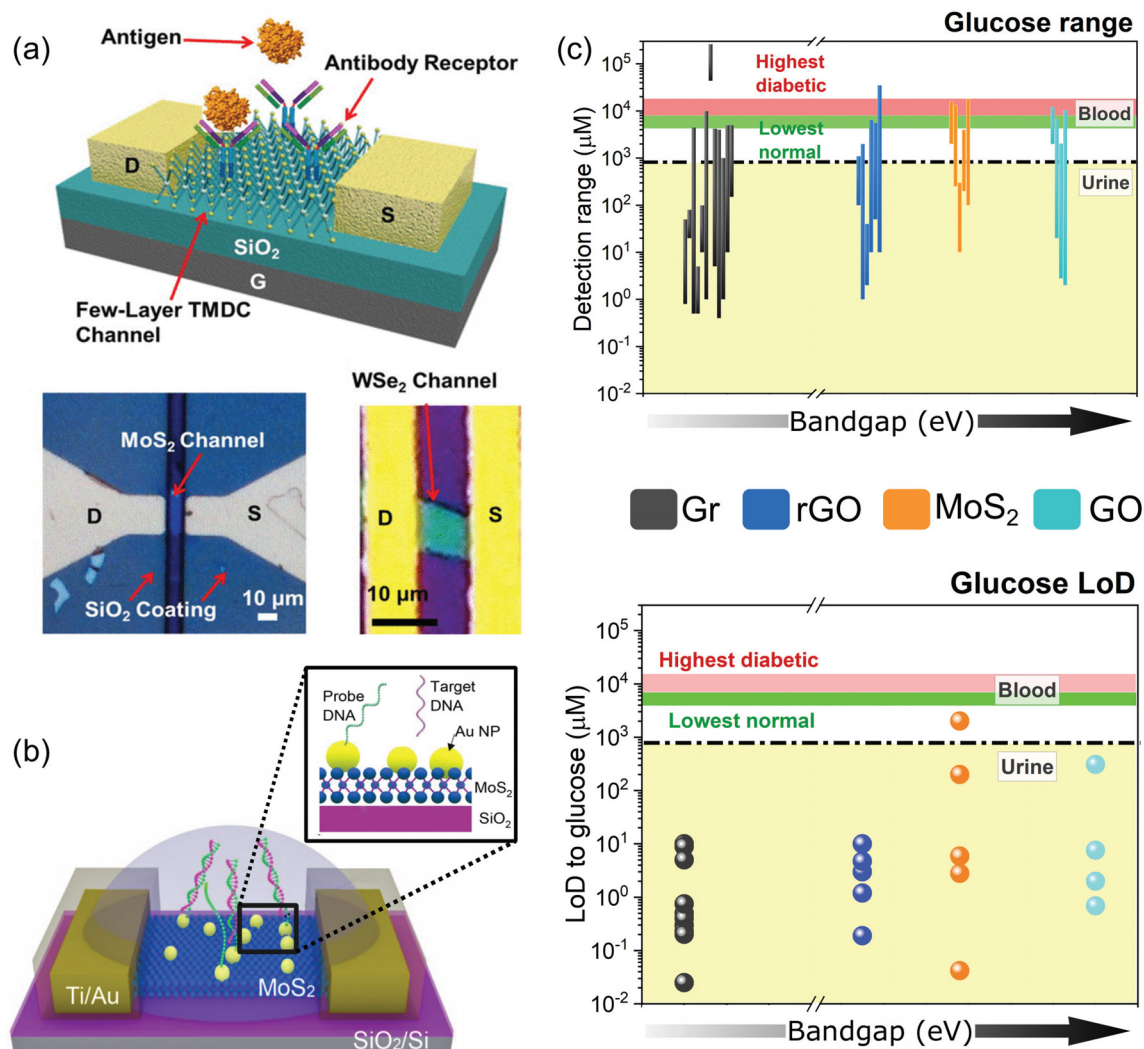


FIG. 13. Biosensors based on 2D materials. (a) Top: the schematic diagram of TMD biosensors for detection of antibody–antigen reactions; bottom: SEM and AFM images of MoS₂ and WSe₂ devices.²⁴⁵ Reprinted with permission from Nam *et al.*, *J. Vac. Sci. Technol. B* **33**, 06FG01 (2015). Copyright 2015 American Vacuum Society. (b) Schematic illustration of the MoS₂-Au NPs-DNA functionalized FET-based biosensor for screening of Down syndrome.²⁴⁷ Adapted with permission from Liu *et al.*, *Nano Lett.* **19**, 1437 (2019); Copyright 2019 American Chemical Society; (c) Comparison of the main FIGS of merit: LoD (top) and detection range (bottom) for glucose detection using graphene, GO, rGO and MoS₂ sensors. The offsets in the horizontal direction are introduced for clarity. The yellow rectangles show the range of glucose in urine, while the green/pink rectangles show the range of glucose in normal/diabetic blood. The values are summarized based on the results presented in this review and in Ref. 195.

compound involved in many biological processes.^{262–266} Similar to glucose detection, enzymatic^{263,264} (typically involving an electrocatalytic reaction with haemoglobin²⁶⁷) and non-enzymatic^{268,269} routes have been explored.

TMDs also exhibit attractive properties for detection of small biomolecules (neurotransmitters, metabolites, vitamins, etc.). Detection and differentiation of DA (dopamine), AA (ascorbic acid), and UA (uric acid) have been demonstrated using MoS₂-sensors.^{260,270–274} TMDs were also employed as a sensing platform for detection of biomarkers, such as carcinoembryonic antigen (CEA).²⁵¹ Recently, MoS₂-based platforms were employed for detection of μ -opioid receptor, a synthetic opioid peptide, and specific μ -opioid receptor agonist.²⁷⁵

MoS₂-based sensors have also been utilized for detection of nucleic acids^{276–278} and selective detection of dsDNA²⁷⁹ and ssDNA.²⁷⁸ where the detection mechanism was based on the different affinity of MoS₂ toward each DNA type.²⁷⁹ Liu *et al.*²⁴⁷ successfully used a MoS₂-Au NPs-DNA-functionalized FET-based biosensor for the screening of Down syndrome [Fig. 13(b)]. The MoS₂ FET biosensors were able to reliably detect target DNA fragments (chromosome 21 or 13) with a detection limit below 100 aM, a high response up to 240%, and a high specificity, which satisfies the requirement for the screening of Down syndrome. In another series of works, MoS₂-based FET sensors have demonstrated high sequence selectivity capable of discriminating the complementary and

noncomplementary DNA,²⁸⁰ RNA and ATP monitoring,^{281,282} and CEA detection.^{251,283}

A recent comprehensive study has highlighted important insights into the bioabsorption of CVD-grown monolayer MoS₂, including long-term cytotoxicity and immunological biocompatibility evaluations on live animal models.²⁴⁴ The authors presented MoS₂-based bioabsorbable and multi-functional sensors for intracranial monitoring of pressure, temperature, strain, and motion in animal models. A simple implantable electrical sensor based on monolayer MoS₂ was capable of monitoring intracranial temperature over a specified period before dissolving completely. They observed no adverse biological effects and verified that biodegradable MoS₂-based electronic systems offer specific, clinically relevant roles in diagnostic and therapeutic functions during recovery from traumatic brain injury.²⁴⁴

Although currently significantly less explored than its MoS₂ counterparts, WSe₂²⁸⁴ and WS₂ bioFETs have also been used for detection of glucose,^{257,285} IgE,^{286,287} steroid hormone (e.g., estradiol²⁸⁷), and nucleic acid aptamers (e.g., DNA^{288,289} and micro-RNA²⁹⁰). Alternatively, working on a higher level of bio applications, wearable electronics, or skin tattoos based on PtSe₂ and PtTe₂ with medical-grade Ag/AgCl gel electrodes has been demonstrated.²⁹¹ Specifically, in terms of sheet resistance, skin contact, and electrochemical impedance, PtTe₂ outperforms state-of-the-art gold and graphene electronic sensors. The PtTe₂ tattoos show 4 times lower impedance and almost 100 times lower sheet resistance compared to monolayer graphene tattoos, opening exciting applications in the development of advanced human-machine interfaces.²⁹¹

An interesting comparative analysis of TMD- and graphene-based biosensors has been performed recently by Bollella *et al.*²³⁷ It concluded that MoS₂-modified graphene platforms have shown the best results in terms of sensitivity.^{259,261} In the case of H₂O₂ detection, the best electrochemical sensing electrode was realized with a MoS₂-CNT nanocomposite, which shows a wide linear range, the lowest LoD and the highest sensitivity.²⁶⁸ The presence of incorporated metal NPs has been shown to improve the electrochemical performances of all sensors, where the MoS₂-based sensing platforms displayed the best results among the other 2D materials employed.²³⁷ Regardless, a comparative analysis (LoD and detection range) of a large number of graphene, GO, rGO, and MoS₂-based electrochemical glucose sensors (based on the results presented here as well as adapted from the comprehensive recent review by Meng *et al.*¹⁹⁵) do not demonstrate an obvious advantage of one material against the other [Fig. 13(c)]. The comparison shows that both the LoD and detection range vary significantly for each material. It is important to note that, although all compared materials demonstrated a generally low LoD, only a limited number of reported cases matched the clinically relevant detection range for glucose in blood.²⁹² Still, both carbon and MoS₂ based sensors could be a good platform for detection of glucose in urine, where significantly lower (only traces of the substance) levels are expected.²⁹³ This example demonstrates a supreme importance of targeting development of 2DM sensors with a clear view on the application niche and on the underlying requirements.

b. Other 2D materials. Compared to TMDs, other 2D materials, such as black phosphorus (BP), boron and silicon nitrides, MXenes, silicenes, etc., have been significantly less explored for biosensing applications. In many cases, the research is still limited to theoretical studies and predictions.

Black phosphorus: BP is a promising candidate for biosensing due to its inherent conductivity, biocompatibility, and electrocatalytic properties. Recently, BP-based sensing platforms have been used for the detection of human immunoglobulin (IgG) and anti-IgG,²⁹⁴ H₂O₂ (through immobilization of hemoglobin),²⁹⁵ myoglobin (iron- and oxygen-binding protein),²⁹⁶ and leptin (a protein hormone, which is an important biomarker for liver diseases).²⁹⁷ However, the primary limitation for the use of BP in bio-applications is its relatively quick degradation due to moisture absorption and oxidation.

h-BN: Compared to BP, use of h-BN in biosensing provides the important advantage of chemical stability. Additionally, the good electrocatalytic performance of h-BN is highly beneficial for the development of electrochemical sensors. For example, h-BN sensors have been used for both enzymatic²⁹⁸ and non-enzymatic²⁹⁹ detection of H₂O₂. h-BN electrodes support a high overpotential required for DA oxidation and have led to successful detection of DA in the presence of UA.^{300,301} Furthermore, the simultaneous presence and differentiation between DA, AA, and UA has been demonstrated^{302,303} and complemented by the development of a non-enzymatic glucose sensor.³⁰⁴ A h-BN based biosensor has also been employed for detection of an important neurotransmitter called serotonin.³⁰⁵

MXenes: They have attracted significant research interest due to their metallic conductivity, hydrophilic surfaces, and good stability in aqueous environments. Ti₃C₂T_x-based FETs have been used for the detection of H₂O₂ (via immobilization of haemoglobin),^{306,307} monitoring of hippocampal neurons (responsible for transmission of brain signals relevant to learning, emotions, and memory),³⁰⁸ and fabrication of an enzymatic glucose biosensor.³⁰⁹ Moreover, Pt-doped Ti₃C₂T_x biosensors have been demonstrated for detection of DA, AA, UA, and acetaminophen.³⁰⁷ Furthermore, MXene-Ti₃C₂T_x-based composites have been utilized for detection of nitrites in environmental water.³¹⁰

c. Summary. The current status of this rapidly developing field forebodes that 2D material-based bio- and electrochemical sensors can be widely used for detection of disease biomarkers in diagnostics and disease monitoring. Due to their advantageous physical and chemical properties (such as tunable conductivity, large surface area, biocompatibility, and electronic anisotropy), 2D materials are well suited for continuous and real-time monitoring of specific molecules, even in complex environments such as the interior of living cells or blood serum.²⁴⁰ Among other detection mechanisms, electrical schemes of detection remain the most robust and versatile for ON/OFF biosensing platforms. Most commonly, they exploit FET-based platforms, which allow an additional degree of freedom (typically either through a back gate or top liquid gate) to tune the device sensitivity and response.

There are still a significant number of obstacles to overcome, biological specificity being one of the most crucial, where a large number of interfering substances in biological fluids may impact the accuracy and specificity of detection. The critical and reliable evaluation of the toxicity and biocompatibility of 2D materials is essential for *in vivo* applications. On a physical side, the limited understanding of the influence of the structural and compositional defects on sensing properties complicates reproducibility and device optimization.¹⁹⁵ Future developments should include novel synthetic methods, with a large degree of structural control. The development of novel hybrid materials and composites, e.g., by addition of other electroactive components,

such as metal oxides, metals, graphene, or conductive polymers, is a huge advantage and has already been widely incorporated into the design of a new generation of biosensors. The improved catalytic activity and low-cost of such complex 2D hybrid materials make them a useful biocatalyst for multiple applications in environmental chemistry, biotechnology, and clinical diagnostics.

3. Strain sensors

Recently, the application of 2D materials in micro/nanoelectromechanical systems (MEMS/NEMS) and energy conversion devices, active flexible sensors, actuators, and more, has relied on the inherent piezoelectric property in their atomically thin crystal structure. Here, we discuss several fascinating developments, mainly related to pressure, strain sensors, and human-computer interfacing, where carrier generation, transport, recombination, or separation is tuned through electrical or mechanical stimuli. For comprehensive reviews in the area, we address the readers to recent publications,^{197,311} see also Sec. IV C: Piezo- and Ferro-electricity in 2D vdW materials for details.

a. TMDs. MoS₂ is probably the most explored piezoelectric semiconductor. The bandgap of MoS₂ is highly strain-tunable, which results in the modulation of its electrical conductivity and manifests itself as the piezoelectric effect. The piezoelectric effect is generally studied through application of external strain to devices, for example, through the use of flexible substrates, where the electrons can be driven to flow into an external circuit when stretching the substrate or flow back when releasing it.³¹² To quantify the piezoelectric response experimentally and measure the piezoelectric coefficient (e_{11}), a freestanding monolayer of MoS₂ has been investigated using a combination of AFM probe-based nano-indentation and a laterally applied electric field with $e_{11} = 2.9 \times 10^{-10} \text{ C m}^{-1}$.³¹³ The effect of the number of layers (i.e., odd vs even) and orientation of crystals was also demonstrated. We further discuss applications of TMD materials in MEMS/NEMS, nanogenerators, and strain-based humidity sensors.

TMDs are model materials for MEMS/NEMS due to their atomically thin nature and coupling between electrical and mechanical properties (see, e.g., Manzeli *et al.*³¹⁶ or Wagner *et al.*³¹⁷). The calculated piezoresistive gauge factor was found comparable to state-of-the-art silicon strain sensors and higher than those based on suspended graphene. Electromechanical piezoresistive sensors were also realized in relatively little explored 2D PtSe₂.³¹⁷ In this work, high negative gauge factors of up to -85 were achieved experimentally in PtSe₂ strain gauges. Integrated NEMS piezoelectric pressure sensors with freestanding PMMA/PtSe₂ membranes have been realized and exhibited very high sensitivity superior to previously reported devices. The low temperature growth makes PtSe₂ compatible with CMOS technology, which is particularly attractive.

MoS₂ has also been widely studied for applications in nanogenerators,^{318,319} providing a new way to effectively harvest mechanical energy for low power-consuming electronics and realizing self-powered sensors. For example, in one of the earlier works, it was demonstrated that a monolayer MoS₂ device on a flexible substrate under 0.53% strain produced a voltage of 15 mV and a current of 20 pA, corresponding to a power density of 2 mW m^{-2} and a 5% mechanical-to-electrical energy conversion efficiency.³¹⁸ In a separate study, it was shown that under applied strain of 0.48%, the output power of an

MoS₂ nanogenerator in the armchair orientation was about twice higher than that in the zigzag orientation.³²⁰

Realization of a novel type of MoS₂ humidity sensor was recently demonstrated, where exploitation of the piezoelectric effect allowed for a simple and stable way to enhance the sensor's sensitivity.^{216,321} The authors showed that tensile strain generated in the sensor led to a larger current output and an enhanced sensitivity to humidity. The observed output current and humidity sensitivity were both enhanced when more electrons are moved to the conduction band under tensile strain at a positive gate bias.¹⁹⁷ The tunability of the sensor by strain was better achieved in a low humidity range, which was attributed to a better manifestation of piezoelectric effect when number of water molecules absorbed on the channel surface was small.

b. Other 2D materials. **InSe:** Although less explored than in TMDs, the piezoelectric effect in other 2D materials is an emerging field with many promising outcomes. Piezoelectric outputs up to 0.363 V for a few-layer α -In₂Se₃ device with a current responsivity of 598 pA for 1% strain were experimentally demonstrated, outperforming other 2D piezoelectrics by an order of magnitude. Self-powered piezoelectric sensors made of these 2D layered materials were successfully applied for real-time health monitoring [Figs. 14(a)–14(c)].³¹⁴ In another work, strain sensors produced from large-scale CVD-grown In₂Se₃ exhibited two orders of magnitude higher sensitivity (gauge factor ≈ 237) than conventional metal-based (gauge factor ≈ 1 –5) and graphene-based strain (gauge factor ≈ 2 –4) sensors under similar uniaxial strain.³²² Additionally, the integrated strain sensor array, fabricated from the template-grown 2D In₂Se₃ films, displayed a high spatial resolution of $\approx 500 \mu\text{m}$ in strain distribution, making this material platform highly attractive as e-skins for robotics and human body motion monitoring.

MXenes: Emerging biowearables, various human-artificial intelligence (AI) interfaces, and soft exoskeletons urgently require high-performance strain sensors satisfying multiple sensing parameters, such as high sensitivity, reliable linearity, and tunable strain ranges.³²³ Recently, a number of fascinating studies have emerged exploring application of MXene hybrids in wearable electronics. Cai *et al.* demonstrated that a percolation network based on Ti₃C₂T_x MXene/CNT composites could be designed and fabricated into versatile strain sensors.^{315,324,325} The weaving architecture combined good electric properties and stretchability (attributed to the CNTs' network) and sensitivity of 2D Ti₃C₂T_x MXene nanoplatelets. The resulting strain sensor was characterized by an ultralow detection limit of 0.1% strain, high stretchability (up to 130%), high sensitivity (gauge factor up to 772.6), tunable sensing range (30%–130% strain), and excellent reliability and stability (>5000 cycles) [Figs. 14(d) and 14(e)]. The versatile and scalable Ti₃C₂T_x MXene/CNT strain sensors were proposed as a material platform for wearable AI, capable of tracking physiological signals for health and sporting applications in real-time. In a similar approach, wearable aerogel sensors that combined insulating 1D aramid nanofibers (ANFs) with conductive 2D MXene sheets demonstrated ultra-light weight, wide sensing range, and good sensing ability. The resulting MXene/ANFs aerogel sensor showed a wide detection range (2.0% to $\approx 80.0\%$ compression strain), sensitivity (128.0 kPa^{-1}) in the pressure range of 0–5 kPa, and ultralow detection limit (0.1 kPa), opening applications in detecting human motions ranging from a light movement to vigorous loads in extreme

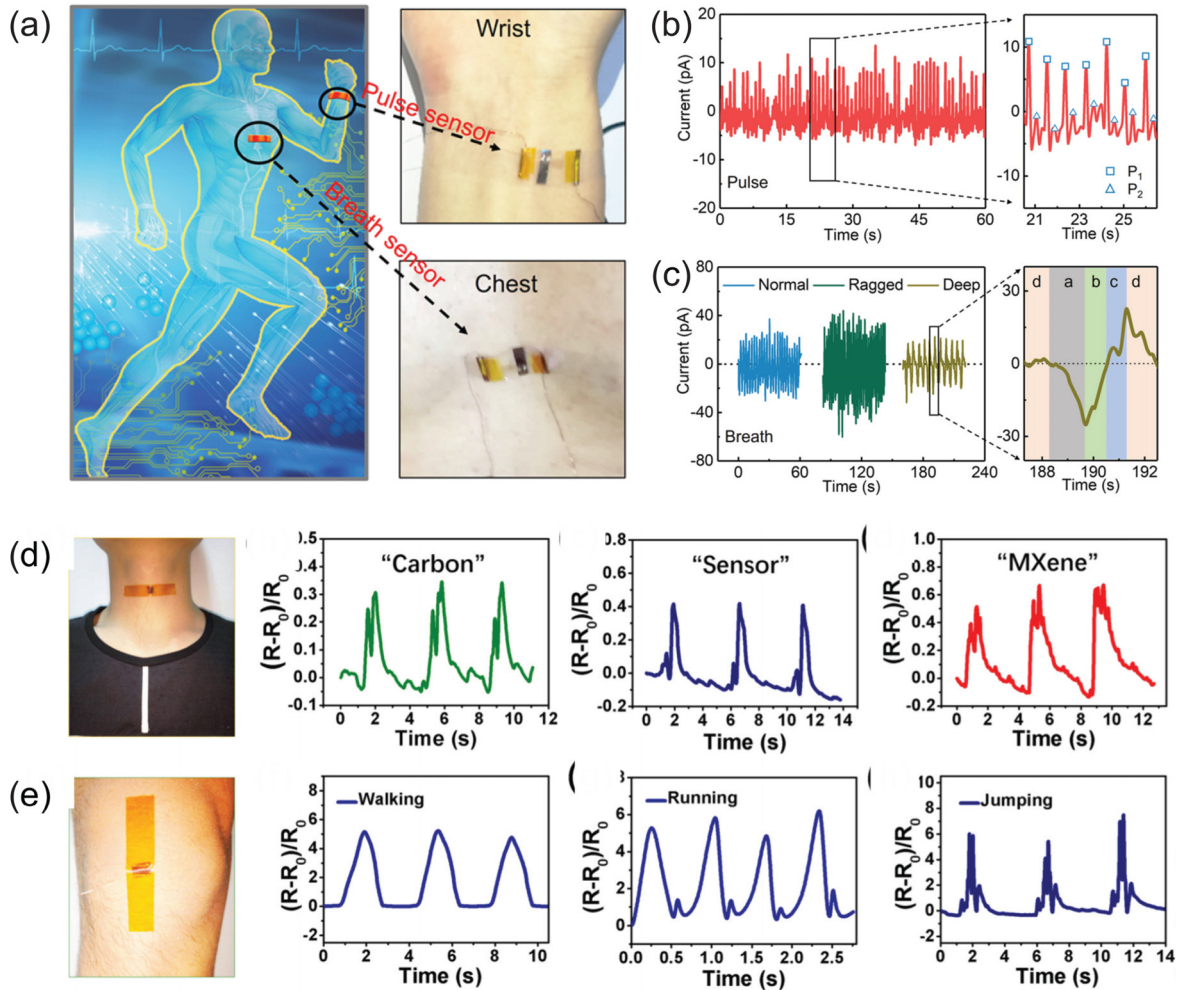


FIG. 14. Strain sensors based on 2D materials (a) Realtime monitoring of physiological signals using a self-powered piezoelectric sensor based on a multilayer α - In_2Se_3 flake (left). The sensor is attached to the wrist (middle top) and chest (middle bottom) for monitoring arterial pulse and breath, respectively. Real-time monitoring of arterial pulse (b) and breath (c) signals. (c) Right: the time synchronization of current tracks to deep breath: a—breath in; b—breath out; c—breath out; d—breath gap.³¹⁴ Adapted with permission from Dai *et al.*, *Nano Lett.* **19**, 5410 (2019). Copyright 2019 American Chemical Society; (d) and (e) left: photographs of a $\text{Ti}_3\text{C}_2\text{T}_x$ MXene/CNT/latex strain sensor attached to the throat and knee of a person. Right/top: relative resistance responses recorded during speaking “carbon,” “sensor,” and “MXene,” respectively. Right/bottom: relative resistance responses of the sensor in detecting human leg movement: walking, running, and jumping, respectively.³¹⁵ Adapted with permission from Cai *et al.*, *ACS Nano* **12**, 56 (2018). Copyright 2018 American Chemical Society.

sports. The MXene/ANFs aerogel with excellent integrated ability was proposed as a potential candidate for a human behavior monitoring sensor, as well as for sensing under extreme conditions. In a recent advanced approach, Yang *et al.* realized wireless $\text{Ti}_3\text{C}_2\text{T}_x$ MXene strain sensing systems by developing hierarchical morphologies on piezoresistive layers and integrating the sensing circuit with near-field communication technology.³²³ The wireless MXene sensor system could simultaneously achieve an ultrahigh sensitivity (gauge factor > 14000) and reliable linearity (≈ 0.99) within multiple user-designated high-strain working windows (130%–900%). The wireless, battery-free MXene e-skin sensing system was able to collectively monitor the multisegmented exoskeleton actuations via a single database channel and was successfully used to assist limb rehabilitation. Other promising recent examples include CNTs and

$\text{Ti}_3\text{C}_2\text{T}_x$ MXene for the monitoring of human activities,³²⁴ breathable $\text{Ti}_3\text{C}_2\text{T}_x$ MXene/protein nanocomposites as a medical pressure sensor,³²⁵ and hetero-dimensional 2D $\text{Ti}_3\text{C}_2\text{T}_x$ MXene and 1D graphene nanoribbon hybrids for machine learning-assisted pressure sensors.³²⁶

Graphene nitride: Anomalous piezoelectricity in 2D graphene nitride nanosheets ($g\text{-C}_3\text{N}_4$) has recently been demonstrated, where $g\text{-C}_3\text{N}_4$ was chosen because it naturally possesses uniform triangular nanopores and has advantageous piezoelectric properties (e.g., the linear relationship between piezoelectric response and applied voltage and the effective vertical piezoelectric coefficient of $\approx 1 \text{ pmV}^{-1}$).⁵³

Germanene: By means of first-principles calculations, it was shown that in an AlAs/germanene heterostructure, both electric field and strain could be used to tailor its electronic bandgap and dielectric

function. Under a negative electric field and compressive strain, the material's bandgaps showed a near-linear decreasing behavior, whereas a dramatic and monotonic decrease in the bandgap as a response to a positive electric field and tensile strain was shown.³⁴ It was also predicted that the optical properties of the heterostructure could be improved by electric field and mechanical strain.

c. Summary. The experimental observations of piezoelectrical phenomena have yet to be fully demonstrated for all the materials predicted to be piezoelectric. In some advanced cases, such as 2D MoS₂ and MXenes, their piezoelectric properties have already enabled active sensing, actuating, and new electronic components for nano-scale devices. Further applications of other 2D materials are expected to emerge in self-power nanodevices, adaptive biosensors, e-skins, and tunable and stretchable electronics. Still, the remaining challenges remain substantial. Most importantly, the existence of interface states and disappearance of piezoelectric properties with thickness remain significant obstacles on the way to device realization. Another vital challenge is improving material stability, which should be addressed by further advances in materials processing and encapsulation technologies.

IV. OUTLOOK ON EMERGING AREAS AND APPLICATION OPPORTUNITIES

A. Tunable quasiparticle dynamics in 2D vdW materials

The presence of a bandgap in many 2D materials lends them much more promise for optoelectronic applications than the gapless graphene. In contrast to bulk semiconductors, these materials feature very weak dielectric screening and strong spatial confinement of charge carriers. A consequence of this is the rich variety of excitonic quasiparticles which exist in these materials, particularly in 2D Mo and W chalcogenides and perovskites. The high binding energies of these quasiparticles mean that they persist even at room temperature dominating the optoelectronic behavior. This makes them exciting candidates for a range of applications, including light detection and emission, as well as spin- and valleytronic devices.

Beyond the neutral exciton, quasiparticles observed in TMDs include the trion, or charged exciton,^{327–329} as well as higher order excitonic particles, such as neutral and charged biexcitons.^{330–334} The relative population of different excitonic species can be effectively controlled in gated devices, making them suited for electrically tunable optoelectronic applications. Additionally, the large spin-orbit coupling and circular dichroism in TMDs results in a spin splitting at the K and K' valleys of opposite sign, enabling selective population of excitons in a particular valley by optically pumping with either right- or left-hand circularly polarized light.^{335–339}

The basic physics of excitons in 2D materials has been studied extensively by other authors, and for more details, we point readers to other reviews.^{139,340,341} In the rest of this section, we shall therefore limit our discussion to only more unusual excitonic quasiparticles: the interlayer exciton and the exciton-polariton.

1. Interlayer excitons

A heterobilayer is formed of two distinct 2D materials, layered together in a vdW heterostructure. For TMDs, the range of different

bandgaps and work functions means heterobilayers typically form vertical p–n junctions, with type II band alignment. This means that electrons and holes in the heterostructure have energy minima in different materials. Experimental measurements, with techniques including angle resolved photoemission spectroscopy and scanning tunneling spectroscopy, have confirmed that this is the case for a wide range of TMD heterobilayers.^{342–345} The band structure of the heterobilayers is then further altered by hybridization of the band structures of its constituents, an effect which is governed by the momentum-varying interlayer hopping potential³⁴⁶ and by the superposition of a moiré period for non-lattice matched and rotated crystals.

In these heterobilayers, an interlayer exciton (IX, often referred to as an indirect exciton) can be formed by the creation of a regular intralayer exciton (DX, or direct exciton) in either layer, followed by interlayer charge transfer, leaving a Coulomb-bound electron-hole pair with each carrier in a different material. The resulting exciton configuration is shown schematically in the insets to Fig. 15(a). A great advantage of interlayer excitons is significantly enhanced lifetimes due to the spatial separation of the carriers.³⁴⁷ For charge transfer to be energetically favorable, the binding energy of the interlayer exciton must be lower than that of the intralayer exciton [Fig. 15(b)]. This means that interlayer excitons can be observed in photoluminescence (PL) spectra as a lower energy peak, arising from the heterobilayer [Figs. 15(a) and 15(c)].^{347–352}

Similar to the case of intralayer excitons, valley polarization has been observed in interlayer excitons.^{353–355} It has also been demonstrated that the charge transfer process, which converts intralayer to interlayer excitons, conserves the spin-valley polarization of the excited charge carriers.^{356,357} However unlike for intralayer excitons, these valley-polarized states are orders of magnitude more persistent, with lifetimes on the order of microseconds. This makes interlayer excitons ripe for exploitation in valleytronic devices.

The properties of interlayer excitons can be further tuned by electrical gating. The broken inversion symmetry of a heterobilayer means that the relative band offsets of the constituent 2D materials can be adjusted via the field effect. This, in combination with the out-of-plane electric dipole possessed by interlayer excitons, allows effective external control of the exciton energy. Gated WSe₂/MoSe₂ devices have shown gate-dependent energy shifts ≈ 70 meV.³⁴⁷ Additionally, time- and polarization-resolved PL revealed significant gate-dependent changes in the lifetimes of interlayer excitons and polarized states [Fig. 15(d)].³⁵³

Beyond electronic tunability, it has recently been demonstrated that the properties of interlayer excitons can also be altered by the twist angle between two layers through modification of the period of the moiré pattern caused by the overlapping lattices.^{350,358–361}

2. Exciton-polaritons

The family of 2D-material quasiparticles is further expanded with the addition of exciton-polaritons. These are hybrid light-matter quasiparticles, resulting from strong coupling between an electromagnetic wave and the electric dipole associated with an exciton. This strong-coupling regime is enhanced by the large exciton-binding energies and sharp resonances in TMDs, meaning these exciton-polaritons persist even at room temperature. These materials are therefore interesting platforms to study strong light-matter interactions.

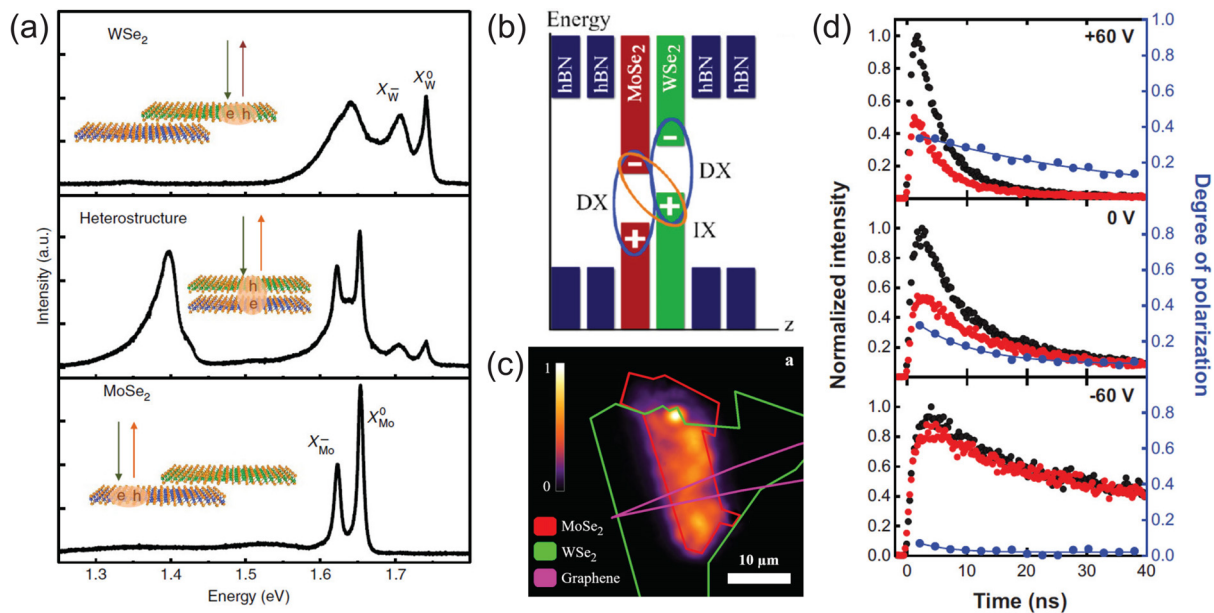


FIG. 15. Interlayer excitons. (a) PL spectra from h-BN encapsulated WSe_2 and $MoSe_2$ monolayers, as well as a heterobilayer of both materials. A lower binding energy interlayer exciton can be seen in the spectrum from the heterobilayer.³⁴⁷ Adapted from Rivera *et al.*, *Nat. Commun.* **6**, 6242 (2015). Copyright 2015 Springer Nature. (b) Simplified band edge alignment of an h-BN encapsulated $MoSe_2/WSe_2$ heterobilayer. The direct (DX) and interlayer (IX) excitons are marked with ellipses. (c) Spatial map of interlayer exciton PL intensity from a graphene-contacted $MoSe_2/WSe_2$ heterobilayer. The light emission is confined to the area of overlap between the two TMDs.³⁵¹ Adapted with permission from Calman *et al.*, *Nano Lett.* **20**, 1869 (2020). Copyright 2020 American Chemical Society. (d) Time- and polarization-resolved IX PL, showing right- and left-hand circularly polarized components (in black and red, respectively) and total degree of polarization (blue) at three different gate voltages.³⁵³ Adapted with permission from Rivera *et al.*, *Science* **351**, 688 (2016). Copyright 2016 AAAS.

Strong coupling is typically achieved by placing 2D materials in a photonic microcavity between two mirrors [Fig. 16(a)], which concentrates the local light intensity by exciting a cavity resonance.^{362–365} In this geometry, exciton–polaritons in monolayer WSe_2 have shown room temperature valley coherence, whose phase can be effectively controlled via the Zeeman effect, through application of a magnetic field.³⁶⁶ Additionally, in a cavity-embedded field-effect device combining WS_2 and MoS_2 , gate-controlled, polariton-mediated energy exchange was demonstrated, between the excitons originating from each 2D material [Fig. 16(b)].³⁶⁷

An alternative method of achieving strong light-matter coupling is through the use of scanning near-field optical microscopy (SNOM). This uses tightly focused near-field light focused at the apex of an atomic force microscope probe to both excite and detect exciton–polaritons, enabling high-resolution spatial mapping [Fig. 16(c)]. In multilayer slabs of TMDs, thickness-dependent internal waveguide resonances can be excited, which can interact strongly with exciton–polaritons. SNOM studies of WSe_2 ³⁶⁸ and $MoSe_2$ ³⁶⁹ have shown that this results in exceptionally long polariton propagation lengths of over 12 μm [Fig. 16(d)], as well as thickness-tunable polariton wavelengths.

Various further methods have been demonstrated to induce exciton–polaritons, without the need for a cavity or SNOM tip. WS_2 nanodiscs have been shown to support internal Mie resonances and novel anapole states, which couple strongly with excitons, forming polaritons whose energy can be tuned via the disk radii.³⁷⁰ In monolayer WS_2 , strong coupling has been demonstrated between excitons and waveguide modes, formed by patterning the TMD into a photonic

crystal.³⁷¹ Additionally, WS_2 nanogratings fabricated on gold have shown strong coupling between excitons, cavity modes, and plasmon polaritons.³⁷²

For further detail on the physics behind exciton–polaritons, we point readers to previous reviews on 2D material polaritonics.^{373,374}

B. Electrically controlled magnetism in 2D vdW materials

1. Magnetism in 2D van der Waals materials and opportunities

Magnetism in 2D vdW materials has been sought after for engineering ultra-scaled magnetic devices and tunable magnetic phenomena in low dimensions. Theoretically, intrinsic magnetism in atomically thin materials was believed to be prohibited due to enhanced thermal fluctuations, as per the Mermin–Wagner theorem.³⁷⁵ Therefore, previous efforts were focused on extrinsically inducing magnetism in 2D vdW materials through defect engineering, doping, intercalation, and/or band structure engineering.^{376–381} Recently, however, it was discovered that several atomically thin vdW materials do, in fact, sustain long-range magnetic order through the inclusion of magnetic anisotropy that opens up a spin wave excitation gap, thereby suppressing the thermal agitations and resulting in finite Curie/Neél temperatures.^{13,14,384} The discovery of intrinsic ferromagnetism (FM) and antiferromagnetism (a-FM) in 2D vdW materials provides unprecedented opportunities for studying various exotic properties such as spin fluctuation-driven generation of new quantum

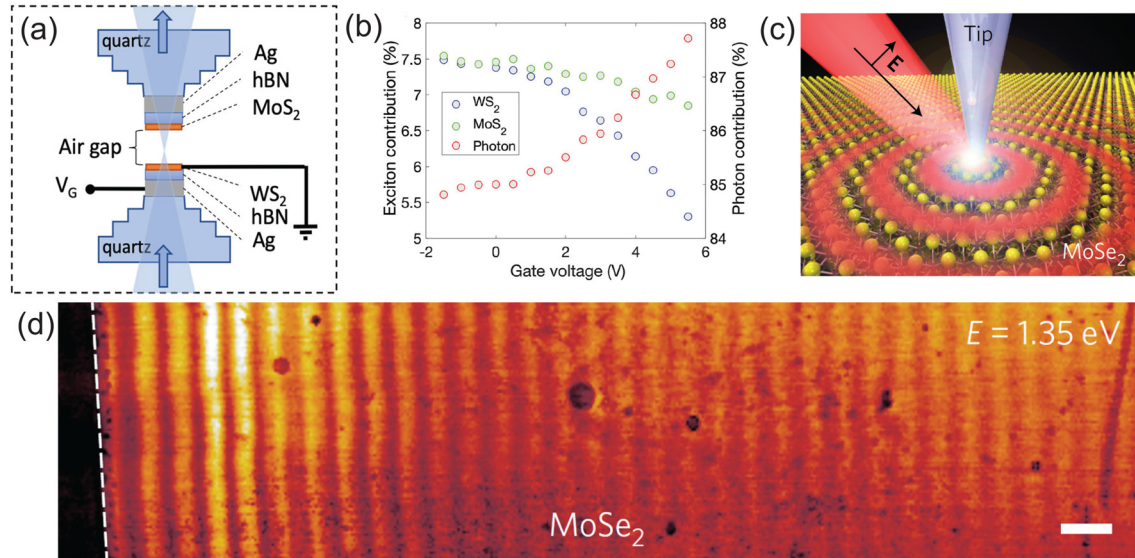


FIG. 16. Exciton polaritons. (a) Schematic fig of a photonic microcavity incorporating MoS₂ and a WS₂-based FET. (b) Contributions to the emission spectrum from WS₂, MoS₂ and cavity modes as a function of gate voltage.³⁶⁷ Adapted with permission from Fernandez *et al.*, Appl. Phys. Lett. **115**, 071103 (2019). Copyright 2019 AIP Publishing LLC. (c) Diagram of a SNOM experiment; near-field light is focused at the apex of a sharp metalized tip, exciting and scattering exciton-polaritons in a 2D material. (d) SNOM image, showing long propagation lengths of waveguide-coupled exciton polaritons in MoSe₂ (scale bar 1 μm).³⁶⁸ Adapted with permission from Hu *et al.*, Nat. Photonics **11**, 356 (2017). Copyright 2017 Springer Nature.

phases and topological orders. In addition, it provides an ideal material platform for experimentally realizing ultrathin 2D spintronic devices for sensing, quantum information, and memory applications.^{385–387} Magnetic 2D vdW materials are easily integrable into heterostructures without the need of lattice matching, making them suitable for exploring emergent interfacial phenomena such as multiferroicity, quantum anomalous Hall effect, and unconventional superconductivity.^{385–387} The 2D heterostructures also provide access to various external stimuli such as optical, electrical, and mechanical tuning of their physical properties. In particular, electrical manipulation of magnetism in 2D vdW materials provides an exciting opportunity for realizing low-power and high-speed spintronic devices compatible with existing semiconductor technology. In this section, we particularly focus on the recent advances and current understanding of electrically manipulating magnetic order of 2D vdW materials and realizing new functional devices.

Electrical control of magnetism through electrostatic gating has been demonstrated in several recently discovered 2D vdW magnets. The carrier density or the Fermi level position of a 2D magnet can be modulated, which in turn affects the magnetic exchange interactions and magnetic anisotropy. However, this state-of-the-art approach is volatile as it requires persistent electrical control. Ferroelectric switching in magnetoelectric-multiferroic systems, where an applied electric field modifies the magnetization in 2D magnets by coupling through electrical polarization, is considered to be an effective approach for achieving nonvolatile electrical control of magnetism for practical applications.

2. Gate controlled magnetism in 2D vdW materials

a. Intrinsic ferromagnetic semiconductors/insulators. Manipulation of magnetism through electrostatic gating was first demonstrated in few-

layer, insulating 2D magnets, such as CrI₃⁵⁶ and Cr₂Ge₂Te₆.³⁶ In particular, atomically thin CrI₃ has been shown to exhibit intriguing layer-dependent magnetic order: each monolayer of CrI₃ has a FM ordering while the stacking between the layers is a-FM. The weak interlayer exchange interactions are easily susceptible to external electrical perturbation, thus enabling a unique route for controlling magnetic order in CrI₃.¹¹ Both the linear magnetoelectric effect (ME) and electrostatic doping have been reported for tuning magnetism using single-gated or dual-gated field-effect devices [Fig. 17(a)]. The magnetism was probed by the magnetic circular dichroism (MCD) or magneto-optical Kerr effect (MOKE) microscopy. For the linear ME effect, bilayer CrI₃ with graphene and h-BN as gate electrodes and dielectric, respectively, in a dual gated device was used.⁵⁶ An increase in both the magnetization in the a-FM stacking state and the critical magnetic field for a spin-flip transition (H_c) was observed with increasing gate voltage due to the linear ME coupling effect. A remarkable phenomenon of complete switching of the magnetic order from FM stacking to a-FM stacking has also been demonstrated near H_c through the application of an external electric field [Fig. 17(b)]. Tuning of the magnetic order by the linear ME effect is only possible in samples with an even number of layers that exhibit both broken time reversal and spatial inversion symmetries. In monolayer CrI₃, spatial inversion symmetry is still present; therefore, no tuning of the magnetism through linear ME effect can be observed.⁵⁶

In contrast to the linear ME effect, electrostatic doping can control magnetism in both even and odd numbers of layers of CrI₃ by controlling the doping density with gate voltage.⁵⁷ In monolayer CrI₃, the magnetic order was found to be strengthened by hole doping and weakened by electron doping, where significant tuning of the coercive force (H_c) up to $\approx 75\%$, saturation magnetism (M_s) up to $\approx 40\%$, and

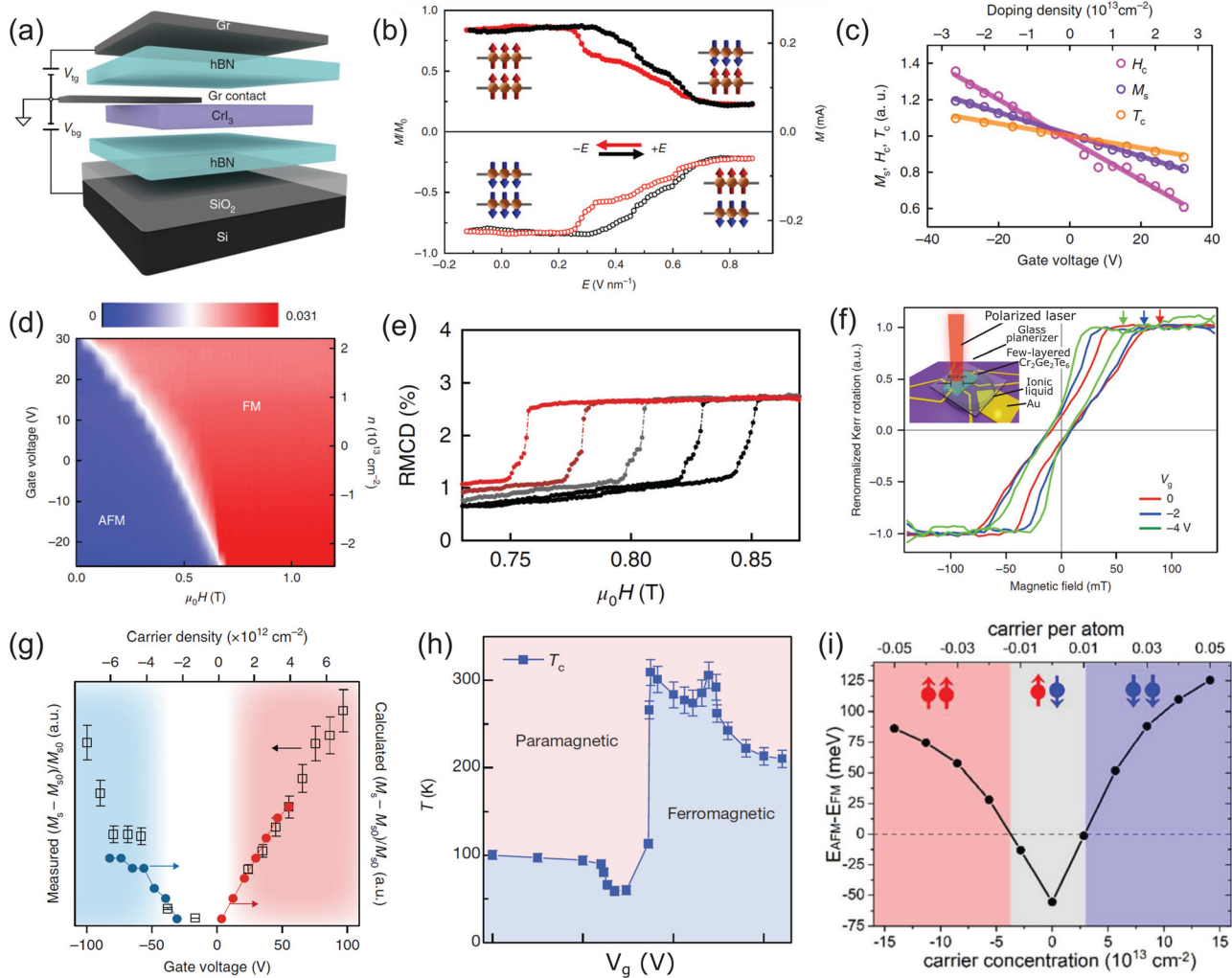


FIG. 17. 2D materials for gate tunable magnetic properties. (a) Schematic of a dual-gated bilayer CrI_3 device.³⁸⁸ Adapted from Huang *et al.*, *Nat. Nanotechnol.* **13**, 544 (2018). Copyright 2018 Springer Nature. (b) Switching of the magnetization as a function of an applied electric field E . The top and bottom panels are measurements at 0.44 and -0.44T , respectively.⁵¹ Adapted from Jiang *et al.*, *Nat. Mater.* **17**, 406 (2018). Copyright 2018 Springer Nature.⁵⁶ (c) Magnetic properties of monolayer CrI_3 as a function of gate voltage V_g and induced doping density n . (d) Doping density-magnetic field phase diagram at 4 K for a bilayer CrI_3 device.⁵⁶ Adapted from Jiang *et al.*, *Nat. Nanotechnol.* **13**, 549 (2018). Copyright 2018 Springer Nature. (e) Reflective magnetic circular dichroism (RMCD) signal of a dual-gated bilayer CrI_3 device as a function of applied magnetic field at different doping levels from 0 cm^{-2} (black) to $4.4 \times 10^{-12}\text{ cm}^{-2}$ (red).³⁸⁸ Adapted from Huang *et al.*, *Nat. Nanotechnol.* **13**, 544 (2018). Copyright 2018 Springer Nature. (f) Renormalized Kerr angle measured at 20 K at different ionic gate voltages of 0, -2 , and -4 V . Arrows indicate saturation field for the loops measured at each V_g . Inset shows a schematic of the experimental setup for Kerr measurement using ionic liquid gating. (g) Normalized spin magnetization as a function of hole and electron carrier density. Open squares are the experimental data points and solid circles with solid lines are the simulated data.⁵² Adapted from Wang *et al.*, *Nat. Nanotechnol.* **13**, 554 (2018). Copyright 2018 Springer Nature. (h) Phase diagram of the trilayer Fe_2GeTe_3 sample as V_g and temperature are varied. Vertical error bars represent uncertainties in determining the onset of the non-zero remanent Hall resistance at zero external magnetic field.³⁹¹ Adapted from Deng *et al.*, *Nature* **563**, 94 (2018). Copyright 2018 Springer Nature. (i) Relative energy of a-FM and FM states under the variation of n for 2D MnPSe_3 calculated with HSE06 functional. The positive and negative values are for electron and hole doping, respectively. The up and down arrows indicate up- and down-spin, respectively.⁴⁰² Adapted with permission from Li *et al.*, *J. Am. Chem. Soc.* **136**, 11065 (2014). Copyright 2014 American Chemical Society.

Curie temperature (T_c) up to $\approx 20\%$ was achieved [Fig. 17(c)]. In bilayer CrI_3 , H_c could be continuously decreased by increasing the electron doping density (n) until, above a certain critical density $n \approx 2.5 \times 10^{13}\text{ cm}^{-2}$, a complete transition from an a-FM to a FM stacking state was attained due to a significant decrease in the

interlayer exchange coupling [Fig. 17(d)]. It can be inferred that electrostatic gating induces both linear ME and doping effects simultaneously. Thus, the exact mechanism for tuning magnetism through electrostatic gating remained elusive, until a recent study investigated both effects independently.³⁸⁸ They found that electrostatic doping

played a major role in controlling the magnetic order in bilayer CrI₃ [Fig. 17(e)]. This shows that doping could be an efficient and more general approach to control the magnetism in 2D vdW magnets.

Furthermore, both ionic liquid [N,N-diethyl-N-methyl-N-(2-methoxyethyl) ammonium bis(trifluoromethylsulfonyl)imide (DEME-TFSI)] as well as thermally grown silicon oxide gate-dielectric on a degenerately doped Si back gate electrode have been used for electrostatic tuning of magnetism in vdW Cr₂Ge₂Te₆.⁵² The doping density with ionic liquid gating is usually ≈ 100 times higher than what can be achieved with a solid-state thermally grown silicon oxide gate dielectric on a degenerately doped Si wafer which serves as the back gate electrode.³⁸⁹ A large tuning of the magnetism with ionic liquid gating was attained for thicker (≈ 19 nm) Cr₂Ge₂Te₆ samples, which could not be obtained with thermally grown silicon oxide gate-dielectric on a degenerately doped Si back gate electrode. An ultrahigh-sensitive MOKE setup was used to investigate the magnetization, and the saturation field (H_{sf}) was found to reduce by a factor of two at gate voltage (V_g) = -4 V, compared to that measured at V_g = 0 V [Fig. 17(f)]. However, for thinner ≈ 3.5 nm Cr₂Ge₂Te₆, solid Si gating was used. Both electron and hole doping resulted in enhanced M_s that was also consistent with first-principles calculations [Fig. 17(g)]. Moreover, electron doping resulted in greater magnetization than hole doping due to shifting of the Fermi level into the conduction band by filling Cr- d orbitals that gives rise to larger magnetizations than the p orbital for the valence band from Te atoms.⁵²

b. Layered metallic ferromagnets. Compared with CrI₃ and Cr₂Ge₂Te₆ ferromagnetic insulators, 2D magnetic metals such as MnSe₂,³⁸³ VSe₂,³⁹⁰ and Fe₃GeTe₂³⁸² exhibit high Curie temperatures. This provides an ideal material platform, wherein coexisting itinerant electrons and local magnetic moments enable interplay of both spin and charge degrees of freedom. As of yet, there are only a few reports that demonstrate gate tunability of the magnetic properties of 2D metallic magnets. Recently, it has been demonstrated that doping induced by ionic gating can elevate the Curie temperature from 100 K to room temperature in thin Fe₃GeTe₂ flakes [Fig. 17(h)].³⁹¹ Under gate voltage, a high electron doping density $n \approx 10^{14}$ cm⁻² was induced in thin flakes (3 layers) of Fe₃GeTe₂, that led to modulation of the Curie temperature up to 300 K accompanied by a large modulation in the coercivity ($\mu_0 H_c$) ≈ 0.6 T.

c. Dilute ferromagnetic semiconductors/insulators. Although MnSe₂, VSe₂, and Fe₃GeTe₂ have been shown to be room temperature ferromagnets, as of yet, there has not been a report of a semiconducting 2D intrinsic ferromagnet at room temperature. Thus, there is a significant effort to impart magnetism to non-magnetic materials through the creation of dilute magnetic semiconductors. There are numerous theoretical papers focused on introducing magnetic dopants into various 2D materials. Some examples include predicted ferromagnetism in Mn-, Fe-, Co-, V-, Cr-, and Zn-doped MoS₂,^{392–394} V-doped WSe₂,³⁹⁵ and Co-doped phosphorene.³⁹⁶ Specifically, for Co-doped phosphorene, the authors demonstrated that the exchange interaction and magnetic ordering could be tuned by adding holes or electrons to the system (e.g., by gating), which may result in a FM to a-FM transition. Experimentally, however, the challenges in synthesizing dilute 2D magnetic semiconductors lie in preventing interstitial substitutions, clusters, or alloy formations, which would result in drastically different

electronic properties of the host material, and magnetism not inherent to the material. Recent reports have successfully demonstrated room temperature FM and confirmed uniform alloying through electron microscopy in Mn-doped MoS₂ (≈ 3 at.%), Fe-doped MoS₂ (≈ 0.5 at.%), V-doped WS₂ (up to 12 at.%), and V-doped WSe₂ (≈ 0.1 to ≈ 4 at.%).^{397–401} However, thus far, the tuning of magnetism via electric fields has only been demonstrated for V-doped (0.1 at.%) WSe₂ by Yun *et al.*⁴⁰⁰ They studied the phase contrast of ferromagnetic domains under back-gate biases from -10 to 20 V using magnetic force microscopy, observing non-monotonic variations in the phase contrast between domains at different gate biases. Although growth of these TMD-based dilute magnetic semiconductors is currently limited to micrometer-sized individual domains, they provide the foundation to explore applications in room temperature spintronic devices.

d. Other layered 2D magnets. a-FM semiconductors, such as MnPSe₃, FePS₃, etc., are theoretically predicted to exhibit transitions from a-FM semiconductor to FM half-metal with both electron and hole doping.^{402,403} The spin polarization direction doping that can be controlled through an external gate voltage is opposite for electrons and holes [Fig. 17(i)]. Such an a-FM to FM transition may provide a new means of magnetization switching for memory devices.

To give an overview of possible magneto-optical applications, a comparison between the Curie/Neel temperature and bandgaps of the 2D magnetic materials explored so far, as well as other bulk ferromagnetic materials and insulators, is plotted in Fig. 18.^{52,57,383,390,391,404–418}

e. Ferroelectric switching controlled magnetism. Ferroelectric switching in magnetolectric-multiferroic devices is an efficient approach to control magnetism due to inherent coupling of magnetic and ferroelectric orders. Heterostructures combining different ferromagnetic and ferroelectric materials can exhibit strain-mediated magnetolectric coupling which holds a great advantage in designing next generation spintronic devices.⁴²⁰ To date, no experimental work on designing magnetolectric 2D vdW heterostructures has been reported. This is most likely because most of the recently investigated 2D vdW ferroelectric materials lack out-of-plane spontaneous polarization, which is a prerequisite for magnetic manipulation. Recently, a few theoretical works have been reported with the aim to probe mechanisms for controlling magnetism in 2D vdW materials by the manipulation of ferroelectric polarization, which could lead to experimental efforts in the near future.^{421–425} Here, we briefly summarize some of these representative works.

Using first-principles calculations, a recent study predicted a robust control over magnetism in 2D FeI₂/In₂Se₃ bilayer vdW heterostructures by changing the direction of the ferroelectric polarization.⁴²¹ The magnetic order of FeI₂ was found to change from FM to a-FM by reversing the polarization direction from $+P$ to $-P$ state. In the $-P$ polarization state, the Fe- $3d$ orbital exhibited a half-filled, high-spin d^5 state and the direct exchange led to a strong a-FM ordering, whereas, in the $+P$ polarization state, the Fe- $3d$ orbital exhibited a half-filled, high-spin d^6 state, which preferred FM ordering via the superexchange interaction. In another work, density functional theory was used to demonstrate a nonvolatile electrical control of 2D ferromagnets in a multiferroic heterostructure consisting of monolayer CrI₃ and ferroelectric Sc₂CO₂.⁴²² By changing the polarization state of Sc₂CO₂, the

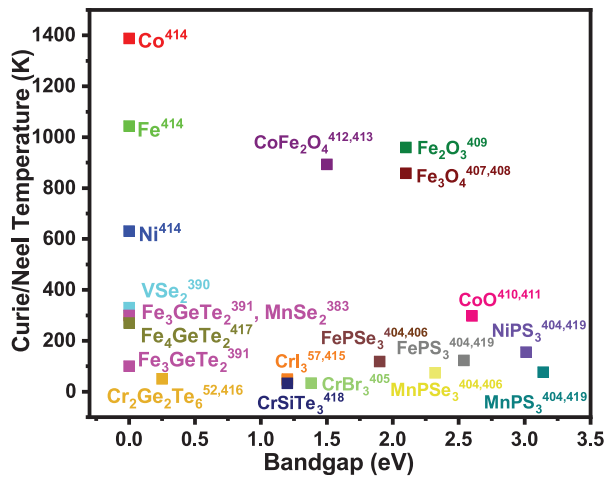


FIG. 18. A comparison plot of ferromagnetic transition temperatures (Curie temperatures for ferromagnets and Neel temperature for antiferromagnets) vs optical bandgap of several 2D magnetic materials including halides, chalcogenides, and phospho-chalcogenides. Non-layered, bulk 3D ferromagnetic materials such as metallic Fe, Co, and Ni as well as their insulating oxides are compared for clarity. The metallic materials are all concentrated on 0 eV bandgap line. The square symbols of varying colors correspond to the experimental data points adopted from the relevant references listed in superscript. The solid square symbols correspond to experimental data adapted from Refs. 52, 57, 383, 390, 391, and 404–419.

CrI₃ 2D FM semiconductor was transformed into a half metal that was attributed to the charge transfer at the heterointerface and the broken time reversal symmetry in the FM state. Similarly, in another report the electrical control of magnetic behavior of a-FM MnPSe₃, by changing the direction of the ferroelectric polarization in a YMnO₃ substrate, was demonstrated. A weak magnetism was introduced owing to an exchange interaction between MnPSe₃ and surface O₂ atoms.⁴²³

3. Gate control of critical spin fluctuations

When a material goes through a continuous magnetic phase transition, strong and highly correlated spin fluctuations are expected near the critical point. These spin fluctuations are dependent on the dimensionality of the magnetism and dictate resulting critical phenomena. For a 1D chain, strong fluctuations typically destroy any long-range magnetic ordering, whereas in 3D, there is a limited range of phase space where fluctuations become critical.^{426,427} For 2D vdW magnets, on the other hand, there is a balance between fluctuations and long-range order such that they provide ideal platforms to access and possibly tune critical spin fluctuations. Recently, researchers have demonstrated real-time imaging of critical spin fluctuations in CrBr₃ encapsulated in h-BN via a custom-engineered magnetic circular dichroism (MCD) imaging technique.⁴²⁸ As the temperature increased toward T_c , they observed spatially resolved fluctuations in the magnetization of monolayer CrBr₃ under zero applied magnetic field, whereas no such fluctuations were observed in a 3D bulk sample. Furthermore, an applied gate voltage using graphene as the gate material could be used to tune T_c , i.e., how far away the system is from the critical point, thus enabling control of the critical spin fluctuations at a

fixed temperature. By turning critical fluctuations on and off with a gate voltage ($V_g < 0.5$ V) and using real-time feedback control, the magnetization state in the monolayer CrBr₃ can be switched between the fully spin-up state (state “1”) and the fully spin-down state (state “0”) by purely electrical means. This concept of switching states with critical fluctuations could potentially lead to opportunities in low-power magnetic processing and storage since, in principle, the energy cost of the switching comes from the feedback measurement.

4. Emerging device applications

a. Magnetic tunnel junctions (MTJ). Magnetic tunnel junctions (MTJs) that exploit magnetoresistance are the fundamental building block of spintronic devices. MTJs based on vdW materials offer a clear advantage of facilitating all area tunneling due to uniform barrier thickness. Recently, several research groups have successfully fabricated vdW MTJs using graphite/CrI₃/graphite heterostructures, taking advantage of the unique a-FM stacking of few-layer CrI₃ [Fig. 19(a)].^{429–431} The CrI₃ functions as a spin filter tunnel barrier, whereby switching the magnetic order with a magnetic field leads to a giant tunneling magnetoresistance (TMR). With its a-FM stacking state, bilayer CrI₃ exhibited low current due to hindrance in the spin-conserving tunneling of electrons through the adjacent layers. However, the application of a magnetic field transformed the bilayer CrI₃ into a fully spin polarized state, resulting in a significant increase in current. Electrical tuning of the TMR in bilayer CrI₃ has also been demonstrated, where a maximum ratio $\approx 530\%$ at 290 mV bias voltage was achieved [Fig. 19(b)].⁴³⁰ For trilayer and four-layer CrI₃ devices, the TMR peaked at $\approx 3200\%$ and 19000% , respectively.⁴³⁰ In a separate study, electrically controlled TMR was demonstrated using a four-layer CrI₃ tunnel barrier sandwiched by monolayer graphene contacts in a dual-gated structure.⁴³² Under fixed magnetic field, bistable magnetic states of the CrI₃ tunnel barrier could be switched reversibly by sweeping V_g between -2.4 V to $+2.4$ V, resulting in different tunneling currents. Further, the V_g -controlled TMR was demonstrated in fully antiparallel or parallel spin configurations, which could be modulated between 57000% and 17000% . A combination of electrically tunable and spin-dependent tunnel barrier, Fermi level variation, and magnetic proximity effects in the graphene contacts induced by CrI₃ were suggested to be possible explanations for the TMR modulation.

b. Spin valves. Tunneling spin valves using vdW Fe₃GeTe₂ magnetic electrodes, separated by a thin h-BN layer, have also been fabricated [Fig. 19(c)].⁴⁴ A relative change in the orientation of magnetization in the Fe₃GeTe₂ electrodes led to a change in the tunneling resistance due to a spin valve effect and a TMR as large as 160% at 4.2 K was achieved, corresponding to a spin polarization of 66% . The TMR was further tuned by applying a voltage bias between two Fe₃GeTe₂ electrodes. A bias-dependent non-linearity in the differential tunneling conductance for the antiparallel configuration, and a steep decrease in TMR upon increasing voltage bias was observed, which originated from bias-dependent opening of inelastic tunneling channels and enhanced spin relaxation rates [Fig. 19(d)].⁴⁴

c. Spin field-effect transistors. Spin FETs hold great promise for nonvolatile and low-power operation of the data storage devices. Spin FETs based on vdW heterostructures have been previously reported;

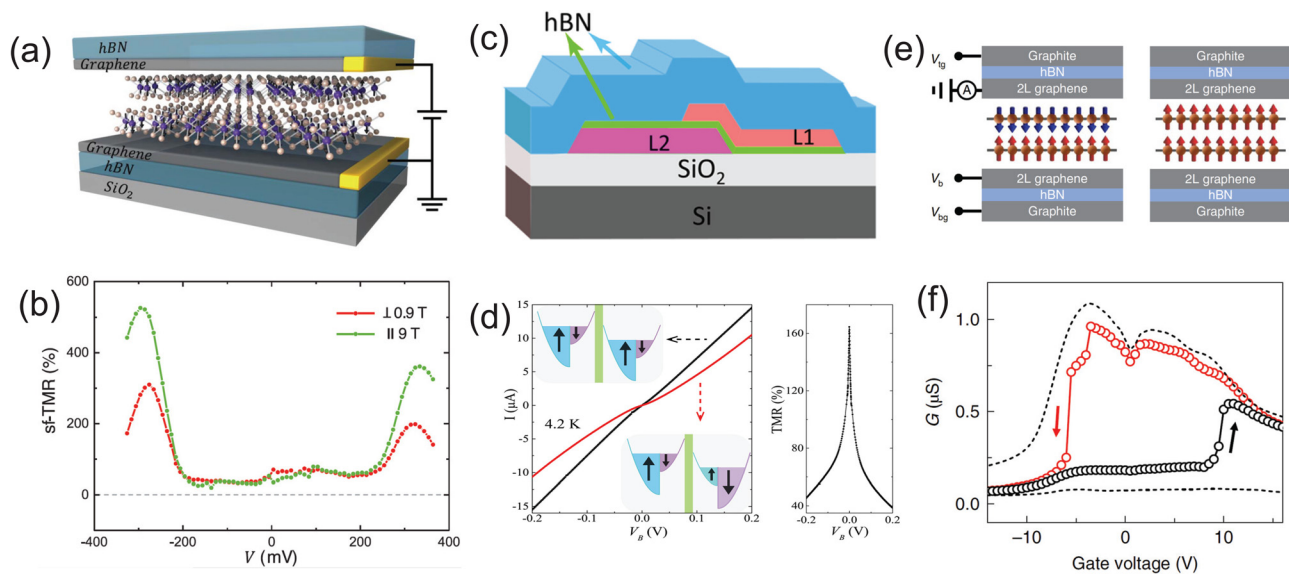


FIG. 19. Devices based on 2D magnetic materials. (a) Schematic of 2D spin-filter magnetic tunnel junction with bilayer CrI_3 functioning as the spin-filter encapsulated between few-layer graphene contacts. (b) Spin filter-tunneling magnetic resistance ratio as a function of bias for the same bilayer CrI_3 magnetic tunnel junction device shown in panel (a).⁴³⁰ Adapted with permission from Song *et al.*, *Science* **360**, 1214 (2018). Copyright 2018 AAAS. (c) Schematic representation of the spin valve device structure Fe_2GeTe_3 FM electrodes (L1 and L2). (d) Bias dependence of I - V curves measured with the magnetization in the two Fe_2GeTe_3 electrodes pointing parallel (in black, $B = 0$ T) and antiparallel (in red, $B = -0.68$ T) to each other, and corresponding bias-dependent tunneling magnetoresistance is shown in the right panel.⁴⁴ Adapted with permission from Wang *et al.*, *Nano Lett.* **18**, 4303 (2018). Copyright 2018 American Chemical Society. (e) Schematic representation of the operating principles of a spin-T-FET based on a gate-controlled, bilayer CrI_3 spin filter in the tunnel junction. Arrows indicate the spin orientation in the CrI_3 layers. The left and right panels correspond to a low and a high tunnel conductance state, respectively. (f) Tunnel conductance of a T-FET with a four-layered CrI_3 tunnel barrier repeatedly switched by gating under a constant magnetic bias of 1.77 T.⁴³⁶ Adapted from Jiang *et al.*, *Nat. Electron.* **2**, 159 (2019). Copyright 2019 Springer Nature.

however, their performance suffers significant challenges due to inefficient spin injection and spin relaxation in the semiconductor channels through the FM contacts.^{433,434} 2D half metals hold great promise for high-efficiency spin FETs. An electric field-induced half metallicity in 2H- VSe_2 , which is an A-type a-FM vdW material, was recently investigated for applications in spin FETs using DFT calculations.⁴³⁵ After applying an electric field above a critical value (e.g., $E > 0.4$ V/Å), the energy levels of the constituent layers were lifted in opposite directions, leading to the gradual closure of the gap of singular spin-polarized states and the opening of the gap of the opposite spin channel, thereby inducing half metallicity. The interlayer charge transfer under electric field also transformed the interlayer exchange coupling of bilayer 2H- VSe_2 from a-FM stacking to FM stacking. A switching in the polarity of the half metal was also realized by reversing the direction of the electric field. Therefore, the vertical electric field can act as a “gate” to switch the half metallicity as well as to control its polarity, in analogy to conventional semiconductor transistors.⁴³⁵ Recently, intrinsic 2D vdW magnetic materials, such as dual gated graphene/ CrI_3 /graphene tunnel junctions, have been exploited for designing tunnel FETs with spin-dependent output [Fig. 19(e)].⁴³⁶ Due to the spin filtering effect of few-layer CrI_3 , which can be easily controlled via V_g under a constant magnetic bias near the spin flip transition, the device was efficiently switched between a low and high conductance state, resulting in a high-low conductance ratio approaching 400% for a tunnel FET with a four-layer CrI_3 tunnel barrier [Fig. 19(f)].

d. Magnonic and Skyrmionic Devices. Electrical control of magnons and magnonic devices: The rich physics of spin waves in magnetic materials has been attractive from both a fundamental and potential applications standpoint.⁴³⁷ Spin waves, which have quanta called magnons, are collective spin excitations in a magnetically ordered material; in a semi-classical sense, they can be understood as precessions of the spins as a wave. Magnons are able to transfer angular momentum, and thus researchers have been considering their use in information transport and processing for next generation “magnonic” devices. The major advantage of using magnons instead of spin diffusive currents to transport information is that, with magnons, the angular momentum transfer occurs without the actual motion of the electrons, thus drastically reducing losses due to Joule heating. In addition, magnons can have frequencies in the low-THz range for fast switching speeds and allow access to wave-based computing concepts.⁴³⁷ Researchers have utilized optical techniques including Raman spectroscopy and magneto-optical Kerr effect, to probe magnons in FePS_3 ,⁴³⁸ NiPS_3 ,⁴³⁹ and CrI_3 .^{440–443} In addition, long-range magnon transport over several micrometers has been measured in vdW antiferromagnet MnPS_3 , demonstrating these materials as possible channel materials for magnonic applications.⁴⁴⁴

Recently, gate tunability of a 2D magnon was demonstrated by using an ultrafast optical pump/magneto-optical Kerr probe technique.⁴⁴¹ The sample included a bilayer CrI_3 -monolayer WSe_2 heterostructure encapsulated in layers of h-BN, where the WSe_2 served to significantly enhance the optical absorption of the pump pulse and

thus increase the magnon excitation in the CrI_3 [Fig. 20(a)]. At a constant applied magnetic field value, the magnon frequency could be tuned continuously from 80 GHz to 55 GHz by varying the voltage from -13 V to $+13$ V. In addition, the saturation field H_S , i.e., the applied magnetic field needed to align the spins in both layers with the field, could be tuned by as much as 1 T with applied gating. Once the magnetic field exceeds H_S and the spins were in the FM stacking configuration, however, the gate voltage had a negligible effect. The change in magnon frequency and H_S as the gate voltage was varied were both the result of the interlayer exchange field H_E and anisotropy field H_A , decreasing linearly with increasing electron doping [Fig. 20(b)]. Being able to locally control magnons via gate control may open avenues for reconfigurable spin-based devices.

Magnon-assisted tunneling in atomically thin magnets has also been studied by using a 2D ferromagnet as a barrier between two layers of graphene.^{429,445,446} In contrast to non-magnetic barriers where conservation of momentum for tunneling electrons is satisfied via phonons, tunneling mechanisms for FM barriers mostly consist of the emission of magnons at low temperatures. Applying a bias voltage V_g across the two graphene layers resulted in a tunneling current I_t through the CrX_3 material ($X = \text{I, Br, Cl}$), where the differential conductance $G = dI_t/dV_g$ displayed step-like increases at values of V_b related to the magnon energies in the material [Figs. 20(c) and 20(d)]. In addition, the tunneling conductance peaks dispersed in V_g under an applied magnetic field, as expected for magnon-assisted tunneling. Tunneling through 2D ferromagnets with magnon emission could lead to novel methods to inject spin-polarized currents into other 2D materials for spintronics since one-magnon processes only allow one type of spin polarization to tunnel.⁴⁴⁵

e. Skyrmions. Recent studies have also focused on stabilizing magnetic skyrmions, i.e., nanoscale vortex-like spin-textures in 2D magnetic materials. Depending upon the type of interaction between the spins, these skyrmions can be categorized as either Néel- or Bloch-type and are stabilized by Dzyaloshinskii–Moriya interactions (DMIs). Several research groups have demonstrated the stabilization of skyrmions in 2D magnetic materials, such as Fe_3GeTe_2 ^{447,448} and $\text{Cr}_2\text{Ge}_2\text{Te}_6$ ⁴⁴⁹ that were imaged using *in situ* Lorentz transmission electron microscopy (L-TEM). These skyrmions could be stabilized in the presence of external magnetic field applied along the out-of-plane direction [Figs. 20(e) and 20(f)]. A recent study demonstrated that Néel-type magnetic skyrmions in an $\text{Fe}_3\text{GeTe}_2/[\text{Co}/\text{Pd}]_{10}$ heterostructure could be stabilized without the need of an external magnetic field, whereby the magnetic interlayer coupling between Fe_3GeTe_2 and out-of-plane magnetized Co/Pd multilayers played a crucial role in stabilizing the skyrmions.⁴⁵⁰ The magnetic field was also not required for stabilizing skyrmions in twisted moiré superlattices consisting of a 2D FM layer twisted on top of an a-FM substrate, in which the coupling between the FM layer and the a-FM substrate produced an effective exchange field.⁴⁵¹ The skyrmion properties can also be tuned with the moiré periodicity and anisotropy. For practical applications of skyrmion-based spintronic devices, an electrical control of the 2D skyrmions is desired. It was demonstrated initially for bulk $\text{BaTiO}_3/\text{SrRuO}_3$ perovskite heterostructures that the electric field generated through ferroelectric polarization can lead to nonvolatile control of skyrmions via the magnetoelectric coupling effect.⁴⁵² A recent experiment demonstrated that the magnetic skyrmions can also exist in the form of bimerons in a vdW $\text{LaCl}/\text{In}_2\text{Se}_3$ heterostructure and can be manipulated by switching the polarization in In_2Se_3 using electric

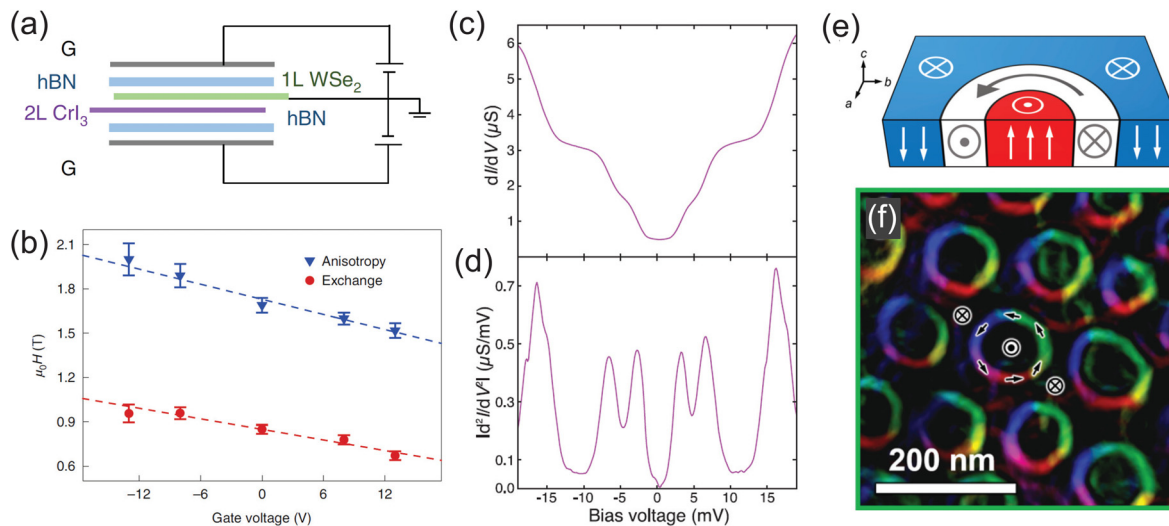


FIG. 20. 2D materials based skyrmionic and magnonic devices. (a) Schematic of the dual-gated device consisting of CrI_3 - WSe_2 heterostructure encapsulated by h-BN. The graphite layers were used as electrical contacts. (b) Anisotropy and exchange fields extracted at different gate voltages. Error bars are standard deviation from linear fitting; dashed line shows linear fit.⁴⁴¹ Adapted from Zhang *et al.*, Nat. Mater. **19**, 838 (2020). Copyright 2020 Springer Nature. (c) Differential conductance vs bias voltage for a bilayer CrI_3 barrier device at zero applied magnetic field. (d) Absolute value of d^2I/dV^2 vs bias voltage extracted from differential conductance data in (c).⁴²⁹ Adapted with permission from Klein *et al.*, Science **360**, 1218 (2018). Copyright 2018 AAAS. The peaks in d^2I/dV^2 correspond to phonon or magnon excitations of the barrier or electrodes. (e) Schematic of the skyrmionic bubble spin texture. (f) Magnetization maps of the Lorentz transmission electron microscopy data of the skyrmionic bubbles.⁴⁴⁹ Adapted with permission from Han *et al.*, Nano Lett. **19**, 7859 (2019). Copyright 2019 American Chemical Society.

fields.⁴⁵³ Owing to the low Curie temperatures of the 2D magnetic materials investigated so far, skyrmion systems have only been stabilized at low temperatures, limiting the practical applications of these systems. Therefore, further efforts to stabilize skyrmions in 2D magnetic materials at room temperature, without an external applied magnetic field, and their efficient manipulation under external electric fields are desired. Spin-texture, including skyrmion engineering via material composition, interfaces, or external stimuli, is therefore expected to be a major area of future research in these classes of materials.

C. Piezo- and ferro-electricity in 2D vdW materials

1. Piezoelectricity in 2D vdW materials

Piezoelectricity refers to a polarization in response to an applied mechanical stress originating from non-centrosymmetry in a structure. When the size of a piezoelectric material changes due to applied mechanical stress, the mass centers of the negative and positive charges shift and no longer coincide with each other, leading to the formation of a dipole. Dipoles inside the material cancel out with each other but those on the surface do not, which results in the polarization. Although non-centrosymmetry is generally regarded as a straightforward and effective method to describe whether a material is potentially piezoelectric,^{454,455} it is worth mentioning that some materials with non-centrosymmetry fail to show piezoelectricity, for example, those belonging to 432 (*O*) point group, because the piezoelectric charges developed along the $\langle 111 \rangle$ polar axes cancel out with each other. A significant amount of research interest has been dedicated to 2D vdW piezoelectric materials due to their ultrathin geometry, weak interlayer interaction and outstanding piezoelectric response, which makes them promising candidates for next-generation flexible nanoelectronics. While some 2D materials do not show any piezoelectricity in their bulk form due to their centrosymmetric crystals, this inversion symmetry can be broken once they are thinned down to few layers. In fact, the percentage of non-centrosymmetric structures increases from 18% in bulk crystals to 43% in monolayers.⁴ In this section, we will review theoretical and experimental reports on the in-plane, out-of-plane, and intercorrelated piezoelectricity within 2D vdW materials.

a. In-plane piezoelectricity. Transition metal dichalcogenides (TMDs): Monolayers of 2H-phase TMDs have a honeycomb structure, in which lattice points are occupied by transition metal and chalcogenide atoms alternatively, which breaks the in-plane centrosymmetry. Thus, monolayer TMDs have been long predicted as potential piezoelectric materials. In 2014, Wu *et al.*³¹⁸ reported the first experimental study on piezoelectricity in single layer MoS₂. Meanwhile, an alternative piezoelectric response between finite and zero was observed in few-layer MoS₂ due to the breaking and recovering of inversion symmetry with odd and even numbers of layers, respectively [Fig. 21(a)].^{318,456} Similar layer-number-dependent piezoelectric response phenomena were also observed in other TMDs.⁴⁰

Additionally, modulation of the bond charges by electric fields has been shown to induce a piezoelectric response in TMDs with even layer numbers [Fig. 21(b)].⁴⁰ A non-zero second harmonic generation (SHG) signal was observed in WSe₂, which is indicative of inversion symmetry breaking and piezoelectricity. The application of a gate voltage between -20 and 40 V led to the bond charges (q_n) on all six

bonds to be shifted upwards. Here the average polarization remained zero; therefore, no electric-field-induced SHG was expected. However, when the gate voltage exceeded a threshold value, a hole accumulation layer formed on the W 5 $d_{x^2-y^2,xy}$ orbitals led to screening of the field. Therefore, the charge on the W-Se bond was compelled to shift further toward the W atoms in the bottom half-monolayer while not affecting the top half-monolayer [Fig. 21(c)]. Consequently, the polarization changes and electric-field-induced SHG is observed. Furthermore, electric fields have also been applied to bilayer MoS₂ to break inversion symmetry. In this case, the nonlinear polarization led to a more hole-like character in the layer in the direction of the DC field. This resulted in a net polarization from the bilayer and therefore a piezoelectric response.⁴⁵⁷

Hexagonal boron nitride (h-BN) and related materials: Similar to the 2H-phase TMD monolayers, the boron and nitrogen atoms in monolayer h-BN alternately occupy the hexagonal lattice points, also leading to a piezoelectric response. Its in-plane piezoelectricity was predicted by Michel *et al.*⁴⁵⁸ based on Born's long-wavelength theory. Later, the non-centrosymmetric structure for monolayer h-BN was probed using SHG, and a similar layer-dependent SHG response was also observed in multilayer h-BN films.⁴⁵⁶ In addition, boron-V group binary and ternary monolayers BX (X = N, P, As, Sb, or mixed) were also investigated by first-principles calculations. This family of 2D materials show excellent in-plane piezoelectricity compared to conventional piezoelectric materials, such as α -quartz, α -SiO₂, and GaN.⁴⁵⁹

b. Intercorrelated piezoelectricity. α -In₂Se₃: This is a layer semiconductor and regarded as the most thermodynamically stable form among the five known phases of In₂Se₃ (α , β , γ , δ , κ) at room temperature. Although the bulk structure of α -In₂Se₃ has been widely studied experimentally, the precise alignments of the atomic layers remain controversial. Possible alignments of the atomic layers have been theoretically investigated by Ding *et al.*⁵¹ using DFT. Based on the alignment of the layers, Ding predicted the existence of both in-plane and out-of-plane piezoelectricity. Unlike in the TMDs or h-BN, the interlayer distances in the Se(1)–In(2)–Se(3)–In(4)–Se(5) quintuple layer are not the same. The Se(3) is slightly shifted off-center toward the neighboring In(2) atom.⁴⁶⁰ Thus, the inversion symmetry along the *c*-axis for each quintuple layer is broken, giving rise to an appreciable out-of-plane piezoelectricity. In-plane piezoelectricity is due to the in-plane centrosymmetry breaking. The observation of multi-directional piezoelectricity in mono- and multilayer α -In₂Se₃ was reported by Xue *et al.*⁴⁶¹ With a thicker α -In₂Se₃ sample, both d_{33} piezoelectrical coefficient (out-of-plane direction) and lateral piezo-response increased and presented a saturated trend up to ≈ 90 nm in thickness [Figs. 21(d) and 21(e)]. Multi-direction piezoelectricity in α -In₂Se₃ offers an opportunity to enable piezoelectric devices responding to strain from all directions.

Janus structures of TMDs: Unlike the conventional TMDs, the transition metal atomic layer in a Janus structure is sandwiched between two different chalcogen atomic layers. Therefore, the inversion symmetry along the *c*-axis in typical TMDs no longer exists, giving rise to multi-directional piezoelectricity. The first Janus of TMDs, MoSSe, was discovered in 2017, and was synthesized by artificially replacing one S-atom layer with one Se-atom layer.⁴⁶² The Janus structure has a great potential in piezoelectric applications due to its

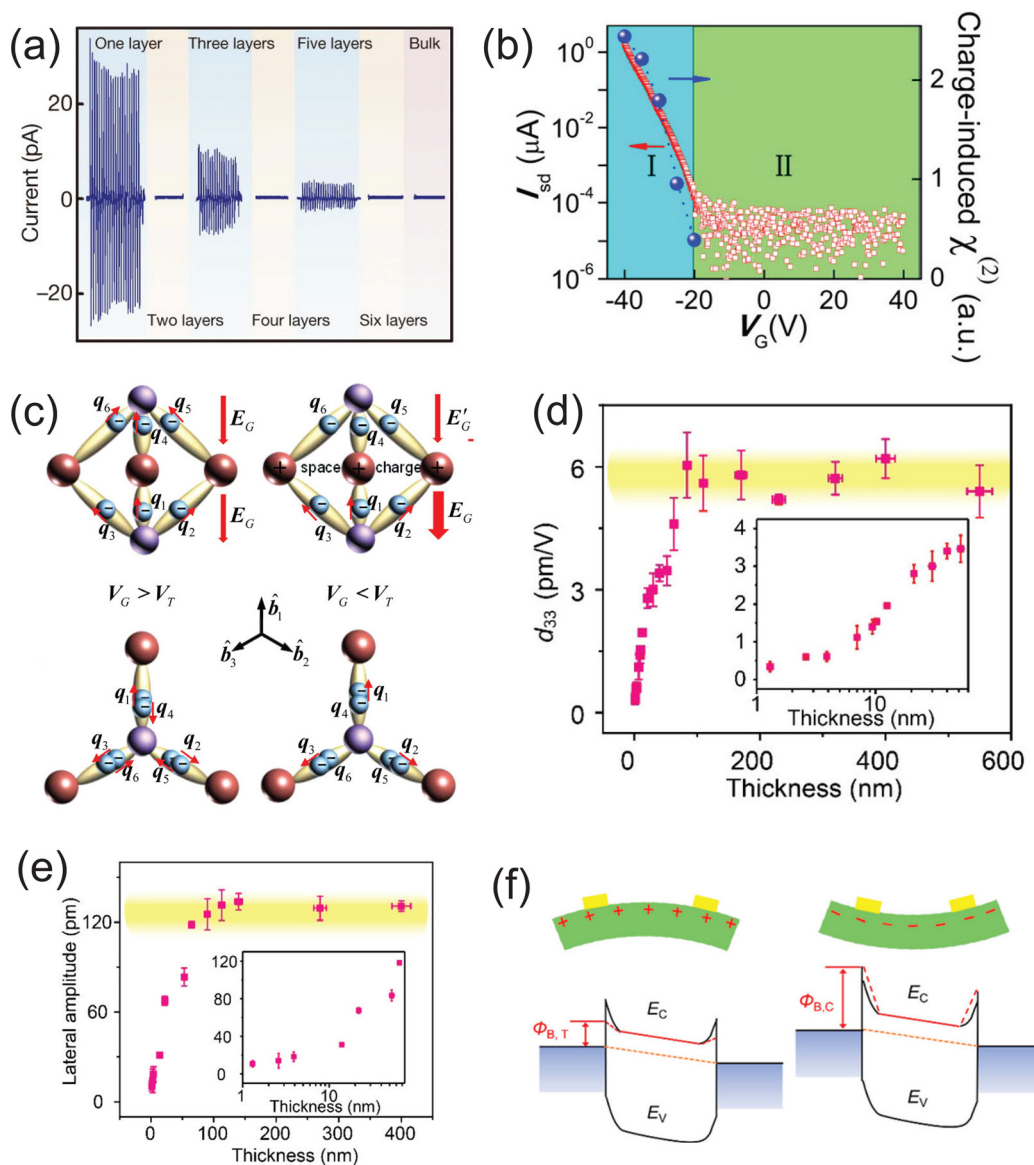


FIG. 21. Piezoelectricity in different 2D materials and its applications. (a) Evolution of the piezoelectric outputs with increasing number of atomic layers (n) in MoS₂ flakes.³¹⁸ Reproduced with permission from Wu *et al.*, Nature **514**, 470–474 (2014). Copyright 2014 Springer Nature. (b) I_{sd} vs V_G curve of the bilayer WSe₂ device. The blue region (I) represents $V_G < V_T$ (hole accumulation) while the green region (II) represents $V_G > V_T$. Here charge-induced second-order susceptibility $\chi^{(2)}$ is related to the magnitude of the square root of SHG intensity. (c) (Top) side-view and (bottom) top-view for the schematic diagram of the bond-charge distributions within one WSe₂ unit cell for $V_G > V_T$ and $V_G < V_T$, respectively.⁴⁰ Reproduced with permission from Yu *et al.*, Nano Lett. **15**, 5653 (2015). Copyright 2015 American Chemical Society. (d) Thickness dependence of the d_{33} piezoelectric coefficient of α -In₂Se₃. (e) Thickness dependence of the lateral piezo-response of α -In₂Se₃. Error bars in (d) and (e) represent standard deviation of sample thickness and piezoelectric response.⁴⁶¹ Reproduced with permission from Xue *et al.*, ACS Nano. **12**, 4976 (2018). Copyright 2018 American Chemical Society. (f) Band diagrams under (left) tensile strain with nonzero source–drain bias; (right) compressive strain with nonzero source–drain bias for In₂Se₃ thin film.⁴⁶⁰ Reproduced with permission from Zhou *et al.*, Nano Lett. **17**, 5508(2017). Copyright 2017 American Chemical Society.

outstanding piezoelectric performance, as supported by theoretical calculations. The strongest out-of-plane piezoelectric response has been theoretically predicted in multilayers of MoSTe. Its piezoelectric coefficient was found to be around 5.7–13.5 pm/V depending on the stacking sequence, which is larger than the commonly used bulk

piezoelectric material AlN (≈ 5.6 pm/V).⁴⁶³ Additionally, 2D Janus Te₂Se monolayers display a large in-plane piezoelectric coefficient (d_{11}) of 16.28 pm/V and out-of-plane piezoelectric coefficient (d_{31}) of 0.24 pm/V, given its structural asymmetry and flexible mechanical properties.⁴⁶⁴

c. Applications utilizing 2D piezoelectric materials. Due to their ultrathin geometry, weak interlayer interaction and outstanding piezoelectric response, 2D piezoelectrics are promising platforms for the design of complex heterostructures with desired functions, which will be needed to meet the urgent requirements of next-generation flexible and nanoscale devices, such as electronic skin. In this section, we will briefly introduce the application of 2D piezoelectric materials in actuators and strain-tuned electronics.

Actuators are an important tool in a wide variety of technologies, including AFM and scanning tunneling microscopy (STM), for positioning objects with high accuracy. Actuators based on ultrathin piezoelectric materials may enable extreme-precision positioning. Two-dimensional piezo-actuators based on CdS film have been proposed by Wang *et al.*⁴⁶⁵ High vertical piezoelectricity ($d_{33} = 32.8 \text{ pm/V}$) in CdS thin film was predicted using finite element calculation, where a 3-nm-thick CdS thin film was used as the actuating material, and DC voltages from -1 to -5 V were applied to its surface as driven voltages. With increasingly negative driven voltage, the deformation of the sample was linearly increased from ≈ 30 to $\approx 150 \text{ pm}$, which could be used for subatomic deformation actuators.

Another area where 2D piezoelectrics can be taken advantage of is mechanical modulation of charge transport on flexible substrates in nanoscale electromechanical devices. It has been demonstrated that the source-drain current in an In_2Se_3 -Pd Schottky junction device increases considerably with a small tensile strain of 0.1% applied to the In_2Se_3 flake and decreases similarly with the same magnitude of compressive strain. The mechanism was similar to a previous report utilizing ZnO thin layers.⁴⁶⁶ Under compression, the Schottky barrier height was lowered, giving rise to an increase in current. Otherwise, the Schottky barrier became higher and current decreased⁴⁶⁰ [Fig. 21(f)].

2. Ferroelectricity in 2D vdW materials

In contrast to piezoelectric materials, which only possess electric polarization upon applied external stresses, ferroelectric materials exhibit spontaneous polarization, which can be reversed by the application of an external electric field, making it possible to achieve a switching in the polarization states. The spontaneous polarization reflects the lack of centrosymmetry in the materials; thus, all ferroelectric materials have piezoelectricity. Typically, these features only exist below the Curie temperature (T_c) and above the critical thickness. Below the critical thickness, materials become paraelectric because the depolarizing field cancels out with the spontaneous polarization.⁴⁶⁷ Recent 2D vdW ferroelectric materials have become highly attractive for device applications due to their flexible bandgap tunability and smaller out-of-plane critical thickness. Thus, they are of growing importance in a variety of applications such as ferroelectric random-access memory (FeRAM), ferroelectric field effect transistors (FeFETs), and ferroelectric tunnel junctions (FTJs). In this section, we will review both theoretical and experimental reports on ferroelectricity in various 2D vdW materials with various polarization directions.

a. In-plane Ferroelectricity. Group-IV monochalcogenides: Group-IV monochalcogenides, with formula MX ($\text{M}=\text{Si}/\text{Ge}/\text{Sn}$ and $\text{X}=\text{S}/\text{Se}/\text{Te}$), have been predicted to possess large spontaneous

polarization based on their hinge-like crystal structures. Interestingly, stable in-plane spontaneous polarization was discovered in ultrathin SnTe films with only one unit-cell thickness, and the corresponding Curie temperature was around 270 K, as reported by Chang *et al.*⁴⁶⁸ Strong evidence of the existence of ferroelectricity in these 2D layers was observed at liquid helium temperatures. This was evident from the stripe domain formation, the slight lattice distortion, and band-bending as well as the ability to manipulate the polarization through the application of an electric field under STM (Fig. 22).⁴⁶⁸ Further experiments revealed that the physical mechanism behind the Curie temperature enhancement in atomically thin SnTe, compared to its bulk counterpart, arises from a phase transition that occurs as the 2D layers are thinned down from the bulk α -phase of SnTe to the γ -phase at the atomic limit, which is an antipolar orthorhombic structure.⁴⁶⁹ In addition, ultrathin SnTe layers with different thickness (from two unit-cell to four unit-cell) exhibited in-plane ferroelectricity with Curie temperatures above room temperature [Fig. 22(d)].⁴⁶⁸

Based on the discovery of stable in-plane ferroelectricity in monolayer SnTe, a growing number of first-principles calculations have been carried out on other group-IV monochalcogenides to investigate the existence of ferroelectricity. 2D GeTe was predicted to possess a stable in-plane spontaneous polarization. The Curie temperature of monolayer GeTe was found to be up to 570 K and could be further enhanced by external tensile strain.⁴⁷⁰ 2D SnS has also been proven to have in-plane ferroelectricity in experiments. Recently, Higashitarumizu *et al.*⁵⁴ put forward the ferroelectric limit of SnS toward monolayer thickness. The polarization was along the armchair direction and robust ferroelectricity was identified in SnS below a critical thickness of 15 monolayers. Due to the inversion symmetry in the c -direction of SnS, the zero net-polarization is expected in even-layer SnS. However, this inversion symmetry can be lifted by an external perturbation such as a substrate or electric field.⁴⁷¹

Other phosphorene analogues: Both monolayer SbN and BiP possess a phosphorene-like structure, which can be regarded as a distorted NaCl-like structure where one type of ion is displaced along the armchair direction with respect to the zigzag direction, leading to a spontaneous in-plane polarization along the armchair direction. Because of the relatively large electronegativity difference and displacement between Sb and N, SbN was predicted to have a much higher spontaneous polarization ($\approx 7.81 \times 10^{-10} \text{ C/m}$) than many other 2D ferroelectric materials. BiP also had a sizeable predicted polarization ($\approx 5.35 \times 10^{-10} \text{ C/m}$) close to that of other strong 2D ferroelectric materials such as GeS. From an *ab initio* molecular dynamics simulation, SbN and BiP have relatively high predicted Curie temperatures (1700 and 800–900 K, respectively), indicating the existence of stable ferroelectricity.⁴⁷²

b. Out-of-plane Ferroelectricity. TMDs: In contrast to in-plane ferroelectricity, out-of-plane ferroelectricity is fairly challenging for ultrathin materials because of the depolarization field along the c -direction. When the thickness of the material approaches a critical thickness, the depolarization becomes stronger due to the uncompensated charge at the surface/interfaces.⁴⁷³ For traditional ferroelectric materials like ultrathin perovskite films, this critical thickness is about 3-unit cells.⁴⁷⁴ In 2018, Fei *et al.*⁵⁵ reported that two- or three-layered $\text{1T}'\text{WTe}_2$ exhibited spontaneous out-of-plane

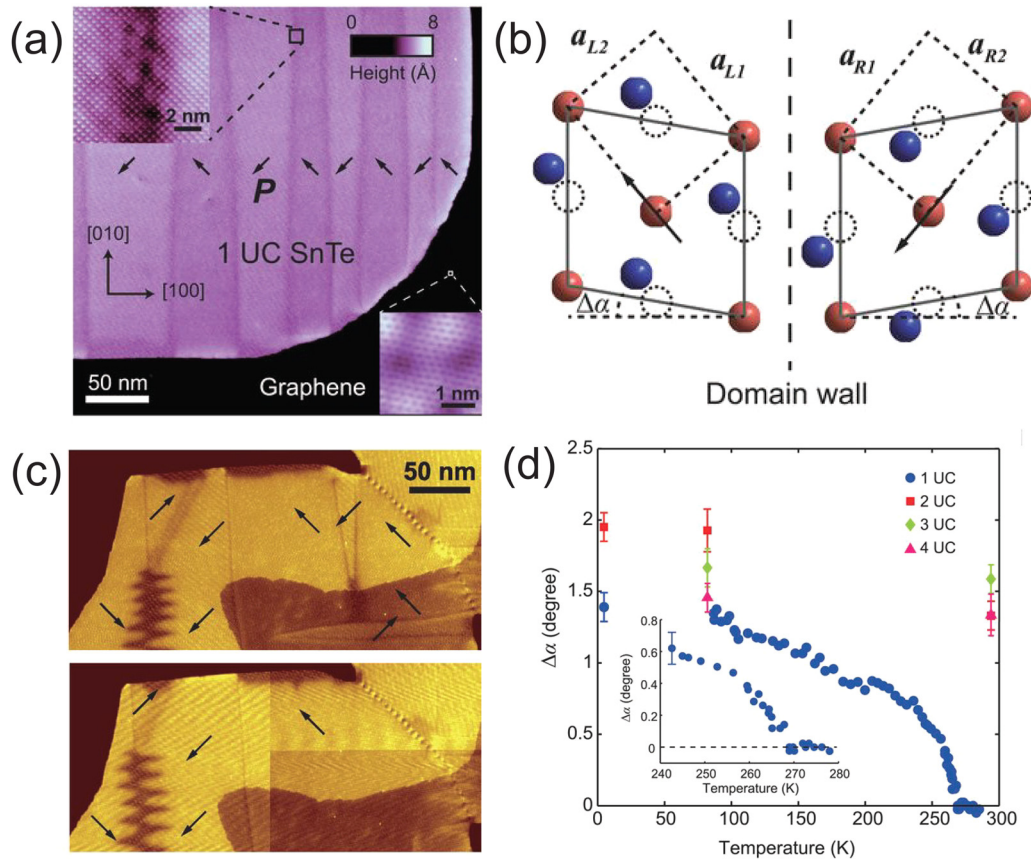


FIG. 22. In-plane ferroelectricity in SnTe thin layers and the observed evidence. (a) Formation of the stripe domain of a one unit-cell SnTe film. The direction of lattice distortion for each domain is indicated by the arrows. (b) Schematic of the lattice distortion and atom displacement in the ferroelectric phase. (c) Topography images of a one-unit-cell, single-domain SnTe island before (top) and after (bottom) a 5V voltage pulse is applied. Polarization direction is indicated by the arrows. (d) Temperature dependence of the distortion angle for the 1–4 unit-cell SnTe films.⁴⁶⁸ Reproduced with permission from Chang *et al.*, *Science* **353**, 274 (2016). Copyright 2016 AAAS.

electric polarization that could be switched using gate electrodes. Bi-stability near $E_{\perp} = 0$ was observed in the conductance G of undoped trilayer and bilayer devices [Figs. 23(a) and 23(b)], which was the characteristic of ferroelectric switching. The corresponding Curie temperature was up to 350 K. However, a similar phenomenon was not observed in the monolayer device [Fig. 23(c)]. First-principles calculations proposed that the polarization of the WTe_2 bilayer stemmed from uncompensated interlayer vertical charge transfer depending on in-plane slippage.⁴⁷⁵ On the other hand, Yuan *et al.*⁴⁷³ reported the discovery of room-temperature out-of-plane ferroelectricity in $d1\text{T-MoTe}_2$ ($t\text{-MoTe}_2$) down to the monolayer limit. Local piezo-response force microscopy (PFM) hysteric loops were recorded, and the PFM contrast revealed that the polarization was anti-parallel in the two domains, confirming the existence of out-of-plane ferroelectricity [Fig. 23(d)]. From cross-sectional STEM images, a few Te atoms were found to move toward the Mo plane in the out-of-plane direction by around 0.6 \AA , while the others largely remained still. This, plus the trimerized structure, both contribute to the rise of spontaneous polarization perpendicular to the lattice plane.

AgBiP_2S_6 : Ferroelectricity in AgBiP_2S_6 comes from the off-center Ag^+ and Bi^{3+} ions with opposite directions. Xu *et al.*⁴⁷⁶ predicted AgBiP_2S_6 exhibited stable out-of-plane ferroelectricity with a thickness of 0.6 nm, with spontaneous polarization of 1.2 pC/m. The depolarization field was overcome by the compensated ferroelectric ordering, which was similar to the previous report on CuInP_2S_6 .⁵⁸

c. Intercorrelated Ferroelectricity. $\alpha\text{-In}_2\text{Se}_3$: In 2017, $\alpha\text{-In}_2\text{Se}_3$ was predicted to possess stable room-temperature in-plane and out-of-plane ferroelectricity simultaneously based on first-principles calculation by Ding *et al.*⁵¹ and proven by experiments one year later. In rhombohedral (3R) $\alpha\text{-In}_2\text{Se}_3$ with thickness from 1 to 6 layers, the phase of in-plane and out-of-plane ferroelectricity changed simultaneously, indicating the existence of intercorrelated ferroelectricity [Figs. 23(e) and 23(f)].⁵¹ There was a 180° difference between the phase contrast of the even and odd layers of $\alpha\text{-In}_2\text{Se}_3$, as shown in Fig. 23(g). For even layers, the polarization canceled out due to the interlayer antiparallel-polarization phenomenon in $\alpha\text{-In}_2\text{Se}_3$. Also, polarization manipulation by electric fields was observed using PFM. For nonvolatile memory devices where good stability at high

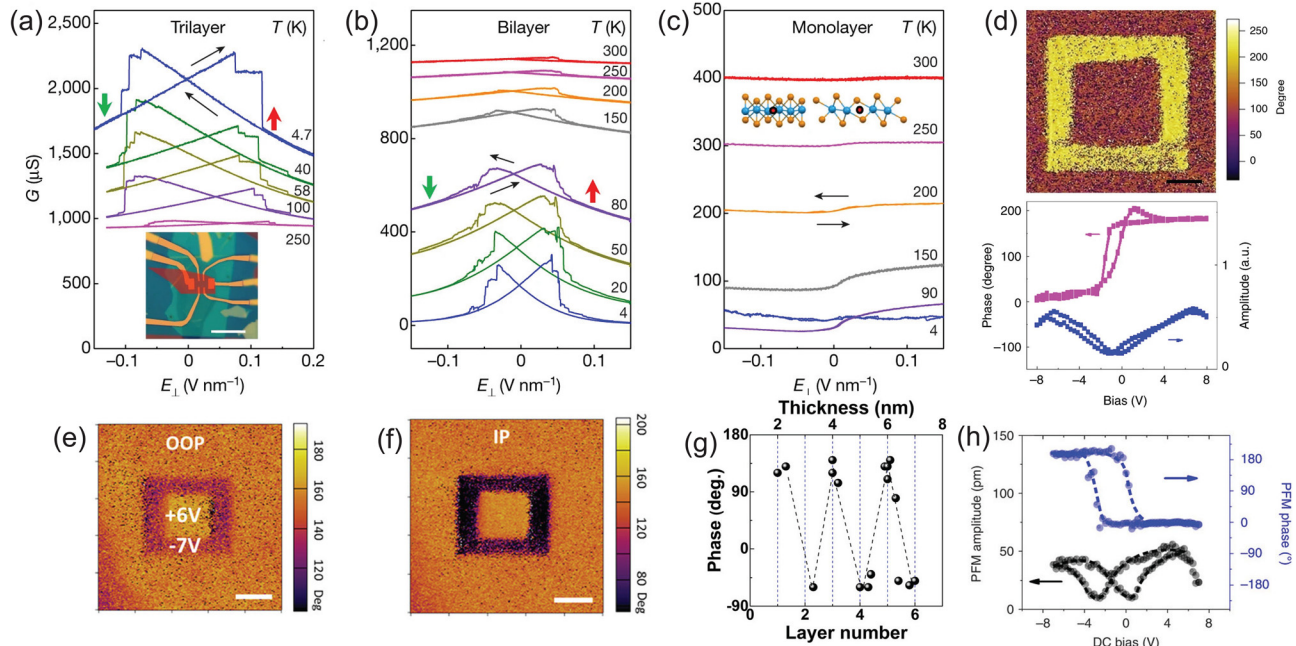


FIG. 23. Out of plane and intercorrelated ferroelectricity in different 2D materials. (a)–(c) Conductance G for undoped trilayer, bilayer and monolayer $1T'$ - WTe_2 devices.⁵⁵ Reproduced with permission from Fei *et al.*, *Nature* **560**, 336 (2018). Copyright 2018 Springer Nature. (d) Top: PFM phase image of monolayer $d1T$ - MoTe_2 —scale bar is $1\ \mu\text{m}$. Bottom: PFM phase hysteresis and butterfly loops of monolayer $d1T$ - MoTe_2 .⁴⁷³ Reproduced with permission from Yuan *et al.*, *Nat. Commun.* **10**, 1775 (2019). Copyright 2019 Springer Nature. (e) Out-of-plane phase image (e) and the corresponding in-plane phase image (f) of a $6\ \text{nm}$ thick In_2Se_3 flake acquired immediately after writing two square patterns with a size of 2 and $1\ \mu\text{m}$ by applying $-7\ \text{V}$ and $+6\ \text{V}$ voltages consecutively. (g) Thickness-dependent in-plane phase (1–6L) of In_2Se_3 flakes.¹¹² Reproduced with permission from Cui *et al.*, *Nano Lett.* **18**, 1253 (2018). Copyright 2018 American Chemical Society (h) PFM amplitude (black) and phase (blue) hysteresis loops of $4\ \text{nm}$ thick CIPS flakes during the switching process.⁵⁸ Reproduced with permission from Liu *et al.*, *Nat. Commun.* **7**, 12357 (2016). Copyright 2016 Springer Nature.

temperature is required, $3R\ \alpha$ - In_2Se_3 is attractive in that it exhibits robust and stable out-of-plane ferroelectricity down to $10\ \text{nm}$ from room-temperature to $\approx 200\ ^\circ\text{C}$.⁴⁷⁷ Intercorrelated ferroelectricity has also been found in hexagonal ($2H$) α - In_2Se_3 at room temperature. Such intercorrelated behavior in $2H\ \alpha$ - In_2Se_3 is similar to that in $3R\ \alpha$ - In_2Se_3 due to its analog structure. Most strikingly, the electric-field-induced polarization switching and hysteresis loop were observed down to bilayer and monolayer ($\approx 1.2\ \text{nm}$) thickness, respectively, which established it as the thinnest layered ferroelectric and verified the corresponding theoretical calculations.⁵⁰

CuInP_2S_6 (CIPS): Room-temperature out-of-plane ferroelectricity has been discovered in 2D CIPS materials dating back to 2015, and the corresponding critical thickness was reported as $50\ \text{nm}$.³⁹ Its spontaneous polarization arises from the off-center ordering in the Cu sublattice and the displacement of cations from the centrosymmetric positions in the In sublattice. Later, ferroelectricity in an ultrathin CIPS film was discovered. Switchable polarization remains as the film is thinned down to $4\ \text{nm}$ (≈ 5 layers) with Curie temperature around $320\ \text{K}$, as confirmed by PFM [Fig. 23(h)].⁵³ Meanwhile, in-plane polarization in ultrathin CIPS was not realized until 2019 by Deng *et al.*⁴⁷⁸ This in-plane polarization did not diminish until it reached its critical thickness, which was around 90 – $100\ \text{nm}$. More importantly, above $90\ \text{nm}$, the in-plane phase changed simultaneously with the out-of-plane phase, indicating that the polarizations were intercorrelated. When the thickness was above $90\ \text{nm}$, Cu atoms moved toward the

sulfur plane, inducing out-of-plane and in-plane displacement simultaneously. However, below $90\ \text{nm}$, the monoclinic structure was transformed into the more stable trigonal structure. In this case, the Cu atomic displacement only led to out-of-plane displacement and thus in-plane ferroelectricity disappeared.

MXene: MXenes have a layer structure resulting from the selective etching of the A atom layer of the parent phase MAX (Sec. II). The out-of-plane ferroelectricity in MXene originates from the asymmetric surface functionalization. Recently, Zhang *et al.* predicted three types of ferroelectric MXene phases, type-I: Nb_2CS_2 and Ta_2CS_2 ; type-II: Sc_2CO_2 and Y_2CO_2 ; and type-III: Sc_2CS_2 and Y_2CS_2 .⁴³ All these phases were predicted to exhibit out-of-plane and in-plane polarization along the c -axis and arm-chair direction, respectively. More importantly, robust out-of-plane and in-plane ferroelectricity have been found in the ferroelectric MXene phases, which was comparable to or even stronger than the reported strong 2D ferroelectric materials such as In_2Se_3 ,⁵¹ GeSe , and GeS .⁴⁷⁹

3. 2D multiferroic materials

Multiferroics refers to a special kind of material that exhibits more than one of the primary ferroic properties simultaneously. Among them, magnetoelectric multiferroic and ferroelastoelectric multiferroic are the most widely reported. Currently, a significant amount of research interest has been dedicated to 2D magnetoelectric

multiferroic materials due to their potential applications in ultrathin ferroelectric and magnetic storage. Additionally, magneto-electric coupling provides a new path to control magnetism using an electric field and vice versa. However, it is difficult for ferroelectricity and ferromagnetism to coexist naturally in one phase. In contrast, many ferromagnets tend to be metallic and thus screen out electric polarization.⁴⁸⁰ Different mechanisms including lone-pair mechanism, charge ordering, and others have been proposed to circumvent this anticorrelation.

Monolayer transition metal phosphorus chalcogenides (TMPCs) CuMP_2X_6 ($M = \text{Cr}, \text{V}; X = \text{S}, \text{Se}$) have been predicted to be promising magnetoelectric multiferroics. Their ferroelectricity originates in the Cu atomic displacement while the magnetism arises from the indirect exchange interaction between the Cr/V atoms.⁴⁸⁰ Moreover, Li *et al.*⁴⁸¹ reported that the introduction of a small twisted angle in vdW bilayers could result in the formation of different ferroelectric domains where some of them possess non-zero polarization. In this way, ferroelectricity could be introduced into 2D ferromagnetic materials, such as MXenes, VS_2 , MoN_2 , and so on. From first-principles calculations, multiferroicity could also be induced by the combination of charge and orbital order.⁴⁸¹ In the case of CrBr_3 , this can be achieved by doping one electron into the primitive cell. This gives rise to an anomalous asymmetric Jahn–Teller distortion of two neighboring Cr–Br₆ units, which brings simultaneous charge and orbital order. This resulting spatial electron–hole separation and spontaneous symmetry breaking leads to 2D multiferroicity in the $\text{CrBr}_3^{0.5-}$ system.⁴⁸²

The coupling of ferroelasticity and ferroelectricity is also intensively studied for its significant potential in future ultrathin mechano-opto-electronic applications. Monolayer group IV monochalcogenides (MXs) were predicted to have ferroelastoelectric multiferroicity by Wang *et al.*⁴⁸³ Similar to monolayer black phosphorus, a well-studied ferroelastic material, MX, has a hinge-like structure and thus also exhibits the ferroelastic order. The two distinct chemical elements in monolayer group IV monochalcogenides give rise to appreciable difference in the electronegativity and a large relative atomic displacement. This represents a new class of 2D multiferroic semiconductors with large in-plane spontaneous polarization, spontaneous ferroelastic lattice strain, and small domain wall energy, which are important additions to the existing realm of multiferroic bulk materials, interface structures, and thin films.

a. Application for 2D ferroelectric materials. Owing to the tunable bandgap and reduced critical thickness in the out-of-plane direction, 2D vdW ferroelectric materials are widely investigated for application to memory and logic devices. Among them, $d1\text{T-MoTe}_2$ is a promising candidate for the construction of nonvolatile FTJ devices at the nanoscale limit because of its small critical thickness in out-of-plane direction (≈ 1 layer) and a T_C above-room-temperature. The corresponding I – V curve of monolayer $d1\text{T-MoTe}_2$ on Pt was measured by conductive atomic force microscopy (C-AFM) and the ON/OFF resistance ratio of the FTJ device was roughly 1000.⁴⁷³ Liu *et al.*⁵⁸ also designed a $\text{Au/CuInP}_2\text{S}_6/\text{Si}$ ferroelectric diode structure with out-of-plane polarization switching in the CuInP_2S_6 ferroelectric thin layer. The ON/OFF resistance ratio was about 100, which was comparable to tunnel junctions based on conventional ferroelectric oxides. Moreover, a lateral $\text{Au}/\alpha\text{-In}_2\text{Se}_3/\text{Au}$ resistive memory device with in-plane polarization switching was demonstrated. The ON/OFF resistance ratio was about 10. Due to the semiconducting nature of $\alpha\text{-In}_2\text{Se}_3$, the device

was also sensitive to visible light. In this case, a multifunctional memory device with four resistive memory states could be tuned by both electric field and light, showing potential application in advanced data storage technologies.¹¹²

Benefiting from the weak vdW interaction between layers, complex heterojunctions could be designed with different functionalities. Si *et al.*¹¹¹ demonstrated a room-temperature FeFET device with MoS_2 and CuInP_2S_6 2D vdW heterostructure, where the $4\text{-}\mu\text{m}$ -thick CuInP_2S_6 layers served as a ferroelectric gate insulator to a 7 nm thick MoS_2 channel. The corresponding ON/OFF resistive ratio was significantly enhanced by back-gating. Furthermore, Huang *et al.*⁴⁸⁴ inserted an extra layer of h-BN between MoS_2 and CuInP_2S_6 , which effectively stabilized the polarization of CuInP_2S_6 and further improved the device performance. An ultrahigh ON/OFF ratio up to 10^7 as well as a large memory window was observed under $V_{\text{GS}} = \pm 80$ V and ultralow programming state current.

D. Phase modulation in 2D materials

At the monolayer limit, TMDs can be stabilized into two prominent crystal phases. These are the H and T phases. In both phases, the transition metal layer is sandwiched between two chalcogen layers; however, these transition metals are trigonally coordinated in the 1H-phase and octahedrally coordinated in the 1T-phase with respect to their chalcogen atoms. These two primary phases can be further developed into more phases due to different stacking sequences of layers (such as 2H- and 3R-phases) and in-plane distortion (such as 1T' and T_d phases). Charge injection has been proposed as one of the major mechanisms to induce phase transformation in these 2D TMD materials. From the interaction of the transition metals with their chalcogen ligands, crystal field theory suggests that the d-orbitals of the transition metal in the H-phase splits into three energy levels ($d_{xz, yz}$, $d_{x^2-y^2, xy}$ and d_{z^2}), while in the T phase, the d-orbitals split into two energy levels ($d_{x^2-y^2, z^2}$ and $d_{xz, yz, xy}$). The free carrier population in the 2D crystal dictates phase stability, and therefore the stability can switch between the two phases depending on the number of electrons filled in those orbitals based on Hund's rule. Other pathways to induce phase transformation in these 2D TMD materials have been widely reported.^{485–494} Here, we review phase transformation induced through carrier density modification that will prove useful in electrically active, tunable, and reconfigurable devices.

1. Charge induced phase transformations through chemical means

One of the most prominent examples to induce phase transformations in TMDs is through the use of n-butyllithium, which has been shown to be an excellent reagent for intercalation of lithium between the 2D layers. The corresponding mechanism is proposed to occur in the following sequence: (a) generation of active species in the form of monomer, dimer or tetramer; (b) surface adsorption and activation of the adsorbent; (c) electron transfer from the lithium–carbon bond to the solid; (d) diffusion of the alkali into the lattice and dimerization and diffusion of the alkane into the solution.⁴⁹⁵ To further understand the transformation of the phase during this process, an *in situ* electrochemical TEM study was carried out on MoS_2 2D flakes.³⁵ The study revealed that the intercalated lithium–ion triggered the sliding of layers in MoS_2 , thus inducing a transformation of the 2H phase

to the 1T. The lithium ion occupied the interlayer S–S tetrahedron site in the 1T-LiMoS₂ structure and can be removed using mild annealing treatment, resulting in the gradual restoration of the semiconducting 2H phase.^{35,496} Based on this approach, phase-engineered low-resistance contacts for ultrathin MoS₂ transistors were designed. Through localized conversion of the semiconducting 2H phase to the metallic 1T, abrupt lateral 2H/1T interfaces can be formed, yielding a contact resistance (R_c) as low as 0.24 k Ω - μm [Figs. 24(a) and 24(b)].⁴⁹⁷ In

2017, Wang *et al.*⁴⁹⁸ experimentally realized the phase transformation between 2H and 1T' phases of monolayer MoTe₂ using ionic liquid (DEME-TFSI) gate in a device structure. Their results were supported by the hysteretic loop of gate-dependent Raman measurements, as the top gate voltage cycled between 0 and 4.4 V as shown in Fig. 25(a). Here, A'_1 (171.5 cm⁻¹) and A_g (167.5 cm⁻¹) are Raman characteristic modes for 2H and 1T' phases, respectively. In addition, the orientation of the crystal was preserved before and after gating as highlighted by

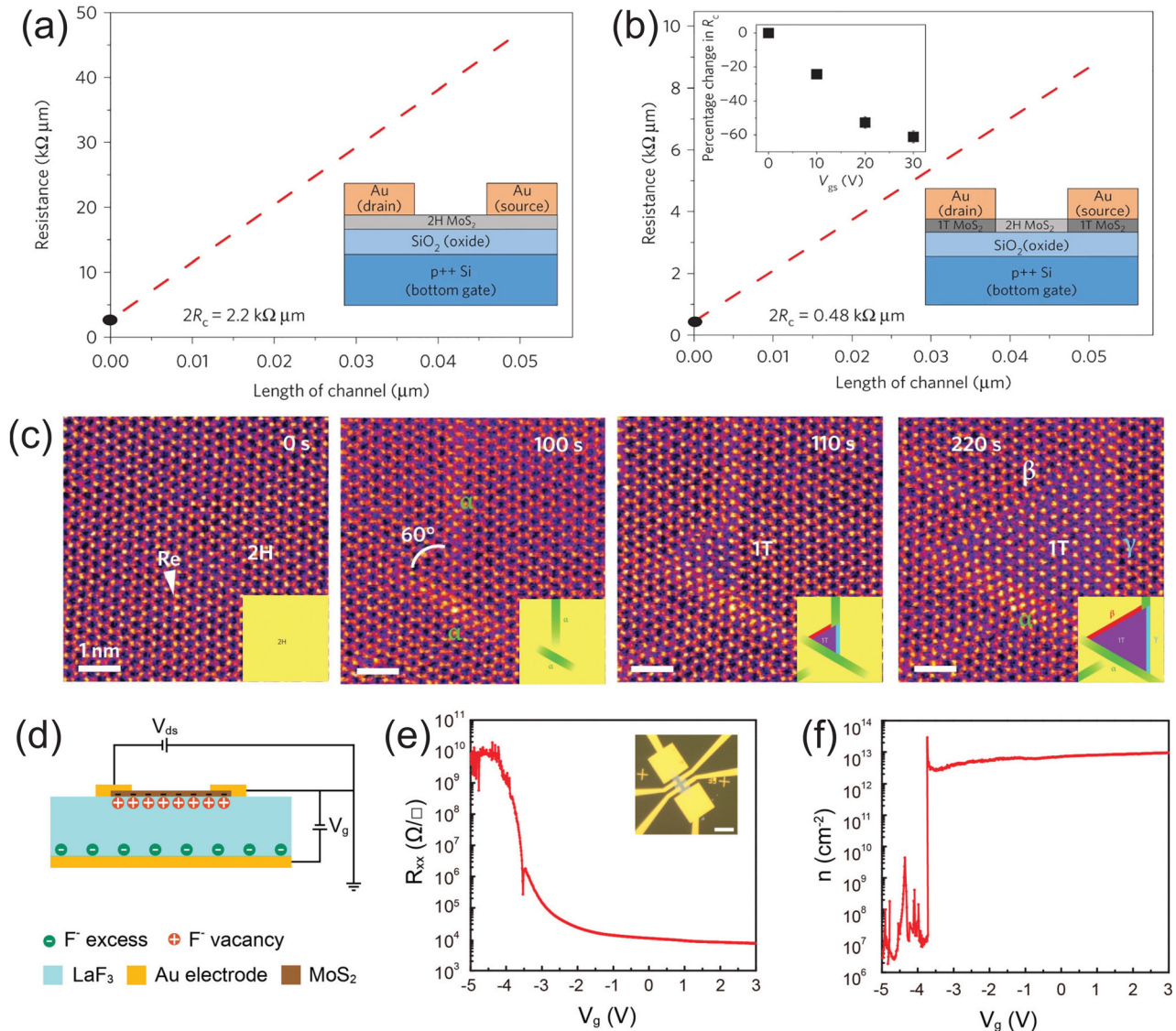


FIG. 24. Phase modulation in MoS₂ thin layers. Resistance vs 2H channel lengths for Au deposited directly on (a) the 2H phase and (b) the 1T' phase of MoS₂.⁴⁹⁷ Reproduced with permission from Kappera *et al.*, Nat. Mater. **13**, 1128 (2014). Copyright 2014 Springer Nature. (c) Atomic movements during 2H \rightarrow 1T phase transformation in the monolayer MoS₂ under electron beam irradiation at an elevated temperature of 600 °C.⁴⁹⁸ Reproduced with permission from Lin *et al.*, Nat. Nanotechnol. **9**, 391 (2014). Copyright 2014 IOP Science. (d) Schematic diagram of a MoS₂/LaF₃ electric-double-layer transistor when $V_g > 0$. Electronic property modulation LaF₃ gating: (e) gate bias-dependent sheet resistance and (f) corresponding carrier density measured at 220 K.⁵⁰¹ Reproduced with permission from Wu *et al.*, Nano Lett. **18**, 2387 (2018). Copyright 2018 American Chemical Society.

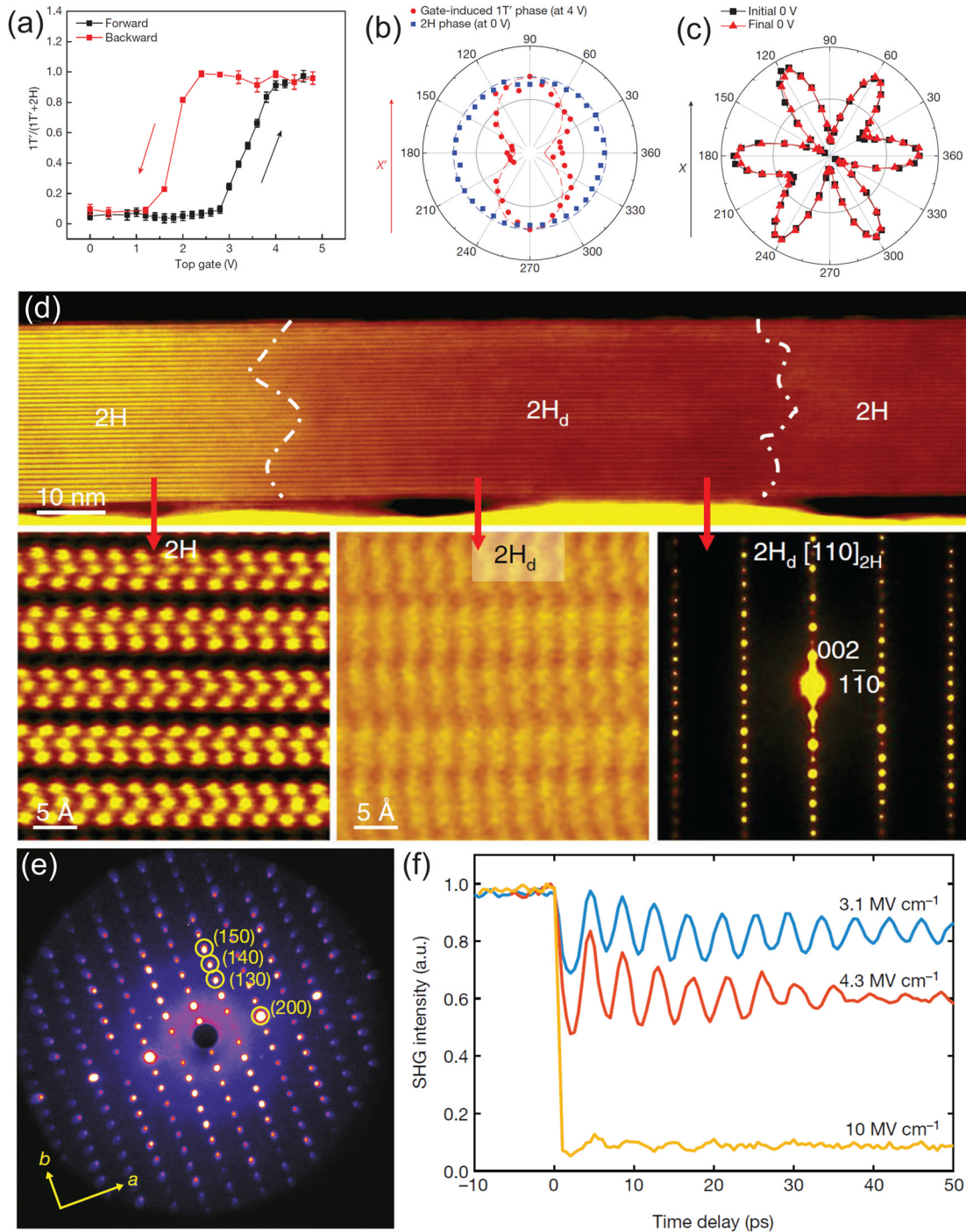


FIG. 25. Phase modulation in MoTe₂ thin layers. (a) Gate-dependent Raman intensity ratios. The ratio $F = 1T'(A_g)/[2H(A'_1) + 1T(A_g)]$ (y-axis) shows hysteresis under an electrical field scan, with a loop width as large as 1.8 V, (b) Raman intensity from monolayer MoTe₂ as a function of crystal angle, and (c) SHG intensity from the same monolayer sample as a function of crystal angle. Error bars in (a) represent standard error propagated from fitting parameters.⁴⁹⁸ Adapted with permission from Wang *et al.*, Nature **550**, 487 (2017). Copyright 2017 Springer Nature. (d) Higher-magnification HAADF image of Mo_{0.96}W_{0.04}Te₂. Bottom images: Atomic-resolution HAADF images taken along the [110]_{2H} zone axis (left and middle) and corresponding nanobeam diffraction pattern for the distorted 2H_d area.⁵⁰⁴ (right) Adapted with permissions from Zhang *et al.*, Nat. Mater. **18**, 55 (2019). Copyright 2019 Springer Nature. (e) Measured diffraction pattern of WTe₂ at equilibrium and (f) pump-induced SHG time traces of WTe₂ at various pump field strengths.⁵⁰⁵ Adapted with permission from Sie *et al.*, Nature **565**, 61 (2019). Copyright 2019 Springer Nature.

polarization-resolved Raman measurements in Fig. 25(b) and SHG measurements in Fig. 25(c). It is worth pointing out that both an electrochemical (vacancy) and an electrostatic component contribute to 2H–1T' phase transformation in MoTe₂.³¹ The introduction of tellurium vacancies, especially when vacancy concentration exceeds >2%, help narrow down the energy barrier between 2H and 1T' phase and thus stabilize the 1T' phase. This opens up the possibility of engineering defects into the monolayer crystal, and with the aid of alloying MoTe₂ with tungsten, one could envision the engineering of low energy barriers for phase transformation for low voltage switching devices.

2. Charge induced phase transformations through non-chemical means

Using *in situ* aberration-corrected scanning transmission electron microscopy (STEM), Lin *et al.*⁴⁹⁹ investigated phase transformations in MoS₂ monolayers. The electron-beam irradiation induced a variety of phase transformations, including the 2H-to-1T, 1T-to-2H and 1T-to-1T' phase transitions as illustrated in Fig. 24(c), where the electron beam introduced vacancies into the lattice, inducing the phase transformation. Although joule heating is inevitable under the electron beam, these results shed light on the great possibility of achieving dynamic control over structural phase transformations in TMD monolayer devices. In fact, modulation of the phase in TMD monolayers through electrostatic gating in devices was suggested by Li *et al.*⁵⁰⁰ using density functional theory. Excess charge introduced into the structure led to switching of the ground state from 2H to the 1T' phase. For an undoped monolayer of MoTe₂ under constant-stress, a semiconductor-to-semimetal phase transition was predicted as the surface charge density was within the range of less than $-0.04 e$ or greater than $0.09 e$ per formula unit. Consequently, a small negative gate voltage was adequate to trigger the phase transition in monolayer MoTe₂. Interestingly, for MoTe₂, the 2H phase is the energetically favorable structure, while for WTe₂, it is the 1T' phase. Therefore, in an alloy of Mo_xW_{1-x}Te₂, the energy difference between the 2H and 1T' phase per formula unit can be further tuned, opening up the possibility of reducing the total energy requirement for phase transformation.⁵⁰⁰

Further optimization of the ionic liquid gating method was proposed to address some of its technical issues including possible side reactions/intercalation, challenges for characterization due to limited access to the active device surface, and strain at the interface.⁵⁰¹ Backgating with solid-state LaF₃ substrates are promising alternatives to ionic liquid gates due to its insulating property, mechanical robustness, and their affective ability to achieve high charge densities through the formation of an electric-double-layer. The fast ion conduction enables the realization of solid-state devices exhibiting comparable performance to ionic-liquid and electrolyte-based devices.⁵⁰¹ To examine the tunability of the electrical properties on MoS₂ with LaF₃ gating, transfer characteristics and the corresponding sheet carrier density were measured at 220 K. [Fig. 24(d)] Within a gate voltage from -5 to 3 V, the channel resistance was tuned from more than $1 \text{ G}\Omega/\square$ to several $\text{k}\Omega/\square$ [Fig. 24(e)], crossing the critical value of resistance for the insulator–metal transition in MoS₂. The measured sheet carrier density, on the order of 10^{12} – 10^{13} cm^{-2} [Fig. 24(f)] in the high conductivity regime, hinted at the possibility of phase transformation from the semiconducting to a possible semi-metallic phase.

3. Field induced phase transformations

Phase transformation in 2D materials using electric fields was first realized in STM. As reported by Zhang *et al.*,⁵⁰² a localized 2H to 1T phase transformation in TaSe₂ was achieved with an electric field developed at the apex an STM tip. The high field induced collective motion of Se atoms by $\frac{\sqrt{3}}{3} a$ along one of its energetically favored directions. The transformed area of the T-phase increased with increasing bias voltage at the tip. Furthermore, the changes in the Ta coordination resulted in a distinct charge density wave (CDW) state in the phases. A similar phase transformation was also observed in TaS₂.⁵⁰³ Later on, Zhang *et al.*⁵⁰⁴ reported phase transformations in MoTe₂ and Mo_xW_{1-x}Te₂ from 2H to 2H_d and T_d phases in resistive random access memory (RRAM) devices. The 2H_d phase was suggested to be a transient state between the semiconducting 2H and the metallic 1T' or T_d phases, which was formed upon the application of a set voltage [Fig. 25(d)]. Pulse measurements also showed that the phase transition time was smaller than 10 ns, opening up the possibility of realizing ultrafast resistive switching in electrically tunable devices. Moreover, the programming voltages were tunable by varying the thickness of the TMD layers, where the ON/OFF ratio went up to 10^6 , which is promising for RRAM. Furthermore, terahertz pulsed light field excitation has also been elucidated as a means to induce phase transformations in TMD layers.⁵⁰⁵ The terahertz pulse was shown to induce a terahertz-frequency interlayer strain shearing with a large strain amplitude in the WTe₂, leading to a topologically distinct metastable phase transformation. A relativistic ultrafast electron diffraction (UED) technique was utilized to reconstruct the shear motion and crystallographically quantify the corresponding atomic displacements by measuring more than 200 Bragg peaks [Fig. 25(e)]. The measured diffraction pattern in equilibrium was consistent with the orthorhombic phase of WTe₂. The modulation of the intensities of many Bragg peaks, plus the changes observed in time-resolved SHG measurements [Fig. 25(f)], indicated a structural transition between a topological phase and a trivial phase in the WTe₂ lattice. It was suggested that the phase transition from the orthorhombic to a monoclinic phase in WTe₂ occurred via hole doping at a density of about 10^{20} cm^{-3} . Microscopically, the field accelerated the electron population away from the topmost valence band, which constituted an interlayer anti-bonding orbital. This destabilized the interlayer coupling strength and launched a shear motion along the in-plane transition pathway from the T_d to the 1T' phase with a new equilibrium position. A similar ultrafast THz-induced phase transformation was discovered in MoTe₂ by Shi *et al.*⁵⁰⁶ with a timescale within 10 ns. An Irreversible 2H to 1T' phase transformation in monolayer and bilayer MoTe₂ occurred owing to a high carrier density generated by the THz electric field through Poole–Frenkel ionization and subsequent cascading process.

E. Controlling correlated states with electric fields in twisted heterostructures

The field of twistrionics, which investigates how the properties of a heterostructure can be tuned by the angle (the twist) between layers, has been a rapidly expanding field in the 2D vdW materials community. The aligned stacking of individual 2D materials is a well-developed technique at this time, where complex heterostructures can be created with sub-degree control over the rotational alignment of two layers. Stacking layers this way creates moiré patterns, where the

wavelength of the superlattice can be tuned either by lattice mismatch or rotational alignment. This type of precise control on the resulting band structure is truly novel to 2D vdW materials, where other subsets of materials are limited by epitaxy. In Sec. IV E 1, we discuss how electric fields, especially used to change the carrier density in an FET, can be used to access correlated states in twisted 2D materials.

In a general sense, among some of the most fascinating states of matter are those where the interaction between particles is very strong, e.g., strongly correlated states of matter. Examples include fractional quantum Hall states and strongly correlated quantum materials, such as heavy fermions, quantum spin liquids, ultra-cold atom lattices, Mott insulators, and high T_c superconductors. In condensed matter systems, strong correlations often occur when the system has a high density of states, such as in electronic “flat bands” where the vanishing Fermi velocity results in Coulomb interactions dominating over kinetic energy, amplifying the effects of Electron–electron interactions.

The electronic bands of a single sheet of graphene, with their Dirac cone nature, are nowhere near flat. In 2011, however, theorists predicted that in twisted bilayer graphene (tBLG) with a small relative twist angle between the layers, exotic phenomena could occur.⁵⁰⁷ While twist angles of $>3^\circ$ generally resulted in the tBLG displaying the properties of two isolated graphene sheets, small twist angles resulted in moiré bands appearing in the band structure due to strong inter-layer coupling. At the “magic angle” of approximately 1.1° , the moiré wavelength was extremely long and the Fermi velocity went to zero, leading to flat moiré bands and thus strong correlations. These results also indicated that the magic-angle flat bands would only contain electron densities of $\approx 10^{12} \text{ cm}^{-2}$, suggesting that, for the first time, back-gating could be used to significantly tune the electron density in a correlated flatband material without the need for chemical doping.

The first graphene moiré superlattices with small twist angles studied showed the presence of moiré bands, with dips in the conductance observed when the carrier density was tuned via a backgate to be at integer filling factors of n_s , with n_s and $-n_s$ corresponding to $+4$ and -4 electrons per moiré unit cell, respectively.^{508,509} Then in 2018, researchers were able to gain enough control over the twist angle to fabricate devices with magic-angle tBLG (MATBLG), with a twist angle of $\approx 1.1^\circ$.^{5,510} By having dual-gated structures, both the carrier density and the displacement field could be tuned by gating. In addition to the insulating states at integer fillings, which could be explained by single particle band gaps, MATBLG devices displayed a plethora of phases associated with strongly correlated electrons, including correlated insulating states at $n_s/2$ filling (where it is expected to be metallic)⁵¹⁰ and superconductivity.⁵ The full phase diagram as a function of temperature and carrier density strongly resembled many of the fascinating properties of the cuprate superconductors. Unlike in the cuprates, where mapping out the phase diagram for different electron densities requires synthesizing a new material with different chemical doping, the full phase diagram as a function of temperature and carrier density for MATBLG could be easily mapped out on the same sample using modest values (minimal carrier density of $1.2 \times 10^{12} \text{ cm}^{-2}$ from charge neutrality) of gate electric field to tune the Fermi energy through the flat bands. The superconductivity in MATBLG occurs at extremely low carrier densities ($\approx 10^{11} \text{ cm}^{-2}$), orders of magnitude lower than carrier densities of typical 2D superconductors. These results revolutionized the field of “twistronics.” Other groups have shown correlated insulating states at $\frac{3}{4}$ filling.^{511,512}

ferromagnetism,^{511,513,514} and twist angle control of 0.02° over a span of $10 \mu\text{m}$.²⁰ Electric field-tunable correlated states have now been observed in different graphene-related heterostructures, including twisted bilayer-bilayer graphene,^{511–517} monolayer-bilayer graphene,⁵¹⁸ and trilayer graphene-h-BN,^{519,520} as well as in twisted “beyond graphene” materials such as TMDs that will be detailed below.

1. Twisted TMD homobilayers

With all the fascinating physics revealed in tBLG, researchers have begun to look toward twisting other 2D materials. The “magic angle” nature of tBLG, where correlated states were observed at angles only slightly larger than 1° , poses a significant experimental challenge of growing large area heterostructures without introducing significant strain or layer reconstruction. Thus, another 2D twisted system to study correlated physics by backgating but without the constraint of specific magic angles is highly desired. Theoretical reports have shown promising results for twisted “beyond graphene” materials, predicting ultraflat bands with narrow bandwidths in twisted bilayers of MoS_2 , WS_2 , MoSe_2 , WSe_2 , MoTe_2 , and h-BN.^{42,48,522} Unlike tBLG, twisted bilayers of TMDs (tTMDs) form two distinct moiré patterns at small twist angles near 0° and 60° , where inversion symmetry is broken (present) for 0° (60°), as shown for MoS_2 in Figs. 26(a) and 26(b), providing an additional degree of control.^{48,49} For homobilayer tTMDs, exotic phenomena were predicted to occur by applying a vertical electrical field, such as quantum anomalous Hall insulators, Mott insulating phases, spin-liquid states, or topological insulating phases.^{48,522} For twisted bilayers of h-BN,⁴² multiple flat bands were predicted to appear that were well isolated from other bands, in contrast with the single pair of flat bands in MATBLG.

Low-energy flat bands and strongly correlated electrons have now been observed in twisted bilayer WSe_2 (t WSe_2) using both transport⁵²¹ and STM/scanning tunneling spectroscopy (STS)⁴⁹ measurements. Wang *et al.*⁵²¹ studied the resistance as a function of carrier density for five t WSe_2 devices with twist angles ranging from 4° to 5.1° , all of which displayed a resistive peak at one hole per moiré unit cell (half filling of the moiré sub-band) at slightly different densities for the five different twist angles [Fig. 26(c)]. This resistive peak was not seen for a naturally occurring Bernal stacked bilayer and is not expected in a single-particle band structure, indicating the presence of strong correlations within the low-energy band. By varying both the top gate and back gate voltages, it was found that the insulating state was only present for a finite range of displacement fields. Inspired by the results on MATBLG, they also investigated whether the strong correlations could result in superconductivity in tTMDs. At densities near the correlated insulator state for the 5.1° twist angle, there were regions where the resistance reached below the instrumentation noise level ($\approx 10 \Omega$), suggesting a possible superconducting transition below 3 K [Fig. 26(d)]. Unfortunately, the large contact resistance due to Schottky barriers in tTMDs hampers direct verification of the superconducting state. In STM/STS measurements, Zhang *et al.*⁴⁹ also measured flat bands in t WSe_2 and showed they are highly localized within the moiré superlattice. Specifically, the spatial distribution is different for 3° vs 57.5° twist angles, where the filled flatband for 3° t WSe_2 is localized on the hexagonal network separating the AA sites, as shown

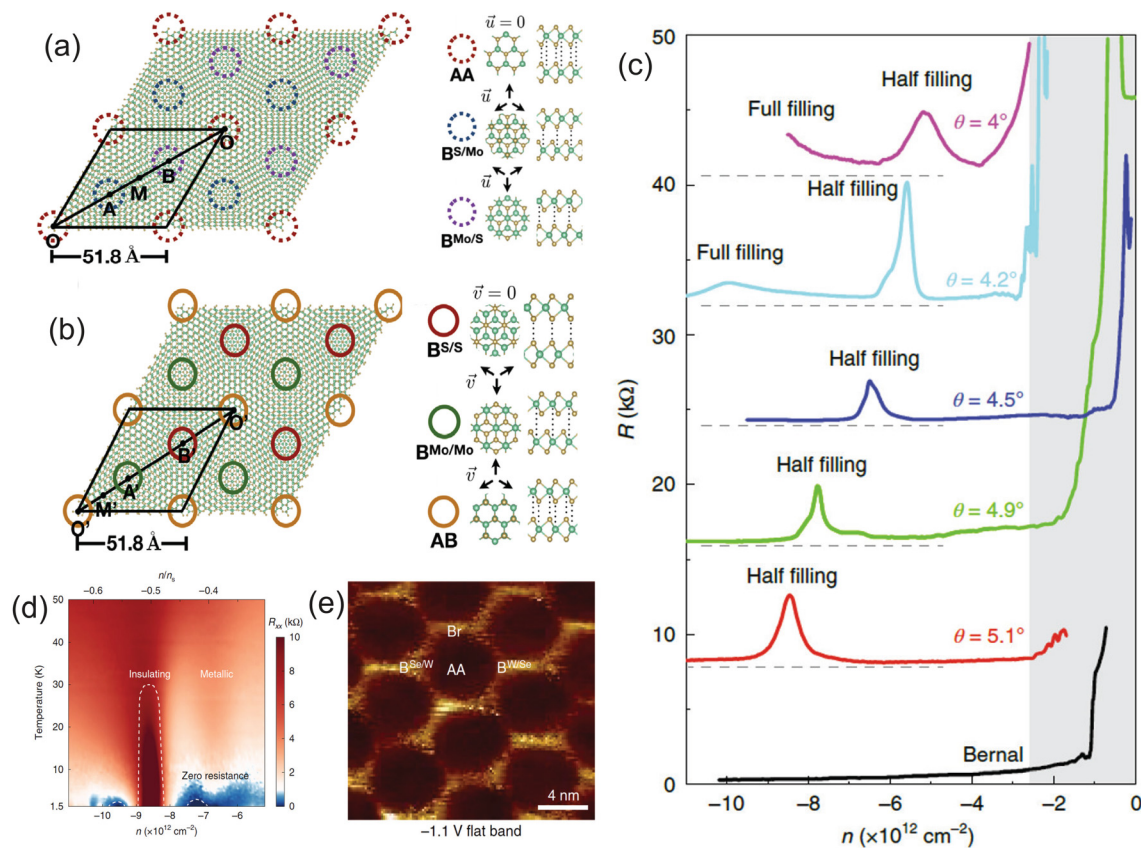


FIG. 26. Comparing moiré superlattices for twisted bilayer MoS₂ at (a) 3.5° and (b) 56.5° twist angle. Stacking sequences at high symmetry points are shown in the circles.⁴⁸ Reprinted with permission from Naik *et al.*, Phys. Rev. Lett. **121**, 266401 (2018). Copyright 2018 by the American Physical Society. (c) Resistance vs carrier density for five different twisted bilayer WSe₂ samples, as well as Bernal stacking (equivalent to 60° twist). Curves are offset for clarity and measured at different displacement fields to capture the peak in resistance. Dashed lines indicate zero resistance for each curve. (d) Resistance as a function of carrier density and temperature for WSe₂ ($\theta = 5.1^\circ$, $V_{tg} = -12.25$ V). When the device is doped away from the correlated insulating state, two zero-resistance domes appear, suggesting possible superconducting behavior.⁵²¹ Reprinted with permission from Wang *et al.*, Nat. Mater. **19**, 861 (2020). Copyright 2020 Springer Nature. (e) Local density of states mapping at the flatband energy for tWSe₂ ($\theta \approx 3^\circ$), showing the flatband is localized on the hexagonal network separating AA sites.⁴⁹ Reprinted with permission from Zhang *et al.*, Nat. Phys. **16**, 1093 (2020). Copyright 2020 Springer Nature.

in Fig. 26(e), whereas for 57.5° the first flatband is localized on the AB sites.

These early observations on homobilayer tTMDs have already confirmed theoretical predictions that the gate-tunable correlated states in tTMDs would be present for a continuum of twist angles, as opposed to the “magic angle” observed in tBLG. Although this research field is just in its infancy, we expect significant advancements on tTMDs in the next few years, following in the footsteps of tBLG. One benefit to using tTMD homobilayers, as compared to heterobilayers that will be discussed next, is that the “tear and stack” technique for fabricating twisted heterostructures allows for more precise control over the relative twist angle.

2. TMD heterobilayers

When bilayer heterostructures are made from two different TMDs, no twist angle is necessary to create a moiré superlattice due to the lattice mismatch between the layers. For example, the 4% lattice

mismatch between WSe₂ and WS₂ results in a moiré pattern with an 8 nm period when the two layers are stacked at a near-zero twist angle. One of the exciting discoveries of these heterobilayer systems is they can simulate the Hubbard model^{523,524} much better than tBLG. In the Hubbard model,⁵²⁵ which is a simple model to describe interacting particles in a crystal lattice, there are only two terms in the Hamiltonian: a kinetic hopping term (t) for particles tunneling between sites and a potential term (U) for on-site Coulomb repulsion, where the physics of the system is governed by the ratio of U and t . The Hubbard model accurately captures the essential physics of metal-insulator phase transitions, high temperature superconductors, and other quantum many-body ground states.^{526,527} Despite its simplicity, the Hubbard model is difficult to solve for dimensions higher than one. Thus, for the 2D case researchers are searching for solid-state systems that can simulate the Hubbard model to help elucidate the physics of many strongly interacting particles.

In 2018, it was theoretically shown that flat, isolated moiré bands in TMD heterobilayers could be described by a generalized triangular

lattice Hubbard model when the chemical potential was within the top-most valence bands, where both U and t could be tuned by varying the twist angle.⁵²³ For the specific case of WS_2/WSe_2 heterostructures, the highest energy moiré valence band in the WSe_2 provided a realization of the triangular lattice Hubbard model if the twist angle was smaller than 3.5° . When the carrier density was tuned to half-filling, they predicted spin-liquid states were likely to occur. Almost two years later, experiments have now caught up with the theoretical predictions, where the phase diagram of the 2D triangular lattice Hubbard model has been obtained using a combination of optical spectroscopy of moiré excitons and transport measurements.⁵²⁴ As expected in the strongly interacting regime of the Hubbard model, they observed a Mott insulating state in both optical and transport measurements [Figs. 27(a) and 27(b)] with a FM Curie–Weiss behavior at half filling (one hole per moiré site) of the first hole moiré band. The ability to gate-tune the carrier density allowed for the phase space of the Hubbard model to be explored over a wider range of carrier densities and temperatures than what is normally possible in cold atoms in optical lattices.

Additional correlated states have been identified in angle-aligned (near zero twist angle) WSe_2/WS_2 heterostructures. We define $\pm n_0$ to be one electron ($+n_0$) or one hole ($-n_0$) per moiré unit cell, which is half filling of the moiré miniband (full filling is two electrons or two holes per moiré unit cell since the TMD heterostructure has a degeneracy of two from spin-valley locking). Taking advantage of strong light-matter interactions in TMDs, Regan *et al.*⁵²⁸ utilized an optically detected resistance and capacitance (ODRC) technique to identify not only the Mott insulating state at $n = -n_0$ (where n is carrier density), but also surprising insulating states at $-1/3n_0$ and $-2/3n_0$ [Figs. 27(c)–27(f)], which they assigned to generalized Wigner crystallization on the underlying lattice. The presence of these generalized Wigner crystal states revealed the need for an extended Hubbard model that included long-range interactions. Xu *et al.*⁵²⁹ identified nearly two dozen correlated insulating states in WSe_2/WS_2 heterostructures at fractional fillings by designing an optical sensing technique that used a monolayer of WSe_2 separated from the heterostructure by a thin h-BN spacer [Figs. 27(g) and 27(h)]. The excitons in the monolayer WSe_2

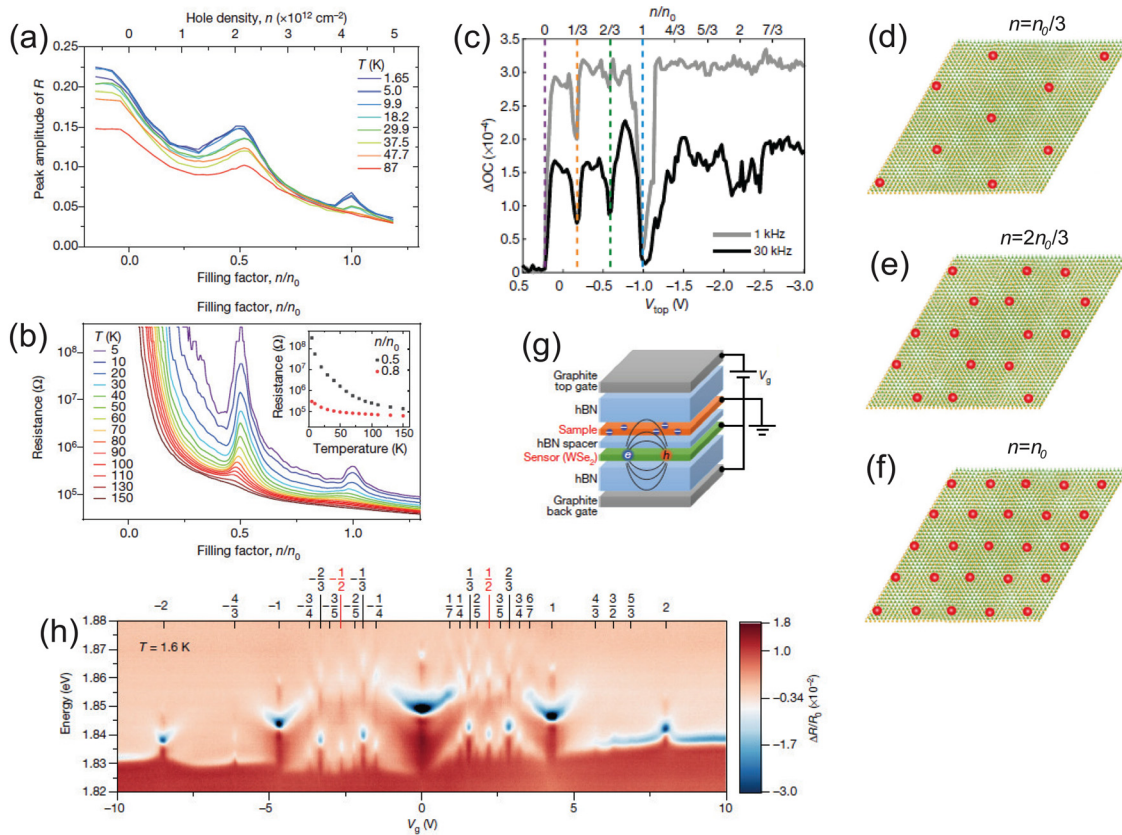


FIG. 27. Correlated insulating states in WSe_2/WS_2 angle-aligned heterostructures. (a) Reflectance at the lowest-energy exciton resonance vs filling factor (bottom) and hole density (top) for various temperatures. (b) Resistance (two-terminal) vs filling factor for the same heterostructure as in (a). Both show two insulating peaks.⁵²⁴ Reprinted with permission from Tang *et al.*, *Nature* **579**, 353 (2020). Copyright 2020 Springer Nature. (c) Optically detected resistance and capacitance signal with increased hole doping, displaying gap-like features at $n = n_0/3$, $n = 2n_0/3$, and $n = n_0$. Schematic of generalized Wigner crystal [(d) and (e)] and Mott insulating state (f) in the WSe_2/WS_2 moiré superlattice, where red dots illustrate holes.⁵²⁸ Reprinted with permission from Regan *et al.*, *Nature*, **579**, 359 (2020). Copyright 2020 Springer Nature. (g) Cartoon illustration of device structure where monolayer WSe_2 is used as a sensor to probe insulating states in WSe_2-WS_2 moiré superlattice. (h) Numerous insulated states identified by measuring blueshifts in the 2s exciton resonance of monolayer WSe_2 in the device in (g).⁵²⁹ Reprinted with permission from Xu *et al.*, *Nature* **587**, 214 (2020). Copyright 2020 Springer Nature.

were very sensitive to their dielectric environment, where their resonance energy and oscillator strength could be used to measure correlated states in the WSe_2/WS_2 in close proximity. They proposed the different insulating states were due to charge-ordering using classical Monte Carlo simulations, including generalized Wigner crystal states and charge density waves. A scanning microwave impedance microscopy technique was utilized by Huang *et al.*⁵³⁰ to identify many correlated insulating states at fractional fillings, some even persisting up to 120 K. With Monte Carlo simulations, they also proposed the charge ordering of the states and revealed surprisingly strong, long-range interactions exceeding nearest-neighbor interactions.

Other works have also reported the observation of numerous correlated insulating states at fractional fillings using scanning microwave impedance microscopy⁵³⁰ and optical anisotropy/electronic compressibility measurements.⁵³¹ Table I summarizes the correlated insulating states observed in recent work. The optical techniques, recently used/developed to study correlated insulating states as a function of electric field-tuned carrier density in these TMD heterostructures, circumvent the large contact resistance (due to the large bandgap) that hinders direct electrical transport measurements, especially for low temperatures and low carrier densities.

3. Future directions in moiré magnets and magnon bands

As was discussed in Subsection IV B, 2D magnetism has been a rapidly growing research area and provides an additional platform to study moiré effects. It has been shown that magnons, which are quantized magnetic excitations, can be used in magnetic insulators to transfer spin angular momenta without the movement of charge, with potential applications in future magnonic devices. It is natural to wonder if twisting two magnetic layers on top of each other would result in tunable magnetic phenomena and magnons, what that would mean for transport phenomena, magnon–magnon or magnon–phonon interactions, and whether nontrivial magnon bands can be generated. In addition, if flat magnon bands do exist, the physics governing them would not be a straightforward comparison to flat bands in electronic systems, considering that magnons are bosons and statistically distinct from electrons. Within the last year, researchers have started to delve into these questions with theoretical predictions of how magnetic phenomena are tuned by the relative twist angles between two magnetic layers, showing the potential for exotic phenomena such as flat and topological magnon bands.^{532–534}

TABLE I. Correlated insulating states observed in twisted-TMD structures.

Heterostructure	n of correlated insulating state	Assignment of correlated insulating state
$tWSe_2$ ($\theta = 4^\circ, 4.2^\circ, 4.5^\circ, 4.9^\circ, 5.1^\circ$)	$n = -1n_0$ for all ⁵²¹	Mott insulating phase
	$n = -2n_0$ for 4.2° and 4.5° (Ref. 528)	Full filling of the moiré subband
	$n = +1n_0,^{529-531} -1n_0^{524,528-530}$	Mott insulating state ^{524,528,529,531} with AFM Curie–Weiss behavior ⁵²⁴
	$n = -0.6n_0^{524}$	Possible phase transition from AFM to weak FM state ⁵²⁴
	$n = 1/6n_0^{530}$	Stripe phase ⁵³⁰
	$n = +1/4n_0,^{529-531} -1/4n_0^{529,530}$	Generalized Wigner crystal states, ⁵²⁹ triangular phase, ⁵³⁰ stripe crystal state ⁵³¹
	$n = +1/3n_0,^{529-531} -1/3n_0^{528-530}$	Generalized Wigner crystal states, ^{528,529} triangular phase, ⁵³⁰ isotropic electron crystals ⁵³¹
	$n = +2/5n_0,^{529,531} -2/5n_0^{529}$	Close to CDW state ⁵²⁹ stripe crystal state ⁵³¹
	$n = +1/2n_0^{529-531}$	Close to generalized Wigner crystal states, ⁵²⁹ stripe phase, ⁵³⁰ stripe crystal ⁵³¹
	$n = -1/2n_0^{529,530}$	Stripe phase ⁵³⁰
	$n = +5/9n_0^{530}$	
	WSe_2/WS_2 ($\theta \approx 0^\circ, \approx 60^\circ$)	$n = +3/5n_0,^{529} -3/5n_0^{529}$
$n = 2/3n_0,^{529-531} -2/3n_0^{528-530}$		Generalized Wigner crystal state, ^{528,529} isotropic electron crystals ⁵³¹
$n = +3/4n_0^{529,530}$		Close to generalized Wigner crystal states ⁵²⁹
$n = -3/4n_0^{529,530}$		Close to CDW state ⁵²⁹
$n = -7/9n_0^{530}$		
$n = -5/6n_0^{530}$		
$n = +6/7n_0^{530}$		
$n = -8/9n_0^{530}$		
$n = +4/3n_0,^{529} -4/3n_0^{529}$		
$n = +3/2n_0,^{529,530} -3/2n_0^{530}$		
$n = +5/3n_0^{529}$		
$n = +2n_0,^{529,530} -2n_0^{524,529}$		Complete filling of conduction miniband ^{529,530}

Hejazi *et al.*⁵³² have provided a theoretical framework to study moiré structures of 2D magnets that allowed for an understanding of magnetic structures and excitations without the need for quasiperiodicity. As an example, they performed detailed calculations for the case of a Néel antiferromagnet on a honeycomb lattice, such as MnPS₃ or MnPSe₃, showing that twisting of two of these layers could lead to noncollinear spin textures, depending on the twist angle and parameters such as the spin stiffness, uniaxial anisotropy, and the interlayer exchange interaction. In the noncollinear phase and at small twist angles, they also predicted some of the magnons will have flat dispersion curves. For twisted bilayer CrI₃, they input experimentally determined parameters to predict that three separate spin ordering phases could be found in this heterostructure depending on the twist angle.

Magnons and their dispersions for twisted magnetic bilayers have been theoretically investigated for both collinear FM^{533,534} and a-FM ordering,⁵³³ predicting flat magnon bands and non-zero Chern numbers for a continuum of twist angles. In particular, the presence of the Dzyaloshinskii–Moriya interaction (DMI) in 2D magnets with broken inversion symmetry⁵³⁵ plays a key role in determining the magnon properties in the twisted bilayer magnet. For two FM layers and with negligible DMI, the situation was analogous to tBLG, with discrete magic angles where the moiré magnon bands are flat. The introduction of even a weak DMI resulted in numerous topological flat magnon bands over a continuum of angles, as opposed to discrete “magic” angles, where they estimated the topological nature of the bands should be present for angles less than 10°. The magnon bands valley Berry curvature, valley Chern numbers, and the valley thermal magnon Hall and Nernst conductivities could be tuned via the twist angle. Li and Cheng⁵³³ extended this to include four different cases of interlayer and intralayer spin ordering, finding that the flat magnon bands and angle-tunable topological Chern numbers are not limited to FM bilayer magnets. If experimental works can verify the topological nature of the magnon bands through the thermal magnon Hall response, we expect moiré magnets to open an intriguing playground where twist-angle could serve as a knob to tune topology. Since magnons and magnon transport are tunable via the application of an electric field, it will be interesting to see how modifying moiré magnets will lead to new opportunities.

V. CONCLUSIONS AND FUTURE OUTLOOK

This review provides a literature review of the multitude of compelling electronic, magnetic, and optical properties that can be electrically tuned in 2D materials beyond graphene. The atomically thin nature of individual layers that can be stacked and twisted into synthetic heterostructures provides unique opportunities for the creation of a variety of devices for applications that span memory and logic to energy harvesting and sensing. The review also provides figures-of-merit and benchmarking targets to highlight exciting areas of opportunity that will require further research and development efforts in both the device structure and materials design.

In terms of future outlook, the review already provides brief summaries at the end of individual sections. In this concluding section, we aim to provide a broader outlook on 2D materials and the impact of their tunable properties at both: basic science and technology levels in the future. With regard to logic and memory devices, the ultrathin-bodies and van der Waals interlayer bonding of 2D materials presents a huge advantage for both electric and mechanical tunability. The

electrostatic tunability of 2D semiconductor bodies has several advantages in emerging logic devices ranging from tunneling FETs⁵³⁶ to reconfigurable transistors^{537,538} that are important for both low-power and secure hardware. On the memory devices side, the key is to recognize which memory technology offers the best competitive advantage for 2D semiconductors. Thus far, resistive memories have failed to compete or outperform oxide based memristors. However, development of single point defect based resistive memory in 2D chalcogenides offers hope on ultimate scaling and low voltage performance.^{539,540} Likewise, use of gate-control for tuning resistive memory states^{94,539} is a big-plus particularly for multistate operations that are desirable for neuromorphic hardware. Similar gate-control over phase transition if achieved will also be a major milestone in terms of phase change memory. Ferroelectric (FE) memories are also a very promising avenue for 2D materials particularly with the discovery of thin, ferroelectric chalcogenide semiconductors.⁵⁴¹ However, the key challenge with ferroelectrics is the retention and cycling stability which is untested yet for 2D ferroelectric chalcogenides. However, the emergence of stacking and twist-controlled ferroelectricity in 2D h-BN bilayers presents a tantalizing possibility for ultrathin, FE memories.⁵⁴² 2D semiconductor channels are also ideal for long retention with minimal depolarization in FE-FETs when combined with another ferroelectric with high remnant polarization. Such demonstrations have been recently made with AlScN based ferroelectrics that are also CMOS BEOL compatible.¹¹⁰ However, longer endurance and large area scalability remain to be demonstrated. Magnetic 2D materials while rich in fundamental physics lack the thermal or chemical stability for replacing or channeling any conventional magnetic memory materials. The cryogenic ferromagnetic transition temperature further adds to practical unviability. Similarly, piezoelectric 2D materials while interesting from a basic science perspective, currently lack piezoelectric co-efficient values (<5 pC/N for monolayer MoS₂) as compared to other commercial piezoceramics such as AlScN (>20 pC/N) and LiNbO₃ (>50 pC/N). Likewise, the mechanical flexibility and van der Waals nature of 2D materials possess a huge advantage in unusual form factor electronics where the intrinsic flexibility and bendability of thin 2D materials either as active layers⁵⁴³ or release layers⁵⁴⁴ will be vital. Finally, for microelectronic applications conductive 2D layers such as metallic chalcogenides and graphene can also serve as flexible interconnects or refractory liners for interconnect layers for minimizing RC losses and maximizing reliability in the smallest interconnect and densest device regions.

For sensing applications, the key advantage for 2D materials is their high surface to volume ratio. Concurrently, the key impediment for 2D materials is their lack of selectivity combined with a stable, passivated surface. While many beyond graphene compound 2D layers are more chemically reactive making their reactive surfaces chemically functional yet selective while retaining long term chemical and thermodynamic stability with large surface/volume ratio. New routes of surface encapsulation and surface chemistry will need to be developed to overcome these limitations.

On the opto-electronics and photonics side, the opportunities and outlook for 2D materials can once again be divided based on light-harvesting vs light-modulation vs light emitting devices. 2D chalcogenides are already well-known to be some of the most absorptive materials¹²² in the visible making them viable for photovoltaics as well as visible frequency photodetectors. However, given the maturity of Si

photovoltaics and photodetectors, TMDCs and other 2D materials need to find an application or a functional niche that is not afforded by Si, Ge, and III–V based photovoltaics and photodetectors. Applications where weight and thickness are of critical importance such as space or aerial vehicle photovoltaics are ones where such 2D semiconductor absorbers maybe desired.⁵⁴⁵ Likewise, for optical modulation the key advantage lies in the extent of tunability of refractive index of 2D semiconductors which relies solely on material quality (resonance width of excitons or other band features) and electric displacement field. However, one aspect of 2D chalcogenides that is often overlooked is their extraordinarily high refractive indices even and especially in the bulk form. These large indices combined with van der Waals nature are a big advantage for nanophotonics, vertically integrated on electronics.^{545,546} Finally, light emitting devices from monolayer, direct bandgap TMDCs has perhaps been studied most extensively. However, the poor quantum yields of 2D semiconductors with the exception of 2D hybrid halide perovskites^{547,548} are a potential drawback for most LED applications. While the quantum yields can be improved to near unity values with chemical treatments, they are only stable for low-level injection.^{549,550} Therefore, developing strategies for improving quantum yield at high injection and over large areas remains a frontier research problem.

One aspect that distinguishes the optical properties of most 2D semiconductors from bulk inorganic semiconductors is the presence of strongly bound excitons which can hybridize into hybrid light-matter states with photons to form polariton states.^{545,551} The use of polaritons is photovoltaics, photodetectors and emitting devices (polariton LEDs and low-threshold lasers) is still in its infancy and big breakthroughs are likely if systematic, electrically tunable device designs are realized which exploits the half-light, half-matter nature of polaritons in these devices. Such devices have been realized in the optical modulator domain,³⁷³ but polariton PVs and lasers are still unrealized/in their infancy.

Finally, in terms of the basic science, new opportunities in discovery of novel quantum or strongly correlated phases remain an area of rich opportunity. In that regards, the control over stacking and twisting degrees of freedom is the most promising approach at the moment. However, most materials subject to stacking and twist-controlled homo and heterostructures are currently isotropic in-plane. Use of in-plane anisotropic crystals such as BP, ReS₂, etc., is expected to produce novel Moire symmetries⁵⁵² unseen in symmetric hexagonal crystals. Mechanical strain and electric field tunability of such Moire superstructures is expected to open up richer and newer avenues for exploration of quantum electronic phases.

Ultimately, from the applications side none of the above devices are possible without achieving wafer scale growth with controlled orientation, crystallinity, phase and grain sizes in addition to controlled defect and dopant densities.^{553–555} With the success in the development of wafer scale growth schemes some of the above is slowly becoming a reality. However, the same needs to be translated for the growth and fabrication of in-plane, out-of-plane, and mixed-dimensional heterostructures with atomic abruptness. Besides growth and heterostructure control, there also needs to be a significant advancement in large-scale wafer transfer, bonding and integration schemes with conventional bulk materials and their wafers. Thus far, growth progress has been maximal on graphene since it is monoelemental; just translating it to binary compounds is significantly difficult

but has been achieved with Mo and W chalcogenides, and h-BN. Layer control is still a lingering problem with binary compounds growth which needs to be addressed. Moving from binary to ternary and quaternary compounds is only going to make the growth more challenging and expertise from III–V and II–VI compounds growth technology will need to be adopted. The success and adoption of any 2D materials post graphene into a successful, mass-market technology will require a concerted effort from all fronts starting from breakthroughs in growth, to hetero-integration to device design and packaging.^{7,556,557}

AUTHOR DECLARATIONS

Author Contributions

T.V., J.L., and S.S. contributed equally to this work

ACKNOWLEDGMENTS

This project has received funding from the European Union's Horizon 2020 Research and Innovation Program under Grant Agreement No. GrapheneCore3 785219. O.K., T.V., and E.C., acknowledge support from the Department for Business, Energy and Industrial Strategy through NMS funding (2D Materials Cross-team project). D.J. acknowledges primary support from the Air Force Office of Scientific Research (AFOSR) Contract Nos. FA9550-21-1-0035 and FA2386-20-1-4074 and U.S. Army Research Office (ARO) Contract No. W911NF-19-1-0109. D.J. also acknowledges partial support from National Science Foundation (NSF)-funded University of Pennsylvania Materials Research Science and Engineering Center (MRSEC)(DMR-1720530) and NSF DMR-1905853. S.S. acknowledges support from Fulbright-Nehru Postdoctoral Fellowship supported by the U.S.-India Educational Foundation. Z.A. acknowledges support of this work by the Laboratory Directed Research and Development Program of Lawrence Berkeley National Laboratory under U.S. Department of Energy Contract No. DE-AC02-05CH11231.

DATA AVAILABILITY

Data sharing is not applicable to this article as no new data were created or analyzed in this study.

REFERENCES

- ¹K. S. Novoselov, "Electric field effect in atomically thin carbon films," *Science* **306**, 666–669 (2004).
- ²R. Ye and J. M. Tour, "Graphene at fifteen," *ACS Nano* **13**, 10872–10878 (2019).
- ³W. Kong, H. Kum, S. H. Bae, J. Shim, H. Kim, L. Kong, Y. Meng, K. Wang, C. Kim, and J. Kim, "Path towards graphene commercialization from lab to market," *Nat. Nanotechnol.* **14**, 927–938 (2019).
- ⁴G. Cheon, K. A. N. Duerloo, A. D. Sendek, C. Porter, Y. Chen, and E. J. Reed, "Data mining for new two- and one-dimensional weakly bonded solids and lattice-commensurate heterostructures," *Nano Lett.* **17**, 1915–1923 (2017).
- ⁵Y. Cao, V. Fatemi, S. Fang, K. Watanabe, T. Taniguchi, E. Kaxiras, and P. Jarillo-Herrero, "Unconventional superconductivity in magic-angle graphene superlattices," *Nature* **556**, 43–50 (2018).
- ⁶C. Lan, Z. Shi, R. Cao, C. Li, and H. Zhang, "2D materials beyond graphene toward Si integrated infrared optoelectronic devices," *Nanoscale* **12**, 11784–11807 (2020).
- ⁷A. McCreary, O. Kazakova, D. Jariwala, and Z. Y. Al Balushi, "An outlook into the flat land of 2D materials beyond graphene: Synthesis, properties and device applications," *2D Mater.* **8**, 013001 (2021).

- ⁸Q. H. Wang, K. Kalantar-Zadeh, A. Kis, J. N. Coleman, and M. S. Strano, "Electronics and optoelectronics of two-dimensional transition metal dichalcogenides," *Nat. Nanotechnol.* **7**, 699–712 (2012).
- ⁹K. S. Novoselov, A. Mishchenko, A. Carvalho, and A. H. Castro Neto, "2D materials and van der Waals heterostructures," *Science* **353**, aac9439 (2016).
- ¹⁰D. S. Schulman, A. J. Arnold, A. Razavieh, J. Nasr, and S. Das, "The prospect of two-dimensional heterostructures: A review of recent breakthroughs," *IEEE Nanotechnol. Mag.* **11**, 6–17 (2017).
- ¹¹B. Huang, G. Clark, E. Navarro-Moratalla, D. R. Klein, R. Cheng, K. L. Seyler, D. Zhong, E. Schmidgall, M. A. McGuire, D. H. Cobden, W. Yao, D. Xiao, P. Jarillo-Herrero, and X. Xu, "Layer-dependent ferromagnetism in a van der Waals crystal down to the monolayer limit," *Nature* **546**, 270–273 (2017).
- ¹²C. Gong, L. Li, Z. Li, H. Ji, A. Stern, Y. Xia, T. Cao, W. Bao, C. Wang, Y. Wang, Z. Q. Qiu, R. J. Cava, S. G. Louie, J. Xia, and X. Zhang, "Discovery of intrinsic ferromagnetism in two-dimensional van der Waals crystals," *Nature* **546**, 265–269 (2017).
- ¹³K. S. Burch, D. Mandrus, and J. G. Park, "Magnetism in two-dimensional van der Waals materials," *Nature* **563**, 47–52 (2018).
- ¹⁴C. Gong and X. Zhang, "Two-dimensional magnetic crystals and emergent heterostructure devices," *Science* **363**, eaav4450 (2019).
- ¹⁵K. F. Mak, C. Lee, J. Hone, J. Shan, and T. F. Heinz, "Atomically thin MoS₂: A new direct-gap semiconductor," *Phys. Rev. Lett.* **105**, 136805 (2010).
- ¹⁶L. Li, J. Kim, C. Jin, G. J. Ye, D. Y. Qiu, F. H. Da Jornada, Z. Shi, L. Chen, Z. Zhang, F. Yang, K. Watanabe, T. Taniguchi, W. Ren, S. G. Louie, X. H. Chen, Y. Zhang, and F. Wang, "Direct observation of the layer-dependent electronic structure in phosphorene," *Nat. Nanotechnol.* **12**, 21–25 (2017).
- ¹⁷X. L. Li, W. P. Han, J. Bin Wu, X. F. Qiao, J. Zhang, and P. H. Tan, "Layer-number dependent optical properties of 2D materials and their application for thickness determination," *Adv. Funct. Mater.* **27**, 1604468 (2017).
- ¹⁸Z. Dai, L. Liu, and Z. Zhang, "Strain engineering of 2D materials: Issues and opportunities at the interface," *Adv. Mater.* **31**, 1805417 (2019).
- ¹⁹D. Akinwande, C. J. Brennan, J. S. Bunch, P. Egberts, J. R. Felts, H. Gao, R. Huang, J. S. Kim, T. Li, Y. Li, K. M. Liechti, N. Lu, H. S. Park, E. J. Reed, P. Wang, B. I. Yakobson, T. Zhang, Y. W. Zhang, Y. Zhou, and Y. Zhu, "A review on mechanics and mechanical properties of 2D materials—Graphene and beyond," *Extreme Mech. Lett.* **13**, 42–77 (2017).
- ²⁰X. Lu, P. Stepanov, W. Yang, M. Xie, M. A. Aamir, I. Das, C. Urgell, K. Watanabe, T. Taniguchi, G. Zhang, A. Bachtold, A. H. MacDonald, and D. K. Efetov, "Superconductors, orbital magnets and correlated states in magic-angle bilayer graphene," *Nature* **574**, 653–657 (2019).
- ²¹M. Chhowalla, D. Jena, and H. Zhang, "Two-dimensional semiconductors for transistors," *Nat. Rev. Mater.* **1**, 16052 (2016).
- ²²B. E. Brown, "The crystal structures of WTe₂ and high-temperature MoTe₂," *Acta Crystallogr.* **20**, 268–274 (1966).
- ²³P. Wu, Y. Ishikawa, M. Hagihala, S. Lee, K. Peng, G. Wang, S. Torii, and T. Kamiyama, "Crystal structure of high-performance thermoelectric materials by high resolution neutron powder diffraction," *Phys. B: Condens. Matter* **551**, 64–68 (2018).
- ²⁴K. El-Sayed, Z. K. Heiba, K. Sedeek, and H. H. Hantour, "Magnetic, electric and crystallographic properties of diluted magnetic InSe_(1-x)Fe(Co)_x semiconductor," *J. Alloys Compd.* **530**, 102–106 (2012).
- ²⁵A. Brown and S. Rundqvist, "Refinement of the crystal structure of black phosphorus," *Acta Crystallogr.* **19**, 684–685 (1965).
- ²⁶D. Yang, W. Yao, Q. Chen, K. Peng, P. Jiang, X. Lu, C. Uher, T. Yang, G. Wang, and X. Zhou, "Cr₂Ge₂Te₆: High thermoelectric performance from layered structure with high symmetry," *Chem. Mater.* **28**, 1611–1615 (2016).
- ²⁷M. A. McGuire, H. Dixit, V. R. Cooper, and B. C. Sales, "Coupling of crystal structure and magnetism in the layered, ferromagnetic insulator CrI₃," *Chem. Mater.* **27**, 612–620 (2015).
- ²⁸V. Maisonneuve, M. Evain, C. Payen, V. B. Cajipe, and P. Molinié, "Room-temperature crystal structure of the layered phase Cu^IIn^{III}P₂S₆," *J. Alloys Compd.* **218**, 157–164 (1995).
- ²⁹V. Y. Verchenko, A. A. Tsirlin, A. V. Sobolev, I. A. Presniakov, A. V. Shevelkov, and F. Order, "Strong magnetocrystalline anisotropy, and magnetocaloric effect in the layered telluride Fe_{3-δ}GeTe₂," *Inorg. Chem.* **54**, 8598–8607 (2015).
- ³⁰R. S. Pease, "An x-ray study of boron nitride," *Acta Crystallogr.* **5**, 356–361 (1952).
- ³¹M. Küpers, P. M. Konze, A. Meledin, J. Mayer, U. Englert, M. Wuttig, and R. Dronskowski, "Controlled crystal growth of indium selenide, In₂Se₃, and the crystal structures of α-In₂Se₃," *Inorg. Chem.* **57**, 11775–11781 (2018).
- ³²Y. Fang, J. Pan, J. He, R. Luo, D. Wang, X. Che, K. Bu, W. Zhao, P. Liu, G. Mu, H. Zhang, T. Lin, and F. Huang, "Structure re-determination and superconductivity observation of bulk 1T MoS₂," *Angew. Chem., Int. Ed.* **57**, 1232–1235 (2018).
- ³³K. D. Bronsema, J. L. De Boer, and F. Jellinek, "On the structure of molybdenum diselenide and disulfide," *ZAAC—J. Inorg. Gen. Chem.* **540**, 15–17 (1986).
- ³⁴C. Tan, Q. Yang, R. Meng, Q. Liang, J. Jiang, X. Sun, H. Ye, and X. P. Chen, "An AlAs/germanene heterostructure with tunable electronic and optical properties: Via external electric field and strain," *J. Mater. Chem. C* **4**, 8171–8178 (2016).
- ³⁵L. Wang, Z. Xu, W. Wang, and X. Bai, "Atomic mechanism of dynamic electrochemical lithiation processes of MoS₂ nanosheets," *J. Am. Chem. Soc.* **136**, 6693–6697 (2014).
- ³⁶W. Xing, Y. Chen, P. M. Odenthal, X. Zhang, W. Yuan, T. Su, Q. Song, T. Wang, J. Zhong, S. Jia, X. C. Xie, Y. Li, and W. Han, "Electric field effect in multilayer Cr₂Ge₂Te₆: A ferromagnetic 2D material," *2D Mater.* **4**, 6–13 (2017).
- ³⁷S. Y. Cho, H. J. Koh, H. W. Yoo, and H. T. Jung, "Tunable chemical sensing performance of black phosphorus by controlled functionalization with noble metals," *Chem. Mater.* **29**, 7197–7205 (2017).
- ³⁸D. Zakhidov, D. A. Rehn, E. J. Reed, and A. Salleo, "Reversible electrochemical phase change in monolayer to bulk-like MoTe₂ by ionic liquid gating," *ACS Nano* **14**, 2894–2903 (2020).
- ³⁹A. Belianinov, Q. He, A. Dziaugys, P. Maksymovych, E. Eliseev, A. Borisevich, A. Morozovska, J. Banys, Y. Vysochanskii, and S. V. Kalinin, "CuInP₂S₆ room temperature layered ferroelectric," *Nano Lett.* **15**, 3808–3814 (2015).
- ⁴⁰H. Yu, D. Talukdar, W. Xu, J. B. Khurgin, and Q. Xiong, "Charge-induced second-harmonic generation in bilayer WSe₂," *Nano Lett.* **15**, 5653–5657 (2015).
- ⁴¹Y. He, D. Li, W. Gao, H. Yin, F. Chen, and Y. Sun, "High-performance NO₂ sensors based on spontaneously functionalized hexagonal boron nitride nanosheets: Via chemical exfoliation," *Nanoscale* **11**, 21909–21916 (2019).
- ⁴²L. Xian, D. M. Kennes, N. Tancogne-Dejean, M. Altarelli, and A. Rubio, "Multiflat bands and strong correlations in twisted bilayer boron nitride: Doping-induced correlated insulator and superconductor," *Nano Lett.* **19**, 4934–4940 (2019).
- ⁴³L. Zhang, C. Tang, C. Zhang, and A. Du, "First-principles screening of novel ferroelectric MXene phases with a large piezoelectric response and unusual auxeticity," *Nanoscale* **12**, 21291–21298 (2020).
- ⁴⁴Z. Wang, D. Sapkota, T. Taniguchi, K. Watanabe, D. Mandrus, and A. F. Morpurgo, "Tunneling spin valves based on Fe₃GeTe₂/hBN/Fe₃GeTe₂ van der Waals heterostructures," *Nano Lett.* **18**, 4303–4308 (2018).
- ⁴⁵L. Kang, L. Shen, Y. J. Chen, S. C. Sun, X. Gu, H. J. Zheng, Z. K. Liu, J. X. Wu, H. L. Peng, F. W. Zheng, P. Zhang, L. X. Yang, and Y. L. Chen, "Surface photovoltaic effect and electronic structure of β-InSe," *Phys. Rev. Mater.* **4**, 124604 (2020).
- ⁴⁶Y. Yang, N. Huo, and J. Li, "Gate tunable photovoltaic effect in a MoSe₂ homojunction enabled with different thicknesses," *J. Mater. Chem. C* **5**, 7051–7056 (2017).
- ⁴⁷C. Chakraborty, L. Kinnischtzke, K. M. Goodfellow, R. Beams, and A. N. Vamivakas, "Voltage-controlled quantum light from an atomically thin semiconductor," *Nat. Nanotechnol.* **10**, 507–511 (2015).
- ⁴⁸M. H. Naik and M. Jain, "Ultraflatbands and shear solitons in moiré patterns of twisted bilayer transition metal dichalcogenides," *Phys. Rev. Lett.* **121**, 266401 (2018).
- ⁴⁹Z. Zhang, Y. Wang, K. Watanabe, T. Taniguchi, K. Ueno, E. Tutuc, and B. J. LeRoy, "Flat bands in twisted bilayer transition metal dichalcogenides," *Nat. Phys.* **16**, 1093–1096 (2020).
- ⁵⁰F. Xue, W. Hu, K. C. Lee, L. S. Lu, J. Zhang, H. L. Tang, A. Han, W. T. Hsu, S. Tu, W. H. Chang, C. H. Lien, J. H. He, Z. Zhang, L. J. Li, and X. Zhang,

- “Room-temperature ferroelectricity in hexagonally layered α - In_2Se_3 nano-flakes down to the monolayer limit,” *Adv. Funct. Mater.* **28**, 1803738 (2018).
- ⁵¹W. Ding, J. Zhu, Z. Wang, Y. Gao, D. Xiao, Y. Gu, Z. Zhang, and W. Zhu, “Prediction of intrinsic two-dimensional ferroelectrics in In_2Se_3 and other III₂-VI₃ van der Waals materials,” *Nat. Commun.* **8**, 14956 (2017).
- ⁵²Z. Wang, T. Zhang, M. Ding, B. Dong, Y. Li, M. Chen, X. Li, J. Huang, H. Wang, X. Zhao, Y. Li, D. Li, C. Jia, L. Sun, H. Guo, Y. Ye, D. Sun, Y. Chen, T. Yang, J. Zhang, S. Ono, Z. Han, and Z. Zhang, “Electric-field control of magnetism in a few-layered van der Waals ferromagnetic semiconductor,” *Nat. Nanotechnol.* **13**, 554–559 (2018).
- ⁵³M. Zelisko, Y. Hanlunmyuang, S. Yang, Y. Liu, C. Lei, J. Li, P. M. Ajayan, and P. Sharma, “Anomalous piezoelectricity in two-dimensional graphene nitride nanosheets,” *Nat. Commun.* **5**, 4284 (2014).
- ⁵⁴N. Higashitarumizu, H. Kawamoto, C. J. Lee, B. H. Lin, F. H. Chu, I. Yonemori, T. Nishimura, K. Wakabayashi, W. H. Chang, and K. Nagashio, “Purely in-plane ferroelectricity in monolayer SnS at room temperature,” *Nat. Commun.* **11**, 2428 (2020).
- ⁵⁵Z. Fei, W. Zhao, T. A. Palomaki, B. Sun, M. K. Miller, Z. Zhao, J. Yan, X. Xu, and D. H. Cobden, “Ferroelectric switching of a two-dimensional metal,” *Nature* **560**, 336–339 (2018).
- ⁵⁶S. Jiang, J. Shan, and K. F. Mak, “Electric-field switching of two-dimensional van der Waals magnets,” *Nat. Mater.* **17**, 406–410 (2018).
- ⁵⁷S. Jiang, L. Li, Z. Wang, K. F. Mak, and J. Shan, “Controlling magnetism in 2D CrI_3 by electrostatic doping,” *Nat. Nanotechnol.* **13**, 549–553 (2018).
- ⁵⁸F. Liu, L. You, K. L. Seyler, X. Li, P. Yu, J. Lin, X. Wang, J. Zhou, H. Wang, H. He, S. T. Pantelides, W. Zhou, P. Sharma, X. Xu, P. M. Ajayan, J. Wang, and Z. Liu, “Room-temperature ferroelectricity in CuInP_2S_6 ultrathin flakes,” *Nat. Commun.* **7**, 12357 (2016).
- ⁵⁹G. Fiori, F. Bonaccorso, G. Iannaccone, T. Palacios, D. Neumaier, A. Seabaugh, S. K. Banerjee, and L. Colombo, “Electronics based on two-dimensional materials,” *Nat. Nanotechnol.* **9**, 768–779 (2014).
- ⁶⁰G. Iannaccone, F. Bonaccorso, L. Colombo, and G. Fiori, “Quantum engineering of transistors based on 2D materials heterostructures,” *Nat. Nanotechnol.* **13**, 183–191 (2018).
- ⁶¹D. Jariwala, V. K. Sangwan, L. J. Lauhon, T. J. Marks, and M. C. Hersam, “Emerging device applications for semiconducting two-dimensional transition metal dichalcogenides,” *ACS Nano* **8**, 1102–1120 (2014).
- ⁶²D. Jariwala, V. K. Sangwan, C. C. Wu, P. L. Prabhuramirashi, M. L. Geier, T. J. Marks, L. J. Lauhon, and M. C. Hersam, “Gate-tunable carbon nanotube- MoS_2 heterojunction p-n diode,” *Proc. Natl. Acad. Sci. U. S. A.* **110**, 18076–18080 (2013).
- ⁶³C. H. Lee, G. H. Lee, A. M. Van Der Zande, W. Chen, Y. Li, M. Han, X. Cui, G. Arefe, C. Nuckolls, T. F. Heinz, J. Guo, J. Hone, and P. Kim, “Atomically thin p-n junctions with van der Waals heterointerfaces,” *Nat. Nanotechnol.* **9**, 676–681 (2014).
- ⁶⁴D. Jariwala, S. L. Howell, K. S. Chen, J. Kang, V. K. Sangwan, S. A. Filippone, R. Turrisi, T. J. Marks, L. J. Lauhon, and M. C. Hersam, “Hybrid, gate-tunable, van der Waals p-n heterojunctions from pentacene and MoS_2 ,” *Nano Lett.* **16**, 497–503 (2016).
- ⁶⁵K. Kobashi, R. Hayakawa, T. Chikyow, and Y. Wakayama, “Multi-valued logic circuits based on organic anti-ambipolar transistors,” *Nano Lett.* **18**, 4355–4359 (2018).
- ⁶⁶D. Jariwala, V. K. Sangwan, J. W. T. Seo, W. Xu, J. Smith, C. H. Kim, L. J. Lauhon, T. J. Marks, and M. C. Hersam, “Large-area, low-voltage, antiambipolar heterojunctions from solution-processed semiconductors,” *Nano Lett.* **15**, 416–421 (2015).
- ⁶⁷D. Jariwala, T. J. Marks, and M. C. Hersam, “Mixed-dimensional van der Waals heterostructures,” *Nat. Mater.* **16**, 170–181 (2017).
- ⁶⁸Y. Wakayama and R. Hayakawa, “Antiambipolar transistor: A newcomer for future flexible electronics,” *Adv. Funct. Mater.* **30**, 1903724 (2020).
- ⁶⁹J. Shim, S. Oh, D. H. Kang, S. H. Jo, M. H. Ali, W. Y. Choi, K. Heo, J. Jeon, S. Lee, M. Kim, Y. J. Song, and J. H. Park, “Phosphorene/rhenium disulfide heterojunction-based negative differential resistance device for multi-valued logic,” *Nat. Commun.* **7**, 13413 (2016).
- ⁷⁰M. Huang, S. Li, Z. Zhang, X. Xiong, X. Li, and Y. Wu, “Multifunctional high-performance van der Waals heterostructures,” *Nat. Nanotechnol.* **12**, 1148–1154 (2017).
- ⁷¹A. Nourbakhsh, A. Zubair, M. S. Dresselhaus, and T. Palacios, “Transport properties of a $\text{MoS}_2/\text{WSe}_2$ heterojunction transistor and its potential for application,” *Nano Lett.* **16**, 1359–1366 (2016).
- ⁷²Y. Li, Y. Wang, L. Huang, X. Wang, X. Li, H. X. Deng, Z. Wei, and J. Li, “Anti-ambipolar field-effect transistors based on few-layer 2D transition metal dichalcogenides,” *ACS Appl. Mater. Interfaces* **8**, 15574–15581 (2016).
- ⁷³V. K. Sangwan, M. E. Beck, A. Henning, J. Luo, H. Bergeron, J. Kang, I. Balla, H. Inbar, L. J. Lauhon, and M. C. Hersam, “Self-aligned van der Waals heterojunction diodes and transistors,” *Nano Lett.* **18**, 1421–1427 (2018).
- ⁷⁴M. E. Beck, A. Shylendra, V. K. Sangwan, S. Guo, W. A. Gaviria Rojas, H. Yoo, H. Bergeron, K. Su, A. R. Trivedi, and M. C. Hersam, “Spiking neurons from tunable Gaussian heterojunction transistors,” *Nat. Commun.* **11**, 1565 (2020).
- ⁷⁵T. H. Choudhury, X. Zhang, Z. Y. Al Balushi, M. Chubarov, and J. M. Redwing, “Epitaxial growth of 2D layered transition metal dichalcogenides,” *Annu. Rev. Mater. Res.* **50**, 155 (2020).
- ⁷⁶Y. Liu, Y. Huang, and X. Duan, “Van der Waals integration before and beyond two-dimensional materials,” *Nature* **567**, 323–333 (2019).
- ⁷⁷H. Yang, J. Heo, S. Park, H. J. Song, D. H. Seo, K. E. Byun, P. Kim, I. K. Yoo, H. J. Chung, and K. Kim, “Graphene barristor, a triode device with a gate-controlled Schottky barrier,” *Science* **336**, 1140–1143 (2012).
- ⁷⁸J. Miao, X. Liu, K. Jo, K. He, R. Saxena, B. Song, H. Zhang, J. He, M. G. Han, W. Hu, and D. Jariwala, “Gate-tunable semiconductor heterojunctions from 2D/3D van der Waals interfaces,” *Nano Lett.* **20**, 2907–2915 (2020).
- ⁷⁹S. Aftab and J. Eom, “Van der Waals 2D layered-material bipolar transistor,” *2D Mater.* **6**, 035005 (2019).
- ⁸⁰L. Liu, N. Xu, Y. Zhang, P. Zhao, H. Chen, and S. Deng, “Van der Waals bipolar junction transistor using vertically stacked two-dimensional atomic crystals,” *Adv. Funct. Mater.* **29**, 1807893 (2019).
- ⁸¹J. Zhou, F. Cai, Q. Wang, B. Chen, S. Gaba, and W. D. Lu, “Very low-programming-current RRAM with self-rectifying characteristics,” *IEEE Electron Device Lett.* **37**, 404–407 (2016).
- ⁸²G. H. Kim, J. H. Lee, Y. Ahn, W. Jeon, S. J. Song, J. Y. Seok, J. H. Yoon, K. J. Yoon, T. J. Park, and C. S. Hwang, “ 32×32 crossbar array resistive memory composed of a stacked Schottky diode and unipolar resistive memory,” *Adv. Funct. Mater.* **23**, 1440–1449 (2013).
- ⁸³J. J. Yang, D. B. Strukov, and D. R. Stewart, “Memristive devices for computing,” *Nat. Nanotechnol.* **8**, 13–24 (2013).
- ⁸⁴K. Tsunoda, Y. Fukuzumi, J. R. Jameson, Z. Wang, P. B. Griffin, and Y. Nishi, “Bipolar resistive switching in polycrystalline TiO_2 films,” *Appl. Phys. Lett.* **90**, 113501 (2007).
- ⁸⁵H. Y. Jeong, Y. I. Kim, J. Y. Lee, and S. Y. Choi, “A low-temperature-grown TiO_2 -based device for the flexible stacked RRAM application,” *Nanotechnology* **21**, 6 (2010).
- ⁸⁶K. Park and J. S. Lee, “Reliable resistive switching memory based on oxygen-vacancy-controlled bilayer structures,” *RSC Adv.* **6**, 21736–21741 (2016).
- ⁸⁷M. M. Rehman, G. U. Siddiqui, S. Kim, and K. H. Choi, “Resistive switching effect in the planar structure of all-printed, flexible and rewritable memory device based on advanced 2D nanocomposite of graphene quantum dots and white graphene flakes,” *J. Phys. D: Appl. Phys.* **50**, 335104 (2017).
- ⁸⁸S. Bertolazzi, P. Bondavalli, S. Roche, T. San, S. Y. Choi, L. Colombo, F. Bonaccorso, and P. Samori, “Nonvolatile memories based on graphene and related 2D materials,” *Adv. Mater.* **31**, 1806663 (2019).
- ⁸⁹M. Xu, T. Liang, M. Shi, and H. Chen, “Graphene-like two-dimensional materials,” *Chem. Rev.* **113**, 3766–3798 (2013).
- ⁹⁰T. J. Echtermeyer, M. C. Lemme, M. Baus, B. N. Szafrank, A. K. Geim, and H. Kurz, “Nonvolatile switching in graphene field-effect devices,” *IEEE Electron Device Lett.* **29**, 952–954 (2008).
- ⁹¹Y. Ji, S. Lee, B. Cho, S. Song, and T. Lee, “Flexible organic memory devices with multilayer graphene electrodes,” *ACS Nano, Am. Chem. Soc.* **5**, 5995–6000 (2011).
- ⁹²Y. J. Doh and G. C. Yi, “Nonvolatile memory devices based on few-layer graphene films,” *Nanotechnology* **21**, 105204 (2010).
- ⁹³N. Ma and D. Jena, “Charge scattering and mobility in atomically thin semiconductors,” *Phys. Rev. X* **4**, 011043 (2014).
- ⁹⁴V. K. Sangwan, D. Jariwala, I. S. Kim, K. S. Chen, T. J. Marks, L. J. Lauhon, and M. C. Hersam, “Gate-tunable memristive phenomena mediated by grain boundaries in single-layer MoS_2 ,” *Nat. Nanotechnol.* **10**, 403–406 (2015).

- ⁹⁵V. K. Sangwan, H. S. Lee, H. Bergeron, I. Balla, M. E. Beck, K. S. Chen, and M. C. Hersam, "Multi-terminal memtransistors from polycrystalline monolayer molybdenum disulfide," *Nature* **554**, 500–504 (2018).
- ⁹⁶J. Jadwiszczak, D. Keane, P. Maguire, C. P. Cullen, Y. Zhou, H. Song, C. Downing, D. Fox, N. McEvoy, R. Zhu, J. Xu, G. S. Duesberg, Z. M. Liao, J. J. Boland, and H. Zhang, "MoS₂ memtransistors fabricated by localized helium ion beam irradiation," *ACS Nano* **13**, 14262–14273 (2019).
- ⁹⁷S. Yin, C. Song, Y. Sun, L. Qiao, B. Wang, Y. Sun, K. Liu, F. Pan, and X. Zhang, "Electric and light dual-gate tunable MoS₂ memtransistor," *ACS Appl. Mater. Interfaces* **11**, 43344–43350 (2019).
- ⁹⁸C. Liu, X. Yan, X. Song, S. Ding, D. W. Zhang, and P. Zhou, "A semi-floating gate memory based on van der Waals heterostructures for quasi-non-volatile applications," *Nat. Nanotechnol.* **13**, 404–410 (2018).
- ⁹⁹Q. A. Vu, Y. S. Shin, Y. R. Kim, V. L. Nguyen, W. T. Kang, H. Kim, D. H. Luong, I. M. Lee, K. Lee, D. S. Ko, J. Heo, S. Park, Y. H. Lee, and W. J. Yu, "Two-terminal floating-gate memory with van der Waals heterostructures for ultrahigh on/off ratio," *Nat. Commun.* **7**, 12725 (2016).
- ¹⁰⁰Y. W. Lan, C. J. Hong, P. C. Chen, Y. Y. Lin, C. H. Yang, C. J. Chu, M. Y. Li, L. J. Li, C. J. Su, B. W. Wu, T. H. Hou, K. S. Li, and Y. L. Zhong, "Nonvolatile molecular memory with the multilevel states based on MoS₂ nanochannel field effect transistor through tuning gate voltage to control molecular configurations," *Nanotechnology* **31**, 275204 (2020).
- ¹⁰¹Y. T. Lee, H. Kwon, J. S. Kim, H. H. Kim, Y. J. Lee, J. A. Lim, Y. W. Song, Y. Yi, W. K. Choi, D. K. Hwang, and S. Im, "Nonvolatile ferroelectric memory circuit using black phosphorus nanosheet-based field-effect transistors with P(VDF-TrFE) polymer," *ACS Nano* **9**, 10394–10401 (2015).
- ¹⁰²A. Lipatov, P. Sharma, A. Gruverman, and A. Sinitskii, "Optoelectrical molybdenum disulfide (MoS₂)—Ferroelectric memories," *ACS Nano* **9**, 8089–8098 (2015).
- ¹⁰³E. B. Song, B. Lian, S. Min Kim, S. Lee, T. K. Chung, M. Wang, C. Zeng, G. Xu, K. Wong, Y. Zhou, H. I. Rasool, D. H. Seo, H. J. Chung, J. Heo, S. Seo, and K. L. Wang, "Robust bi-stable memory operation in single-layer graphene ferroelectric memory," *Appl. Phys. Lett.* **99**, 042109 (2011).
- ¹⁰⁴W. Y. Kim, H. D. Kim, T. T. Kim, H. S. Park, K. Lee, H. J. Choi, S. H. Lee, J. Son, N. Park, and B. Min, "Graphene-ferroelectric metadevices for nonvolatile memory and reconfigurable logic-gate operations," *Nat. Commun.* **7**, 10429 (2016).
- ¹⁰⁵S. Wan, Y. Li, W. Li, X. Mao, C. Wang, C. Chen, J. Dong, A. Nie, J. Xiang, Z. Liu, W. Zhu, and H. Zeng, "Nonvolatile ferroelectric memory effect in ultrathin α -In₂Se₃," *Adv. Funct. Mater.* **29**, 1808606 (2019).
- ¹⁰⁶S. M. Poh, S. J. R. Tan, H. Wang, P. Song, I. H. Abidi, X. Zhao, J. Dan, J. Chen, Z. Luo, S. J. Pennycook, A. H. Castro Neto, and K. P. Loh, "Molecular-beam epitaxy of two-dimensional In₂Se₃ and its giant electroresistance switching in ferroresistive memory junction," *Nano Lett.* **18**, 6340–6346 (2018).
- ¹⁰⁷H. S. Lee, S. W. Min, M. K. Park, Y. T. Lee, P. J. Jeon, J. H. Kim, S. Ryu, and S. Im, "MoS₂ nanosheets for top-gate nonvolatile memory transistor channel," *Small* **8**, 3111–3115 (2012).
- ¹⁰⁸X. Wang, C. Liu, Y. Chen, G. Wu, X. Yan, H. Huang, P. Wang, B. Tian, Z. Hong, Y. Wang, S. Sun, H. Shen, T. Lin, W. Hu, M. Tang, P. Zhou, J. Wang, J. Sun, X. Meng, J. Chu, and Z. Li, "Ferroelectric FET for nonvolatile memory application with two-dimensional MoSe₂ channels," *2D Mater.* **4**, 025036 (2017).
- ¹⁰⁹C. Ko, Y. Lee, Y. Chen, J. Suh, D. Fu, A. Suslu, S. Lee, J. D. Clarkson, H. S. Choe, S. Tongay, R. Ramesh, and J. Wu, "Ferroelectrically gated atomically thin transition-metal dichalcogenides as nonvolatile memory," *Adv. Mater.* **28**, 2923–2930 (2016).
- ¹¹⁰X. Liu, D. Wang, J. Zheng, P. Musavigharavi, J. Miao, E. A. Stach, R. H. Olsson, and D. Jariwala, "Post-CMOS compatible aluminum scandium nitride/2D channel ferroelectric field-effect-transistor," *Nano Lett.* **21**, 3753 (2021).
- ¹¹¹M. Si, P. Y. Liao, G. Qiu, Y. Duan, and P. D. Ye, "Ferroelectric field-effect transistors based on MoS₂ and CuInP₂S₆ two-dimensional van der Waals heterostructure," *ACS Nano* **12**, 6700–6705 (2018).
- ¹¹²C. Cui, W. J. Hu, X. Yan, C. Addiego, W. Gao, Y. Wang, Z. Wang, L. Li, Y. Cheng, P. Li, X. Zhang, H. N. Alshareef, T. Wu, W. Zhu, X. Pan, and L. J. Li, "Intercorrelated in-plane and out-of-plane ferroelectricity in ultrathin two-dimensional layered semiconductor In₂Se₃," *Nano Lett.* **18**, 1253–1258 (2018).
- ¹¹³Y. Yuan, X. Cao, Y. Sun, J. Su, C. Liu, L. Cheng, L. Yuan, H. Zhang, and J. Li, "Memristive behavior in In₂Se₃ asymmetrical hetero-structures," *RSC Adv.* **7**, 46431–46435 (2017).
- ¹¹⁴P. Hou, S. Xing, X. Liu, C. Chen, X. Zhong, J. Wang, and X. Ouyang, "Resistive switching behavior in α -In₂Se₃ nanoflakes modulated by ferroelectric polarization and interface defects," *RSC Adv.* **9**, 30565–30569 (2019).
- ¹¹⁵F. Xue, X. He, J. R. D. Retamal, A. Han, J. Zhang, Z. Liu, J. Huang, W. Hu, V. Tung, J. He, L. Li, and X. Zhang, "Gate-tunable and multidirection-switchable memristive phenomena in a van der Waals ferroelectric," *Adv. Mater.* **31**, 1901300 (2019).
- ¹¹⁶L. Wang, X. Wang, Y. Zhang, R. Li, T. Ma, K. Leng, Z. Chen, I. Abdelwahab, and K. P. Loh, "Exploring ferroelectric switching in α -In₂Se₃ for neuromorphic computing," *Adv. Funct. Mater.* **30**, 2004609 (2020).
- ¹¹⁷M. D. Tran, H. Kim, J. S. Kim, M. H. Doan, T. K. Chau, Q. A. Vu, J.-H. Kim, and Y. H. Lee, "Two-terminal multibit optical memory via van der Waals heterostructure," *Adv. Mater.* **31**, 1807075 (2019).
- ¹¹⁸T. Kobayashi, N. Hori, T. Nakajima, and T. Kawae, "Electrical characteristics of MoS₂ field-effect transistor with ferroelectric vinylidene fluoride-trifluoroethylene copolymer gate structure," *Appl. Phys. Lett.* **108**, 132903 (2016).
- ¹¹⁹R. Cariou, J. Benick, F. Feldmann, O. Höhn, H. Hauser, P. Beutel, N. Razek, M. Wimplinger, B. Bläsi, D. Lackner, M. Hermlle, G. Siefer, S. W. Glunz, A. W. Bett, and F. Dimroth, "III-V-on-silicon solar cells reaching 33% photoconversion efficiency in two-terminal configuration," *Nat. Energy* **3**, 326–333 (2018).
- ¹²⁰S. Essig, C. Allebé, T. Remo, J. F. Geisz, M. A. Steiner, K. Horowitz, L. Barraud, J. S. Ward, M. Schnabel, A. Descoedres, D. L. Young, M. Woodhouse, M. Despeisse, C. Ballif, and A. Tamboli, "Raising the one-sun conversion efficiency of III-V/Si solar cells to 32.8% for two junctions and 35.9% for three junctions," *Nat. Energy* **2**, 17144 (2017).
- ¹²¹K. Wang, L. Zheng, T. Zhu, X. Yao, C. Yi, X. Zhang, Y. Cao, L. Liu, W. Hu, and X. Gong, "Efficient perovskite solar cells by hybrid perovskites incorporated with heterovalent neodymium cations," *Nano Energy* **61**, 352–360 (2019).
- ¹²²D. Jariwala, A. R. Davoyan, J. Wong, and H. A. Atwater, "Van der Waals materials for atomically-thin photovoltaics: Promise and outlook," *ACS Photonics* **4**, 2962–2970 (2017).
- ¹²³B. W. H. Baugher, H. O. H. Churchill, Y. Yang, and P. Jariillo-Herrero, "Optoelectronic devices based on electrically tunable p-n diodes in a monolayer dichalcogenide," *Nat. Nanotechnol.* **9**, 262–267 (2014).
- ¹²⁴A. Pospischil, M. M. Furchi, and T. Mueller, "Solar-energy conversion and light emission in an atomic monolayer p-n diode," *Nat. Nanotechnol.* **9**, 257–261 (2014).
- ¹²⁵D. J. Groenendijk, M. Buscema, G. A. Steele, S. Michaelis De Vasconcellos, R. Bratschkitsch, H. S. J. Van Der Zant, and A. Castellanos-Gomez, "Photovoltaic and photothermoelectric effect in a double-gated WSe₂ device," *Nano Lett.* **14**, 5846–5852 (2014).
- ¹²⁶M. Buscema, D. J. Groenendijk, G. A. Steele, H. S. J. Van Der Zant, and A. Castellanos-Gomez, "Photovoltaic effect in few-layer black phosphorus PN junctions defined by local electrostatic gating," *Nat. Commun.* **5**, 5651 (2014).
- ¹²⁷S. Memaran, N. R. Pradhan, Z. Lu, D. Rhodes, J. Ludwig, Q. Zhou, O. Ogunsolu, P. M. Ajayan, D. Smirnov, A. I. Fernández-Domínguez, F. J. García-Vidal, and L. Balicas, "Pronounced photovoltaic response from multi-layered transition-metal dichalcogenides pn-junctions," *Nano Lett.* **15**, 7532–7538 (2015).
- ¹²⁸S. A. Svatek, E. Antolin, D. Y. Lin, R. Frisenda, C. Reuter, A. J. Molina-Mendoza, M. Muñoz, N. Agraït, T. S. Ko, D. P. De Lara, and A. Castellanos-Gomez, "Gate tunable photovoltaic effect in MoS₂ vertical p-n homojunctions," *J. Mater. Chem. C* **5**, 854–861 (2017).
- ¹²⁹M. M. Furchi, A. Pospischil, F. Libisch, J. Burgdörfer, and T. Mueller, "Photovoltaic effect in an electrically tunable Van der Waals heterojunction," *Nano Lett.* **14**, 4785–4791 (2014).
- ¹³⁰S. Lin, P. Wang, X. Li, Z. Wu, Z. Xu, S. Zhang, and W. Xu, "Gate tunable monolayer MoS₂/InP heterostructure solar cells," *Appl. Phys. Lett.* **107**, 153904 (2015).
- ¹³¹F. Qin, F. Gao, M. Dai, Y. Hu, M. Yu, L. Wang, W. Feng, B. Li, and P. A. Hu, "Multilayer InSe-Te van der Waals heterostructures with an ultrahigh

- rectification ratio and ultrasensitive photoresponse,” *ACS Appl. Mater. Interfaces* **12**, 37313–37319 (2020).
- ¹³²S. Zhao, J. Wu, K. Jin, H. Ding, T. Li, C. Wu, N. Pan, and X. Wang, “Highly polarized and fast photoresponse of black phosphorus-InSe vertical p-n heterojunctions,” *Adv. Funct. Mater.* **28**, 1802011 (2018).
- ¹³³Y. Zhou, W. Xu, Y. Sheng, H. Huang, Q. Zhang, L. Hou, V. Shautsova, and J. H. Warner, “Symmetry-controlled reversible photovoltaic current flow in ultrathin all 2D vertically stacked graphene/MoS₂/WS₂/graphene devices,” *ACS Appl. Mater. Interfaces* **11**, 2234–2242 (2019).
- ¹³⁴P. Lin and J. Yang, “Tunable WSe₂/WS₂ van der Waals heterojunction for self-powered photodetector and photovoltaics,” *J. Alloys Compd.* **842**, 155890 (2020).
- ¹³⁵N. Cavassilas, D. Logoteta, Y. Lee, F. Michelini, M. Lannoo, M. Bescond, and M. Luisier, “Dual-Gated WTe₂/MoSe₂ van der Waals tandem solar cells,” *J. Phys. Chem. C* **122**, 28545–28549 (2018).
- ¹³⁶S. Lin, X. Li, P. Wang, Z. Xu, S. Zhang, H. Zhong, Z. Wu, W. Xu, and H. Chen, “Interface designed MoS₂/GaAs heterostructure solar cell with sandwich stacked hexagonal boron nitride,” *Sci. Rep.* **5**, 15103 (2015).
- ¹³⁷X. Wang, X. Zhao, C. Hu, Y. Zhang, B. Song, L. Zhang, W. Liu, Z. Lv, Y. Zhang, J. Tang, Y. Sui, and B. Song, “Large lateral photovoltaic effect with ultrafast relaxation time in SnSe/Si junction,” *Appl. Phys. Lett.* **109**, 023502 (2016).
- ¹³⁸S. G. Kim, S. H. Kim, J. Park, G. S. Kim, J. H. Park, K. C. Saraswat, J. Kim, and H. Y. Yu, “Infrared detectable MoS₂ phototransistor and its application to artificial multilevel optic-neural synapse,” *ACS Nano* **13**, 10294–10300 (2019).
- ¹³⁹K. F. Mak and J. Shan, “Photonics and optoelectronics of 2D semiconductor transition metal dichalcogenides,” *Nat. Photonics* **10**, 216–226 (2016).
- ¹⁴⁰C. Xia, J. Li, X. Congxin, and L. Jongbo, “Recent advances in optoelectronic properties and applications of two-dimensional metal chalcogenides,” *J. Semicond.* **37**, 051001 (2016).
- ¹⁴¹J. S. Ross, P. Klement, A. M. Jones, N. J. Ghimire, J. Yan, D. G. Mandrus, T. Taniguchi, K. Watanabe, K. Kitamura, W. Yao, D. H. Cobden, and X. Xu, “Electrically tunable excitonic light-emitting diodes based on monolayer WSe₂p-n junctions,” *Nat. Nanotechnol.* **9**, 268–272 (2014).
- ¹⁴²R. S. Sundaram, M. Engel, A. Lombardo, R. Krupke, A. C. Ferrari, P. Avouris, and M. Steiner, “Electroluminescence in single layer MoS₂,” *Nano Lett.* **13**, 1416–1421 (2013).
- ¹⁴³S. Jo, N. Ubrig, H. Berger, A. B. Kuzmenko, and A. F. Morpurgo, “Mono- and bilayer WS₂ light-emitting transistors,” *Nano Lett.* **14**, 2019–2025 (2014).
- ¹⁴⁴E. Ponomarev, I. Gutiérrez-Lezama, N. Ubrig, and A. F. Morpurgo, “ambipolar light-emitting transistors on chemical vapor deposited monolayer MoS₂,” *Nano Lett.* **15**, 8289–8294 (2015).
- ¹⁴⁵J. Pu, T. Fujimoto, Y. Ohasi, S. Kimura, C.-H. Chen, L.-J. Li, T. Sakanoue, and T. Takenobu, “A versatile and simple approach to generate light emission in semiconductors mediated by electric double layers,” *Adv. Mater.* **29**, 1606918 (2017).
- ¹⁴⁶H. Zhao, Y. Zhao, Y. Song, M. Zhou, W. Lv, L. Tao, Y. Feng, B. Song, Y. Ma, J. Zhang, J. Xiao, Y. Wang, D. H. Lien, M. Amani, H. Kim, X. Chen, Z. Wu, Z. Ni, P. Wang, Y. Shi, H. Ma, X. Zhang, J. Bin Xu, A. Troisi, A. Javey, and X. Wang, “Strong optical response and light emission from a monolayer molecular crystal,” *Nat. Commun.* **10**, 5589 (2019).
- ¹⁴⁷D. H. Lien, M. Amani, S. B. Desai, G. H. Ahn, K. Han, J. H. He, J. W. Ager, M. C. Wu, and A. Javey, “Large-area and bright pulsed electroluminescence in monolayer semiconductors,” *Nat. Commun.* **9**, 1229 (2018).
- ¹⁴⁸O. Lopez-Sanchez, E. Alarcón Llado, V. Koman, A. Fontcuberta I Morral, A. Radenovic, and A. Kis, “Light generation and harvesting in a van der Waals heterostructure,” *ACS Nano* **8**, 3042–3048 (2014).
- ¹⁴⁹D. Li, R. Cheng, H. Zhou, C. Wang, A. Yin, Y. Chen, N. O. Weiss, Y. Huang, and X. Duan, “Electric-field-induced strong enhancement of electroluminescence in multilayer molybdenum disulfide,” *Nat. Commun.* **6**, 8509 (2015).
- ¹⁵⁰J. S. Ross, P. Rivera, J. Schaibley, E. Lee-Wong, H. Yu, T. Taniguchi, K. Watanabe, J. Yan, D. Mandrus, D. Cobden, W. Yao, and X. Xu, “Interlayer exciton optoelectronics in a 2D heterostructure p-n junction,” *Nano Lett.* **17**, 638–643 (2017).
- ¹⁵¹J. Binder, J. Howarth, F. Withers, M. R. Molas, T. Taniguchi, K. Watanabe, C. Faugeras, A. Wyszomolek, M. Danovich, V. I. Fal’ko, A. K. Geim, K. S. Novoselov, M. Potemski, and A. Kozikov, “Upconverted electroluminescence via Auger scattering of interlayer excitons in van der Waals heterostructures,” *Nat. Commun.* **10**, 2335 (2019).
- ¹⁵²F. Withers, O. Del Pozo-Zamudio, A. Mishchenko, A. P. Rooney, A. Gholinia, K. Watanabe, T. Taniguchi, S. J. Haigh, A. K. Geim, A. I. Tartakovskii, and K. S. Novoselov, “Light-emitting diodes by band-structure engineering in van der Waals heterostructures,” *Nat. Mater.* **14**, 301–306 (2015).
- ¹⁵³F. Withers, O. Del Pozo-Zamudio, S. Schwarz, S. Dufferwiel, P. M. Walker, T. Godde, A. P. Rooney, A. Gholinia, C. R. Woods, P. Blake, S. J. Haigh, K. Watanabe, T. Taniguchi, I. L. Aleiner, A. K. Geim, V. I. Fal’ko, A. I. Tartakovskii, and K. S. Novoselov, “WSe₂ light-emitting tunneling transistors with enhanced brightness at room temperature,” *Nano Lett.* **15**, 8223–8228 (2015).
- ¹⁵⁴C. H. Liu, G. Clark, T. Fryett, S. Wu, J. Zheng, F. Hatami, X. Xu, and A. Majumdar, “Nanocavity integrated van der Waals heterostructure light-emitting tunneling diode,” *Nano Lett.* **17**, 200–205 (2017).
- ¹⁵⁵S. Wang, J. Wang, W. Zhao, F. Giustiniano, L. Chu, I. Verzhbitskiy, J. Zhou Yong, and G. Eda, “Efficient carrier-to-exciton conversion in field emission tunnel diodes based on MIS-type van der Waals heterostack,” *Nano Lett.* **17**, 5156–5162 (2017).
- ¹⁵⁶J. Wang, F. Lin, I. Verzhbitskiy, K. Watanabe, T. Taniguchi, J. Martin, and G. Eda, “Polarity tunable trionic electroluminescence in monolayer WSe₂,” *Nano Lett.* **19**, 7470–7475 (2019).
- ¹⁵⁷M. Paur, A. J. Molina-Mendoza, R. Bratschitsch, K. Watanabe, T. Taniguchi, and T. Mueller, “Electroluminescence from multi-particle exciton complexes in transition metal dichalcogenide semiconductors,” *Nat. Commun.* **10**, 1709 (2019).
- ¹⁵⁸Y. J. Zhang, T. Oka, R. Suzuki, J. T. Ye, and Y. Iwasa, “Electrically switchable chiral light-emitting transistor,” *Science* **344**, 725–728 (2014).
- ¹⁵⁹W. Yang, J. Shang, J. Wang, X. Shen, B. Cao, N. Peimiyoo, C. Zou, Y. Chen, Y. Wang, C. Cong, W. Huang, and T. Yu, “Electrically tunable valley-light emitting diode (vLED) based on CVD-grown monolayer WS₂,” *Nano Lett.* **16**, 1560–1567 (2016).
- ¹⁶⁰M. Onga, Y. Zhang, R. Suzuki, and Y. Iwasa, “High circular polarization in electroluminescence from MoSe₂,” *Appl. Phys. Lett.* **108**, 073107 (2016).
- ¹⁶¹Y. Ye, J. Xiao, H. Wang, Z. Ye, H. Zhu, M. Zhao, Y. Wang, J. Zhao, X. Yin, and X. Zhang, “Electrical generation and control of the valley carriers in a monolayer transition metal dichalcogenide,” *Nat. Nanotechnol.* **11**, 598–602 (2016).
- ¹⁶²O. L. Sanchez, D. Ovchinnikov, S. Misra, A. Allain, and A. Kis, “Valley polarization by spin injection in a light-emitting van der Waals heterojunction,” *Nano Lett.* **16**, 5792–5797 (2016).
- ¹⁶³S. Schwarz, A. Kozikov, F. Withers, J. K. Maguire, A. P. Foster, S. Dufferwiel, L. Hague, M. N. Makhonin, L. R. Wilson, A. K. Geim, K. S. Novoselov, and A. I. Tartakovskii, “Electrically pumped single-defect light emitters in WSe₂,” *2D Mater.* **3**, 025038 (2016).
- ¹⁶⁴G. Clark, J. R. Schaibley, J. Ross, T. Taniguchi, K. Watanabe, J. R. Hendrickson, S. Mou, W. Yao, and X. Xu, “Single defect light-emitting diode in a van der Waals heterostructure,” *Nano Lett.* **16**, 3944–3948 (2016).
- ¹⁶⁵C. Palacios-Berraquero, M. Barbone, D. M. Kara, X. Chen, I. Goykhman, D. Yoon, A. K. Ott, J. Beitner, K. Watanabe, T. Taniguchi, A. C. Ferrari, and M. Atatüre, “Atomically thin quantum light-emitting diodes,” *Nat. Commun.* **7**, 12978 (2016).
- ¹⁶⁶W. Li, B. Chen, C. Meng, W. Fang, Y. Xiao, X. Li, Z. Hu, Y. Xu, L. Tong, H. Wang, W. Liu, J. Bao, and Y. R. Shen, “Ultrafast all-optical graphene modulator,” *Nano Lett.* **14**, 955 (2014).
- ¹⁶⁷J. Leuthold, C. Koos, W. Freude, L. Alloati, R. Palmer, D. Korn, J. Pfeifle, M. Laueremann, R. Dinu, S. Wehrli, M. Jazbinsek, P. Gunter, M. Waldow, T. Wahlbrink, J. Bolten, M. Fournier, J. M. Fedeli, W. Bogaerts, and H. Yu, “High-speed, low-power optical modulators in silicon,” in International Conference on Transparent Optical Networks (2013).
- ¹⁶⁸Z. Sun, A. Martinez, and F. Wang, “Optical modulators with 2D layered materials,” *Nat. Photonics* **10**, 227 (2016).
- ¹⁶⁹R. Hao, J. Jiao, X. Peng, Z. Shen, R. Dagarbek, Y. Zou, and E. Li, “Experimental demonstration of a graphene-based hybrid plasmonic modulator,” *Opt. Lett.* **44**, 2586 (2019).
- ¹⁷⁰C. Zhong, J. Li, and H. Lin, “Graphene-based all-optical modulators,” *Front. Optoelectron.* **13**, 114 (2020).

- ¹⁷¹S. Yu, X. Wu, Y. Wang, X. Guo, and L. Tong, "2D Materials for Optical Modulation: Challenges and Opportunities," *Adv. Mater.* **29**, 1606128 (2017).
- ¹⁷²Y. Yu, Y. Yu, L. Huang, H. Peng, L. Xiong, and L. Cao, "Giant gating tunability of optical refractive index in transition metal dichalcogenide monolayers," *Nano Lett.* **17**, 3613 (2017).
- ¹⁷³V. G. Kravets, F. Wu, G. H. Auton, T. Yu, S. Imaizumi, and A. N. Grigorenko, "Measurements of electrically tunable refractive index of MoS₂ monolayer and its usage in optical modulators," *npj 2D Mater. Appl.* **3**, 36 (2019).
- ¹⁷⁴S. Joshi and B. K. Kaushik, "Transition metal dichalcogenides integrated waveguide modulator and attenuator in silicon nitride platform," *Nanotechnology* **31**, 435202 (2020).
- ¹⁷⁵B. Li, S. Zu, J. Zhou, Q. Jiang, B. Du, H. Shan, Y. Luo, Z. Liu, X. Zhu, and Z. Fang, "Single-nanoparticle plasmonic electro-optic modulator based on MoS₂ monolayers," *ACS Nano* **11**, 9720 (2017).
- ¹⁷⁶B. Lee, W. Liu, C. H. Naylor, J. Park, S. C. Malek, J. S. Berger, A. T. C. Johnson, and R. Agarwal, "Electrical tuning of exciton-plasmon polariton coupling in monolayer MoS₂ integrated with plasmonic nanoantenna lattice," *Nano Lett.* **17**, 4541–4547 (2017).
- ¹⁷⁷H. S. Lee, D. H. Luong, M. S. Kim, Y. Jin, H. Kim, S. Yun, and Y. H. Lee, "Reconfigurable exciton-plasmon interconversion for nanophotonic circuits," *Nat. Commun.* **7**, 13663 (2016).
- ¹⁷⁸I. Datta, S. H. Chae, G. R. Bhatt, M. A. Tadayon, B. Li, Y. Yu, C. Park, J. Park, L. Cao, D. N. Basov, J. Hone, and M. Lipson, "Low-loss composite photonic platform based on 2D semiconductor monolayers," *Nat. Photonics* **14**, 256 (2020).
- ¹⁷⁹C. Lin, R. Grassi, T. Low, and A. S. Helmy, "Multilayer black phosphorus as a versatile mid-infrared electro-optic material," *Nano Lett.* **16**, 1683 (2016).
- ¹⁸⁰W. S. Whitney, M. C. Sherrott, D. Jariwala, W. H. Lin, H. A. Bechtel, G. R. Rossman, and H. A. Atwater, "Field effect optoelectronic modulation of quantum-confined carriers in black phosphorus," *Nano Lett.* **17**, 78 (2020).
- ¹⁸¹R. Peng, K. Khaliji, N. Youngblood, R. Grassi, T. Low, and M. Li, "Midinfrared electro-optic modulation in few-layer black phosphorus," *Nano Lett.* **17**, 6315 (2017).
- ¹⁸²M. C. Sherrott, W. S. Whitney, D. Jariwala, S. Biswas, C. M. Went, J. Wong, G. R. Rossman, and H. A. Atwater, "Anisotropic quantum well electro-optics in few-layer black phosphorus," *Nano Lett.* **19**, 269 (2019).
- ¹⁸³M. Liu, X. Yin, E. Ulin-Avila, B. Geng, T. Zentgraf, L. Ju, F. Wang, and X. Zhang, "A graphene-based broadband optical modulator," *Nature* **474**, 64–67 (2011).
- ¹⁸⁴M. Li, J. Ling, Y. He, U. A. Javid, S. Xue, and Q. Lin, "Lithium niobate photonic-crystal electro-optic modulator," *Nat. Commun.* **11**, 4123 (2020).
- ¹⁸⁵J.-H. H. Han, F. Boeuf, J. Fujikata, S. Takahashi, S. Takagi, and M. Takenaka, "Efficient low-loss InGaAsP/Si hybrid MOS optical modulator," *Nat. Photonics* **11**, 486–490 (2017).
- ¹⁸⁶D. Vella, D. Ovchinnikov, N. Martino, V. Vega-Mayoral, D. Dumcenco, Y. C. Kung, M. R. Antognazza, A. Kis, G. Lanzani, D. Mihailovic, and C. Gadermaier, "Unconventional electroabsorption in monolayer MoS₂," *2D Mater.* **4**, 021005 (2017).
- ¹⁸⁷M. Mohsin, D. Schall, M. Otto, A. Noculak, D. Neumaier, and H. Kurz, "Graphene based low insertion loss electro-absorption modulator on SOI waveguide," *Opt. Express* **22**, 15292 (2014).
- ¹⁸⁸M. Liu, X. Yin, and X. Zhang, "Double-layer graphene optical modulator," *Nano Lett.* **12**, 1482–1485 (2012).
- ¹⁸⁹Y. Ding, X. Zhu, S. Xiao, H. Hu, L. H. Frandsen, N. A. Mortensen, and K. Yvind, "Effective electro-optical modulation with high extinction ratio by a graphene-silicon microring resonator," *Nano Lett.* **15**, 4393–4400 (2015).
- ¹⁹⁰C. T. Phare, Y. H. Daniel Lee, J. Cardenas, and M. Lipson, "Graphene electro-optic modulator with 30 GHz bandwidth," *Nat. Photonics* **9**, 511–514 (2015).
- ¹⁹¹Y. Gao, R.-J. J. Shiue, X. Gan, L. Li, C. Peng, I. Meric, L. Wang, A. Szep, D. Walker, J. Hone, and D. Englund, "High-speed electro-optic modulator integrated with graphene-boron nitride heterostructure and photonic crystal nanocavity," *Nano Lett.* **15**, 2001–2005 (2015).
- ¹⁹²M. M. Badr, M. Y. Abdelatty, and M. A. Swillam, "Ultra-fast silicon electro-optic modulator based on ITO-integrated directional coupler," *Phys. Scr.* **94**, 065502 (2019).
- ¹⁹³M. Streshinsky, R. Ding, Y. Liu, A. Novack, Y. Yang, Y. Ma, X. Tu, E. K. S. Chee, A. E.-J. Lim, P. G.-Q. Lo, T. Baehr-Jones, and M. Hochberg, "Low power 50 Gb/s silicon traveling wave Mach-Zehnder modulator near 1300 nm," *Opt. Express* **21**, 30350 (2013).
- ¹⁹⁴C. Haffner, W. Heni, Y. Fedoryshyn, J. Niegemann, A. Melikyan, D. L. Elder, B. Baeuerle, Y. Salamin, A. Josten, U. Koch, C. Hoessbacher, F. Ducry, L. Juchli, A. Emboras, D. Hillerkuss, M. Kohl, L. R. Dalton, C. Hafner, and J. Leuthold, "All-plasmonic Mach-Zehnder modulator enabling optical high-speed communication at the microscale," *Nat. Photonics* **9**, 525–528 (2015).
- ¹⁹⁵Z. Meng, R. M. Stolz, L. Mendecki, and K. A. Mirica, "Electrically-transduced chemical sensors based on two-dimensional nanomaterials," *Chem. Rev.* **119**, 478–598 (2019).
- ¹⁹⁶D. J. Buckley, N. C. G. Black, E. G. Castanon, C. Melios, M. Hardman, and O. Kazakova, "Frontiers of graphene and 2D material-based gas sensors for environmental monitoring," *2D Mater.* **7**, 032002 (2020).
- ¹⁹⁷Y. Peng, M. Que, J. Tao, X. Wang, J. Lu, G. Hu, B. Wan, Q. Xu, and C. Pan, "Progress in piezotronic and piezo-phototronic effect of 2D materials," *2D Mater.* **5**, 042003 (2018).
- ¹⁹⁸See <https://www.graphenea.com/blogs/graphene-news/graphene-field-effect-transistors-for-chemical-sensing> for Graphenea.
- ¹⁹⁹S. G. Noyce, J. L. Doherty, S. Zauscher, and A. D. Franklin, "Understanding and mapping sensitivity in MoS₂ field-effect-transistor-based sensors," *ACS Nano* **14**, 11637–11647 (2020).
- ²⁰⁰UNEP, <https://unece.org/gothenburg-protocol> for Gothenburg Protocol, 1999 (last accessed January 10, 2021).
- ²⁰¹United Nations: Climate Change, <https://unfccc.int/process-and-meetings/the-paris-agreement/the-paris-agreement> for The Paris Agreement (last accessed January 10, 2021).
- ²⁰²H. Li, J. Wu, Z. Yin, and H. Zhang, "Preparation and applications of mechanically exfoliated single-layer and multilayer MoS₂ and WSe₂ nanosheets," *Acc. Chem. Res.* **47**, 1067–1075 (2014).
- ²⁰³H. Li, Z. Yin, Q. He, H. Li, X. Huang, G. Lu, D. W. H. Fam, A. I. Y. Tok, Q. Zhang, and H. Zhang, "Fabrication of single- and multilayer MoS₂ film-based field-effect transistors for sensing NO at room temperature," *Small* **8**, 63–67 (2012).
- ²⁰⁴D. J. Late, Y. K. Huang, B. Liu, J. Acharya, S. N. Shirodkar, J. Luo, A. Yan, D. Charles, U. V. Waghmare, V. P. Dravid, and C. N. R. Rao, "Sensing behavior of atomically thin-layered MoS₂ transistors," *ACS Nano* **7**, 4879–4891 (2013).
- ²⁰⁵K. Lee, R. Gatenby, N. McEvoy, T. Hallam, and G. S. Duesberg, "High-performance sensors based on molybdenum disulfide thin films," *Adv. Mater.* **25**, 6699–6702 (2013).
- ²⁰⁶Q. He, Z. Zeng, Z. Yin, H. Li, S. Wu, X. Huang, and H. Zhang, "Fabrication of flexible MoS₂ thin-film transistor arrays for practical gas-sensing applications," *Small* **8**, 2994–2999 (2012).
- ²⁰⁷R. Kumar, N. Goel, and M. Kumar, "UV-activated MoS₂ based fast and reversible NO₂ sensor at room temperature," *ACS Sens.* **2**, 1744–1752 (2017).
- ²⁰⁸H. Long, A. Harley-Trochimczyk, T. Pham, Z. Tang, T. Shi, A. Zettl, C. Carraro, M. A. Worsley, and R. Maboudian, "High surface area MoS₂/graphene hybrid aerogel for ultrasensitive NO₂ detection," *Adv. Funct. Mater.* **26**, 5158–5165 (2016).
- ²⁰⁹C. Kuru, C. Choi, A. Kargar, D. Choi, Y. J. Kim, C. H. Liu, S. Yavuz, and S. Jin, "MoS₂ Nanosheet-Pd nanoparticle composite for highly sensitive room temperature detection of hydrogen," *Adv. Sci.* **2**, 1500004 (2015).
- ²¹⁰C. H. Park, W. T. Koo, Y. J. Lee, Y. H. Kim, J. Lee, J. S. Jang, H. Yun, I. D. Kim, and B. J. Kim, "Hydrogen sensors based on MoS₂ hollow architectures assembled by pickering emulsion," *ACS Nano* **14**, 9652–9661 (2020).
- ²¹¹N. Yu, L. Wang, M. Li, X. Sun, T. Hou, and Y. Li, "Molybdenum disulfide as a highly efficient adsorbent for non-polar gases," *Phys. Chem. Chem. Phys.* **17**, 11700–11704 (2015).
- ²¹²D. Zhong, C. Jiang, P. Li, and Y. Sun, "Layer-by-layer self-assembly of Co₃O₄ nanorod-decorated MoS₂ nanosheet-based nanocomposite toward high-performance ammonia detection," *ACS Appl. Mater. Interfaces* **9**, 6462–6471 (2017).
- ²¹³D. Zhang, Y. Sun, C. Jiang, and Y. Zhang, "Room temperature hydrogen gas sensor based on palladium decorated tin oxide/molybdenum disulfide ternary hybrid via hydrothermal route," *Sens. Actuators, B* **242**, 15–24 (2017).
- ²¹⁴E. Wu, Y. Xie, B. Yuan, H. Zhang, X. Hu, J. Liu, and D. Zhang, "Ultrasensitive and fully reversible NO₂ gas sensing based on p-type MoTe₂ under ultraviolet illumination," *ACS Sens.* **3**, 1719–1726 (2018).

- ²¹⁵A. N. Abbas, B. Liu, L. Chen, Y. Ma, S. Cong, N. Aroonyadet, M. Köpf, T. Nilges, and C. Zhou, "Black phosphorus gas sensors," *ACS Nano* **9**, 5618–5624 (2017).
- ²¹⁶J. Zhao, N. Li, H. Yu, Z. Wei, M. Liao, P. Chen, S. Wang, D. Shi, Q. Sun, and G. Zhang, "Highly sensitive MoS₂ humidity sensors array for noncontact sensation," *Adv. Mater.* **29**, 1702076 (2017).
- ²¹⁷X. Li, X. Li, Z. Li, J. Wang, and J. Zhang, "WS₂ nanoflakes based selective ammonia sensors at room temperature," *Sens. Actuators, B* **240**, 273–277 (2017).
- ²¹⁸D. Liu, Z. Tang, and Z. Zhang, "Comparative study on NO₂ and H₂S sensing mechanisms of gas sensors based on WS₂ nanosheets," *Sens. Actuators, B* **303**, 127114 (2020).
- ²¹⁹S.-Y. Tang, C.-C. Yang, T.-Y. Su, T.-Y. Yang, S.-C. Wu, Y.-C. Hsu, Y.-Z. Chen, T.-N. Lin, J.-L. Shen, H.-N. Lin, P.-W. Chiu, H.-C. Kuo, and Y.-L. Chueh, "Design of core-shell quantum dots-3D WS₂ nanowall hybrid nanostructures with high-performance bifunctional sensing applications," *ACS Nano* **14**, 12668–12678 (2020).
- ²²⁰J. Z. Ou, W. Ge, B. Carey, T. Daeneke, A. Rotbart, W. Shan, Y. Wang, Z. Fu, A. F. Chrimes, W. Wlodarski, S. P. Russo, Y. X. Li, and K. Kalantar-Zadeh, "Physisorption-based charge transfer in two-dimensional SnS₂ for selective and reversible NO₂ gas sensing," *ACS Nano* **9**, 10313–10323 (2015).
- ²²¹Y. Kim, K. C. Kwon, S. Kang, C. Kim, T. H. Kim, S. P. Hong, S. Y. Park, J. M. Suh, M. J. Choi, S. Han, and H. W. Jang, "Two-dimensional NbS₂ gas sensors for selective and reversible NO₂ detection at room temperature," *ACS Sens.* **4**, 2395–2402 (2019).
- ²²²A. Azizi, M. Dogan, H. Long, J. D. Cain, K. Lee, R. Eskandari, A. Varieschi, E. C. Glazer, M. L. Cohen, and A. Zettl, "High-performance atomically-thin room-temperature NO₂ sensor," *Nano Lett.* **20**, 6120–6127 (2020).
- ²²³L. Kou, T. Frauenheim, and C. Chen, "Phosphorene as a superior gas sensor: Selective adsorption and distinct I-V response," *J. Phys. Chem. Lett.* **5**, 2675–2681 (2014).
- ²²⁴H. Liu, K. Hu, D. Yan, R. Chen, Y. Zou, H. Liu, and S. Wang, "Recent advances on black phosphorus for energy storage, catalysis, and sensor applications," *Adv. Mater.* **30**, 1800295 (2018).
- ²²⁵G. Lee, S. Jung, S. Jang, and J. Kim, "Platinum-functionalized black phosphorus hydrogen sensors," *Appl. Phys. Lett.* **110**, 242103 (2017).
- ²²⁶C. C. Mayorga-Martinez, Z. Sofer, and M. Pumera, "Layered black phosphorus as a selective vapor sensor," *Angew. Chem.* **127**, 14525–14528 (2015).
- ²²⁷N. Liu and S. Zhou, "Gas adsorption on monolayer blue phosphorus: Implications for environmental stability and gas sensors," *Nanotechnology* **28**, 175708 (2017).
- ²²⁸F. A. L. De Souza, G. Sivaraman, J. Hertkorn, R. G. Amorim, M. Fyta, and W. L. Scopel, "Hybrid 2D nanodevices (graphene/h-BN): Selecting NO: X gas through the device interface," *J. Mater. Chem. A* **7**, 8905–8911 (2019).
- ²²⁹A. R. Cadore, E. Mania, A. B. Alencar, N. P. Rezende, S. de Oliveira, K. Watanabe, T. Taniguchi, H. Chacham, L. C. Campos, and R. G. Lacerda, "Enhancing the response of NH₃ graphene-sensors by using devices with different graphene-substrate distances," *Sens. Actuators, B* **266**, 438–446 (2018).
- ²³⁰W. Y. Chen, S. Lai, C. Yen, X. Jiang, D. Peroulis, and L. A. Stanciu, "Surface functionalization of Ti₃C₂T_xMXene with highly reliable superhydrophobic protection for volatile organic compounds sensing," *ACS Nano* **14**, 11490 (2020).
- ²³¹European Environmental Agency, "Air quality in Europe—2018," Report No. 12/2018, 2018.
- ²³²United States Environmental Protection Agency, <https://www.epa.gov/criteria-air-pollutants/naaqs-table> for "National Ambient Air Quality Standards (NAAQS) Pollutants Table," 2016 (last accessed January 11, 2021).
- ²³³D. Zhang, Y. Sun, P. Li, and Y. Zhang, "Facile fabrication of MoS₂-modified SnO₂ hybrid nanocomposite for ultrasensitive humidity sensing," *ACS Appl. Mater. Interfaces* **8**, 14142–14149 (2016).
- ²³⁴H. Guo, C. Lan, Z. Zhou, P. Sun, D. Wei, and C. Li, "Transparent, flexible, and stretchable WS₂ based humidity sensors for electronic skin," *Nanoscale* **9**, 6246–6253 (2017).
- ²³⁵J. Feng, L. Peng, C. Wu, X. Sun, S. Hu, C. Lin, J. Dai, J. Yang, and Y. Xie, "Giant moisture responsiveness of VS₂ ultrathin nanosheets for novel touchless positioning interface," *Adv. Mater.* **24**, 1969–1974 (2012).
- ²³⁶P. Yasaee, A. Behranginia, T. Foroozan, M. Asadi, K. Kim, F. Khalili-Araghi, and A. Salehi-Khojin, "Stable selective humidity sensing using stacked black phosphorus flakes," *ACS Nano* **9**, 9898–9905 (2015).
- ²³⁷P. Bollella, G. Fusco, C. Tortolini, G. Sanzò, G. Favero, L. Gorton, and R. Antiochia, "Beyond graphene: Electrochemical sensors and biosensors for biomarkers detection," *Biosens. Bioelectron.* **89**, 152–166 (2017).
- ²³⁸C. Zhu, D. Du, and Y. Lin, "Graphene-like 2D nanomaterial-based biointerfaces for biosensing applications," *Biosens. Bioelectron.* **89**, 43–55 (2017).
- ²³⁹Y. Hu, Y. Huang, C. Tan, X. Zhang, Q. Lu, M. Sindoro, X. Huang, W. Huang, L. Wang, and H. Zhang, "Two-dimensional transition metal dichalcogenide nanomaterials for biosensing applications," *Mater. Chem. Front.* **1**, 24–36 (2017).
- ²⁴⁰J. Kou, E. P. Nguyen, A. Merkoçi, and Z. Guo, "2-dimensional materials-based electrical/optical platforms for smart on-off diagnostics applications," *2D Mater.* **7**, 032001 (2020).
- ²⁴¹R. Lv, J. A. Robinson, R. E. Schaak, D. Sun, Y. Sun, T. E. Mallouk, and M. Terrones, "Transition metal dichalcogenides and beyond: Synthesis, properties, and applications of single- and few-layer nanosheets," *Acc. Chem. Res.* **48**, 56–64 (2015).
- ²⁴²Y. Huang, J. Guo, Y. Kang, Y. Ai, and C. M. Li, "Two dimensional atomically thin MoS₂ nanosheets and their sensing applications," *Nanoscale* **7**, 19358–19376 (2015).
- ²⁴³K. Kalantar-Zadeh and J. Z. Ou, "Biosensors based on two-dimensional MoS₂," *ACS Sens.* **1**, 5–16 (2016).
- ²⁴⁴X. Chen, Y. J. Park, M. Kang, S. K. Kang, J. Koo, S. M. Shinde, J. Shin, S. Jeon, G. Park, Y. Yan, M. R. MacEwan, W. Z. Ray, K. M. Lee, J. A. Rogers, and J. H. Ahn, "CVD-grown monolayer MoS₂ in bioabsorbable electronics and biosensors," *Nat. Commun.* **9**, 1690 (2018).
- ²⁴⁵H. Nam, B.-R. Oh, M. Chen, S. Wi, D. Li, K. Kurabayashi, and X. Liang, "Fabrication and comparison of MoS₂ and WSe₂ field-effect transistor biosensors," *J. Vac. Sci. Technol. B* **33**, 06FG01 (2015).
- ²⁴⁶W. Zhang, P. Zhang, Z. Su, and G. Wei, "Synthesis and sensor applications of MoS₂-based nanocomposites," *Nanoscale* **7**, 18364–18378 (2015).
- ²⁴⁷J. Liu, X. Chen, Q. Wang, M. Xiao, D. Zhong, W. Sun, G. Zhang, and Z. Zhang, "Ultrasensitive monolayer MoS₂ field-effect transistor based DNA sensors for screening of down syndrome," *Nano Lett.* **19**, 1437–1444 (2019).
- ²⁴⁸D. Sarkar, W. Liu, X. Xie, A. C. Anselmo, S. Mitragotri, and K. Banerjee, "MoS₂ field-effect transistor for next-generation label-free biosensors," *ACS Nano* **8**, 3992–4003 (2014).
- ²⁴⁹Y. Wang, G. Ning, H. Bi, Y. Wu, G. Liu, and Y. Zhao, "A novel ratiometric electrochemical assay for ochratoxin A coupling Au nanoparticles decorated MoS₂ nanosheets with aptamer," *Electrochim. Acta* **285**, 120–127 (2018).
- ²⁵⁰N. Hao, Z. Dai, X. Meng, R. Hua, J. Lu, and K. Wang, "A portable solar-driven ratiometric photo-electrochromic visualization biosensor for detection of ochratoxin A," *Sens. Actuators, B* **306**, 127594 (2020).
- ²⁵¹X. Wang, C. Chu, L. Shen, W. Deng, M. Yan, S. Ge, J. Yu, and X. Song, "An ultrasensitive electrochemical immunosensor based on the catalytic activity of MoS₂-Au composite using Ag nanospheres as labels," *Sens. Actuators, B* **206**, 30–36 (2015).
- ²⁵²M. Cheng, X. Zhang, M. Wang, H. Huang, and J. Ma, "A facile electrochemical sensor based on well-dispersed graphene-molybdenum disulfide modified electrode for highly sensitive detection of dopamine," *J. Electroanal. Chem.* **786**, 1–7 (2017).
- ²⁵³L. Wang, Y. Wang, J. I. Wong, T. Palacios, J. Kong, and H. Y. Yang, "Functionalized MoS₂ nanosheet-based field-effect biosensor for label-free sensitive detection of cancer marker proteins in solution," *Small* **10**, 1101–1105 (2014).
- ²⁵⁴J. Lee, P. Dak, Y. Lee, H. Park, W. Choi, M. A. Alam, and S. Kim, "Two-dimensional layered MoS₂ biosensors enable highly sensitive detection of biomolecules," *Sci. Rep.* **4**, 7352 (2014).
- ²⁵⁵H. Nam, B. R. Oh, P. Chen, M. Chen, S. Wi, W. Wan, K. Kurabayashi, and X. Liang, "Multiple MoS₂ transistors for sensing molecule interaction kinetics," *Sci. Rep.* **5**, 10546 (2015).
- ²⁵⁶H. Nam, B. R. Oh, P. Chen, J. S. Yoon, S. Wi, M. Chen, K. Kurabayashi, and X. Liang, "Two different device physics principles for operating MoS₂ transistor biosensors with femtomolar-level detection limits," *Appl. Phys. Lett.* **107**, 012105 (2015).
- ²⁵⁷N. Rohaizad, C. C. Mayorga-Martinez, Z. Sofer, and M. Pumera, "1T-phase transition metal dichalcogenides (MoS₂, MoSe₂, WS₂, and WSe₂) with fast

- heterogeneous electron transfer: Application on second-generation enzyme-based biosensor,” *ACS Appl. Mater. Interfaces* **9**, 40697–40706 (2017).
- ²⁵⁸S. Su, H. Sun, F. Xu, L. Yuwen, C. Fan, and L. Wang, “Direct electrochemistry of glucose oxidase and a biosensor for glucose based on a glass carbon electrode modified with MoS₂ nanosheets decorated with gold nanoparticles,” *Microchim. Acta* **181**, 1497–1503 (2014).
- ²⁵⁹J. Huang, Z. Dong, Y. Li, J. Li, W. Tang, H. Yang, J. Wang, Y. Bao, J. Jin, and R. Li, “MoS₂ nanosheet functionalized with Cu nanoparticles and its application for glucose detection,” *Mater. Res. Bull.* **48**, 4544–4547 (2013).
- ²⁶⁰S. Wu, Z. Zeng, Q. He, Z. Wang, S. J. Wang, Y. Du, Z. Yin, X. Sun, W. Chen, and H. Zhang, “Electrochemically reduced single-layer MoS₂ nanosheets: Characterization, properties, and sensing applications,” *Small* **8**, 2264–2270 (2012).
- ²⁶¹S. Ji, Z. Yang, C. Zhang, Y. E. Miao, W. W. Tjiu, J. Pan, and T. Liu, “Nonenzymatic sensor for glucose based on a glassy carbon electrode modified with Ni(OH)₂ nanoparticles grown on a film of molybdenum sulfide,” *Microchim. Acta* **180**, 1127–1134 (2013).
- ²⁶²A. Sarkar, A. B. Ghosh, N. Saha, G. R. Bhadu, and B. Adhikary, “Newly designed amperometric biosensor for hydrogen peroxide and glucose based on vanadium sulfide nanoparticles,” *ACS Appl. Nano Mater.* **1**, 1339–1347 (2018).
- ²⁶³G. X. Wang, W. J. Bao, J. Wang, Q. Q. Lu, and X. H. Xia, “Immobilization and catalytic activity of horseradish peroxidase on molybdenum disulfide nanosheets modified electrode,” *Electrochem. Commun.* **35**, 146–148 (2013).
- ²⁶⁴H. Song, Y. Ni, and S. Kokot, “Investigations of an electrochemical platform based on the layered MoS₂-graphene and horseradish peroxidase nanocomposite for direct electrochemistry and electrocatalysis,” *Biosens. Bioelectron.* **56**, 137–143 (2014).
- ²⁶⁵J. Yoon, T. Lee, B. Bapurao, J. Jo, B. K. Oh, and J. W. Choi, “Electrochemical H₂O₂ biosensor composed of myoglobin on MoS₂ nanoparticle-graphene oxide hybrid structure,” *Biosens. Bioelectron.* **93**, 14–20 (2017).
- ²⁶⁶T. Wang, H. Zhu, J. Zhuo, Z. Zhu, P. Papakonstantinou, G. Lubarsky, J. Lin, and M. Li, “Biosensor based on ultrasmall MoS₂ nanoparticles for electrochemical detection of H₂O₂ released by cells at the nanomolar level,” *Anal. Chem.* **85**, 10289–10295 (2013).
- ²⁶⁷J. Chao, M. Zou, C. Zhang, H. Sun, D. Pan, H. Pei, S. Su, L. Yuwen, C. Fan, and L. Wang, “A MoS₂-based system for efficient immobilization of hemoglobin and biosensing applications,” *Nanotechnology* **26**, 274005 (2015).
- ²⁶⁸Y. Lin, X. Chen, Y. Lin, Q. Zhou, and D. Tang, “Non-enzymatic sensing of hydrogen peroxide using a glassy carbon electrode modified with a nanocomposite made from carbon nanotubes and molybdenum disulfide,” *Microchim. Acta* **182**, 1803–1809 (2015).
- ²⁶⁹Y. Chen, C. Tan, H. Zhang, and L. Wang, “Two-dimensional graphene analogues for biomedical applications,” *Chem. Soc. Rev.* **44**, 2681–2701 (2015).
- ²⁷⁰S. Su, H. Sun, F. Xu, L. Yuwen, and L. Wang, “Highly sensitive and selective determination of dopamine in the presence of ascorbic acid using gold nanoparticles-decorated MoS₂ nanosheets modified electrode,” *Electroanalysis* **25**, 2523–2529 (2013).
- ²⁷¹H. Sun, J. Chao, X. Zuo, S. Su, X. Liu, L. Yuwen, C. Fan, and L. Wang, “Gold nanoparticle-decorated MoS₂ nanosheets for simultaneous detection of ascorbic acid, dopamine and uric acid,” *RSC Adv.* **4**, 27625–27629 (2014).
- ²⁷²K. J. Huang, J. Z. Zhang, Y. J. Liu, and L. L. Wang, “Novel electrochemical sensing platform based on molybdenum disulfide nanosheets-polyaniline composites and Au nanoparticles,” *Sens. Actuators, B* **194**, 303–310 (2014).
- ²⁷³X. Huang, C. Tan, Z. Yin, and H. Zhang, “25th anniversary article: Hybrid nanostructures based on two-dimensional nanomaterials,” *Adv. Mater.* **26**, 2185–2204 (2014).
- ²⁷⁴T. N. Narayanan, C. S. R. Vusa, and S. Alwarappan, “Selective and efficient electrochemical biosensing of ultrathin molybdenum disulfide sheets,” *Nanotechnology* **25**, 335702 (2014).
- ²⁷⁵C. De-Eknankul, X. Zhang, M. Q. Zhao, W. Huang, R. Liu, A. T. C. Johnson, and E. Cubukcu, “MoS₂-enabled dual-mode optoelectronic biosensor using a water soluble variant of μ -opioid receptor for opioid peptide detection,” *2D Mater.* **7**, 0104004 (2020).
- ²⁷⁶T. Yang, M. Chen, F. Nan, L. Chen, X. Luo, and K. Jiao, “Enhanced electro-polymerization of poly(xanthurenic acid)-MoS₂ film for specific electrocatalytic detection of guanine and adenine,” *J. Mater. Chem. B* **3**, 4884–4891 (2015).
- ²⁷⁷D. W. Lee, J. Lee, I. Y. Sohn, B. Y. Kim, Y. M. Son, H. Bark, J. Jung, M. Choi, T. H. Kim, C. Lee, and N. E. Lee, “Field-effect transistor with a chemically synthesized MoS₂ sensing channel for label-free and highly sensitive electrical detection of DNA hybridization,” *Nano Res.* **8**, 2340–2350 (2015).
- ²⁷⁸T. Yang, M. Chen, Q. Kong, X. Luo, and K. Jiao, “Toward DNA electrochemical sensing by free-standing ZnO nanosheets grown on 2D thin-layered MoS₂,” *Biosens. Bioelectron.* **89**, 538–544 (2017).
- ²⁷⁹T. Wang, R. Zhu, J. Zhuo, Z. Zhu, Y. Shao, and M. Li, “Direct detection of DNA below ppb level based on thionin-functionalized layered MoS₂ electrochemical sensors,” *Anal. Chem.* **86**, 12064–12069 (2014).
- ²⁸⁰J. Mei, Y. T. Li, H. Zhang, M. M. Xiao, Y. Ning, Z. Y. Zhang, and G. J. Zhang, “Molybdenum disulfide field-effect transistor biosensor for ultrasensitive detection of DNA by employing morpholino as probe,” *Biosens. Bioelectron.* **110**, 71–77 (2018).
- ²⁸¹D. Zhu, W. Liu, D. Zhao, Q. Hao, J. Li, J. Huang, J. Shi, J. Chao, S. Su, and L. Wang, “Label-free electrochemical sensing platform for microRNA-21 detection using thionine and gold nanoparticles co-functionalized MoS₂ Nanosheet,” *ACS Appl. Mater. Interfaces* **9**, 35597–35603 (2017).
- ²⁸²S. Su, H. Sun, W. Cao, J. Chao, H. Peng, X. Zuo, L. Yuwen, C. Fan, and L. Wang, “Dual-Target electrochemical biosensing based on DNA structural switching on gold nanoparticle-decorated MoS₂ nanosheets,” *ACS Appl. Mater. Interfaces* **8**, 6826–6833 (2016).
- ²⁸³S. Su, M. Zou, H. Zhao, C. Yuan, Y. Xu, C. Zhang, L. Wang, C. Fan, and L. Wang, “Shape-controlled gold nanoparticles supported on MoS₂ nanosheets: Synergistic effect of thionine and MoS₂ and their application for electrochemical label-free immunosensing,” *Nanoscale* **7**, 19129–19135 (2015).
- ²⁸⁴H. W. Lee, D. H. Kang, J. H. Cho, S. Lee, D. H. Jun, and J. H. Park, “Highly sensitive and reusable membraneless field-effect transistor (FET)-type tungsten diselenide (WSe₂) biosensors,” *ACS Appl. Mater. Interfaces* **10**, 17639–17645 (2018).
- ²⁸⁵Q. Chen, J. Chen, C. Gao, M. Zhang, J. Chen, and H. Qiu, “Hemin-functionalized WS₂ nanosheets as highly active peroxidase mimetics for label-free colorimetric detection of H₂O₂ and glucose,” *Analyst* **140**, 2857–2863 (2015).
- ²⁸⁶K. J. Huang, Y. J. Liu, J. T. Cao, and H. B. Wang, “An aptamer electrochemical assay for sensitive detection of immunoglobulin E based on tungsten disulfide-graphene composites and gold nanoparticles,” *RSC Adv.* **4**, 36742–36748 (2014).
- ²⁸⁷K. J. Huang, Y. J. Liu, J. Z. Zhang, and Y. M. Liu, “A novel aptamer sensor based on layered tungsten disulfide nanosheets and Au nanoparticles amplification for 17 β -estradiol detection,” *Anal. Methods* **6**, 8011–8017 (2014).
- ²⁸⁸X. Liu, H. L. Shuai, Y. J. Liu, and K. J. Huang, “An electrochemical biosensor for DNA detection based on tungsten disulfide/multi-walled carbon nanotube composites and hybridization chain reaction amplification,” *Sens. Actuators, B* **235**, 603–613 (2016).
- ²⁸⁹K. J. Huang, Y. J. Liu, H. B. Wang, T. Gan, Y. M. Liu, and L. L. Wang, “Signal amplification for electrochemical DNA biosensor based on two-dimensional graphene analogue tungsten sulfide-graphene composites and gold nanoparticles,” *Sens. Actuators, B* **191**, 828–836 (2014).
- ²⁹⁰Q. Xi, D. M. Zhou, Y. Y. Kan, J. Ge, Z. K. Wu, R. Q. Yu, and J. H. Jiang, “Highly sensitive and selective strategy for microRNA detection based on WS₂ nanosheet mediated fluorescence quenching and duplex-specific nucleic acid amplification,” *Anal. Chem.* **86**, 1361–1365 (2014).
- ²⁹¹D. Kireev, E. Okogbue, R. T. Jayanth, T. Ko, Y. Jung, and D. Akinwande, “Multipurpose and reusable ultrathin electronic tattoos based on PtSe₂ and PtTe₂,” *ACS Nano* **15**, 2800 (2021).
- ²⁹²See https://www.diabetes.co.uk/diabetes_care/blood-sugar-level-ranges.html for Blood glucose level ranges—National Institute of Health Care and Excellence (NICE) guidelines (last accessed January 11, 2021).
- ²⁹³Healthline, <https://www.healthline.com/health/glucose-test-urine#diabetes> for Urine glucose test (last accessed January 11, 2021).
- ²⁹⁴C. C. Mayorga-Martinez, N. Mohamad Latiff, A. Y. S. Eng, Z. Sofer, and M. Pumera, “Black phosphorus nanoparticle labels for immunoassays via hydrogen evolution reaction mediation,” *Anal. Chem.* **88**, 10074–10079 (2016).

- ²⁹⁵Y. Zhao, Y. H. Zhang, Z. Zhuge, Y. H. Tang, J. W. Tao, and Y. Chen, "Synthesis of a poly-L-lysine/black phosphorus hybrid for biosensors," *Anal. Chem.* **90**, 3149–3155 (2018).
- ²⁹⁶V. Kumar, J. R. Brent, M. Shorie, H. Kaur, G. Chadha, A. G. Thomas, E. A. Lewis, A. P. Rooney, L. Nguyen, X. L. Zhong, M. G. Burke, S. J. Haigh, A. Walton, P. D. McNaught, A. A. Tedstone, N. Savjani, C. A. Muryn, P. O'Brien, A. K. Ganguli, D. J. Lewis, and P. Sabherwal, "Nanostructured aptamer-functionalized black phosphorus sensing platform for label-free detection of myoglobin, a cardiovascular disease biomarker," *ACS Appl. Mater. Interfaces* **8**, 22860–22868 (2016).
- ²⁹⁷J. Cai, X. Gou, B. Sun, W. Li, D. Li, J. Liu, F. Hu, and Y. Li, "Porous graphene-black phosphorus nanocomposite modified electrode for detection of leptin," *Biosens. Bioelectron.* **137**, 88–95 (2019).
- ²⁹⁸Q. Xu, L. Cai, H. Zhao, J. Tang, Y. Shen, X. Hu, and H. Zeng, "Forchlorfenuron detection based on its inhibitory effect towards catalase immobilized on boron nitride substrate," *Biosens. Bioelectron.* **63**, 294–300 (2015).
- ²⁹⁹G. H. Yang, A. Abulizi, and J. J. Zhu, "Sonochemical fabrication of gold nanoparticles-boron nitride sheets nanocomposites for enzymeless hydrogen peroxide detection," *Ultrason. Sonochem.* **21**, 1958–1963 (2014).
- ³⁰⁰A. F. Khan, D. A. C. Brownson, E. P. Randviir, G. C. Smith, and C. E. Banks, "2D hexagonal boron nitride (2D-hBN) explored for the electrochemical sensing of dopamine," *Anal. Chem.* **88**, 9729–9737 (2016).
- ³⁰¹A. F. Khan, D. A. C. Brownson, C. W. Foster, G. C. Smith, and C. E. Banks, "Surfactant exfoliated 2D hexagonal boron nitride (2D-hBN) explored as a potential electrochemical sensor for dopamine: Surfactants significantly influence sensor capabilities," *Analyst* **142**, 1756–1764 (2017).
- ³⁰²Q. Li, C. Huo, K. Yi, L. Zhou, L. Su, and X. Hou, "Preparation of flake hexagonal BN and its application in electrochemical detection of ascorbic acid, dopamine and uric acid," *Sens. Actuators, B* **260**, 346–356 (2018).
- ³⁰³B. Aksoy, A. Paşahan, Ö. Güngör, S. Köytepe, and T. Seçkin, "A novel electrochemical biosensor based on polyimide-boron nitride composite membranes," *Int. J. Polym. Mater. Polym. Biomater.* **66**, 203–212 (2017).
- ³⁰⁴S. Ranganathan, S. Lee, J. Lee, and S. Chang, "Electrochemical non-enzymatic glucose sensor based on hexagonal boron nitride with metal-organic framework composite," *J. Sens. Sci. Technol.* **26**, 379–385 (2017).
- ³⁰⁵M. L. Yola and N. Atar, "A novel detection approach for serotonin by graphene quantum dots/two-dimensional (2D) hexagonal boron nitride nanosheets with molecularly imprinted polymer," *Appl. Surf. Sci.* **458**, 648–655 (2018).
- ³⁰⁶F. Wang, C. H. Yang, M. Duan, Y. Tang, and J. F. Zhu, "TiO₂ nanoparticle modified organ-like Ti₃C₂ MXene nanocomposite encapsulating hemoglobin for a mediator-free biosensor with excellent performances," *Biosens. Bioelectron.* **74**, 1022–1028 (2015).
- ³⁰⁷L. Lorencova, T. Bertok, E. Dosekova, A. Holazova, D. Paprckova, A. Vikartovska, V. Sasinkova, J. Filip, P. Kasak, M. Jerigova, D. Velic, K. A. Mahmoud, and J. Tkac, "Electrochemical performance of Ti₃C₂T_xMXene in aqueous media: Towards ultrasensitive H₂O₂ sensing," *Electrochim. Acta* **235**, 471–479 (2017).
- ³⁰⁸B. Xu, M. Zhu, W. Zhang, X. Zhen, Z. Pei, Q. Xue, C. Zhi, and P. Shi, "Ultrathin MXene-micropattern-based field-effect transistor for probing neural activity," *Adv. Mater.* **28**, 3333–3339 (2016).
- ³⁰⁹R. B. Rakhii, P. Nayuk, C. Xia, and H. N. Alshareef, "Novel amperometric glucose biosensor based on MXene nanocomposite," *Sci. Rep.* **6**, 36422 (2016).
- ³¹⁰H. Liu, C. Duan, C. Yang, W. Shen, F. Wang, and Z. Zhu, "A novel nitrite biosensor based on the direct electrochemistry of hemoglobin immobilized on MXene-Ti₃C₂," *Sens. Actuators, B* **218**, 60–66 (2015).
- ³¹¹C. Cui, F. Xue, W. J. Hu, and L. J. Li, "Two-dimensional materials with piezoelectric and ferroelectric functionalities," *npj 2D Mater. Appl.* **2**, 18 (2018).
- ³¹²K. He, C. Poole, K. F. Mak, and J. Shan, "Experimental demonstration of continuous electronic structure tuning via strain in atomically thin MoS₂," *Nano Lett.* **13**, 2931–2936 (2013).
- ³¹³H. Zhu, Y. Wang, J. Xiao, M. Liu, S. Xiong, Z. J. Wong, Z. Ye, Y. Ye, X. Yin, and X. Zhang, "Observation of piezoelectricity in free-standing monolayer MoS₂," *Nat. Nanotechnol.* **10**, 151–155 (2015).
- ³¹⁴M. Dai, Z. Wang, F. Wang, Y. Qiu, J. Zhang, C. Y. Xu, T. Zhai, W. Cao, Y. Fu, D. Jia, Y. Zhou, and P. A. Hu, "Two-dimensional van der Waals materials with aligned in-plane polarization and large piezoelectric effect for self-powered piezoelectric sensors," *Nano Lett.* **19**, 5410–5416 (2019).
- ³¹⁵Y. Cai, J. Shen, G. Ge, Y. Zhang, W. Jin, W. Huang, J. Shao, J. Yang, and X. Dong, "Stretchable Ti₃C₂T_x MXene/carbon nanotube composite based strain sensor with ultrahigh sensitivity and tunable sensing range," *ACS Nano* **12**, 56–62 (2018).
- ³¹⁶S. Manzeli, A. Allain, A. Ghadimi, and A. Kis, "Piezoresistivity and strain-induced band gap tuning in atomically thin MoS₂," *Nano Lett.* **15**, 5330–5335 (2015).
- ³¹⁷S. Wagner, C. Yim, N. McEvoy, S. Kataria, V. Yokaribas, A. Kuc, S. Pindl, C. P. Fritzen, T. Heine, G. S. Duesberg, and M. C. Lemme, "Highly sensitive electromechanical piezoresistive pressure sensors based on large-area layered PtSe₂ films," *Nano Lett.* **18**, 3738–3745 (2018).
- ³¹⁸W. Wu, L. Wang, Y. Li, F. Zhang, L. Lin, S. Niu, D. Chenet, X. Zhang, Y. Hao, T. F. Heinz, J. Hone, and Z. L. Wang, "Piezoelectricity of single-atomic-layer MoS₂ for energy conversion and piezotronics," *Nature* **514**, 470–474 (2014).
- ³¹⁹S. K. Kim, R. Bhatia, T.-H. Kim, D. Seol, J. H. Kim, H. Kim, W. Seung, Y. Kim, Y. H. Lee, and S.-W. Kim, "Directional dependent piezoelectric effect in CVD grown monolayer MoS₂ for flexible piezoelectric nanogenerators," *Nano Energy* **22**, 483–489 (2016).
- ³²⁰J. Qi, Y. W. Lan, A. Z. Stieg, J. H. Chen, Y. L. Zhong, L. J. Li, C. D. Chen, Y. Zhang, and K. L. Wang, "Piezoelectric effect in chemical vapour deposition-grown atomic-monolayer triangular molybdenum disulfide piezotronics," *Nat. Commun.* **6**, 8430 (2015).
- ³²¹J. Guo, R. Wen, Y. Liu, K. Zhang, J. Kou, J. Zhai, and Z. L. Wang, "Piezotronic effect enhanced flexible humidity sensing of monolayer MoS₂," *ACS Appl. Mater. Interfaces* **10**, 8110–8116 (2018).
- ³²²W. Feng, W. Zheng, F. Gao, X. Chen, G. Liu, T. Hasan, W. Cao, and P. Hu, "Sensitive electronic-skin strain sensor array based on the patterned two-dimensional α -In₂Se₃," *Chem. Mater.* **28**, 4278–4283 (2016).
- ³²³H. Yang, X. Xiao, Z. Li, K. Li, N. Cheng, S. Li, J. H. Low, L. Jing, X. Fu, S. Achavananthadith, F. Low, Q. Wang, P. L. Yeh, H. Ren, J. S. Ho, C. H. Yeow, and P. Y. Chen, "Wireless Ti₃C₂T_xMXene strain sensor with ultrahigh sensitivity and designated working windows for soft exoskeletons," *ACS Nano* **14**, 11860–11875 (2020).
- ³²⁴H. Wang, R. Zhou, D. Li, L. Zhang, G. Ren, L. Wang, J. Liu, D. Wang, Z. Tang, G. Lu, G. Sun, H.-D. Yu, and W. Huang, "High-performance foam-shaped strain sensor based on carbon nanotubes and Ti₃C₂T_x MXene for the monitoring of human activities," *ACS Nano* **15**, 9690 (2021).
- ³²⁵M. Chao, L. He, M. Gong, N. Li, X. Li, L. Peng, F. Shi, L. Zhang, and P. Wan, "Breathable Ti₃C₂T_x MXene/protein nanocomposites for ultrasensitive medical pressure sensor with degradability in solvents," *ACS Nano* **15**, 9746 (2021).
- ³²⁶H. J. Lee, J. C. Yang, J. Choi, J. Kim, G. S. Lee, S. P. Sasikala, G.-H. Lee, S.-H. K. Park, H. M. Lee, J. Y. Sim, S. Park, and S. O. Kim, "Hetero-dimensional 2D Ti₃C₂T_x MXene and 1D graphene nanoribbon hybrids for machine learning-assisted pressure sensors," *ACS Nano* **15**, 10347 (2021).
- ³²⁷J. S. Ross, S. Wu, H. Yu, N. J. Ghimire, A. M. Jones, G. Aivazian, J. Yan, D. G. Mandrus, D. Xiao, W. Yao, and X. Xu, "Electrical control of neutral and charged excitons in a monolayer semiconductor," *Nat. Commun.* **4**, 2498 (2013).
- ³²⁸T. Kümmell, W. Qitsch, S. Matthis, T. Litwin, and G. Bacher, "Gate control of carrier distribution in k-space in MoS₂ monolayer and bilayer crystals," *Phys. Rev. B* **91**, 125305 (2015).
- ³²⁹A. P. S. Gaur, A. M. Rivera, S. P. Dash, S. Dey, R. S. Katiyar, and S. Sahoo, "Manipulation of exciton and trion quasiparticles in monolayer WS₂ via charge transfer," *Appl. Phys. Lett.* **115**, 173103 (2019).
- ³³⁰M. Barbone, A. R. P. Montblanch, D. M. Kara, C. Palacios-Berraquero, A. R. Cadore, D. De Fazio, B. Pingault, E. Mostaani, H. Li, B. Chen, K. Watanabe, T. Taniguchi, S. Tongay, G. Wang, A. C. Ferrari, and M. Atatüre, "Charge-tunable biexciton complexes in monolayer WSe₂," *Nat. Commun.* **9**, 3721 (2018).
- ³³¹M. S. Kim, S. J. Yun, Y. Lee, C. Seo, G. H. Han, K. K. Kim, Y. H. Lee, and J. Kim, "Biexciton emission from edges and grain boundaries of triangular WS₂ monolayers," *ACS Nano* **10**, 2399–2405 (2016).
- ³³²T. Li, M. Li, Y. Lin, H. Cai, Y. Wu, H. Ding, S. Zhao, N. Pan, and X. Wang, "Probing exciton complexes and charge distribution in inkblab-like WSe₂ homojunction," *ACS Nano* **12**, 4959–4967 (2018).

- ³³³A. Steinhoff, M. Florian, A. Singh, K. Tran, M. Kolarczik, S. Helmrich, A. W. Achtstein, U. Woggon, N. Owschimikow, F. Jahnke, and X. Li, "Biexciton fine structure in monolayer transition metal dichalcogenides," *Nat. Phys.* **14**, 1199–1204 (2018).
- ³³⁴Y. You, X. X. Zhang, T. C. Berkelbach, M. S. Hybertsen, D. R. Reichman, and T. F. Heinz, "Observation of biexcitons in monolayer WSe₂," *Nat. Phys.* **11**, 477–481 (2015).
- ³³⁵T. Cao, G. Wang, W. Han, H. Ye, C. Zhu, J. Shi, Q. Niu, P. Tan, E. Wang, B. Liu, and J. Feng, "Valley-selective circular dichroism of monolayer molybdenum disulphide," *Nat. Commun.* **3**, 887 (2012).
- ³³⁶A. M. Jones, H. Yu, N. J. Ghimire, S. Wu, G. Aivazian, J. S. Ross, B. Zhao, J. Yan, D. G. Mandrus, D. Xiao, W. Yao, and X. Xu, "Optical generation of excitonic valley coherence in monolayer WSe₂," *Nat. Nanotechnol.* **8**, 634–638 (2013).
- ³³⁷K. F. Mak, K. He, J. Shan, and T. F. Heinz, "Control of valley polarization in monolayer MoS₂ by optical helicity," *Nat. Nanotechnol.* **7**, 494–498 (2012).
- ³³⁸H. Zeng, J. Dai, W. Yao, D. Xiao, and X. Cui, "Valley polarization in MoS₂ monolayers by optical pumping," *Nat. Nanotechnol.* **7**, 490–493 (2012).
- ³³⁹D. Xiao, G. Bin Liu, W. Feng, X. Xu, and W. Yao, "Coupled spin and valley physics in monolayers of MoS₂ and other group-VI dichalcogenides," *Phys. Rev. Lett.* **108**, 196802 (2012).
- ³⁴⁰T. Mueller and E. Malic, "Exciton physics and device application of two-dimensional transition metal dichalcogenide semiconductors," *npj 2D Mater. Appl.* **2**, 29 (2018).
- ³⁴¹K. F. Mak, D. Xiao, and J. Shan, "Light-valley interactions in 2D semiconductors," *Nat. Photonics* **12**, 451–460 (2018).
- ³⁴²M. H. Chiu, C. Zhang, H. W. Shiu, C. P. Chuu, C. H. Chen, C. Y. S. Chang, C. H. Chen, M. Y. Chou, C. K. Shih, and L. J. Li, "Determination of band alignment in the single-layer MoS₂ WSe₂ heterojunction," *Nat. Commun.* **6**, 7666 (2015).
- ³⁴³H. M. Hill, A. F. Rigosi, K. T. Rim, G. W. Flynn, and T. F. Heinz, "Band alignment in MoS₂/WS₂ transition metal dichalcogenide heterostructures probed by scanning tunneling microscopy and spectroscopy," *Nano Lett.* **16**, 4831–4837 (2016).
- ³⁴⁴N. R. Wilson, P. V. Nguyen, K. Seyler, P. Rivera, A. J. Marsden, Z. P. L. Laker, G. C. Constantinescu, V. Kandyba, A. Barinov, N. D. M. Hine, X. Xu, and D. H. Cobden, "Determination of band offsets, hybridization, and exciton binding in 2D semiconductor heterostructures," *Sci. Adv.* **3**, e1601832 (2017).
- ³⁴⁵C. Zhang, C.-P. Chuu, X. Ren, M.-Y. Li, L.-J. Li, C. Jin, M.-Y. Chou, and C.-K. Shih, "Interlayer couplings, Moiré patterns, and 2D electronic superlattices in MoS₂/WSe₂ hetero-bilayers," *Sci. Adv.* **3**, e1601459 (2017).
- ³⁴⁶Y. Wang, Z. Wang, W. Yao, G. Bin Liu, and H. Yu, "Interlayer coupling in commensurate and incommensurate bilayer structures of transition-metal dichalcogenides," *Phys. Rev. B* **95**, 115429 (2017).
- ³⁴⁷P. Rivera, J. R. Schaibley, A. M. Jones, J. S. Ross, S. Wu, G. Aivazian, P. Klement, K. Seyler, G. Clark, N. J. Ghimire, J. Yan, D. G. Mandrus, W. Yao, and X. Xu, "Observation of long-lived interlayer excitons in monolayer MoSe₂-WSe₂ heterostructures," *Nat. Commun.* **6**, 6242 (2015).
- ³⁴⁸D. Unuchek, A. Ciarrocchi, A. Avsar, K. Watanabe, T. Taniguchi, and A. Kis, "Room-temperature electrical control of exciton flux in a van der Waals heterostructure," *Nature* **560**, 340–344 (2018).
- ³⁴⁹L. A. Jauregui, A. Y. Joe, K. Pistunova, D. S. Wild, A. A. High, Y. Zhou, G. Scuri, K. D. Greve, A. Sushko, C.-H. Yu, T. Taniguchi, K. Watanabe, D. J. Needleman, M. D. Lukin, H. Park, and P. Kim, "Electrical control of interlayer exciton dynamics in atomically thin heterostructures," *Science* **366**, 870–875 (2019).
- ³⁵⁰K. L. Seyler, P. Rivera, H. Yu, N. P. Wilson, E. L. Ray, D. G. Mandrus, J. Yan, W. Yao, and X. Xu, "Signatures of moiré-trapped valley excitons in MoSe₂/WSe₂ heterobilayers," *Nature* **567**, 66 (2019).
- ³⁵¹E. V. Calman, L. H. Fowler-Gerace, D. J. Choksy, L. V. Butov, D. E. Nikonov, I. A. Young, S. Hu, A. Mishchenko, and A. K. Geim, "Indirect excitons and trions in MoSe₂/WSe₂ van der Waals Heterostructures," *Nano Lett.* **20**, 1869–1875 (2020).
- ³⁵²Y. Meng, T. Wang, C. Jin, Z. Li, S. Miao, Z. Lian, T. Taniguchi, K. Watanabe, F. Song, and S. F. Shi, "Electrical switching between exciton dissociation to exciton funneling in MoSe₂/WS₂ heterostructure," *Nat. Commun.* **11**, 2640 (2020).
- ³⁵³P. Rivera, K. L. Seyler, H. Yu, J. R. Schaibley, J. Yan, D. G. Mandrus, W. Yao, and X. Xu, "Valley-polarized exciton dynamics in a 2D semiconductor heterostructure," *Science* **351**, 688–691 (2016).
- ³⁵⁴M. Baranowski, A. Surrente, L. Klopotoski, J. M. Urban, N. Zhang, D. K. Maude, K. Wiwatoski, S. Mackowski, Y. C. Kung, D. Dumcenco, A. Kis, and P. Plochocka, "Probing the interlayer exciton physics in a MoS₂/MoSe₂/MoS₂ van der Waals Heterostructure," *Nano Lett.* **17**, 6360–6365 (2017).
- ³⁵⁵C. Jiang, W. Xu, A. Rasmita, Z. Huang, K. Li, Q. Xiong, and W. B. Gao, "Microsecond dark-exciton valley polarization memory in two-dimensional heterostructures," *Nat. Commun.* **9**, 753 (2018).
- ³⁵⁶J. R. Schaibley, P. Rivera, H. Yu, K. L. Seyler, J. Yan, D. G. Mandrus, T. Taniguchi, K. Watanabe, W. Yao, and X. Xu, "Directional interlayer spin-valley transfer in two-dimensional heterostructures," *Nat. Commun.* **7**, 13747 (2016).
- ³⁵⁷J. Kim, C. Jin, B. Chen, H. Cai, T. Zhao, P. Lee, S. Kahn, K. Watanabe, T. Taniguchi, S. Tongay, M. F. Crommie, and F. Wang, "Observation of ultra-long valley lifetime in WSe₂/MoS₂ heterostructures," *Sci. Adv.* **3**, e1700518 (2017).
- ³⁵⁸E. M. Alexeev, D. A. Ruiz-Tijerina, M. Danovich, M. J. Hamer, D. J. Terry, P. K. Nayak, S. Ahn, S. Pak, J. Lee, J. I. Sohn, M. R. Molas, M. Koperski, K. Watanabe, T. Taniguchi, K. S. Novoselov, R. V. Gorbachev, H. S. Shin, V. I. Fal'ko, and A. I. Tartakovskii, "Resonantly hybridized excitons in moiré superlattices in van der Waals heterostructures," *Nature* **567**, 81–86 (2019).
- ³⁵⁹C. Jin, E. C. Regan, A. Yan, M. Iqbal Bakti Utama, D. Wang, S. Zhao, Y. Qin, S. Yang, Z. Zheng, S. Shi, K. Watanabe, T. Taniguchi, S. Tongay, A. Zettl, and F. Wang, "Observation of moiré excitons in WSe₂/WS₂ heterostructure superlattices," *Nature* **567**, 76 (2019).
- ³⁶⁰K. Tran, G. Moody, F. Wu, X. Lu, J. Choi, K. Kim, A. Rai, D. A. Sanchez, J. Quan, A. Singh, J. Embley, A. Zepeda, M. Campbell, T. Autry, T. Taniguchi, K. Watanabe, N. Lu, S. K. Banerjee, K. L. Silverman, S. Kim, E. Tutuc, L. Yang, A. H. MacDonald, and X. Li, "Evidence for moiré excitons in van der Waals heterostructures," *Nature* **567**, 71–75 (2019).
- ³⁶¹A. Tartakovskii, "Moiré or not," *Nat. Mater.* **19**, 581–582 (2020).
- ³⁶²S. Dufferwiel, S. Schwarz, F. Withers, A. A. P. Trichet, F. Li, M. Sich, O. Del Pozo-Zamudio, C. Clark, A. Nalitov, D. D. Solnyshkov, G. Malpuech, K. S. Novoselov, J. M. Smith, M. S. Skolnick, D. N. Krizhanovskii, and A. I. Tartakovskii, "Exciton-polaritons in van der Waals heterostructures embedded in tunable microcavities," *Nat. Commun.* **6**, 8579 (2015).
- ³⁶³J. Gu, B. Chakraborty, M. Khatoniar, and V. M. Menon, "A room-temperature polariton light-emitting diode based on monolayer WS₂," *Nat. Nanotechnol.* **14**, 1024–1028 (2019).
- ³⁶⁴I. Epstein, A. J. Chaves, D. A. Rhodes, B. Frank, K. Watanabe, T. Taniguchi, H. Giessen, J. C. Hone, N. M. R. Peres, and F. H. L. Koppens, "Highly confined in-plane propagating exciton-polaritons on monolayer semiconductors," *2D Mater.* **7**, 035031 (2020).
- ³⁶⁵M. Król, K. Rechcińska, K. Nogajewski, M. Grzeszczyk, K. Łempicka, R. Mirek, S. Piotrowska, K. Watanabe, T. Taniguchi, M. R. Molas, M. Potemski, J. Szczytko, and B. Piętko, "Exciton-polaritons in multilayer WSe₂ in a planar microcavity," *2D Mater.* **7**, 015006 (2020).
- ³⁶⁶C. Rupprecht, E. Sedov, M. Klaas, H. Knopf, M. Blei, N. Lundt, S. Tongay, T. Taniguchi, K. Watanabe, U. Schulz, A. Kavokin, F. Eilenberger, S. Höfling, and C. Schneider, "Manipulation of room-temperature valley-coherent exciton-polaritons in atomically thin crystals by real and artificial magnetic fields," *2D Mater.* **7**, 035025 (2020).
- ³⁶⁷H. A. Fernandez, F. Withers, S. Russo, and W. L. Barnes, "Electrically tuneable exciton energy exchange between spatially separated 2-dimensional semiconductors in a microcavity," *Appl. Phys. Lett.* **115**, 071103 (2019).
- ³⁶⁸Z. Fei, M. E. Scott, D. J. Gosztola, J. J. Foley, J. Yan, D. G. Mandrus, H. Wen, P. Zhou, D. W. Zhang, Y. Sun, J. R. Guest, S. K. Gray, W. Bao, G. P. Wiederrecht, and X. Xu, "Nano-optical imaging of WSe₂ waveguide modes revealing light-exciton interactions," *Phys. Rev. B* **94**, 084102 (2016).
- ³⁶⁹F. Hu, Y. Luan, M. E. Scott, J. Yan, D. G. Mandrus, X. Xu, and Z. Fei, "Imaging exciton-polariton transport in MoSe₂ waveguides," *Nat. Photonics* **11**, 356–360 (2017).
- ³⁷⁰R. Verre, D. G. Baranov, B. Munkhbat, J. Cuadra, M. Käll, and T. Shegai, "Transition metal dichalcogenide nanodisks as high-index dielectric Mie nanoresonators," *Nat. Nanotechnol.* **14**, 679–683 (2019).

- ³⁷¹X. Zhang, C. De-Eknankul, J. Gu, A. L. Boehmke, V. M. Menon, J. Khurgin, and E. Cubukcu, "Guiding of visible photons at the Ångström thickness limit," *Nat. Nanotechnol.* **14**, 844–850 (2019).
- ³⁷²H. Zhang, B. Abhiraman, Q. Zhang, J. Miao, K. Jo, S. Roccasecca, M. W. Knight, A. R. Davoyan, and D. Jariwala, "Hybrid exciton-plasmon-polaritons in van der Waals semiconductor gratings," *Nat. Commun.* **11**, 3552 (2020).
- ³⁷³T. Low, A. Chaves, J. D. Caldwell, A. Kumar, N. X. Fang, P. Avouris, T. F. Heinz, F. Guinea, L. Martin-Moreno, and F. Koppens, "Polaritons in layered two-dimensional materials," *Nat. Mater.* **16**, 182–194 (2017).
- ³⁷⁴D. N. Basov, M. M. Fogler, and F. J. García De Abajo, "Polaritons in van der Waals materials," *Science* **354**, aag1992 (2016).
- ³⁷⁵N. D. Mermin and H. Wagner, "Absence of ferromagnetism or antiferromagnetism in one- or two-dimensional isotropic heisenberg models," *Phys. Rev. Lett.* **17**, 1133–1136 (1966).
- ³⁷⁶V. Kochat, A. Apte, J. A. Hachtel, H. Kumazoe, A. Krishnamoorthy, S. Susarla, J. C. Idrobo, F. Shimojo, P. Vashishta, R. Kalia, A. Nakano, C. S. Tiwary, and P. M. Ajayan, "Re doping in 2D transition metal dichalcogenides as a new route to tailor structural phases and induced magnetism," *Adv. Mater.* **29**, 1703754 (2017).
- ³⁷⁷S. Mathew, K. Gopinadhan, T. K. Chan, X. J. Yu, D. Zhan, L. Cao, A. Rusydi, M. B. H. Breese, S. Dhar, Z. X. Shen, T. Venkatesan, and J. T. L. Thong, "Magnetism in MoS₂ induced by proton irradiation," *Appl. Phys. Lett.* **101**, 102103 (2012).
- ³⁷⁸R. Mishra, W. Zhou, S. J. Pennycook, S. T. Pantelides, and J. C. Idrobo, "Long-range ferromagnetic ordering in manganese-doped two-dimensional dichalcogenides," *Phys. Rev. B* **88**, 144409 (2013).
- ³⁷⁹J. Zhang, J. M. Soon, K. P. Loh, J. Yin, J. Ding, M. B. Sullivan, and P. Wu, "Magnetic molybdenum disulfide nanosheet films," *Nano Lett.* **7**, 2370–2376 (2007).
- ³⁸⁰B. Li, T. Xing, M. Zhong, L. Huang, N. Lei, J. Zhang, J. Li, and Z. Wei, "A two-dimensional Fe-doped SnS₂ magnetic semiconductor," *Nat. Commun.* **8**, 1958 (2017).
- ³⁸¹Y. Yamasaki, R. Moriya, M. Arai, S. Masubuchi, S. Pyon, T. Tamegai, K. Ueno, and T. Machida, "Exfoliation and van der Waals heterostructure assembly of intercalated ferromagnet CrI₃/TaS₂," *2D Mater.* **4**, 041007 (2017).
- ³⁸²Z. Fei, B. Huang, P. Malinowski, W. Wang, T. Song, J. Sanchez, W. Yao, D. Xiao, X. Zhu, A. F. May, W. Wu, D. H. Cobden, J. H. Chu, and X. Xu, "Two-dimensional itinerant ferromagnetism in atomically thin Fe₃GeTe₂," *Nat. Mater.* **17**, 778–782 (2018).
- ³⁸³D. J. O'Hara, T. Zhu, A. H. Trout, A. S. Ahmed, Y. K. Luo, C. H. Lee, M. R. Brenner, S. Rajan, J. A. Gupta, D. W. McComb, and R. K. Kawakami, "Room temperature intrinsic ferromagnetism in epitaxial manganese selenide films in the monolayer limit," *Nano Lett.* **18**, 3125–3131 (2018).
- ³⁸⁴V. O. Jimenez, V. Kalappattil, T. Eggers, M. Bonilla, S. Kolekar, P. T. Huy, M. Batzill, and M. H. Phan, "A magnetic sensor using a 2D van der Waals ferromagnetic material," *Sci. Rep.* **10**, 4789 (2020).
- ³⁸⁵H. R. Fuh, B. Yan, S. C. Wu, C. Felsler, and C. R. Chang, "Metal-insulator transition and the anomalous Hall effect in the layered magnetic materials VS₂ and VSe₂," *New J. Phys.* **18**, 113038 (2016).
- ³⁸⁶M. A. Rahimi, A. G. Moghaddam, C. Dykstra, M. Governale, and U. Zülicke, "Unconventional superconductivity from magnetism in transition-metal dichalcogenides," *Phys. Rev. B* **95**, 104515 (2017).
- ³⁸⁷J. Yang, A. Wang, S. Zhang, J. Liu, Z. Zhong, and L. Chen, "Coexistence of piezoelectricity and magnetism in two-dimensional vanadium dichalcogenides," *Phys. Chem. Chem. Phys.* **21**, 132–136 (2019).
- ³⁸⁸B. Huang, G. Clark, D. R. Klein, D. MacNeill, E. Navarro-Moratalla, K. L. Seyler, N. Wilson, M. A. McGuire, D. H. Cobden, D. Xiao, W. Yao, P. Jarillo-Herrero, and X. Xu, "Electrical control of 2D magnetism in bilayer CrI₃," *Nat. Nanotechnol.* **13**, 544–548 (2018).
- ³⁸⁹H. Yuan, H. Shimotoani, J. Ye, S. Yoon, H. Aliah, A. Tsukazaki, M. Kawasaki, and Y. Iwasa, "Electrostatic and electrochemical nature of liquid-gated electric-double-layer transistors based on oxide semiconductors," *J. Am. Chem. Soc.* **132**, 18402–18407 (2010).
- ³⁹⁰M. Bonilla, S. Kolekar, Y. Ma, H. C. Diaz, V. Kalappattil, R. Das, T. Eggers, H. R. Gutierrez, M. H. Phan, and M. Batzill, "Strong room-temperature ferromagnetism in VSe₂ monolayers on van der Waals substrates," *Nat. Nanotechnol.* **13**, 289–293 (2018).
- ³⁹¹Y. Deng, Y. Yu, Y. Song, J. Zhang, N. Z. Wang, Z. Sun, Y. Yi, Y. Z. Wu, S. Wu, J. Zhu, J. Wang, X. H. Chen, and Y. Zhang, "Gate-tunable room-temperature ferromagnetism in two-dimensional Fe₃GeTe₂," *Nature* **563**, 94–99 (2018).
- ³⁹²Y. C. Cheng, Z. Y. Zhu, W. B. Mi, Z. B. Guo, and U. Schwingenschlögl, "Prediction of two-dimensional diluted magnetic semiconductors: Doped monolayer MoS₂ systems," *Phys. Rev. B* **87**, 100401 (2013).
- ³⁹³A. Ramasubramaniam and D. Naveh, "Mn-doped monolayer MoS₂: An atomically thin dilute magnetic semiconductor," *Phys. Rev. B* **87**, 195201 (2013).
- ³⁹⁴Q. Yue, S. Chang, S. Qin, and J. Li, "Functionalization of monolayer MoS₂ by substitutional doping: A first-principles study," *Phys. Lett. A* **377**, 1362–1367 (2013).
- ³⁹⁵D. L. Duong, S. J. Yun, Y. Kim, S. G. Kim, and Y. H. Lee, "Long-range ferromagnetic ordering in vanadium-doped WSe₂ semiconductor," *Appl. Phys. Lett.* **115**, 242406 (2019).
- ³⁹⁶L. Seixas, A. Carvalho, and A. H. Castro Neto, "Atomically thin dilute magnetism in Co-doped phosphorene," *Phys. Rev. B* **91**, 155138 (2015).
- ³⁹⁷H. Tan, W. Hu, C. Wang, C. Ma, H. Duan, W. Yan, L. Cai, P. Guo, Z. Sun, Q. Liu, X. Zheng, F. Hu, and S. Wei, "Intrinsic ferromagnetism in Mn-substituted MoS₂ nanosheets achieved by supercritical hydrothermal reaction," *Small* **13**, 1701389 (2017).
- ³⁹⁸S. Fu, K. Kang, K. Shayan, A. Yoshimura, S. Dadras, X. Wang, L. Zhang, S. Chen, N. Liu, A. Jindal, X. Li, A. N. Pasupathy, A. N. Vamvakas, V. Meunier, S. Strauf, and E. H. Yang, "Enabling room temperature ferromagnetism in monolayer MoS₂ via *in situ* iron-doping," *Nat. Commun.* **11**, 2034 (2020).
- ³⁹⁹F. Zhang, B. Zheng, A. Sebastian, H. Olson, M. Liu, K. Fujisawa, Y. T. H. Pham, V. O. Jimenez, V. Kalappattil, L. Miao, T. Zhang, R. Pendurthi, Y. Lei, A. L. Elías, Y. Wang, N. Alem, P. E. Hopkins, S. Das, V. H. Crespi, M.-H. Phan, and M. Terrones, "Monolayer vanadium-doped tungsten disulfide: A room-temperature dilute magnetic semiconductor," *Adv. Sci.* **7**, 2001174 (2020).
- ⁴⁰⁰S. J. Yun, D. L. Duong, D. M. Ha, K. Singh, T. L. Phan, W. Choi, Y. Kim, and Y. H. Lee, "Ferromagnetic order at room temperature in monolayer WSe₂ semiconductor via vanadium dopant," *Adv. Sci.* **7**, 1903076 (2020).
- ⁴⁰¹Y. T. H. Pham, M. Liu, V. O. Jimenez, F. Zhang, V. Kalappattil, Z. Yu, K. Wang, T. Williams, M. Terrones, and M.-H. Phan, "Tunable ferromagnetism and thermally induced spin flip in vanadium-doped tungsten diselenide monolayers at room temperature," *Adv. Mater.* **32**, 2003607 (2020).
- ⁴⁰²X. Li, X. Wu, and J. Yang, "Half-metallicity in MnPSe₃ exfoliated nanosheet with carrier doping," *J. Am. Chem. Soc.* **136**, 11065–11069 (2014).
- ⁴⁰³B. L. Chittari, Y. Park, D. Lee, M. Han, A. H. Macdonald, E. Hwang, and J. Jung, "Electronic and magnetic properties of single-layer M PX₃ metal phosphorous trichalcogenides," *Phys. Rev. B* **94**, 184428 (2016).
- ⁴⁰⁴X. Zhang, X. Zhao, D. Wu, Y. Jing, and Z. Zhou, "MnPSe₃ monolayer: A promising 2D visible-light photocatalytic catalyst with high carrier mobility," *Adv. Sci.* **3**, 1600062 (2016).
- ⁴⁰⁵Z. Zhang, J. Shang, C. Jiang, A. Rasmita, W. Gao, and T. Yu, "Direct photoluminescence probing of ferromagnetism in monolayer two-dimensional CrBr₃," *Nano Lett.* **19**, 3138–3142 (2019).
- ⁴⁰⁶A. Wiedenmann, J. Rossat-Mignod, A. Louisy, R. Brec, and J. Rouxel, "Neutron diffraction study of the layered compounds MnPSe₃ and FePSe₃," *Solid State Commun.* **40**, 1067–1072 (1981).
- ⁴⁰⁷K. Matsuzaki, V. K. Lazarov, L. Lari, H. Hosono, and T. Susaki, "Fe₃O₄(111) thin films with bulk-like properties: Growth and atomic characterization," *J. Phys. D: Appl. Phys.* **46**, 022001 (2013).
- ⁴⁰⁸A. Manikandan, J. J. Vijaya, J. A. Mary, L. J. Kennedy, and A. Dinesh, "Structural, optical and magnetic properties of Fe₃O₄ nanoparticles prepared by a facile microwave combustion method," *J. Ind. Eng. Chem.* **20**, 2077–2085 (2014).
- ⁴⁰⁹E. del Barco, M. Duran, J. M. Hernandez, J. Tejada, R. D. Zysler, M. Vasquez Mansilla, and D. Fiorani, "Magnetic relaxation measurements of (formula presented) antiferromagnetic particles below 1 K," *Phys. Rev. B* **65**, 052404 (2002).
- ⁴¹⁰M. Ghosh, E. V. Sampathkumaran, and C. N. R. Rao, "Synthesis and magnetic properties of CoO nanoparticles," *Chem. Mater.* **17**, 2348–2352 (2005).

- ⁴¹¹L. Liao, Q. Zhang, Z. Su, Z. Zhao, Y. Wang, Y. Li, X. Lu, D. Wei, G. Feng, Q. Yu, X. Cai, J. Zhao, Z. Ren, H. Fang, F. Robles-Hernandez, S. Baldelli, and J. Bao, "Efficient solar water-splitting using a nanocrystalline CoO photocatalyst," *Nat. Nanotechnol.* **9**, 69–73 (2014).
- ⁴¹²A. V. Ravindra, P. Padhan, and W. Prellier, "Electronic structure and optical band gap of CoFe₂O₄ thin films," *Appl. Phys. Lett.* **101**, 161902 (2012).
- ⁴¹³R. Sato Turtelli, G. V. Duong, W. Nunes, R. Grössinger, and M. Knobel, "Magnetic properties of nanocrystalline CoFe₂O₄ synthesized by modified citrate-gel method," *J. Magn. Magn. Mater.* **320**, e339–e342 (2008).
- ⁴¹⁴P. Mohn and E. P. Wohlforth, "The Curie temperature of the ferromagnetic transition metals and their compounds," *J. Phys. F: Met. Phys.* **17**, 2421–2430 (1987).
- ⁴¹⁵X. Liu, C. Song, Z. Wu, J. Wang, J. Pan, and C. Li, "Bandgap opening and magnetic anisotropy switching by uniaxial strain in graphene/CrI₃ heterojunction," *J. Phys. D: Appl. Phys.* **53**, 385002 (2020).
- ⁴¹⁶K. Wang, T. Hu, F. Jia, G. Zhao, Y. Liu, I. V. Solovyev, A. P. Pyatakov, A. K. Zvezdin, and W. Ren, "Magnetic and electronic properties of Cr₂Ge₂Te₆ monolayer by strain and electric-field engineering," *Appl. Phys. Lett.* **114**, 092405 (2019).
- ⁴¹⁷J. Seo, D. Y. Kim, E. S. An, K. Kim, G. Y. Kim, S. Y. Hwang, D. W. Kim, B. G. Jang, H. Kim, G. Eom, S. Y. Seo, R. Stania, M. Muntwiler, J. Lee, K. Watanabe, T. Taniguchi, Y. J. Jo, J. Lee, B. Il Min, M. H. Jo, H. W. Yeom, S. Y. Choi, J. H. Shim, and J. S. Kim, "Nearly room temperature ferromagnetism in a magnetic metal-rich van der Waals metal," *Sci. Adv.* **6**, eaay8912 (2020).
- ⁴¹⁸L. D. Casto, A. J. Clune, M. O. Yokosuk, J. L. Musfeldt, T. J. Williams, H. L. Zhuang, M. W. Lin, K. Xiao, R. G. Hennig, B. C. Sales, J. Q. Yan, and D. Mandrus, "Strong spin-lattice coupling in CrSiTe₃," *APL Mater.* **3**, 041515 (2015).
- ⁴¹⁹P. A. Joy and S. Vasudevan, "Magnetism in the layered transition-metal thiophosphates MPS₃ (M = Mn, Fe, and Ni)," *Phys. Rev. B* **46**, 5425–5433 (1992).
- ⁴²⁰A. Molinari, H. Hahn, and R. Kruk, "Voltage-control of magnetism in all-solid-state and solid/liquid magnetoelectric composites," *Adv. Mater.* **31**, 1806662 (2019).
- ⁴²¹W. Sun, W. Wang, D. Chen, Z. Cheng, and Y. Wang, "Valence mediated tunable magnetism and electronic properties by ferroelectric polarization switching in 2D FeI₂/In₂Se₃ van der Waals heterostructures," *Nanoscale* **11**, 9931–9936 (2019).
- ⁴²²Y. Zhao, J. Zhang, S. Yuan, and Z. Chen, "Nonvolatile electrical control and heterointerface-induced half-metallicity of 2D ferromagnets," *Adv. Funct. Mater.* **29**, 1901420. (2019).
- ⁴²³Q. Pei and W. Mi, "Electrical control of magnetic behavior and valley polarization of monolayer antiferromagnetic MnPSe₃ on an insulating ferroelectric substrate from first principles," *Phys. Rev. Appl.* **11**, 014011 (2019).
- ⁴²⁴C. Gong, E. M. Kim, Y. Wang, G. Lee, and X. Zhang, "Multiferroicity in atomic van der Waals heterostructures," *Nat. Commun.* **10**, 2657 (2019).
- ⁴²⁵Y. Lu, R. Fei, X. Lu, L. Zhu, L. Wang, and L. Yang, "Artificial multiferroics and enhanced magnetoelectric effect in van der Waals heterostructures," *ACS Appl. Mater. Interfaces.* **12**, 6243–6249 (2020).
- ⁴²⁶C. Pfeleiderer, G. McMullan, S. Julian, and G. Lonzarich, "Magnetic quantum phase transition in MnSi under hydrostatic pressure," *Phys. Rev. B* **55**, 8330–8338 (1997).
- ⁴²⁷I. I. Mazin and D. J. Singh, "Spin fluctuations and the magnetic phase diagram of ZrZn₂," *Phys. Rev. B* **69**, 020402 (2004).
- ⁴²⁸C. Jin, Z. Tao, K. Kang, K. Watanabe, T. Taniguchi, K. F. Mak, and J. Shan, "Imaging and control of critical fluctuations in two-dimensional magnets," *Nat. Mater.* **19**, 1290 (2020).
- ⁴²⁹D. R. Klein, D. MacNeill, J. L. Lado, D. Soriano, E. Navarro-Moratalla, K. Watanabe, T. Taniguchi, S. Manni, P. Canfield, J. Fernández-Rossier, and P. Jarillo-Herrero, "Probing magnetism in 2D van der Waals crystalline insulators via electron tunneling," *Science* **360**, 1218–1222 (2018).
- ⁴³⁰T. Song, X. Cai, M. W. Y. Tu, X. Zhang, B. Huang, N. P. Wilson, K. L. Seyler, L. Zhu, T. Taniguchi, K. Watanabe, M. A. McGuire, D. H. Cobden, D. Xiao, W. Yao, and X. Xu, "Giant tunneling magnetoresistance in spin-filter van der Waals heterostructures," *Science* **360**, 1214–1218 (2018).
- ⁴³¹Z. Wang, I. Gutiérrez-Lezama, N. Ubrig, M. Kroner, M. Gibertini, T. Taniguchi, K. Watanabe, A. Imamoğlu, E. Giannini, and A. F. Morpurgo, "Very large tunneling magnetoresistance in layered magnetic semiconductor CrI₃," *Nat. Commun.* **9**, 2516 (2018).
- ⁴³²T. Song, M. W. Y. Tu, C. Carnahan, X. Cai, T. Taniguchi, K. Watanabe, M. A. McGuire, D. H. Cobden, D. Xiao, W. Yao, and X. Xu, "Voltage control of a van der Waals spin-filter magnetic tunnel junction," *Nano Lett.* **19**, 915 (2019).
- ⁴³³A. Dankert and S. P. Dash, "Electrical gate control of spin current in van der Waals heterostructures at room temperature," *Nat. Commun.* **8**, 16093 (2017).
- ⁴³⁴W. Yan, O. Txoperena, R. Llopis, H. Dery, L. E. Hueso, and F. Casanova, "A two-dimensional spin field-effect switch," *Nat. Commun.* **7**, 13372 (2016).
- ⁴³⁵S. J. Gong, C. Gong, Y. Y. Sun, W. Y. Tong, C. G. Duan, J. H. Chu, and X. Zhang, "Electrically induced 2D half-metallic antiferromagnets and spin field effect transistors," *Proc. Natl. Acad. Sci. U. S. A.* **115**, 8511–8516 (2018).
- ⁴³⁶S. Jiang, L. Li, Z. Wang, J. Shan, and K. F. Mak, "Spin tunnel field-effect transistors based on two-dimensional van der Waals heterostructures," *Nat. Electron.* **2**, 159–163 (2019).
- ⁴³⁷A. V. Chumak, V. I. Vasyuchka, A. A. Serga, and B. Hillebrands, "Magnon spintronics," *Nat. Phys.* **11**, 453–461 (2015).
- ⁴³⁸A. McCreary, J. R. Simpson, T. T. Mai, R. D. McMichael, J. E. Douglas, N. Butch, C. Dennis, R. Valdés Aguilar, and A. R. Hight Walker, "Quasi-two-dimensional magnon identification in antiferromagnetic FePS₃ via magneto-Raman spectroscopy," *Phys. Rev. B* **101**, 064416 (2020).
- ⁴³⁹K. Kim, S. Y. Lim, J. U. Lee, S. Lee, T. Y. Kim, K. Park, G. S. Jeon, C. H. Park, J. G. Park, and H. Cheong, "Suppression of magnetic ordering in XXZ-type antiferromagnetic monolayer NiPS₃," *Nat. Commun.* **10**, 345 (2019).
- ⁴⁴⁰S. Li, Z. Ye, X. Luo, G. Ye, H. H. Kim, B. Yang, S. Tian, C. Li, H. Lei, A. W. Tsen, K. Sun, R. He, and L. Zhao, "Magnetic-field-induced quantum phase transitions in a van der Waals magnet," *Phys. Rev. X* **10**, 011075 (2020).
- ⁴⁴¹X. X. Zhang, L. Li, D. Weber, J. Goldberger, K. F. Mak, and J. Shan, "Gate-tunable spin waves in antiferromagnetic atomic bilayers," *Nat. Mater.* **19**, 838–842 (2020).
- ⁴⁴²A. McCreary, T. T. Mai, F. G. Utermohlen, J. R. Simpson, K. F. Garrity, X. Feng, D. Shcherbakov, Y. Zhu, J. Hu, D. Weber, K. Watanabe, T. Taniguchi, J. E. Goldberger, Z. Mao, C. N. Lau, Y. Lu, N. Trivedi, R. Valdés Aguilar, and A. R. Hight Walker, "Distinct magneto-Raman signatures of spin-flip phase transitions in CrI₃," *Nat. Commun.* **11**, 3879 (2020).
- ⁴⁴³J. Cenker, B. Huang, N. Suri, P. Thijssen, A. Miller, T. Song, T. Taniguchi, K. Watanabe, M. A. McGuire, D. Xiao, and X. Xu, "Direct observation of two-dimensional magnons in atomically thin CrI₃," *Nat. Phys.* **17**, 20 (2020).
- ⁴⁴⁴W. Xing, L. Qiu, X. Wang, Y. Yao, Y. Ma, R. Cai, S. Jia, X. C. Xie, and W. Han, "Magnon transport in quasi-two-dimensional van der Waals antiferromagnets," *Phys. Rev. X* **9**, 011026 (2019).
- ⁴⁴⁵D. Ghazaryan, M. T. Greenaway, Z. Wang, V. H. Guarochico-Moreira, I. J. Vera-Marun, J. Yin, Y. Liao, S. V. Morozov, O. Kristanovski, A. I. Lichtenstein, M. I. Katsnelson, F. Withers, A. Mishchenko, L. Eaves, A. K. Geim, K. S. Novoselov, and A. Misra, "Magnon-assisted tunnelling in van der Waals heterostructures based on CrBr₃," *Nat. Electron.* **1**, 344–349 (2018).
- ⁴⁴⁶H. H. Kim, B. Yang, S. Li, S. Jiang, C. Jin, Z. Tao, G. Nichols, F. Sfigakis, S. Zhong, C. Li, S. Tian, D. G. Cory, G. X. Miao, J. Shan, K. F. Mak, H. Lei, K. Sun, L. Zhao, and A. W. Tsen, "Evolution of interlayer and intralayer magnetism in three atomically thin chromium trihalides," *Proc. Natl. Acad. Sci. U. S. A.* **166**, 11131–11136 (2019).
- ⁴⁴⁷B. Ding, Z. Li, G. Xu, H. Li, Z. Hou, E. Liu, X. Xi, F. Xu, Y. Yao, and W. Wang, "Observation of magnetic skyrmion bubbles in a van der Waals ferromagnet Fe₃GeTe₂," *Nano Lett.* **20**, 868–873 (2020).
- ⁴⁴⁸Y. Wu, S. Zhang, J. Zhang, W. Wang, Y. L. Zhu, J. Hu, G. Yin, K. Wong, C. Fang, C. Wan, X. Han, Q. Shao, T. Taniguchi, K. Watanabe, J. Zang, Z. Mao, X. Zhang, and K. L. Wang, "Néel-type skyrmion in WTe₂/Fe₃GeTe₂ van der Waals heterostructure," *Nat. Commun.* **11**, 3860 (2020).
- ⁴⁴⁹M.-G. Han, J. A. Garlow, Y. Liu, H. Zhang, J. Li, D. Dimarzio, M. W. Knight, C. Petrovic, D. Jariwala, and Y. Zhu, "Topological magnetic-spin textures in two-dimensional van der Waals Cr₂Ge₂Te₆," *Nano Lett.* **19**, 7859–7865 (2019).
- ⁴⁵⁰M. Yang, Q. Li, R. V. Chopdekar, R. Dhall, J. Turner, J. D. Carlström, C. Ophus, C. Klewe, P. Shafer, A. T. N'Diaye, J. W. Choi, G. Chen, Y. Z. Wu, C.

- Hwang, F. Wang, and Z. Q. Qiu, "Creation of skyrmions in van der Waals ferromagnet Fe_3GeTe_2 on (Co/Pd) n superlattice," *Sci. Adv.* **6**, eabb5157 (2020).
- ⁴⁵¹M. Akram and O. Erten, "Skyrmions in twisted van der Waals magnets," *Phys. Rev. B* **103**, L140406 (2021).
- ⁴⁵²L. Wang, Q. Feng, Y. Kim, R. Kim, K. H. Lee, S. D. Pollard, Y. J. Shin, H. Zhou, W. Peng, D. Lee, W. Meng, H. Yang, J. H. Han, M. Kim, Q. Lu, and T. W. Noh, "Ferroelectrically tunable magnetic skyrmions in ultrathin oxide heterostructures," *Nat. Mater.* **17**, 1087–1094 (2018).
- ⁴⁵³W. Sun, W. Wang, H. Li, G. Zhang, D. Chen, J. Wang, and Z. Cheng, "Controlling bimerons as skyrmion analogues by ferroelectric polarization in 2D van der Waals multiferroic heterostructures," *Nat. Commun.* **11**, 5930 (2020).
- ⁴⁵⁴A. L. Kholkin, N. A. Pertsev, and A. V. Goltsev, *Piezoelectricity and Crystal Symmetry* (Springer, Boston, MA, 2008), pp. 17–38.
- ⁴⁵⁵S. Trolier-McKinstry, "Crystal chemistry of piezoelectric materials," in *Piezoelectric and Acoustic Materials for Transducer Applications* (Springer Science+ Business Media, 2008), pp. 39–56.
- ⁴⁵⁶Y. Li, Y. Rao, K. F. Mak, Y. You, S. Wang, C. R. Dean, and T. F. Heinz, "Probing symmetry properties of few-layer MoS_2 and h-BN by optical second-harmonic generation," *Nano Lett.* **13**, 3329–3333 (2013).
- ⁴⁵⁷J. Klein, J. Wierzbowski, A. Steinhoff, M. Florian, M. Rösner, F. Heimbach, K. Müller, F. Jahnke, T. O. Wehling, J. J. Finley, and M. Kaniber, "Electric-field switchable second-harmonic generation in bilayer MoS_2 by inversion symmetry breaking," *Nano Lett.* **17**, 392–398 (2017).
- ⁴⁵⁸K. H. Michel and B. Verberck, "Theory of elastic and piezoelectric effects in two-dimensional hexagonal boron nitride," *Phys. Rev. B* **80**, 224301 (2009).
- ⁴⁵⁹J. Shi, C. Han, X. Wang, and S. Yun, "Electronic, elastic and piezoelectric properties of boron-V group binary and ternary monolayers," *Phys. B: Condens. Matter* **574**, 311634 (2019).
- ⁴⁶⁰Y. Zhou, D. Wu, Y. Zhu, Y. Cho, Q. He, X. Yang, K. Herrera, Z. Chu, Y. Han, M. C. Downer, H. Peng, and K. Lai, "Out-of-plane piezoelectricity and ferroelectricity in layered $\alpha\text{-In}_2\text{Se}_3$ nanoflakes," *Nano Lett.* **17**, 5508–5513 (2017).
- ⁴⁶¹F. Xue, J. Zhang, W. Hu, W. T. Hsu, A. Han, S. F. Leung, J. K. Huang, Y. Wan, S. Liu, J. Zhang, J. H. He, W. H. Chang, Z. L. Wang, X. Zhang, and L. J. Li, "Multidirection piezoelectricity in mono- and multilayered hexagonal $\alpha\text{-In}_2\text{Se}_3$," *ACS Nano* **12**, 4976–4983 (2018).
- ⁴⁶²A. Y. Lu, H. Zhu, J. Xiao, C. P. Chuu, Y. Han, M. H. Chiu, C. C. Cheng, C. W. Yang, K. H. Wei, Y. Yang, Y. Wang, D. Sokaras, D. Nordlund, P. Yang, D. A. Muller, M. Y. Chou, X. Zhang, and L. J. Li, "Janus monolayers of transition metal dichalcogenides," *Nat. Nanotechnol.* **12**, 744–749 (2017).
- ⁴⁶³L. Dong, J. Lou, and V. B. Shenoy, "Large in-plane and vertical piezoelectricity in Janus transition metal dichalcogenides," *ACS Nano* **11**, 8242–8248 (2017).
- ⁴⁶⁴Y. Chen, J. Liu, J. Yu, Y. Guo, and Q. Sun, "Symmetry-breaking induced large piezoelectricity in Janus tellurene materials," *Phys. Chem. Chem. Phys.* **21**, 1207–1216 (2019).
- ⁴⁶⁵X. Wang, X. He, H. Zhu, L. Sun, W. Fu, X. Wang, L. C. Hoong, H. Wang, Q. Zeng, W. Zhao, J. Wei, Z. Jin, Z. Shen, J. Liu, T. Zhang, and Z. Liu, "Subatomic deformation driven by vertical piezoelectricity from CdS ultrathin films," *Sci. Adv.* **2**, e1600209 (2016).
- ⁴⁶⁶X. Wen, W. Wu, Y. Ding, and Z. L. Wang, "Piezotronic effect in flexible thin-film based devices," *Adv. Mater.* **25**, 3371–3379 (2013).
- ⁴⁶⁷J. Junquera and P. Ghosez, "Critical thickness for ferroelectricity in perovskite ultrathin films," *Nature* **422**, 506–509 (2003).
- ⁴⁶⁸K. Chang, J. Liu, H. Lin, N. Wang, K. Zhao, A. Zhang, F. Jin, Y. Zhong, X. Hu, W. Duan, Q. Zhang, L. Fu, Q.-K. Xue, X. Chen, and S.-H. Ji, "Discovery of robust in-plane ferroelectricity in atomic-thick SnTe ," *Science* **353**, 274–278 (2016).
- ⁴⁶⁹K. Chang, T. P. Kaloni, H. Lin, A. Bedoya-Pinto, A. K. Pandeya, I. Kostanovskiy, K. Zhao, Y. Zhong, X. Hu, Q. K. Xue, X. Chen, S. H. Ji, S. Barraza-Lopez, and S. S. P. Parkin, "Enhanced spontaneous polarization in ultrathin SnTe films with layered antipolar structure," *Adv. Mater.* **31**, 1804428 (2019).
- ⁴⁷⁰W. Wan, C. Liu, W. Xiao, and Y. Yao, "Promising ferroelectricity in 2D group IV tellurides: A first-principles study," *Appl. Phys. Lett.* **111**, 132904 (2017).
- ⁴⁷¹Y. Bao, P. Song, Y. Liu, Z. Chen, M. Zhu, I. Abdelwahab, J. Su, W. Fu, X. Chi, W. Yu, W. Liu, X. Zhao, Q.-H. Xu, M. Yang, and K. P. Loh, "Gate-tunable in-plane ferroelectricity in few-layer SnS ," *Nano Lett.* **19**, 5109 (2019).
- ⁴⁷²C. Liu, W. Wan, J. Ma, W. Guo, and Y. Yao, "Robust ferroelectricity in two-dimensional SbN and BiP ," *Nanoscale* **10**, 7984–7990 (2018).
- ⁴⁷³S. Yuan, X. Luo, H. L. Chan, C. Xiao, Y. Dai, M. Xie, and J. Hao, "Room-temperature ferroelectricity in MoTe_2 down to the atomic monolayer limit," *Nat. Commun.* **10**, 1775 (2019).
- ⁴⁷⁴D. D. Fong, G. B. Stephenson, S. K. Streiffer, J. A. Eastman, O. Auciello, P. H. Fuoss, and C. Thompson, "Ferroelectricity in ultrathin perovskite films," *Science* **304**, 1650–1653 (2004).
- ⁴⁷⁵Q. Yang, M. Wu, and J. Li, "Origin of two-dimensional vertical ferroelectricity in WTe_2 bilayer and multilayer," *J. Phys. Chem. Lett.* **9**, 7160–7164 (2018).
- ⁴⁷⁶B. Xu, H. Xiang, Y. Xia, K. Jiang, X. Wan, J. He, J. Yin, and Z. Liu, "Monolayer $\text{AgBiP}_2\text{Se}_6$: An atomically thin ferroelectric semiconductor with out-plane polarization," *Nanoscale* **9**, 8427–8434 (2017).
- ⁴⁷⁷W. F. Io, S. Yuan, S. Y. Pang, L. W. Wong, J. Zhao, and J. Hao, "Temperature- and thickness-dependence of robust out-of-plane ferroelectricity in CVD grown ultrathin van der Waals $\alpha\text{-In}_2\text{Se}_3$ layers," *Nano Res.* **13**, 1897–1902 (2020).
- ⁴⁷⁸J. Deng, Y. Liu, M. Li, S. Xu, Y. Lun, P. Lv, T. Xia, P. Gao, X. Wang, and J. Hong, "Thickness-dependent in-plane polarization and structural phase transition in van der Waals ferroelectric CuInP_2S_6 ," *Small* **16**, 1904529 (2020).
- ⁴⁷⁹R. Fei, W. Kang, and L. Yang, "Ferroelectricity and phase transitions in monolayer group-IV monochalcogenides," *Phys. Rev. Lett.* **117**(9), 097601 (2016).
- ⁴⁸⁰J. Qi, H. Wang, X. Chen, and X. Qian, "Two-dimensional multiferroic semiconductors with coexisting ferroelectricity and ferromagnetism," *Appl. Phys. Lett.* **113**, 043102 (2018).
- ⁴⁸¹L. Li and M. Wu, "Binary compound bilayer and multilayer with vertical polarizations: two-dimensional ferroelectrics, multiferroics, nanogenerators," *ACS Nano* **11**, 6382–6388 (2017).
- ⁴⁸²C. Huang, Y. Du, H. Wu, H. Xiang, K. Deng, and E. Kan, "Prediction of intrinsic ferromagnetic ferroelectricity in a transition-metal halide monolayer," *Phys. Rev. Lett.* **120**, 147601 (2018).
- ⁴⁸³H. Wang and X. Qian, "Two-dimensional multiferroics in monolayer group IV monochalcogenides," *2D Mater.* **4**, 015042 (2017).
- ⁴⁸⁴W. Huang, F. Wang, L. Yin, R. Cheng, Z. Wang, M. G. Sendeku, J. Wang, N. Li, Y. Yao, and J. He, "Gate-coupling-enabled robust hysteresis for nonvolatile memory and programmable rectifier in van der Waals ferroelectric heterojunctions," *Adv. Mater.* **32**, 1908040 (2020).
- ⁴⁸⁵F. Wypych and R. Schöllhorn, "1T- MoS_2 , a new metallic modification of molybdenum disulfide," *J. Chem. Soc. Chem. Commun.* **1992**, 1386–1388.
- ⁴⁸⁶H. L. Tsai, J. Heising, J. L. Schindler, C. R. Kannewurf, and M. G. Kanatzidis, "Exfoliated-restacked phase of WS_2 ," *Chem. Mater.* **9**, 879–882 (1997).
- ⁴⁸⁷X. Zhang, H. Nan, S. Xiao *et al.*, "Transition metal dichalcogenides bilayer single crystals by reverse-flow chemical vapor epitaxy," *Nature Commun.* **10**(1), 598 (2019).
- ⁴⁸⁸Z. Zeng, X. Sun, D. Zhang *et al.*, "Controlled vapor growth and nonlinear optical applications of large-area 3R phase WS_2 and WSe_2 atomic layers," *Adv. Funct. Mater.* **29**(11), 1806874 (2019).
- ⁴⁸⁹L. Zhou, A. Zubair, Z. Wang *et al.*, "Synthesis of high-quality large-area homogenous 1T' MoTe_2 from chemical vapor deposition," *Adv. Mater.* **28**(43), 9526–9531 (2016).
- ⁴⁹⁰L. Zhou, K. Xu, A. Zubair *et al.*, "Large-area synthesis of high-quality uniform few-layer MoTe_2 ," *J. Am. Chem. Soc.* **137**(37), 11892–11895 (2015).
- ⁴⁹¹K. Duerloo, Y. Li, and E. J. Reed, "Structural phase transitions in two-dimensional Mo- and W-dichalcogenide monolayers," *Nat. Commun.* **5**(May), 4214 (2014).
- ⁴⁹²Q. Tang, "Tuning the phase stability of Mo-based TMD monolayers through coupled vacancy defects and lattice strain," *J. Mater. Chem. C* **6**(35), 9561–9568 (2018).
- ⁴⁹³X. Tong, Y. Qi, J. Chen, N. Wang, and Q. Xu, "Supercritical CO_2 -assisted reverse-micelle-induced solution-phase fabrication of two-dimensional metallic 1T- MoS_2 and 1T- WS_2 ," *ChemNanoMat* **3**(7), 466–471 (2017).
- ⁴⁹⁴Y. Qi, Q. Xu, Y. Wang, B. Yan, Y. Ren, and Z. Chen, " CO_2 -induced phase engineering: Protocol for enhanced photoelectrocatalytic performance of 2D MoS_2 nanosheets," *ACS Nano* **10**(2), 2903–2909 (2016).

- ⁴⁹⁵M. B. Dines, "Lithium intercalation via n-butyllithium of the layered transition metal dichalcogenides," *Mater. Res. Bull.* **10**, 287–291 (1975).
- ⁴⁹⁶G. Eda, H. Yamaguchi, D. Voiry, T. Fujita, M. Chen, and M. Chhowalla, "Photoluminescence from chemically exfoliated MoS₂," *Nano Lett.* **11**, 5111–5116 (2011).
- ⁴⁹⁷R. Kappera, D. Voiry, S. E. Yalcin, B. Branch, G. Gupta, A. D. Mohite, and M. Chhowalla, "Phase-engineered low-resistance contacts for ultrathin MoS₂ transistors," *Nat. Mater.* **13**, 1128–1134 (2014).
- ⁴⁹⁸Y. Wang, J. Xiao, H. Zhu, Y. Li, Y. Alsaïd, K. Y. Fong, Y. Zhou, S. Wang, W. Shi, Y. Wang, A. Zettl, E. J. Reed, and X. Zhang, "Structural phase transition in monolayer MoTe₂ driven by electrostatic doping," *Nature* **550**, 487–491 (2017).
- ⁴⁹⁹Y. C. Lin, D. O. Dumcenco, Y. S. Huang, and K. Suenaga, "Atomic mechanism of the semiconducting-to-metallic phase transition in single-layered MoS₂," *Nat. Nanotechnol.* **9**, 391–396 (2014).
- ⁵⁰⁰Y. Li, K. A. N. Duerloo, K. Wauson, and E. J. Reed, "Structural semiconductor-to-semimetal phase transition in two-dimensional materials induced by electrostatic gating," *Nat. Commun.* **7**, 10671 (2016).
- ⁵⁰¹C. L. Wu, H. Yuan, Y. Li, Y. Gong, H. Y. Hwang, and Y. Cui, "Gate-induced metal-insulator transition in MoS₂ by solid superionic conductor LaF₃," *Nano Lett.* **18**, 2387–2392 (2018).
- ⁵⁰²J. Zhang, J. Liu, J. L. Huang, P. Kim, and C. M. Lieber, "Creation of nanocrystals through a solid-solid phase transition induced by an STM tip," *Science* **274**, 757–760 (1996).
- ⁵⁰³J. Kim, C. Park, W. Yamaguchi, O. Shiino, and K. Kitazawa, "Observation of a phase transition from the phase to the phase induced by a STM tip," *Phys. Rev. B* **56**, R15573–R15576 (1997).
- ⁵⁰⁴F. Zhang, H. Zhang, S. Krylyuk, C. A. Milligan, Y. Zhu, D. Y. Zemlyanov, L. A. Bendersky, B. K. Ofori-Okai, R. Li, A. H. Reid, S. Weathersby, E. Mannebach, N. Finney, D. Rhodes, D. Chenet, A. Antony, L. Balicas, J. Hone, T. P. Devereaux, T. F. Heinz, X. Wang, and A. M. Lindenberg, "An ultrafast symmetry switch in a Weyl semimetal," *Nature* **565**, 61–66 (2019).
- ⁵⁰⁵J. Shi, Y. Q. Bie, W. Chen, S. Fang, J. Han, Z. Cao, T. Taniguchi, K. Watanabe, V. Bulović, E. Kaxiras, P. Jarillo-Herrero, and K. A. Nelson, "Terahertz-driven irreversible topological phase transition in two-dimensional MoTe₂," *arXiv:1910.13609* (2019).
- ⁵⁰⁷R. Bistritzer and A. H. MacDonald, "Moiré bands in twisted double-layer graphene," *Proc. Natl. Acad. Sci. U. S. A.* **108**, 12233–12237 (2011).
- ⁵⁰⁸Y. Cao, J. Y. Luo, V. Fatemi, S. Fang, J. D. Sanchez-Yamagishi, K. Watanabe, T. Taniguchi, E. Kaxiras, and P. Jarillo-Herrero, "Superlattice-induced insulating states and valley-protected orbits in twisted bilayer graphene," *Phys. Rev. Lett.* **117**, 116804 (2016).
- ⁵⁰⁹K. Kim, A. DaSilva, S. Huang, B. Fallahzad, S. Larentis, T. Taniguchi, K. Watanabe, B. J. LeRoy, A. H. MacDonald, and E. Tutuc, "Tunable moiré bands and strong correlations in small-twist-angle bilayer graphene," *Proc. Natl. Acad. Sci. U. S. A.* **114**, 3364–3369 (2017).
- ⁵¹⁰Y. Cao, V. Fatemi, A. Demir, S. Fang, S. L. Tomarken, J. Y. Luo, J. D. Sanchez-Yamagishi, K. Watanabe, T. Taniguchi, E. Kaxiras, R. C. Ashoori, and P. Jarillo-Herrero, "Correlated insulator behaviour at half-filling in magic-angle graphene superlattices," *Nature* **556**, 80–84 (2018).
- ⁵¹¹A. L. Sharpe, E. J. Fox, A. W. Barnard, J. Finney, K. Watanabe, T. Taniguchi, M. A. Kastner, and D. Goldhaber-Gordon, "Emergent ferromagnetism near three-quarters filling in twisted bilayer graphene," *Science* **365**, 605–608 (2019).
- ⁵¹²M. Yankowitz, S. Chen, H. Polshyn, Y. Zhang, K. Watanabe, T. Taniguchi, D. Graf, A. F. Young, and C. R. Dean, "Tuning superconductivity in twisted bilayer graphene," *Science* **363**, 1059–1064 (2019).
- ⁵¹³T. M. R. Wolf, J. L. Lado, G. Blatter, and O. Zilberberg, "Electrically tunable flat bands and magnetism in twisted bilayer graphene," *Phys. Rev. Lett.* **123**, 096802 (2019).
- ⁵¹⁴L. A. Gonzalez-Arraga, J. L. Lado, F. Guinea, and P. San-Jose, "Electrically controllable magnetism in twisted bilayer graphene," *Phys. Rev. Lett.* **119**, 107201 (2017).
- ⁵¹⁵C. Shen, Y. Chu, Q. S. Wu, N. Li, S. Wang, Y. Zhao, J. Tang, J. Liu, J. Tian, K. Watanabe, T. Taniguchi, R. Yang, Z. Y. Meng, D. Shi, O. V. Yazyev, and G. Zhang, "Correlated states in twisted double bilayer graphene," *Nat. Phys.* **16**, 520–525 (2020).
- ⁵¹⁶Y. Cao, D. Rodan-Legrain, O. Rubies-Bigorda, J. M. Park, K. Watanabe, T. Taniguchi, and P. Jarillo-Herrero, "Tunable correlated states and spin-polarized phases in twisted bilayer-bilayer graphene," *Nature* **583**, 215–220 (2020).
- ⁵¹⁷X. Liu, Z. Hao, E. Khalaf, J. Y. Lee, Y. Ronen, H. Yoo, D. Haei Najafabadi, K. Watanabe, T. Taniguchi, A. Vishwanath, and P. Kim, "Tunable spin-polarized correlated states in twisted double bilayer graphene," *Nature* **583**, 221–225 (2020).
- ⁵¹⁸S. Chen, M. He, Y. H. Zhang, V. Hsieh, Z. Fei, K. Watanabe, T. Taniguchi, D. H. Cobden, X. Xu, C. R. Dean, and M. Yankowitz, "Electrically tunable correlated and topological states in twisted monolayer-bilayer graphene," *Nat. Phys.* **17**, 374 (2020).
- ⁵¹⁹G. Chen, L. Jiang, S. Wu, B. Lyu, H. Li, B. L. Chittari, K. Watanabe, T. Taniguchi, Z. Shi, J. Jung, Y. Zhang, and F. Wang, "Evidence of a gate-tunable Mott insulator in a trilayer graphene moiré superlattice," *Nat. Phys.* **15**, 237–241 (2019).
- ⁵²⁰G. Chen, A. L. Sharpe, P. Gallagher, I. T. Rosen, E. J. Fox, L. Jiang, B. Lyu, H. Li, K. Watanabe, T. Taniguchi, J. Jung, Z. Shi, D. Goldhaber-Gordon, Y. Zhang, and F. Wang, "Signatures of tunable superconductivity in a trilayer graphene moiré superlattice," *Nature* **572**, 215–219 (2019).
- ⁵²¹L. Wang, E. M. Shih, A. Ghiotto, L. Xian, D. A. Rhodes, C. Tan, M. Claassen, D. M. Kennes, Y. Bai, B. Kim, K. Watanabe, T. Taniguchi, X. Zhu, J. Hone, A. Rubio, A. N. Pasupathy, and C. R. Dean, "Correlated electronic phases in twisted bilayer transition metal dichalcogenides," *Nat. Mater.* **19**, 861–866 (2020).
- ⁵²²F. Wu, T. Lovorn, E. Tutuc, I. Martin, and A. H. MacDonald, "Topological insulators in twisted transition metal dichalcogenide homobilayers," *Phys. Rev. Lett.* **122**, 086402 (2019).
- ⁵²³F. Wu, T. Lovorn, E. Tutuc, and A. H. MacDonald, "Hubbard model physics in transition metal dichalcogenide moiré bands," *Phys. Rev. Lett.* **121**, 026402 (2018).
- ⁵²⁴Y. Tang, L. Li, T. Li, Y. Xu, S. Liu, K. Barmak, K. Watanabe, T. Taniguchi, A. H. MacDonald, J. Shan, and K. F. Mak, "Simulation of Hubbard model physics in WSe₂/WS₂ moiré superlattices," *Nature* **579**, 353–358 (2020).
- ⁵²⁵J. Hubbard, "Electron correlations in narrow energy bands," *Proc. R. Soc. London A* **276**, 238–257 (1963).
- ⁵²⁶J. Quintanilla and C. Hooley, "The strong-correlations puzzle," *Phys. World* **22**, 32 (2009).
- ⁵²⁷"The Hubbard model at half a century," *Nat. Phys.* **9**, 523 (2013).
- ⁵²⁸E. C. Regan, D. Wang, C. Jin, M. I. Bakti Utama, B. Gao, X. Wei, S. Zhao, W. Zhao, Z. Zhang, K. Yumigeta, M. Blei, J. D. Carlström, K. Watanabe, T. Taniguchi, S. Tongay, M. Crommie, A. Zettl, and F. Wang, "Mott and generalized Wigner crystal states in WSe₂/WS₂ moiré superlattices," *Nature* **579**, 359–363 (2020).
- ⁵²⁹Y. Xu, S. Liu, D. A. Rhodes, K. Watanabe, T. Taniguchi, J. Hone, V. Elser, K. F. Mak, and J. Shan, "Correlated insulating states at fractional fillings of moiré superlattices," *Nature* **587**, 214–218 (2020).
- ⁵³⁰X. Huang, T. Wang, S. Miao, C. Wang, Z. Li, Z. Lian, T. Taniguchi, K. Watanabe, S. Okamoto, D. Xiao, S.-F. Shi, and Y.-T. Cui, "Correlated insulating states at fractional fillings of the WS₂/WSe₂ moiré lattice," *Nat. Phys.* **17**, 715 (2020).
- ⁵³¹C. Jin, Z. Tao, T. Li, Y. Xu, Y. Tang, J. Zhu, S. Liu, K. Watanabe, T. Taniguchi, J. C. Hone, L. Fu, J. Shan, and K. F. Mak, "Stripe phases in WSe₂/WS₂ moiré superlattices," *Nat. Mater.* **20**, 940 (2020).
- ⁵³²K. Hejazi, Z. X. Luo, and L. Balents, "Noncollinear phases in moiré magnets," *Proc. Natl. Acad. Sci. U. S. A.* **117**, 10721–10726 (2020).
- ⁵³³Y. H. Li and R. Cheng, "Moiré magnons in twisted bilayer magnets with collinear order," *Phys. Rev. B* **102**, 094404 (2020).
- ⁵³⁴D. Ghader, "Magnon magic angles and tunable Hall conductivity in 2D twisted ferromagnetic bilayers," *Sci. Rep.* **10**, 15069 (2020).
- ⁵³⁵J. H. Moon, S. M. Seo, K. J. Lee, K. W. Kim, J. Ryu, H. W. Lee, R. D. McMichael, and M. D. Stiles, "Spin-wave propagation in the presence of interfacial Dzyaloshinskii–Moriya interaction," *Phys. Rev. B* **88**, 184404 (2013).

- ⁵³⁶G. H. Shin, B. Koo, H. Park, Y. Woo, J. E. Lee, and S. Y. Choi, "Vertical-tunnel field-effect transistor based on a silicon-MoS₂ three-dimensional-two-dimensional heterostructure," *ACS Appl. Mater. Interfaces* **10**, 40212–40218 (2018).
- ⁵³⁷P. Wu, D. Reis, X. S. Hu, and J. Appenzeller, "Two-dimensional transistors with reconfigurable polarities for secure circuits," *Nat. Electron.* **4**, 45–53 (2021).
- ⁵³⁸T. Mikolajick, A. Heinzig, J. Trommer, T. Baldauf, and W. M. Weber, "The RFET—A reconfigurable nanowire transistor and its application to novel electronic circuits and systems," *Semicond. Sci. Technol.* **32**, 043001 (2017).
- ⁵³⁹K. Berggren, Q. Xia, K. K. Likharev, D. B. Strukov, H. Jiang, T. Mikolajick, D. Querlioz, M. Salinga, J. R. Erickson, S. Pi, F. Xiong, P. Lin, C. Li, Y. Chen, S. Xiong, B. D. Hoskins, M. W. Daniels, A. Madhavan, J. A. Liddle, J. J. McClelland, Y. Yang, J. Rupp, S. S. Nonnenmann, K.-T. Cheng, N. Gong, M. A. Lastras-Montaño, A. A. Talin, A. Salleo, B. J. Shastri, T. F. d. Lima, P. Prucnal, A. N. Tait, Y. Shen, H. Meng, C. Roques-Carmes, Z. Cheng, H. Bhaskaran, D. Jariwala, H. Wang, J. M. Shainline, K. Segall, J. J. Yang, K. Roy, S. Datta, and A. Raychowdhury, "Roadmap on emerging hardware and technology for machine learning," *Nanotechnology* **32**, 012002 (2021).
- ⁵⁴⁰R. Ge, X. Wu, M. Kim, J. Shi, S. Sonde, L. Tao, Y. Zhang, J. C. Lee, and D. Akinwande, "Atomristor: Nonvolatile Resistance switching in atomic sheets of transition metal dichalcogenides," *Nano Lett.* **18**, 434–441 (2018).
- ⁵⁴¹Z. Guan, H. Hu, X. Shen, P. Xiang, N. Zhong, J. Chu, and C. Duan, "Recent progress in two-dimensional ferroelectric materials," *Adv. Electron. Mater.* **6**, 1900818 (2020).
- ⁵⁴²K. Yasuda, X. Wang, K. Watanabe, T. Taniguchi, and P. Jarillo-Herrero, "Stacking-engineered ferroelectricity in bilayer boron nitride," *Science* **372**, 1458 (2020).
- ⁵⁴³D. Akinwande, N. Petrone, and J. Hone, "Two-dimensional flexible nano-electronics," *Nat. Commun.* **5**, 5678 (2014).
- ⁵⁴⁴N. R. Glavin, C. Muratore, and M. Snure, "Toward 2D materials for flexible electronics: Opportunities and outlook," *Oxford Open Mater. Sci.* **1**, itaa002 (2020).
- ⁵⁴⁵V. W. Brar, M. C. Sherrott, and D. Jariwala, "Emerging photonic architectures in two-dimensional opto-electronics," *Chem. Soc. Rev.* **47**, 6824–6844 (2018).
- ⁵⁴⁶H. Ling, R. Li, and A. R. Davoyan, "All van der Waals integrated nanophotonics with bulk transition metal dichalcogenides," *ACS Photonics* **8**, 721 (2021).
- ⁵⁴⁷B. Song, J. Hou, H. Wang, S. Sidhik, J. Miao, H. Gu, H. Zhang, S. Liu, Z. Fakhraei, J. Even, J. C. Blancon, A. D. Mohite, and D. Jariwala, "Determination of dielectric functions and exciton oscillator strength of two-dimensional hybrid perovskites," *ACS Mater. Lett.* **3**, 148–159 (2021).
- ⁵⁴⁸J. C. Blancon, J. Even, C. C. Stoumpos, M. G. Kanatzidis, and A. D. Mohite, "Semiconductor physics of organic-inorganic 2D halide perovskites," *Nat. Nanotechnol.* **15**, 969–985 (2020).
- ⁵⁴⁹H. Kim, G. H. Ahn, J. Cho, M. Amani, J. P. Mastandrea, C. K. Groschner, D. H. Lien, Y. Zhao, J. W. Ager, M. C. Scott, D. C. Chrzan, and A. Javey, "Synthetic WSe₂ monolayers with high photoluminescence quantum yield," *Sci. Adv.* **5**, eaau4728 (2019).
- ⁵⁵⁰M. Amani, D. H. Lien, D. Kiriya, J. Xiao, A. Azcatl, J. Noh, S. R. Madhupathy, R. Addou, K. C. Santosh, M. Dubey, K. Cho, R. M. Wallace, S. C. Lee, J. H. He, J. W. Ager, X. Zhang, E. Yablonovitch, and A. Javey, "Near-unity photoluminescence quantum yield in MoS₂," *Science* **350**, 1065–1068 (2015).
- ⁵⁵¹S. B. Anantharaman, K. Jo, and D. Jariwala, "Exciton-photonics: From fundamental science to applications," *ACS Nano* **15**, 12628 (2021).
- ⁵⁵²J. Gou, L. Kong, X. He, Y. L. Huang, J. Sun, S. Meng, K. Wu, L. Chen, and A. T. S. Wee, "The effect of moiré superstructures on topological edge states in twisted bismuthene homojunctions," *Sci. Adv.* **6**, eaba2773 (2020).
- ⁵⁵³X. Zhang, Z. Y. Al Balushi, F. Zhang, T. H. Choudhury, S. M. Eichfeld, N. Alem, T. N. Jackson, J. A. Robinson, and J. M. Redwing, "Influence of carbon in metalorganic chemical vapor deposition of few-layer WSe₂ thin films," *J. Electron. Mater.* **45**, 6273–6279 (2016).
- ⁵⁵⁴X. Zhang, T. H. Choudhury, M. Chubarov, Y. Xiang, B. Jariwala, F. Zhang, N. Alem, G. C. Wang, J. A. Robinson, and J. M. Redwing, "Diffusion-controlled epitaxy of large area coalesced WSe₂ monolayers on sapphire," *Nano Lett.* **18**, 1049–1056 (2018).
- ⁵⁵⁵Y. C. Lin, B. Jariwala, B. M. Bersch, K. Xu, Y. Nie, B. Wang, S. M. Eichfeld, X. Zhang, T. H. Choudhury, Y. Pan, R. Addou, C. M. Smyth, J. Li, K. Zhang, M. A. Haque, S. Fölsch, R. M. Feenstra, R. M. Wallace, K. Cho, S. K. Fullerton-Shirey, J. M. Redwing, and J. A. Robinson, "Realizing large-scale, electronic-grade two-dimensional semiconductors," *ACS Nano* **12**, 965–975 (2018).
- ⁵⁵⁶H. Li, Y. Li, A. Aljarb, Y. Shi, and L. J. Li, "Epitaxial growth of two-dimensional layered transition-metal dichalcogenides: Growth mechanism, controllability, and scalability," *Chem. Rev.* **118**, 6134–6150 (2018).
- ⁵⁵⁷T. Chowdhury, E. C. Sadler, and T. J. Kempa, "Progress and prospects in transition-metal dichalcogenide research beyond 2D," *Chem. Rev.* **120**, 12563–12591 (2020).